CRANFIELD UNIVERSITY

ELISABETE FERNANDES REIA DA COSTA

LIQUID MOULDING OF CARBON NANOPARTICLE FILLED COMPOSITES

SCHOOL OF APPLIED SCIENCES

PhD Thesis

Academic Year: 2010 - 2011

Supervisors: Dr Alexandros A. Skordos
Professor Ivana K. Partridge
October 2011

CRANFIELD UNIVERSITY

SCHOOL OF APPLIED SCIENCES

PhD

Academic Year 2010 - 2011

ELISABETE FERNANDES REIA DA COSTA

LIQUID MOULDING OF CARBON NANOPARTICLE FILLED COMPOSITES

Supervisors: Dr Alexandros A. Skordos
Professor Ivana K. Partridge

October 2011

Abstract

This thesis focuses on the incorporation of carbon nanoparticles within continuous fibre reinforcements by liquid composite moulding processes, in order to provide enhanced electrical and delamination properties to the multiscale composites. The mechanisms controlling the flow and filtration of these nanoparticles during liquid composite moulding are studied, in order to develop a predictive 1-D model which allows design of the processing of these composite materials.

Five different carbon nanoparticles at 0.25 wt% loading, three unmodified and one surface modified carbon nanotube systems and one carbon nanofibre system, were utilised to modify a commercial two-component epoxy resin utilised to impregnate carbon and glass reinforcements at high fibre volume fraction by resin transfer moulding. The dispersion of the nanofillers in the prepolymer was carried out by ultrasonication, high shear mixing or triple roll milling or a combination of the three. Electrical conductivity measurements of the carbon nanoparticle liquid suspensions during dispersion, alongside optical microscopy imaging and rheological analysis of these allowed the selection of the concentration of nanofiller and the appropriate dispersion technique for each nanoparticle system.

The resin transfer moulding process required adaptation to incorporate the dispersion and modify degassing steps, especially when utilising unmodified carbon nanoparticles suspensions, due to their higher viscosity and tendency to be filtered. Nanoparticle filtration was identified by electrical conductivity measurements and microscopy of specimens cut at increasing distances from the inlet. Cake filtration was observed for some of the unmodified systems, whereas deep bed filtration occurred for the surface modified CNT material. Property graded composites were obtained due to filtration, where the average electrical conductivity of the carbon and glass composites produced increased by a factor of two or one order of magnitude respectively. The effect of filler on the delamination properties of the carbon fibre composites was tested under mode I. The results do not show a statistically significant improvement of delamination resistance with the presence of nanoparticles, although localised toughening mechanisms such as nanoparticle pull-out and crack bridging as well as inelastic deformation have been observed on fracture surfaces.

Particle filtration and gradients in concentration resulted in non-linear flow behaviour. An 1-D analytical and a finite difference model, based on Darcy's law accompanied by particle mass conservation and filtration kinetics were developed to describe the flow and filtration of carbon nanoparticle filled thermosets. The numerical model describes the non-linear problem by incorporating material property update laws, i.e. permeability, porosity and viscosity variations on concentration of retained and suspended particles with location and time. The finite difference model is consistent and converges to the analytical solution. The range of applicability of the analytical model is limited to lower filtration coefficients and shorter filling lengths, providing an approximate solution for through thickness infusion; whereas the numerical model presents a solution outside this range, i.e. in-plane filling processes. These models allow process design, with specified carbon nanoparticle concentration distributions achieved via modifying the nanofiller loading at the inlet as a function of time.

Keywords:

dispersion, RTM, flow, filtration, modelling, finite differences, electrical conductivity, delamination

A meus pais e

à minha querida avó São

Acknowledgements

I would like to express my immense gratitude to my supervisors Dr Alex Skordos and Professor Ivana Partridge for having me as a PhD student in the Composites group. It has been an enormous pleasure to work here. I am extremely grateful to have had Dr Skordos as supervisor, for the enormous dedication, patience, respect and care shown for his students. His brilliant and broad knowledge on composites science has continuously motivated my research. I would like to specially thank Prof. Partridge for always providing extremely useful advice either in work or personal life matters. Her motherly support in the most difficult moments throughout this time in Cranfield will never be forgotten. I am also particularly grateful to Jim Hurley, Gary Muir, Andrew Dyer and Ben Hopper for sharing their technical knowledge and for all the assistance in the lab whenever was needed in such a pleasant and friendly way. I would also like to acknowledge Dr. Denis Cartié, Dr David Ayre, Dr. Dell'Anno and Dr. Manos Logakis for very important guidance and advice in scientific matters related to this thesis. I am especially thankful to Johannes for his friendship and help in commissioning the new RTM equipment, along with many helpful discussions and advices on the engineering aspects of composites manufacturing. Many thanks to all the friends and colleagues who have made my stay in Cranfield such a pleasant period; thankfully they are too many to name them all. Special thanks to Shelli and Tom for their friendship and for making England feel like home. I am also in dept with my parents and family for their continuous support and belief in me, despite the long periods away from home. I am profoundly grateful to Pedro for his immeasurable love, patience and support when deciding to share this life journey with me. Thank you Pedro, Willow and Ginge for making home such a relaxing place after a hard day of work.

Table of contents

List of figures

List of tables

Nomenclature

Flow and filtration modelling:

A	*Kozeny-Carman constant*
η	*viscosity [Pa.s]*
η_I	*intrinsic viscosity[-]*
φ_m	*filler maximum packing fraction*
ε	*porosity [-]*
ρ	*density [kg/m^3]*
h	*flow front position [m]*
C	*concentration of suspended carbon nanoparticles[kg/m^3]*
σ	*retention of carbon nanoparticles[kg/m^3]*
K	*permeability [m^{-2}]*
k_0	*filtration coefficient[1/m]*
k_r	*re-suspension coefficient [1/m]*
L	*length [m]*
U	*Darcy's velocity [m/s]*
M	*total number of time increments [-]*
N	*total number of grid points [-]*
P_o	*inlet Pressure [Pa]*
P_∞	*outlet Pressure[Pa]*
V_f	*fibre volume fraction [%]*
V_o	*initial prescribed velocity [m/s]*
T	*total concentration of nanofiller in the composite[kg/m^3]*
Indices	
o	*initial*
i, j	*position, time*

Mode I delamination testing:

P	*load [N]*
δ	*load line displacement [mm]*
a	*crack delamination length [mm]*
a_o	*initial pre-crack length [mm]*
b	*specimen width [mm]*
l	*specimen length [m]*
h	*half DCB beam thickness [mm]*
G_{IC}	*critical strain energy release rate for mode I [J/m^2]*
K_{IC}	*critical stress intensity factor [Pa.m$^{1/2}$]*
C	*beam compliance [N/mm]*
F	*correction factor for large beam deformation [-]*
N	*correction factor for stiffening of the load blocks [-]*
Δ	*correction factor for accounting with not perfectly built-in specimen [-]*
Indices	
init	*crack initiation values*
re-init	*crack re-initiation values*
prop	*crack propagation values*
arrest	*crack arrest values during propagation*

Uniaxial compression testing:

A	*area [m^2]*
F	*load [N]*
σ_{yc}	*uniaxial compressive yield strength [MPa]*
ε	*strain [%]*
ν	*Poisson's ratio [-]*
Indices	
o	*initial*
c	*compression values*
y	*yield*
t	*tension values*

Abbreviations

AC	Alternating Current
BSI	British Standards Institution
CNF	Carbon Nanofibre
CNP	Carbon Nanoparticles
CNT	Carbon Nanotube
COSHH	Control of Substances Hazardous to Health
CVD	Catalytic vapour deposition
DC	Direct Current
E-glass	Electrical grade glass
FDS	Finite Difference Scheme
LCM	Liquid Composite Moulding
LSP	Lightning Strike Protection
MWCNT	Multi-Walled Carbon Nanotube
NP	Nanoparticles
PTFE	Polytetrafluoroethylene
RTM	Resin Transfer Moulding
SEM	Scanning Electron Microscope
SM	Shear Mixing
SWCNT	Single-Walled Carbon Nanotube
TEM	Transmission Electron Microscope
TRM	Triple Roll Milling
UD	Unidirectional
μPIV	micro-Particle Image Velocimetry
US	Ultrasonication
VARTM	Vacuum Assisted Resin Transfer Moulding
VBA	Visual Basic for Applications

Terminology

Resin + CNT = Nanocomposites

Resin + CNT + Fibres = Multiscale composites

1 Introduction

In recent years, significant research efforts have focused on the processing and performance of fibrous composites with nanoparticle modified resins, in particular carbon nanotubes and carbon nanofibres. The extraordinary electrical, mechanical and thermal properties of these nanofillers can offer potential multifunctionality when incorporated within conventional fibrous composites, along with improved out-of-plane properties. These multiscale composites can present additional functions such as strain, stress and damage sensing, preventing crack propagation, alongside electromagnetic interference shielding, internal self-healing and active noise and vibration control [1]. Ultimately, these multiscale polymer composites have attracted great interest from the aerospace industry as a lightweight solution for the efficient lightning strike protection of composite structures. The electrically conductive nature of these nanofillers offers a lightweight solution for dissipation of the high current (up to 200 kA) carried by lightning strikes. The currently available lightning strike protection (LSP) structures rely on bonded aluminium and copper foils or meshes. These are normally placed on the outer skin in order to dissipate the current flow along a conductive pathway. Ideally, the current should flow throughout the composite skin to avoid degradation of the laminate layers (Figure 1.2), damaging the structure or interfering with sensitive electronic equipment on board.

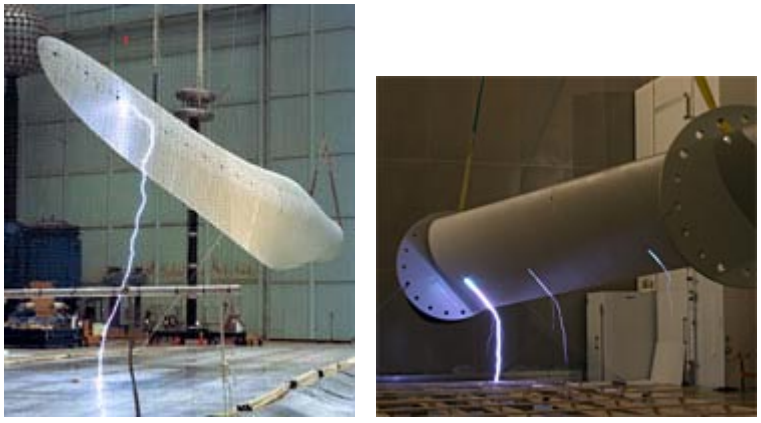

Figure 1.1 Lightning strike tests being performed on wind blade structures [2, 3]

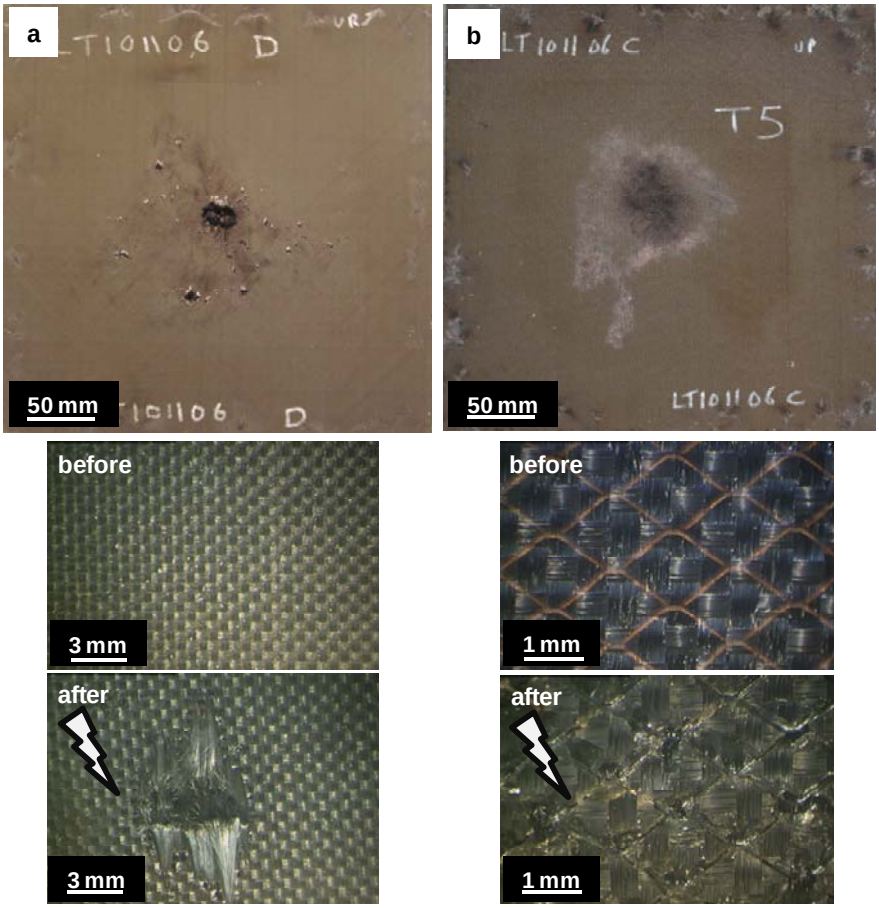

Figure 1.2 Epoxy/carbon fibre composite panels lightning strike tested, where (a) has no LSP and (b) has an embedded copper mesh at the top surface. After the lightning strike test, tufting and copper sublimation occurs for panel (a) and (b), respectively.

The multifunctional behaviour of these fillers offers advantages when aiming to combine electrical conductivity with enhanced delamination properties, known to be a frequent failure mode in fibre reinforced composites. At present, processing and transferring carbon nanoparticles exceptional properties to these fibrous composites is still seen as a challenge. The transfer of carbon nanofiller properties to composites hinges primarily on the achievement of homogenous and stable dispersions. Liquid composite moulding processes are widely utilised to produce these multiscale composites. However, increasing suspension viscosities associated to higher concentration of fillers and filtration phenomena taking place during infusion lead to longer process cycles and to a composite structure characterised by a graded concentration of carbon nanoparticles. Process optimisation and the possibility of using graded concentration versions of these hybrid composites as lightning strike protection

solutions (Figure 1.3) motivates the development of predictive models of the flow of carbon nanoparticle filled resins during liquid composite moulding, and of the concentration distribution *C* of these nanoparticles in the final component.

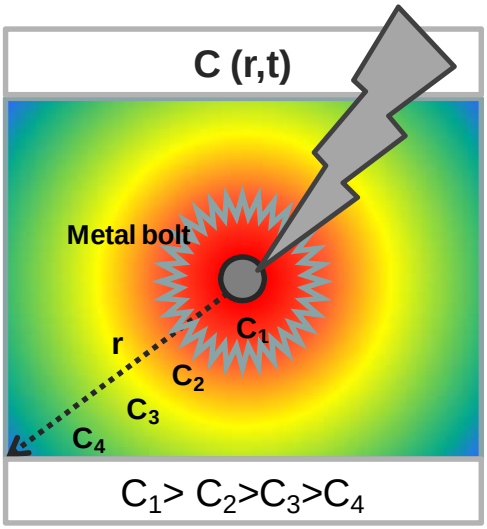

Figure 1.3 Schematic representation of a carbon filled composite with a graded conductive structure suitable for lightning strike protection applications.

This thesis focuses on the feasibility of incorporating different carbon nanoparticles into polymer matrices to infuse carbon and glass performs by liquid moulding processes, in order to provide enhanced electrical properties to the multiscale composites produced, whilst ensuring no degradation of mechanical performance. The study of the relationship between particle filtration and transfer of properties to the final composite was analysed. An analytical and a finite difference model, which describes the flow and filtration in liquid moulding, when utilising carbon nanoparticle modified resins was developed. The aim of this study was to control the flow and filtration of nano-filled resins during liquid composite moulding in order to tailor the final composite structure properties to suit the requirement of their end application. For this purpose a set of objectives was defined:

- ✓ development of dispersion methodologies for the carbon nanofiller/epoxy resin systems of this study;

- ✓ establishing the relationship between the dispersion state of carbon nanoparticles in epoxy, concentration and type of nanofiller, and corresponding electrical conductivity of such suspensions;
- ✓ adaptation and optimisation of resin transfer moulding for carbon nanoparticle filled epoxy systems;
- ✓ measurement of the effect of carbon nanoparticles on the flow of suspensions during RTM, alongside with identification of particle filtration by microscopy;
- ✓ evaluation of the enhancement of dielectric and delamination properties of the carbon nanoparticle hybrid composite panels produced by RTM;
- ✓ development and verification of predictive analytical and numerical models of the flow of nanoparticle filled resins during liquid composite moulding, which accounts for filtration of particles;
- ✓ implementation of the flow and filtration model in process design.

The current state of the art in processing carbon nanoparticle modified composites and modelling approaches for the prediction of the flow and particle filtration during liquid composite moulding is presented in chapter 2. The electrical and mechanical performance of multiscale composites is also reviewed in this chapter.

A detailed description of the materials utilised to manufacture the nanocomposites and multiscale composites in this study is presented in chapter 3. The dispersion methodologies, manufacturing procedures and characterisation are detailed in chapter 4.

The main outcomes of this work are reported in chapters 5 to 8. Chapter 5 and chapter 8 are extended and edited versions of papers submitted for publication. The main results are presented and discussed and the main conclusions are summarised in each of these chapters. Chapters 5 and 6 are dedicated to the processing of carbon nanotube and carbon nanofibre composites respectively. Detailed characterisation of nanofiller dispersion in epoxy, achieved by microscopy imaging and electrical conductivity measurements is presented alongside dispersion monitoring results using impedance spectroscopy. The results on flow of suspensions and particle filtration during filling of the fibrous reinforcement are also reported and form the basis for the development of the process model described in chapter 8. The delamination properties of the carbon

nanoparticle multiscale composites presented in chapter 5 and 6 are reported in chapter 7. The potential of using carbon nanoparticles for toughening is investigated.

Analytical and numerical finite difference models, incorporating appropriate material sub-models simulating the flow and filtration phenomena in liquid composite moulding of nanoparticle loaded resins are presented in chapter 8. These models are verified in terms of consistency and convergence and the process applicability of each of them is investigated. Process design examples are presented to demonstrate the capability of utilising these models in an industrial scale.

The main scientific findings are brought together in chapter 9, in the form of an overall discussion on the processing and modelling of carbon nanoparticle multifunctional composites. This chapter also discusses suggestions for future research aiming at exploiting the full potential of carbon nanoparticles on offering enhanced properties to polymer composites, alongside with strategies for the validation of the models proposed. Chapter 10 summarises the main conclusions of the work.

2 Literature review

2.1 Liquid moulding of composite materials containing carbon nanoparticles

The use of nanocomposites as part of high performance components in the aerospace industry necessitates the incorporation of nanoparticles within continuous fibre, usually carbon, composites. In recent years fibrous nanoparticles, such as CNFs and CNTs, have been introduced into the manufacture of high performance continuous fibre reinforced structural composites for aerospace applications, mainly in an attempt to improve their out-of-plane mechanical and electrical properties [4]. These hierarchically structured materials are usually referred to as 'multiscale polymer composites'. Conductive multiscale composites have also attracted great interest as structural health monitoring structures. For this function, carbon black nanoparticles [5] have been recently replaced by CNTs [6-8], due to their better electrical properties, which allow stress-strain monitoring, detection of structural damage, or even hydrothermal degradation [9], since variations in the composite electrical resistivity can be related to structural damage at the matrix level. The use of conductive matrix fillers for health monitoring is especially relevant in insulating materials, such as glass reinforced composites; in carbon composites, the conductive carbon fibres can act as sensors [10]. The enhancement in the electrical conductivity of these multiscale composites relies on the achievement of a percolated conductive network of carbon nanoparticles in the resin matrix prior infusion by liquid moulding routes.

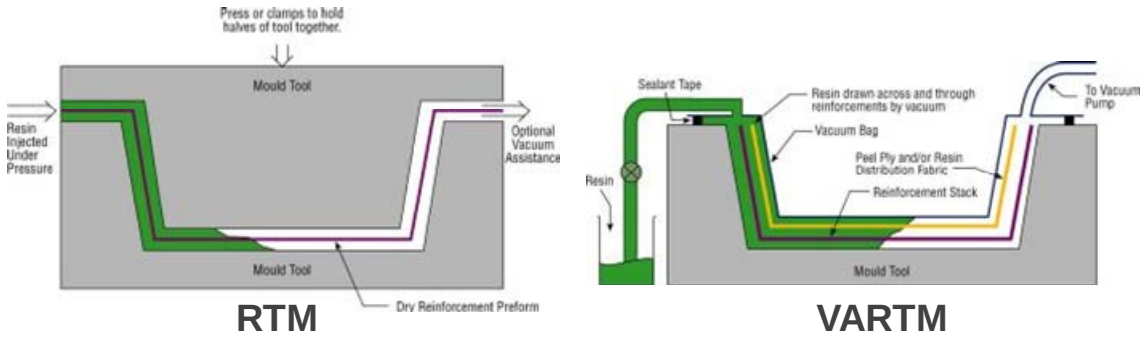

Figure 2.1 Schematic of RTM and VARTM processes [11]

The manufacture of these composites is generally achieved by employing and adapting existing liquid moulding processes, such as Resin Transfer Moulding (RTM) [12-15] and Vacuum Assisted Resin Transfer Moulding (VARTM) [6, 16-19]. The transfer of the unique properties of CNPs to these hierarchically structured composites still remains a challenge, and depends strongly on optimising the liquid moulding processing steps (Figure 2.2) to manufacture a multiscale polymer composite laminate.

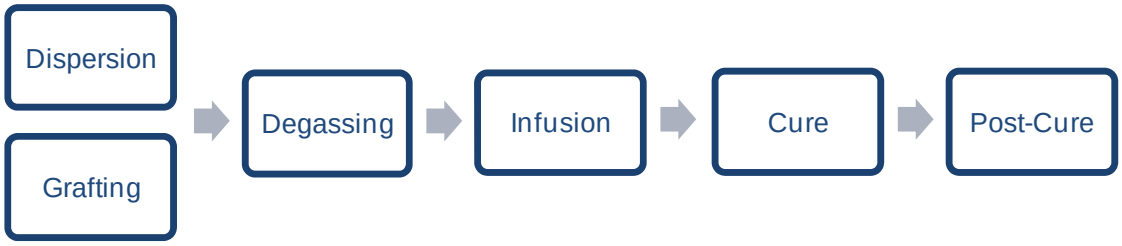

Figure 2.2 Liquid Composite Moulding processing steps

The manufacture of multiscale composites begins with the incorporation of the CNPs within the composite: either by dispersing the CNPs in a liquid polymer matrix, or by grafting them onto the fibrous reinforcement (Figure 2.3). This is followed by the removal of moisture and volatiles within the polymer resin or suspension prior to infusion. At this stage, the resin is brought into contact with the fibrous preform until its complete impregnation. Cure followed by post cure allows the complete solidification of the composite.

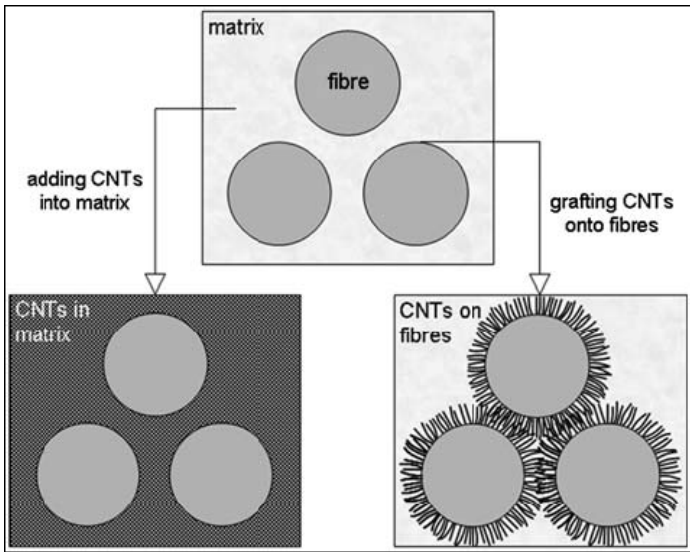

Figure 2.3 CNTs incorporation in fibre reinforced polymer composites [20].

The dispersion of carbon nanoparticles in polymer matrices is a crucial and still challenging step on the preparation of these materials. The achievement of a homogeneous and stable dispersion is the first and possibly the most important step towards the transferability of CNP properties to the final composite structure [21, 22]. The definition of a 'good' dispersion is not yet clear in quantitative terms and relies mainly on a qualitative assessment using microscopy techniques, such as optical and scanning electron microscopy (SEM). Freiman et al. [23] introduced the term 'optically dispersed', for suspensions where the aggregate size falls below 1μm. However, a good dispersion, characterised by very small aggregates, may not lead to transferable properties to the final composite, e.g. better electrical properties are obtained when a certain level of reaggregation is allowed [24].

The difficulty in dispersing CNTs arises from a combination of factors. Commercial CNTs are usually supplied in an entangled form. This is a consequence of the way commercial CNTs are manufactured, generally growing in entangled assemblies. In addition, strong van der Waals forces acting on a high specific surface area - which can reach values over 1000 m^2/g [7] - generate a high attractive force between CNTs. In order to overcome this problem, both physical and chemical dispersion enhancement methods have been used to obtain satisfactory and stable suspensions. The main techniques utilised to disperse CNTs in polymeric matrices were reviewed by a number of authors [25-27]. When processing thermosetting resins, ultrasonication, shear mixing and triple roll milling are among the most common physical dispersion methods, whilst CNP surface functionalisation, polymer wrapping and surfactant assistance promote the bonding of CNPs to the polymer, by modification of nanofiller surface properties [28].
Ultrasonication is the process of applying ultrasound energy to agitate particles in a suspension, causing the loosening of the outer layers of dense aggregates. It is the most common dispersion technique in low viscosity liquids. This technique can be applied in two ways, i.e. in low power mode using an ultrasonic bath [12, 29], or by means of a high specific power source, when using an ultrasonic horn or tip immersed in the liquid suspension [16, 30]. Shear mixing is generally associated to stirring processes, where the size and shape of the propeller and the mixing speed control the efficiency of the process. Usually for highly entangled CNPs systems high shear forces are required [30, 31]. Triple roll milling employs the shear force generated by the movement of three

rollers, running at different speeds to disperse CNP within the polymer. In order to maximise this dispersion, a viscous suspension is forced to pass between adjustable rollers several times, while the minimum gap distance between rollers can be set to 1-5 μm. This technique offers the advantage of processing large quantities of material without compromising the efficiency of the dispersion [32]. Successful dispersions of CNTs have been achieved when employing this technique [32, 33]

Surface and defect functionalisation are chemical methods based on the covalent linkage of functional groups onto CNT sidewalls or ends. Surface functionalisation is achieved through a series of chemical treatments, causing a change of hybridisation from sp^2 to sp^3, together with delocalisation of the π electron of the graphene outer layer of a nanotube. Defect functionalisation uses defect sites, such as open ends or holes in the sidewalls, pentagon or heptagon irregularities in the hexagon graphene lattice, or creates new defects by carrying out oxidative processes with strong acids in order to attach functional groups to CNTs (e.g. –OH and –COOH). These chemical techniques promote the interfacial bonding of functionalised CNPs to the polymer, providing enhanced mechanical and functional properties to the nanocomposite. However, these covalent methods generate a large number of defects on the CNTs sidewalls, and can ultimately originate CNT fragmentation. Lower aspect ratios and disruption of the π electron system of CNTs have a detrimental effect especially on their transport properties, as defect sites scatter electrons and phonons responsible for the electrical and thermal conduction of CNTs [25, 27].

Polymer wrapping and surfactant assistance/adsorption are alternative non-covalent functionalisation methods. Polymer wrapping consists of wrapping a polymer containing aromatic rings around CNTs by van der Waals interactions and π-π stacking. Surfactant assistance consists of the physical adsorption of a surfactant on the CNT surface. This physical method reduces CNT surface tension, preventing the formation of CNT aggregates. These methods increase the compatibility between polymer and functionalised CNPs, promoting the process of dispersion [25, 34, 35].

The liquid suspension route is advantageous over the fibre grafting technique, due to its simplicity and compatibility with the conventional industrial practice. However it is

limited to CNT contents below 0.3 wt%, as stable and homogenous dispersions of suspensions containing higher CNT loadings may lead to unacceptably high resin viscosities and render the application of liquid moulding technologies very difficult [13, 15]. As an exception, Thostenson et al. [17] reported the successful impregnation of unidirectional glass preforms by VARTM, with vinyl ester suspensions containing MWCNT loadings as high as 0.75 wt%. Degassing of the polymeric suspension is required prior to impregnation of the preform for the removal of volatiles and moisture. High temperatures or extremely long degassing times can promote reaggregation to undesirable levels. Therefore, this is an important stage, which might require optimisation in order to guarantee that the level of dispersion achieved in previous steps is not compromised.

In addition to the viscosity issues related to high CNT contents [13], filtration of the nanofiller by the fibrous medium during LCM [12, 36] may also lead to inadequate final component quality. Particle filtration causes the clogging of the porous medium channels, slowing down the resin flow front progression and thus resulting in longer infusion cycles and filler concentration gradients in the final composite structure.

Grafting of CNPs onto the fibrous reinforcement [37-39], or even manufacturing processes such as hand layup [14, 38, 40, 41] or 'transfer-printing' of CNTs forests to prepregs [42] (Figure 2.4) offer potential solutions for the manufacture of multiscale composites with higher concentrations of nanoparticles.

When designing LCM processes with CNPs, the effect of post-cure also needs to be taken into account. Gojny et al. [13] found that post-cure had a detrimental effect on the composite electrical conductivity. This suggests that reaggregation was related to the loss of conductive links during this stage. Despite the problems associated with the processing of such multiscale composites, enhanced mechanical and electrical properties have been reported and are reviewed in subsequent sections.

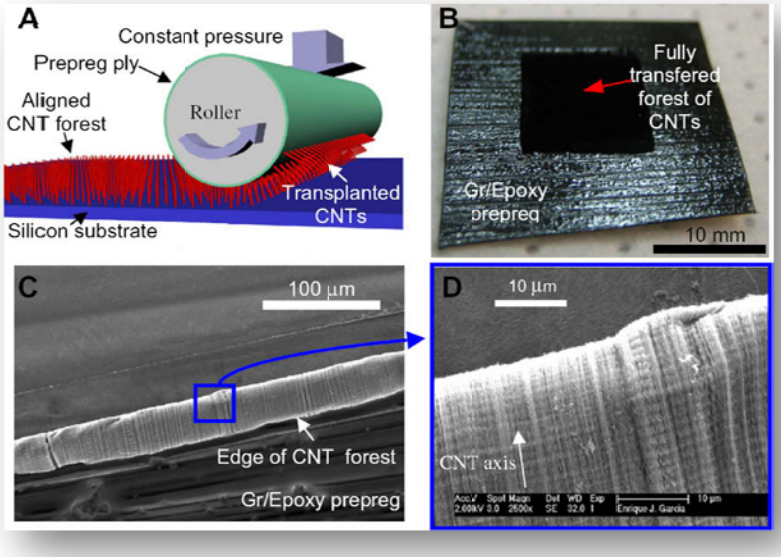

Figure 2.4 Transfer printing of CNTs to a prepreg [42]**.**

2.2 Modelling the flow and filtration of particle filled composites

2.2.1 Introduction

Particle filtration is a complex phenomenon dependent on a combination of processing conditions, such as the injection pressure or flow rate and the flow direction; and material properties, namely chemical and physical characteristics of the particles, the suspending liquid and the porous media. A good understanding of the infusion process and the main effect carbon nanoparticle filtration has on parameters such as viscosity, porosity and permeability is paramount for process control and model development of the flow and filtration of carbon nanoparticles during liquid moulding of composite materials.

2.2.2 Background

The flow and filtration of suspensions through porous media occurs in a variety of natural processes, in technological/industrial applications, and also in the manufacturing of multiscale composite materials. Filtration phenomena have been extensively studied specially in areas such as oil extraction [43-45], wastewater treatment [46, 47],

contaminated ground water flow [48, 49], paper processing [50], among others; where a high filter efficiency is essential.

The two-phase flow can be described by the flow of a suspension of either solid, gaseous or liquid domains dispersed in a liquid or gaseous medium through a granular or fibrous porous media. The operating filtration mechanisms involved in two-phase flow depend on the particles size, type of porous media, fluid flow rate, and mechanical and physicochemical interactions in the particle-fluid-porous medium system [51].

This work is focused on the two phase flow of solid particles in liquids through fibrous porous media. The two main filtration mechanisms in this case are cake filtration and deep bed filtration, which are depicted in Figure 2.5.

Cake filtration is a mechanism of volume capture taking place when the particle size is larger than the pore size. It is generally characterised by a deposit of particles, the filter cake, which builds-up at the surface of the porous media (filter), blocking the passage of particles suspended in the incoming fluid made to pass through the filter. It is usually employed in chemical processing industries to separate particles from dense suspensions with solid volume fractions higher than 2000 ppm [52].

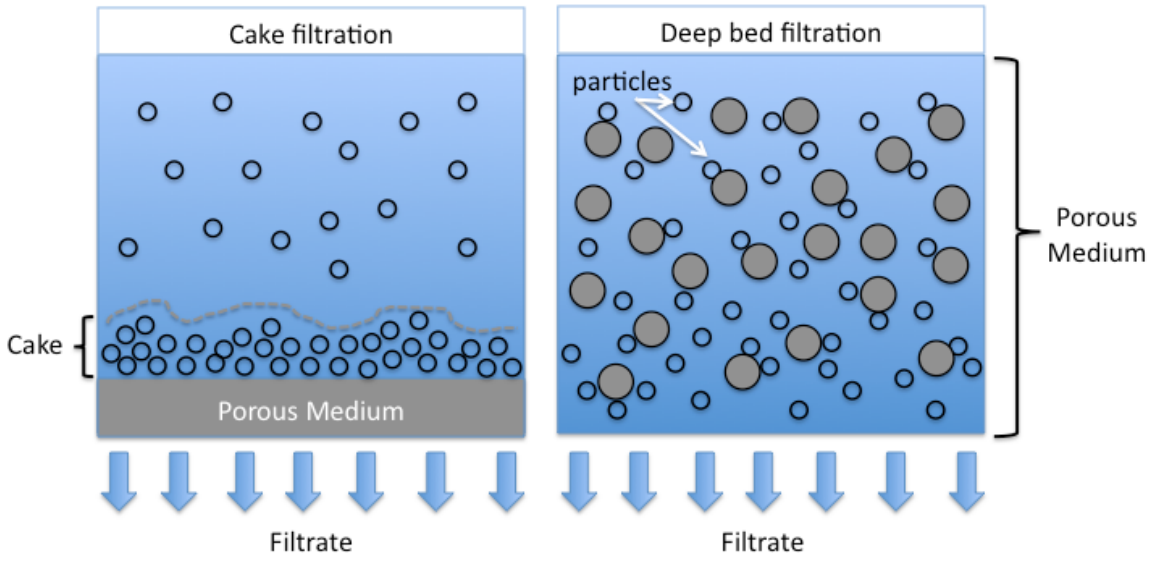

Figure 2.5 Schematic representation of cake filtration and deep bed filtration through porous medium.

Deep bed filtration is characterised by the gradual capture of particles smaller than the pore channels through a deep porous medium. In contrast to cake filtration, where the accumulation of particles happens at the surface of the filter medium, in deep bed filtration retention occurs inside the porous bed. Particles are brought into contact with the available retention sites when flowing through the porous medium. These particles can be retained on those sites or be carried further away by the flow of liquid. Moreover, retained particles can be eventually re-suspended spontaneously or when the flow conditions change. Continuous capture of particles leads to the narrowing of the available pore channels which may result ultimately in cake filtration behaviour.

Deep bed filtration can be divided into two main variants, ‘dead end’ and ‘cross flow’ filtration, as depicted in Figure 2.6. The main difference between them is the direction of the fluid feed stream, which occurs perpendicular or parallel to the filter bed for dead end or cross flow filtration, respectively.

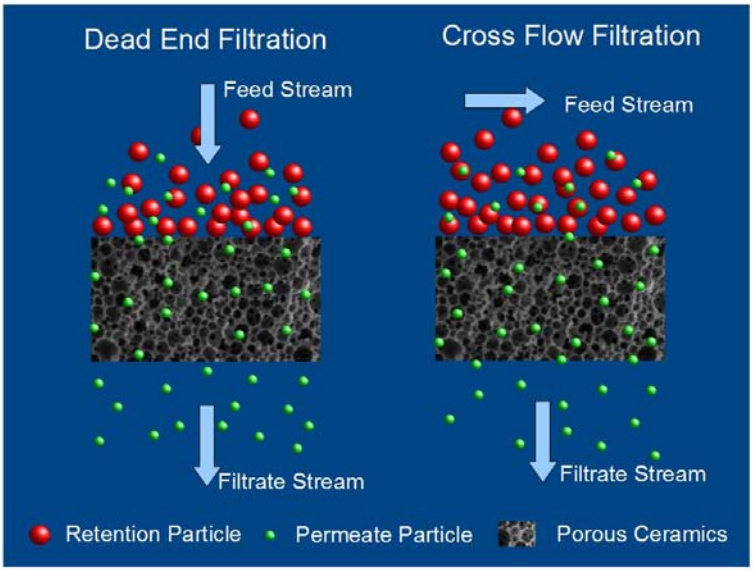

Figure 2.6 Schematic of the two types of deep bed filtration, namely dead end filtration and cross-flow filtration [53].

The capture of particles by the porous media (Figure 2.7) can occur by [51, 54]:

- Inertial impact. When particles have high inertia, either due to their weight, or high flow velocity they can deviate from the fluid streamlines and be deposited on the porous medium.
- Direct interception, can occur even when the particles pass in the vicinity of the porous bed, colliding with the walls of the filter bed due to their size.
- Diffusion by Brownian motion results from the random motion of very small particles, making them reach areas which are not typically irrigated by the liquid, resulting in their capture. Their zigzag path increases the probability of capture.
- Electrostatic attraction is another form of deposition which happens when opposite electric charges exist between the particles and the porous media.
- Hydrodynamic effects occur due to a non-uniform shear field and non-sphericity of particles, causing lateral migration of suspended particles which may be brought into contact with retention sites.
- Size exclusion or sieving, occurs when the particles are trapped at the entrance of a pore due to their larger dimensions. The larger the particles and the smaller the pores are the more intensive is the filtration process resulting in increased permeability drop [55-57].
- Sedimentation or gravitational settling. When the particles have a different density from the liquid, they are subjected to gravity forces and their velocity is not the same as the fluid they are in.

According to Herzig et al. [54], particle size governs the distinct volume and/or surface phenomena taking place during deep bed filtration. Generally, for suspensions containing large particles (diameter $d \geq 30$ μm) volume phenomena prevail over surface phenomena; whilst for small particles ($d \sim 1$ μm) surface phenomena are predominant; whereas for particles with dimensions between 3 μm and 30 μm, both volume and surface phenomena are as likely to occur. Other classifications of the filtration mechanisms are based on the ratio between the particle mean diameter and the grain mean diameter of a grain bed [58, 59]. These criteria are hardly applicable to fibrous porous reinforcements and tubular particles like the ones used for liquid moulding of

composites filled with carbon nanotubes and carbon nanofibres since they refer to geometrically distinct porous media and particle shape. Besides, in a liquid moulding scenario for manufacturing composite structures, filtration involves not only a drop in porosity and consequently permeability of the porous media, but it also affects the suspension viscosity and may slow down the resin flow front progression leading ultimately to longer infusion cycles.

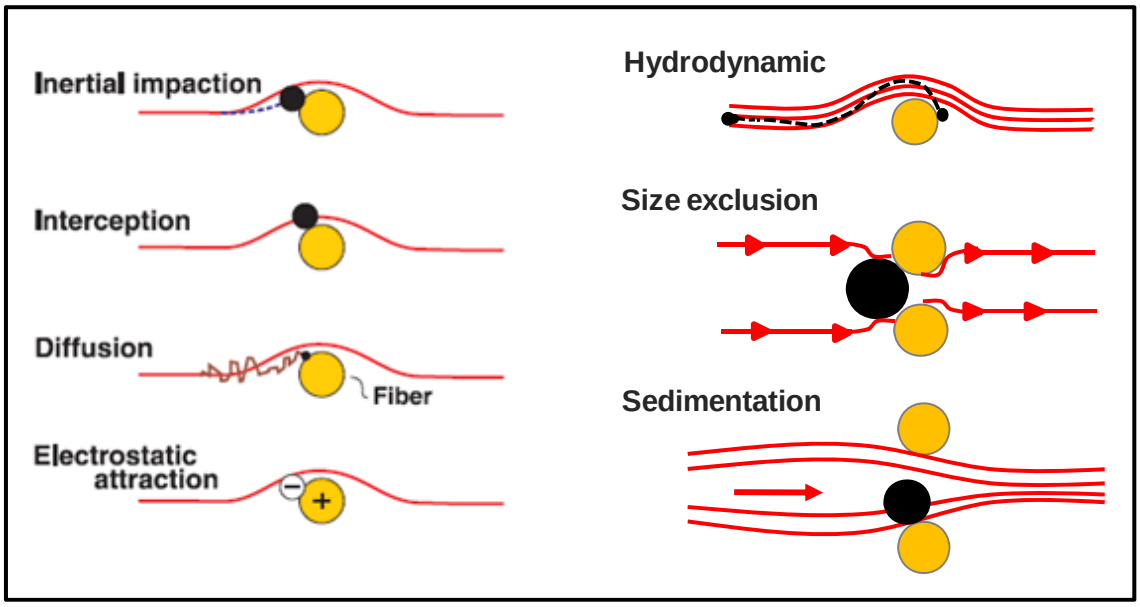

Figure 2.7 Main particle capture processes during two-phase flow (adapted from [60, 61]).

In order to describe the intrinsically transient deep filtration phenomena, both macroscopic and microscopic modelling approaches have been proposed in the literature. In macroscopic models the physical and chemical characteristics of the suspension and the flow field of the porous media are implicitly accounted for [62]. In contrast, microscopic approaches characterise the geometrical structure of the porous medium and accounts for dynamic changes caused by particle deposition, in order to establish a relationship with the macroscopic properties, providing knowledge on the nature of the filtration mechanisms present during processing. The microscopic approach can take into account the type of porous media or even the particle trajectory during flow. Generally, phenomenological models utilised to predict the filter efficiency are based on the classical deep bed filtration model.

2.2.2.1 Classical deep bed filtration model

The classical deep bed filtration theory which is utilised to model the flow and filtration of suspensions through porous media is generally described by a combination of Darcy's law [63], mass conservation and kinetics of particle retention [54, 64]. The classical system of equations for deep bed filtration is as follows,

$$\begin{cases} \dfrac{\varepsilon\,\partial C(x,t)}{\partial t} + \dfrac{U\,\partial C(x,t)}{\partial x} + \dfrac{\partial \sigma(x,t)}{\partial t} = 0 \\ \dfrac{\partial \sigma(x,t)}{\partial t} = k_o F(\sigma) U C(x,t) \\ U = -\dfrac{K_o K(\sigma)}{\eta}\dfrac{\partial P}{\partial x} \end{cases} \tag{2.1}$$

In this system of equations, $U(t)$ is Darcy's velocity; $C(x, t)$ is the concentration of suspended particles; $\sigma(x, t)$ is the concentration of deposited/filtered particles; ε is the porosity of medium; K_o the initial permeability of the porous medium, while $K(\sigma)$ is a function which accounts for changes in permeability with particle filtration, generally named 'formation damage function'; k_o is the initial filtration coefficient and $F(\sigma)$ is the retention function. The model described in (2.1) is accompanied by the following boundary and initial conditions:

$$\begin{cases} x = 0 : C(0,t) = C_o \\ t = 0 : C(x,0) = 0; \quad \sigma(x,0) = 0 \end{cases} \tag{2.2}$$

These conditions correspond to a constant fluid concentration at the inlet; and a zero concentration of suspended and retained particles before injection, which corresponds to a clean state of the porous medium.

The filtration coefficient can be described by a function which accounts for the probability of filtering a particle during the flux of liquid through a porous medium. This coefficient can not be determined beforehand as in the microscopic approach, but it needs to be determined from experimental results for the system being studied. This coefficient depends on the concentration of filtered particles σ, and also on the

geometrical characteristics of the particles and pores and the interaction forces within the system. It can be determined from the concentration curve corresponding to the liquid exiting the porous media (breakthrough curve), by solution of the inverse problem [44]. After the calibration of model parameters using the breakthrough curve, the profile of deposited particles can be predicted by either solving the direct analytical or numerical problem [43]. According to Herzig et al. [54] this coefficient is dynamic since it changes with particle deposition. Several expressions have been proposed in the literature to describe the particle filtration kinetics equation [52, 54, 64]; the one shown in the system of equations (2.1) describes the case where spontaneous re-suspension is negligible and the probability of retention $k_o F(\sigma)$ is independent of the suspension concentration C. The empirical determination of the retention function $F(\sigma)$ can be described by a general equation proposed by Ives [61] and Mohanka [65] as follows,

$$F(\sigma) = \left(1 + \frac{\sigma}{1-\varepsilon_o}\right)^{\alpha_1} \left(1 - \frac{\sigma}{\varepsilon_o}\right)^{\alpha_2} \left(1 - \frac{\sigma}{\sigma_{\max}}\right)^{\alpha_3} \tag{2.3}$$

where α_1, α_2 and α_3 are empirical constants, and $\sigma_{\max}$ is the maximum value of σ. According to Tien and Payatakes [52], experimental data indicate that $\sigma_{\max}$ varies from system to system but is usually in the range of $0.2\,\varepsilon_o$ to $0.4\,\varepsilon_o$.

A constant filtration coefficient k_o, can be determined using equation (2.4) [66], where L is the porous media length, and C_{in} and C_{out} are the particle contents at the inlet and outlet of the filter medium, respectively.

$$k_o = \frac{1}{L} \ln\left(\frac{C_{in}}{C_{out}}\right) \tag{2.4}$$

If the re-suspension coefficient k_r is considered independent of σ and C, then the filtration kinetics equation can be written as follows,

$$\frac{\partial \sigma}{\partial t} = k_o U C - k_r \sigma \tag{2.5}$$

The re-suspension term at the RHS of equation (2.5) can be particularly relevant if flow conditions change, mainly in terms of the magnitude and especially the direction of the

fluid flow. This effect is particularly important when medium and small sized particles (diameter < 30 μm) are present in the suspension [54]. In contrast, large particles (diameter ≥ 30 μm) seem to be irreversibly attached to the porous media even when subjected to changes in the fluid flow rate. Only changes in the flow direction can cause considerable re-suspension of such particles. Spontaneous re-suspension of particles, which is caused by local variations of the flow conditions, such as flow rate and pressure, in the vicinity of deposited particles; or even due to the collision of a moving with a retained particle is less likely. This is especially unlikely at the initial stages of filtration, but could be relevant when the bed is saturated at which point the interstitial velocity becomes considerably higher.

Macroscopic approaches are focused on the phenomenological description of the process, the prediction of its dynamic behaviour, and the development of methodologies and techniques for design, calculation and optimisation of the process. In contrast, microscopic theories, though more complex, provide information and understanding of the mechanisms of filtration and the conditions at which filtration is likely to occur. In addition, these approaches characterise the structure of the porous medium and how the deposition of particles affects that structure. The filter bed is generally described by an array of single collectors, characterised by a particular geometry, around or through which the fluid flows. The collector is defined as the fibre or grain of the porous medium at which the particles are deposited. There are three main categories of porous media models which are commonly used to study the physical and chemical phenomena taking place in the porous media, namely the capillary model, a number of spherical models and the constricted tube model [62]. The determination of the rate of particle filtration can be done by trajectory analysis. The collector geometry and size, the flow field around or within the specified collector, as well as the forces acting on particles during flow need to be specified for trajectory calculation [52].

Destephen and Choi [67], proposed a stochastic approach based on the Monte Carlo method as an alternative to both conventional macroscopic and microscopic models, to simulate liquid filtration of spherical particles through fibrous media including re-suspension phenomena. The re-suspension term is an essential factor in predicting the drop in efficiency of the filter as a function of time. The major advantage of this model

is the calculation of the global filter efficiency, instead of the prediction of the initial filtration performance. However, better description of the particle and fluid flow can be obtained via the trajectory analysis, rather than a simplified three-dimensional particle random motion.

Several changes have been made to the classical model described in (2.1) to incorporate other physical factors into the problem, such as the particle diffusivity [68], and particle and pore size distributions [45]. Santos et al. [45] applied average micro-models, by incorporating particle and pore-size distributions, in order to predict pore blocking and the permeability reduction during deep bed microfiltration in membranes, both in dead end and cross-flow filtration. A detailed description of the pore and particle size distributions is essential for the accuracy of this type of model prediction [45].

2.2.3 State of the art for particle filled composite materials

The phenomena of particle filtration during composites manufacturing by liquid moulding should not only be seen in the light of conventional filtration processes, where filtration efficiency is of primary importance, but as a phenomenon which can be controlled to the benefit of the end application. In composites manufacturing by liquid moulding, the objective may be to entrap all the particles in one layer, or achieve a uniform distribution of particles all over the composite, or even create a particle concentration gradient characterised by high content at specific regions to reinforce and negligible loadings at unimportant areas. Therefore, a good understanding of the process and the parameters involved is essential for efficient control of the process in order to achieve reproducible and optimum results. However, the subject of modelling flow and filtration of particle filled resins in fibrous porous media in the manufacture of fibre reinforced composites by LCM has received limited attention up to date.

2D Eulerian and Lagrangian multiphase approaches combined with a control volume finite element model have been developed by Elgafy et al. [69, 70] in order to predict the trajectories of spherical carbon nanoparticles in a resin suspension during liquid moulding. The Eulerian approach considers both the fluid and solid phase as a

continuous medium; whilst the Lagrangian approach treats the solid phase as separated particles that interact with the fluid flow, with position and velocity traced by means of a Lagrangian equation of motion. The effects of the solid phase are accounted for by adding mass and force terms into the continuity and momentum equations of the continuum fluid phase. The Lagrangian approach is especially relevant when interested in studying the behaviour and interaction of the solid phase entities, i.e. particles, with the continuous phase, i.e. fluid. The interfacial fluid layers around the microfibers are areas of high friction, which may result in sticking of particles on those sites. This effect was found preventable by applying convective currents around the fibre walls, causing vortices around them, preventing the deposition of particles on the microfiber walls. Other research works concluded that particles tend to be deposited in regions where shear strain rates are low [71, 72].

Particle filtration mechanisms were also investigated by Nordlund et al. [73] in a resin infusion scenario by means of micro-particle image velocimetry (μPIV) and microscopy, by setting up various meso-scale experiments and performing in-plane infusions in order to validate the meso-scale experiments. The use of fluorescent particles was used for tracking particle locations by μPIV. Preferential retention sites were identified around and in front of the fibre bundles. Particle size relative to intra-bundle spacing, and stationary flow regions located in channels perpendicular to the main flow direction were identified as the main factors responsible for particle filtration. Though several suggestions are given by Nordlund et al. [73] to minimise particle deposition, some of them like utilising preferably fabrics consisting of straight and unperturbed inter-bundle channels or orienting the fabric in order to reduce possible stagnation regions of the flow seem to be unrealistic when manufacturing advanced composite structures where very complex fabric reinforcements and lay-ups are required.

According to Destephen and Choi [67], when a fibrous porous medium is present, at least four capture mechanisms should be considered, such as particle capture by sieving, particle capture by fibres, particle capture by blocked pores and particle re-suspension.

Erdal et al. [74] developed a 2D macroscopic model which incorporates Darcy's law with transient particle filtration kinetics to describe moulding of particle filled

preceramic polymers of continuous fibre ceramic composites. This model takes into account an empirical viscosity function which is dependent on particle loading, as well as a dependence of the filtration coefficient on permeability. The modelling results provided a better understanding of the process. Particle filtration was found to be insensitive to the injection flow rate and to the concentration of particles in the suspending fluid.

Darcy's law combined with permeability drop, as a function of particle filtration, was used in combination with probabilistic methods by Chohra et al. [75] in order to determine the particle concentration distribution in each layer of a composite manufactured by through the thickness VARTM infusion. A non curing resin was used for this purpose in order to facilitate the quantification of the amount of particles in each layer. Results of the parametric study confirmed the importance of particle size distribution in relation to pore size distribution on the particle deposition pattern in the composite structure.

Macroscopic models of filtration were enhanced by Lefevre et al. [76, 77], who combined Darcy's flow solution coupled with conservation of mass, and filtration kinetics, to solve the 1D problem of infusing a fibrous reinforcement during liquid moulding. In addition Lefevre et al. [76, 77] accounted for porosity and permeability changes with retention content and viscosity variation with suspended particle content and shear rate, in time and position. The simulation process starts with the determination of Darcy's law solution by means of a finite difference solver; this solution then feeds to a finite element code which solves the filtration problem. At this point the material properties are updated and the process is repeated for each time step and position. The results seem to describe better the cases where lower particle contents are utilised. Lefevre et al. [76, 77] utilised an unsaturated polyester resin filled with spherical glass or ceramic microbeads to infuse either a synthetic or an E-glass fibre mat. These materials are convenient choices when burning off samples along the composite length for the evaluation of particle content. In addition the micron-sized particles and their relatively high content are advantageous when compared to carbon nanoparticles, which cause an increase of the suspension viscosity, and their small content becomes very difficult to be determined by a process of sample burning off.

A recent work from Akinyede et al. [78] presented an experimental study of nanoparticle filtration in a VARTM infusion scenario. Nano-alumina was utilised as a filler of an epoxy resin at 4 wt% content. Particle concentration was evaluated by thermo gravimetric analysis (TGA) using samples collected at various locations along the mould. According to this study, a higher rate of filtration is observed for fibre lay-ups which do not include a flow media on top of the plies.

2.3 Electrical behaviour of fibrous composites filled with carbon nanoparticles

2.3.1 Nanocomposites

The high electrical conductivity of carbon nanoparticles makes them very attractive polymer fillers, as minimal CNT loadings in an insulating resin can result in considerable improvements in the electrical properties of the produced nanocomposites [79, 80]. The transition from an insulating to a conducting polymer system as a function of carbon nanoparticles content is described by percolation theory. The percolation threshold is defined as the critical CNP volume fraction to allow the formation of a continuous network. This corresponds to a substantial increase of the system electrical conductivity by several orders of magnitude (Figure 2.8).

Four main classes of percolation models can be found in the literature [81], i.e. statistical, thermodynamic, geometrical and structure oriented, which take into account the surface energies, viscosity, orientation and aspect ratio of the filler. However, the majority of the percolation models found are statistical predictions of the system conductivity, according to the probability of particle contact formation within the composite. The statistical percolation model [82] predicts the dependence of conductivity on filler concentration, in the form of a power law,

$$\sigma = \sigma_f \cdot (\phi - \phi_c)^t, \phi \geq \phi_c \tag{2.8}$$

where σ is the composite conductivity, σ_f is the filler conductivity, ϕ is the volume fraction of the filler, ϕ_c is the percolation threshold and t is an exponent dependent on the geometry of the lattice.

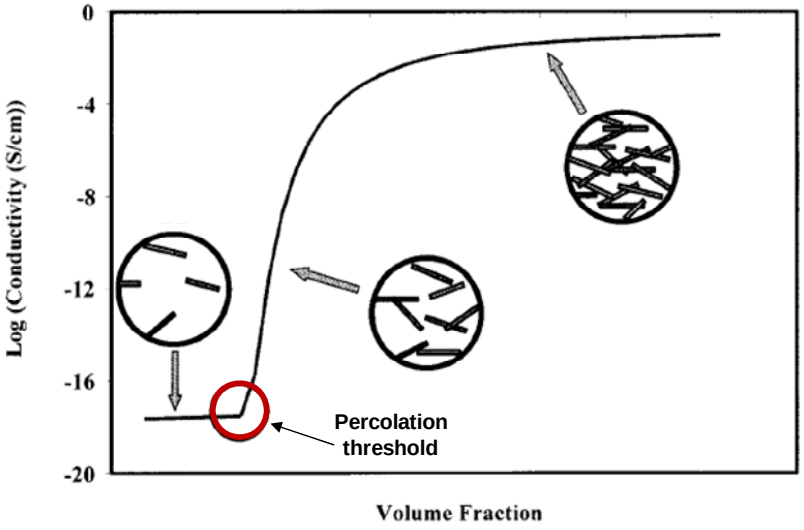

Figure 2.8 Electrical conductivity dependence on filler content (adapted from [81]).

A theoretical approach to estimate the percolation threshold of composites filled with statistically dispersed non-spherical particles is the excluded volume theory. The excluded volume $\langle V_{ex} \rangle$ is defined as "*the volume around an object in which the centre of another similarly shaped object is not allowed to penetrate*" [83, 84]. The percolation threshold ϕ_c can be approximated by the ratio between the volume of randomly oriented cylinders in the composite and $\langle V_{ex} \rangle$, and consequently becomes a function of the aspect ratio, i.e $\phi_c \approx 1/a$ [83], and $\phi_c \approx 0.7/a$ [84].

Kovacs et al. [24] proposed the coexistence of two characteristic percolation thresholds for composite materials with low viscosity behaviour during processing, i.e. a static and kinetic network formation processes. The higher threshold is described by the statistical percolation model and is independent of the processing conditions. The kinetic percolation threshold can reach very low filler concentrations, since it accounts for particle movement and reaggregation during dispersion processing. In fact, conductivity is highly dependent on process parameters, and a certain level of reaggregation is favourable to the formation of a conductive network [24, 85, 86]. This is in line with the extremely good dispersions, but higher percolation thresholds achieved when utilising functionalised CNTs as fillers [79]. The filler functional groups react with the polymer matrix forming an electrically insulating layer between nanoparticles, which increases the distance between CNTs. The higher compatibility with the polymer matrix hinders

reaggregation, reducing the final conductivity of the composite [79]. Nevertheless, functionalisation boosts the interfacial adhesion between CNTs and polymeric matrix, leading to enhanced mechanical properties. Furthermore, lower percolation thresholds are generally obtained for fibre-shaped particles, like CNTs, than for spherical particles which have a lower aspect ratio [79].

A comprehensive review on the electrical percolation of CNTs in polymer nanocomposites has been recently published by Bauhofer and Kovacs [87]. Most of the publications found in the literature are based on epoxy composites. The lowest percolation thresholds have been reported for epoxy systems. According to Bauhofer and Kovacs [87], the high percolation thresholds and high CNT contents to achieve maximum conductivity reported in Figure 2.9(a) and (b) are a consequence of poor CNT dispersion processing.

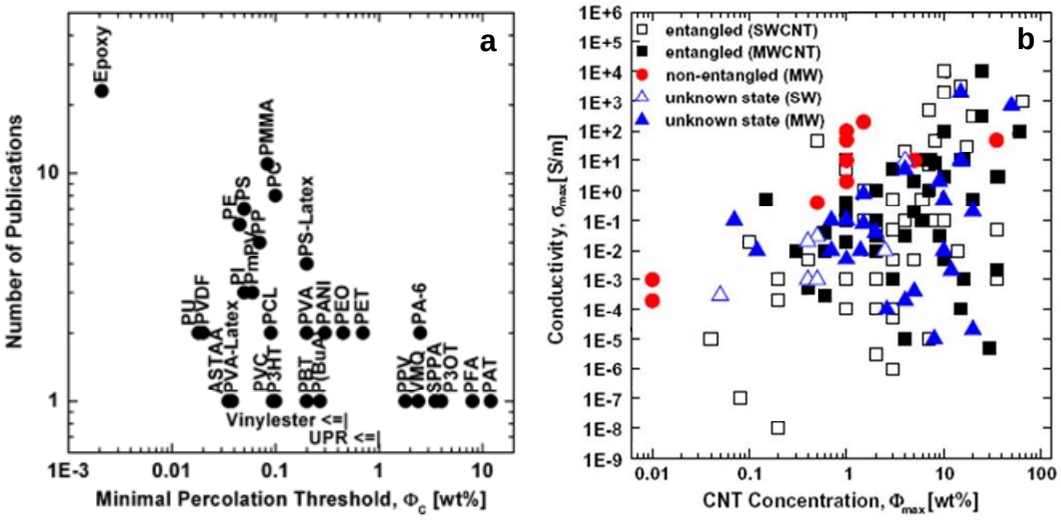

Figure 2.9 Comparative study of the maximum electrical properties of polymeric CNTs systems as a function of the CNT content (adapted from [87]).

According to Gojny et al. [79], MWCNTs have the highest potential to improve the electrical conductivity of epoxy composites, due to their high aspect ratio and relatively low surface area. The percolation threshold is increased if any kind of treatment, e.g. functionalisation, ultrasonication, results in the reduction of the aspect ratio of CNTs. However, the minimum percolation thresholds and maximum conductivities are dependent more on the polymer type and dispersion method, than on the type and manufacturing method of CNTs [87].

2.3.2 Multiscale composites

A number of publications have reported improvements in the electrical conductivity of multiscale composites when carbon nanoparticles are used as fillers at contents above the percolation threshold. A highly anisotropic electrical behaviour was reported for glass fibre based composites [13, 15, 17], where the in-plane conductivity was found to be more than one order of magnitude higher than in the out-of-plane direction [13, 15]. The matrix channels between glass fibres were reported to be preferential sites for the formation of an electrically conductive CNT network [13]. In addition, the composite in-plane conductivity in the fibre direction was reported by Thostenson et al. [17], to be one order of magnitude higher than in the transverse direction and independent of the processing conditions, i.e. the fibre alignment with the flow direction. However, the anisotropic behaviour is essentially explained by the alignment of the resistive components of the composite, i.e. resin and fibres, in relation to the direction of the measurement. For measurements in the fibre direction, resin and fibres behave like parallel resistors, while in the transverse direction, they behave like serial resistors. Hence higher resistance values are expected in the transverse direction.

A detrimental effect of post-cure on the overall electrical conductivity of 0.3 wt% functionalised DWCNT-NH_2 glass composite was reported by Gojny et al. [13]. This behaviour was related to the breaking up and interruption of the conductive paths formed by CNTs during post-cure and shrinkage, respectively. Figure 2.10 (b) summarises the electrical conductivity dependence on direction and cure stage of these modified composites. Despite better dispersability and mechanical properties associated with functionalised CNTs fillers, functionalisation processes reduce CNT electrical conductivity and consequently compromise the transferability of this property to multiscale composites [13, 18].

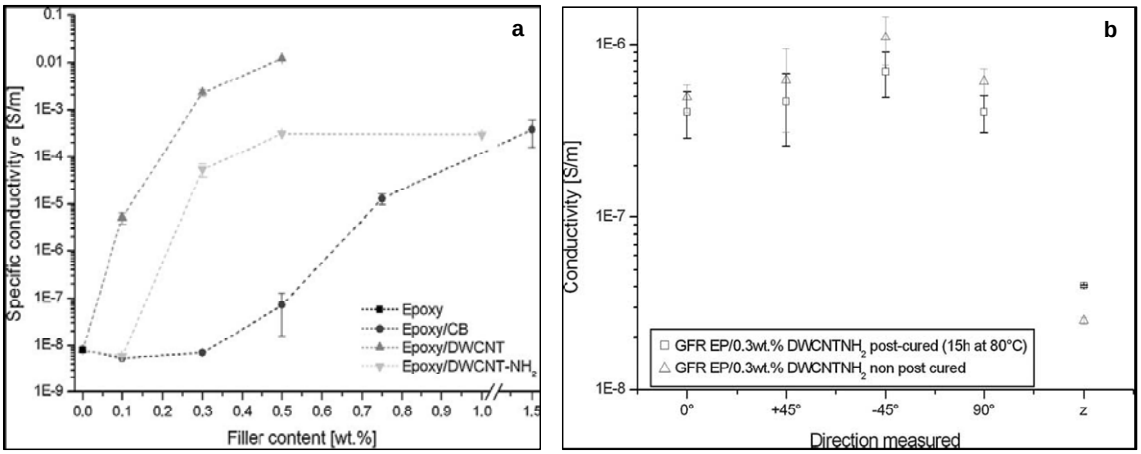

Figure 2.10 Electrical conductivity of the carbon nanoparticle filled epoxy (a) and of the nano-filled glass fibre composite in different orientations (adapted from [13]])

According to Wichmann et al. [15], a better enhancement is obtained when MWCNTs are utilised as matrix fillers. A comparative study of the electrical conductivity of glass composites modified with a number of distinct carbon nanoparticles at 0.3 wt% loading was presented in [15], and is shown in Figure 2.11. MWCNTs were found to be preferential modifiers for enhancing electrical conductivity of fibre composites, when compared to carbon black (CB), pristine and functionalised DWCNTs, reaching conductivity values similar to the corresponding nanocomposite system. Two fibre volume fractions were utilised in DWCNT systems in order to evaluate the effect of fibre volume fraction on electrical conductivity. It was found that higher fibre volume fractions cause a slight improvement of the overall composite conductivity instead of its reduction. This occurs, as long as an increase in fibre volume fraction does not cause the destruction or blocking of the conductive network by e.g. the insulating glass fibres, otherwise a detrimental effect would be expected. In the z-direction, the glass fibres perpendicular to the electric pathway act as stronger barriers to the current passage. The application of an electric field in the z-direction during the cure process can oppose this effect, leading to improvements of more than one order of magnitude for the DWCNTs system (Figure 2.11(b)).

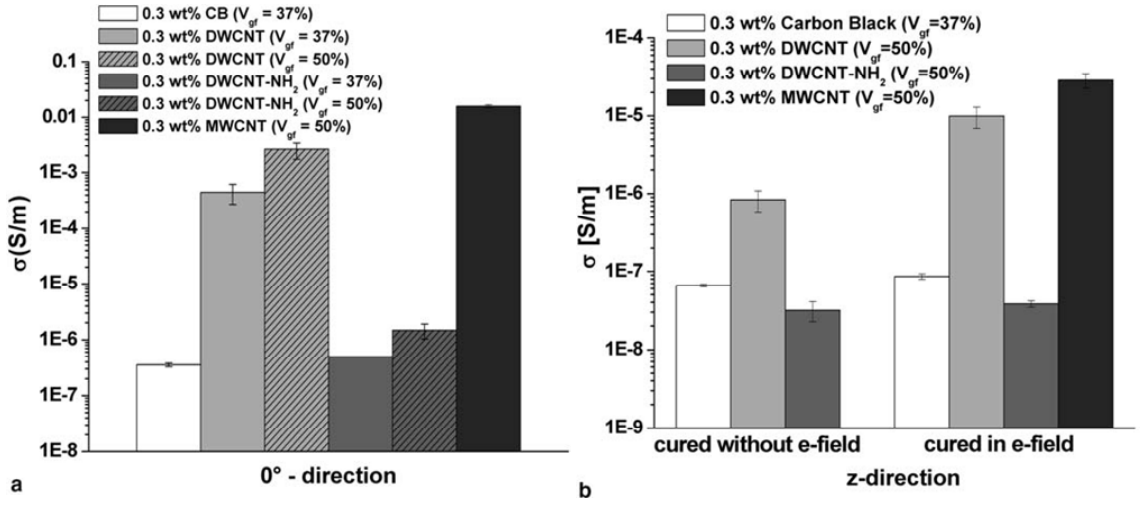

Figure 2.11 Electrical conductivity of the carbon nanoparticle filled laminates in the 0º-direction (a), and z-direction (b) (adapted from [15]).

Improvements in the electrical conductivity of carbon fibre composites have been also reported despite their intrinsic conductive nature [4, 88]. The intrinsically anisotropic electrical behaviour encountered in carbon composites is mainly governed by the conductivity [89] and orientation of the carbon fibres, the fibre type, the fibre volume fraction and the stacking sequence of the plies [90]. In glass composites the formation of CNP conductive pathways, especially along the flow direction, controls this anisotropic behaviour. Similar behaviour may be present in carbon composites, yet the inherent carbon fibre conductivity could be disguising this effect [91]. Hence, the higher improvements in electrical conductivity are expected to occur in the out-of-plane direction, where these composites generally exhibit poorer performance, since this direction is dominated by the polymer matrix.

A two fold improvement in the through thickness electrical conductivity of SWCNTs filled carbon composites was reported by Bekyarova et al. [4], when depositing 0.25 wt% CNTs (with respect to the fibre reinforcement) by electrophoresis; whilst the in-plane conductivity was unaffected. When higher contents of MWCNTs and CNF, such as 0.6 and 0.5 wt% are deposited by electrophoresis in carbon fibres, improvements of about one order of magnitude were reported by Lee et al. [88].

Exceptional improvement of the overall electrical conductivity are achieved when very high volume fraction (0.5 - 3%) of extremely long, dense and aligned MWCNTs are

grown on a ceramic fibre reinforcement [38, 92], achieving a 3D reinforcement. Reductions of 10^6 and 10^8 Ohm.mm were reported by Garcia et al. [38] for the in-plane and out-of-plane directions, respectively. The lower resistivity results in the through thickness direction are attributed to the orientation of the CNT long axis in this direction, bridging the insulating epoxy matrix between the fabric plies.

2.4 Delamination properties of carbon nanoparticle filled composites

Fibre reinforced composite materials are primarily chosen for their excellent in-plane mechanical properties. However, in general these composites present poor interlaminar properties when subjected to out-of-plane stresses. As a result delamination occurs. Overcoming this problem is still one of the major challenges for the composites industry. Several toughening techniques are available and include 3D-reinforcement and matrix modification. 3D weaving, z-pinning, tufting and stitching have shown good results in improving interlaminar toughness [93-96] . The damage caused by the through thickness reinforcement can compromise in-plane properties [97, 98]; however, careful selection of process parameters can minimise or eliminate this effect [99]. Toughening can be also achieved by adding modifiers to the thermoset resin such as thermoplastics, rubbers, and inorganic particles. Stiffness can remain unaltered or be adversely affected when thermoplastics [100, 101] or rubbers [102] are utilised as modifiers.

Nanoparticles can be seen as promising materials for matrix toughening in nanocomposites or multiscale composites. The mechanisms of nanoparticle toughening taking place in composite materials, along with reported improvements in the toughenability of multiscale composites when utilising different manufacturing approaches, are reviewed in the following sections.

2.4.1 Mechanisms of nanoparticle toughening

The main parameters influencing nanocomposites toughening are the intrinsic toughenability of the matrix, particle volume fraction, particle size and shape, interfacial bonding, and dispersion state. The most important micro-mechanical mechanisms leading to the increase of toughness in a resin when incorporating micro and nano-

particles have been widely studied in [103-106]. The mechanisms involved in toughening are as follows:

- ***Localised inelastic matrix deformation and void nucleation*** is characterised by the inelastic deformation of the matrix around the voids left by the debonded particles [105, 107]. According to Kinloch and Taylor [107] such voids can close when subjected to thermal treatment, above the glass transition temperature, and allowed to relax, as shown in Figure 2.12. Gojny et al. [108] report observation of shear bands around the agglomerates of DWCNTs and cavities.

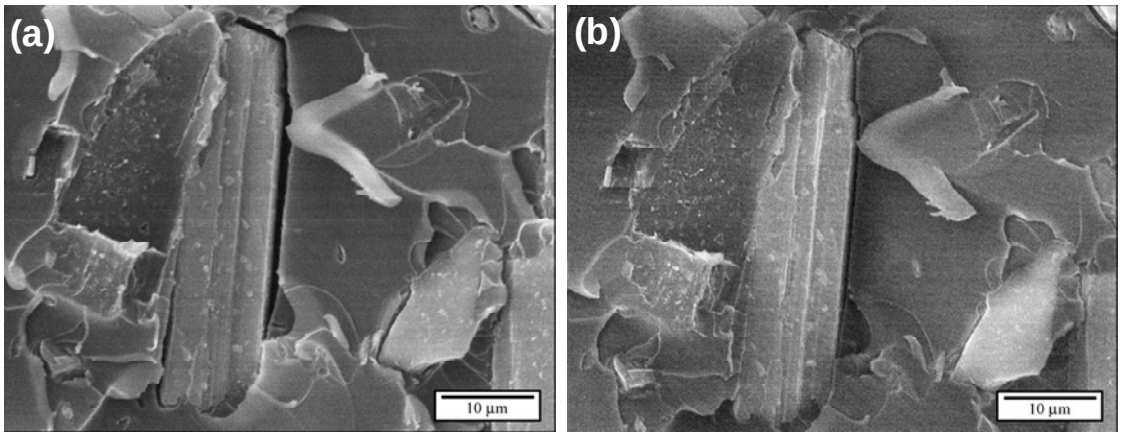

Figure 2.12 Fracture surface of cyanate-ester polymer modified with 10% wollastonite tested at 150°C: (a) fracture surface, and (b) fracture surface after heating for 10 minutes at 10°C above *T*g [107].

- ***Crack deflection*** occurs when the crack front tilts on encountering particles and then twists when propagating around them (Figure 2.13). As reported by Faber et al. [109] higher toughening is expected for rod-shaped particles than disc-shaped or spherical ones. The higher aspect ratio of the rod-shaped particles the more effective in toughening they are since a higher deflection results in the generation of an increasing surface area, as illustrated schematically in Figure 2.14 [109].

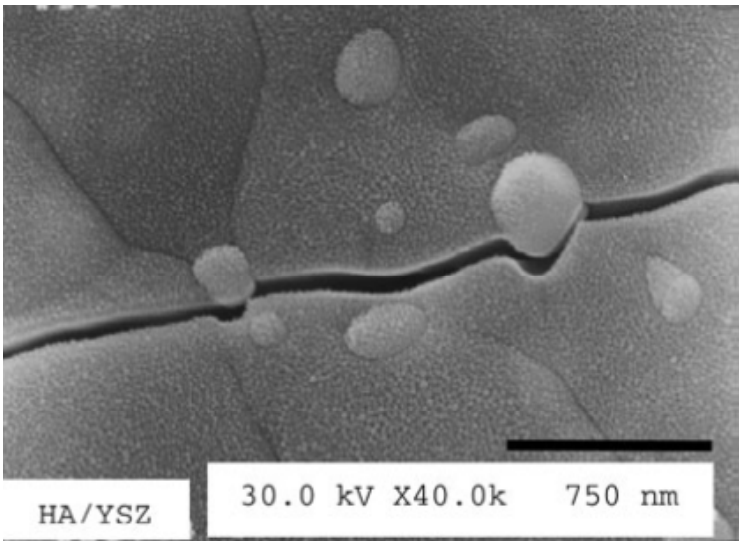

Figure 2.13 SEM picture during indentation fracture showing crack deflection by zirconia particles in a hydroxyapatite matrix [110].

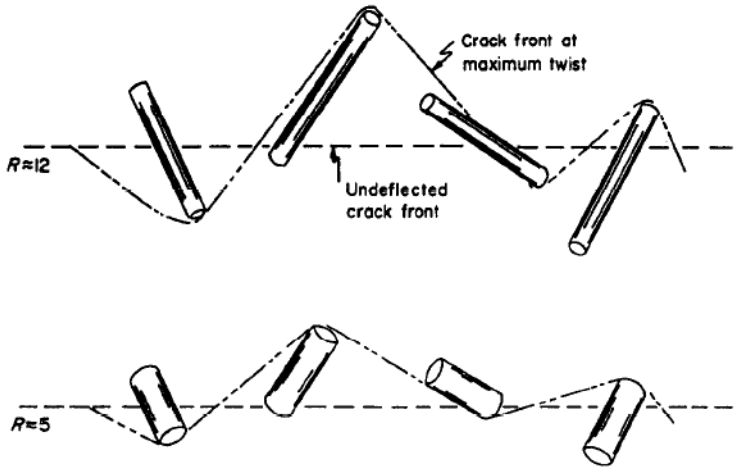

Figure 2.14 Schematic representation of crack deflection around rod-shaped particles with two aspect ratios *R*, at constant volume fraction [109].

- ***Crack pinning***, [111] which is shown in Figure 2.15, is comparable to the resistance to movement of dislocations in metals, which occurs when interstitial defects, interfaces and other dislocations act as pinning point during the movement of dislocations in the crystal lattice. Dislocations bow between particles and therefore increase in length. In a similar way cracks bow between particles increasing the energy required for propagation. Generally the presence of bowing lines on the fracture surface, such as these shown in Figure 2.16, is

indicative of this toughening mechanism. This mechanism is unlikely to occur in nanoparticles toughening since the crack-opening displacement is much larger than the actual particle size. Nonetheless, for the cases where micrometric CNT agglomerates are present in the final suspension, crack pinning could be considered as a possible toughening mechanism.

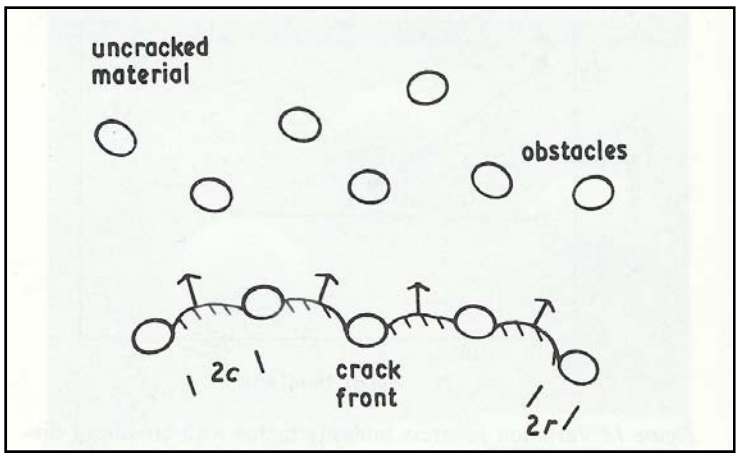

Figure 2.15 Schematic representation of the toughening process of crack pinning (adapted from [104])

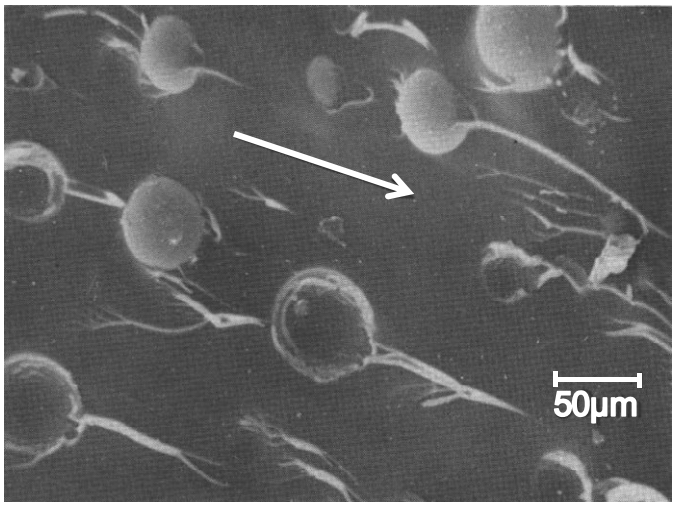

Figure 2.16 SEM micrograph of a fracture surface of an epoxy resin filled with spherical glass particles showing the 'tails' behind the particles. Arrow indicates the direction of crack propagation (adapted from [112])

- ***Fibre pull out*** can significantly increase the work of fracture due to interfacial friction between fibre and matrix, while bridging the crack. The interfacial strength and the interfacial area are the main contributors for an improved G_{IC}

[21]. These properties are particularly relevant for modifiers such as surface modified CNTs, which combine extraordinary high interface area with very strong interfacial bonding. Amino-functionalised and as-received DWCNTs were shown bridging the crack while being pulled out of the epoxy matrix by Gojny et al. [108], see Figure 2.17.

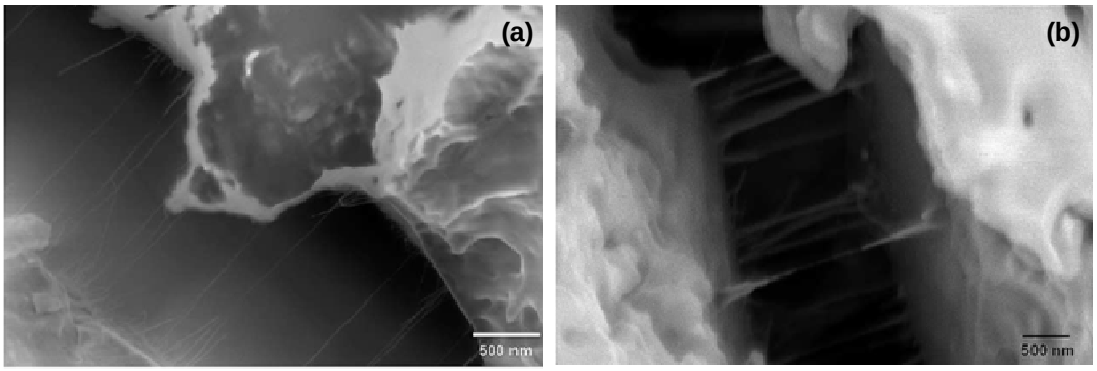

Figure 2.17 SEM-micrographs of amino-functionalised (a) and non-functionalised (b) DWCNTs bridging a crack induced by etching on epoxy nanocomposites [108].

Special attention has been given to CNTs as toughenners due to their excellent mechanical properties. However, for a better exploitation of CNTs properties, a sufficient stress transfer from the CNTs to the matrix is necessary. This can be achieved by means of an efficient CNTs dispersion and by utilising functionalised CNTs, which will promote the interfacial bonding between CNT and matrix [108, 113].

Possible fracture mechanism of CNTs are suggested by Gojny et al. [108], as shown in Figure 2.18. The initial situation refers to an isolated CNT completely surrounded by the resin (Figure 2.18(a)). The failure mechanisms depicted in Figure 2.18 (b) - (e) were proposed for CNTs bridging a crack. These failure mechanisms are mainly dependent on the interfacial adhesion and the mechanical properties of CNTs. For poor interfacial adhesion, simple pull-out from the matrix occurs (Figure 2.18 (b)). Stronger bonding between the matrix and the CNTs leads to CNT rupture (Figure 2.18 (c)) or to the fracture of the outer layer and a telescopic pull out of the inner tube(s) (Figure 2.18 (d)). This mechanism is also named ‘sword-in-sheath’. For stronger interfacial bonding between the reactive groups and the matrix, partial debonding allows the bridging of the crack (Figure 2.18 (e)). Increasing stresses would ultimately lead to CNT failure, as shown in Figure 2.18 (c) and (d).

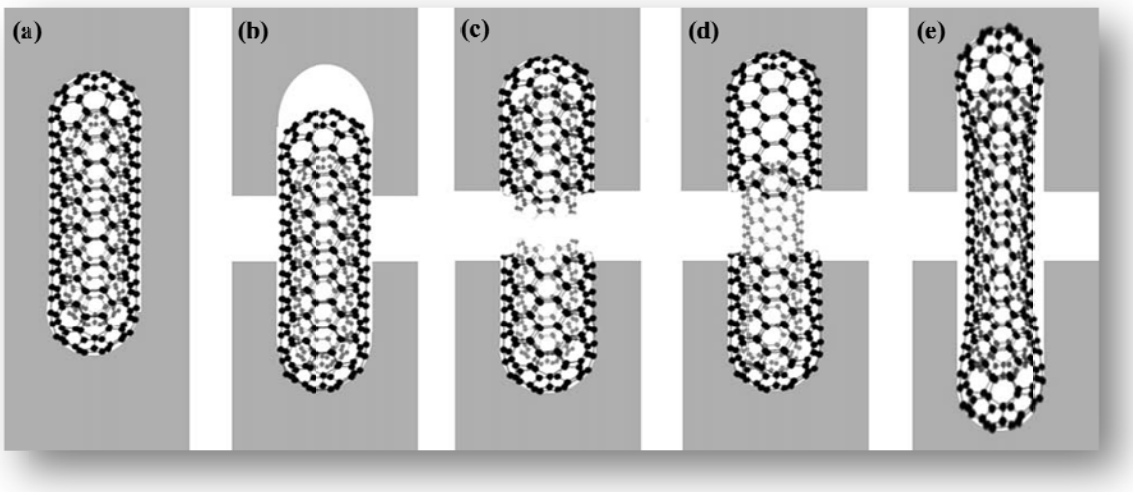

Figure 2.18 Schematic description of possible fracture mechanism of CNTs (adapted from [108]).

A combined analysis based on atomistic simulation, shear lag theory and fracture mechanics was carried out by Cheng et al [114]. This analysis focused on the importance of the interface area and strength to the composite fracture toughness properties. Optimal CNT-bridging stiffness, strength and toughness control the transition from interfacial debonding to CNT fracture. Maximum fracture toughness values can be achieved by tailoring these properties by means of optimised CNT length and interface functionalisation bond density values. These results are in agreement with previous work from Gojny et al. [108] which recognised the better dispersability and interfacial adhesion associated to surface functionalised CNTs, but considered a very strong interfacial adhesion detrimental to toughening because it inhibits interfacial failure.

Extraordinary improvements in matrix toughness were reported in [115] when testing a number of nanocomposites modified with a range of carbon nanoparticles with different quality of dispersion. The highest enhancement in properties was achieved when well dispersed amino functionalised CNT nanocomposites were tested. A toughness energy of ~917 J/m^2 is necessary to fracture this nanocomposite, while ~ 335 J/m^2 is required to propagate a crack in the unmodified epoxy resin. This enhancement of ~175% of the toughness is explained by the stronger interfacial adhesion between these CNTs and the resin, provided that a pull-out mechanism is active. Significant improvements in matrix

toughness have been reported when adding carbon nanoparticles. However the transfer of these improvements to a fibre reinforced composite is still considered a challenge.

2.4.2 Improvements in toughness properties of carbon nanoparticles multiscale composites

The enhancement of the interlaminar properties of multiscale composites modified with rod-shaped carbon nanoparticles has been an important matter of research within the composites community. Improvements in composites interlaminar properties have been reported when utilising different manufacturing routes.

A successful example of employing this technique in composites toughening is described in [36] when 1wt% functionalised CNF were incorporated in a polyester resin for subsequent impregnation of a glass preform by VARTM. Improvements of 100% in delamination resistance were observed and attributed to the fibre bridging toughening mechanism. In contrast, Wichmann et al [15], reported a decrease in the interlaminar toughness of 0.3 wt% DWCNTs filled epoxy glass fibre reinforced specimens tested in Mode I. This decrease was associated to difficulties during the testing caused by the obstructed tracking of the crack tip in the opaque resin using the conventional visual crack tracking method. These results contradict the improvements reported in previous work at the nanocomposite level [108, 113]. Zhou et al. [19] used a similar manufacturing process to produce MWCNTs modified multiscale composites, reporting improved toughness for the nanocomposite materials.

As high carbon nanoparticle content is a requirement for a significant improvement in toughness, the high viscosities associated with suspensions would hinder the use of liquid moulding processes. As a consequence alternative manufacturing routes to liquid moulding processes have been devised, to avoid problems associated with dispersion and reaggregation of nanoparticles, viscosity, and eventual filtration of the particles.

A technique involving the use of an interleaf film filled with 0.5 wt% functionalised or as-received CNTs on the composite mid-plane was utilised by Sager et al. [116]. An increase of 18% and 36% in G_{IC} for crack initiation was measured for the composite containing the functionalised CNTs filled interleaf film when compared to standard and

neat epoxy interleaved panels, respectively. No relevant improvement was observed for the as-received CNT filled panels for crack initiation. The crack propagation results suggest a decreasing trend especially for neat and as-received CNT interleaved panels when compared to standard ones. In contrast, the crack propagation for the functionalised interleaved panel remained similar to the non interleaved material. However, these results are presented and compared by Sager et al.[116] considering panels with variable interleaved film thicknesses. Toughness increases with the thickness of the interleaf film until a maximum value where a plateau is reached [117]. Therefore, for an adequate comparison of toughness a constant interleaf thickness would be necessary. A similar manufacturing route to the one described in [116] is present in [118] but utilising CNFs as modifiers of the interlayer films instead of CNTs. Improvements of 50 % and 20 % were reported for the initiation and propagation fracture toughness, respectively, for a CNF density of 20 g/m^2. This CNF density corresponds to an interleaf thickness of 100-150 μm, which was found to lead to optimal delamination properties of the CNF filled composites studied.

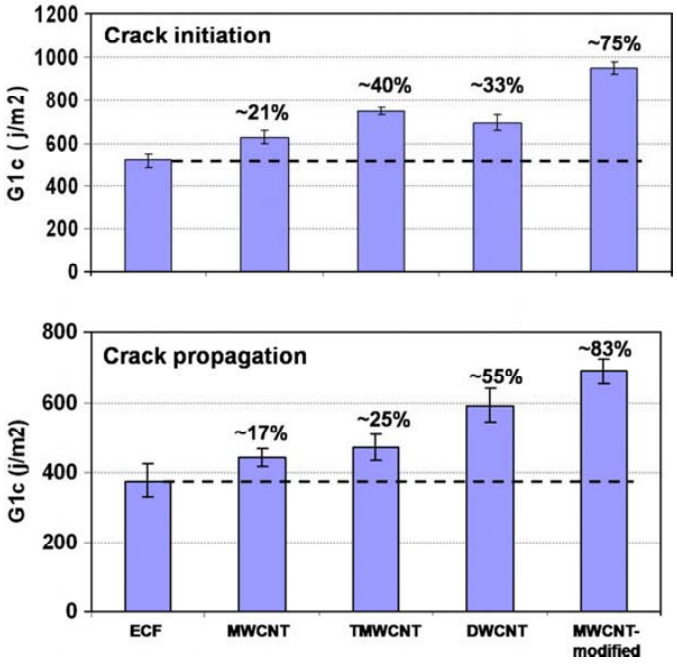

Figure 2.19 Carbon fibre reinforced composites fracture toughness for crack initiation and crack propagation between crack lengths 70-90 mm, as in [119].

The prepreg technique was utilised by Godara et al. [119] to manufacture a range of fibre composites modified with different CNTs. For 0.5 wt% CNT content in the resin, fracture toughness was improved in crack initiation and propagation (Figure 2.19). Moreover, improvements of approximately 83% in crack propagation resistance were achieved when modified CNTs were utilised as fillers which was attributed to deflection and crack bridging.

An alternative route for producing multiscale composites with a focus on high loading in the direct incorporation of CNTs on the surface of the reinforcement was utilised in [4] to deposit by electrophoresis MWCNTs and SWCNTs on woven carbon fabric for subsequent VARTM, and improvements of ~ 30 % were reported for interlaminar shear strength. The idea of growing CNTs on the surface of the carbon fibres has been tested and resulted in improvement of the fracture toughness of about 50% [120, 121]. Blanco et al. [122] consider vertically aligned CNTs, also named "nano-stitches" advantageous when compared to stitches or z-pins. These CNTs can bridge the crack until they are completely pulled out from the matrix.

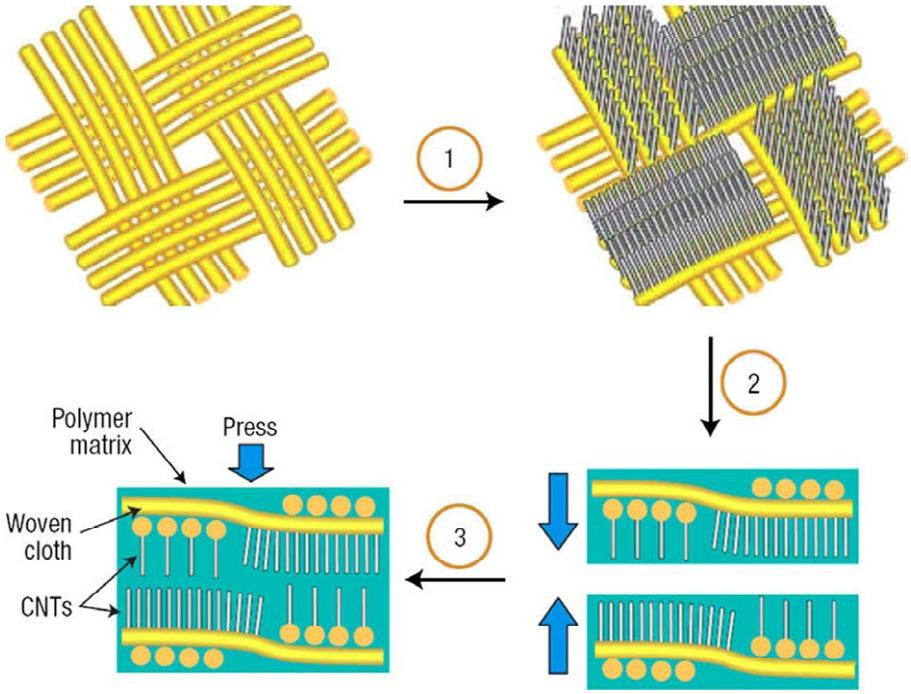

Figure 2.20 Schematic diagram of the steps involved in manufacturing multiscale composites [92].

Improvements in toughness are explained by frictional sliding during pull-out from the matrix or 'sword-in-sheath' pull-out, where the outer layer remains attached to the matrix whilst the inner tube(s) are pulled out from this outer tube followed by their fracture [122]. CNT forests were grown on SiC plain-weave fabric by CVD and the multiscale composites were processed following the scheme shown in Figure 2.20 [92]. Significant improvements (> 300%) in mode I fracture toughness were associated to CNT bridging of the plies.

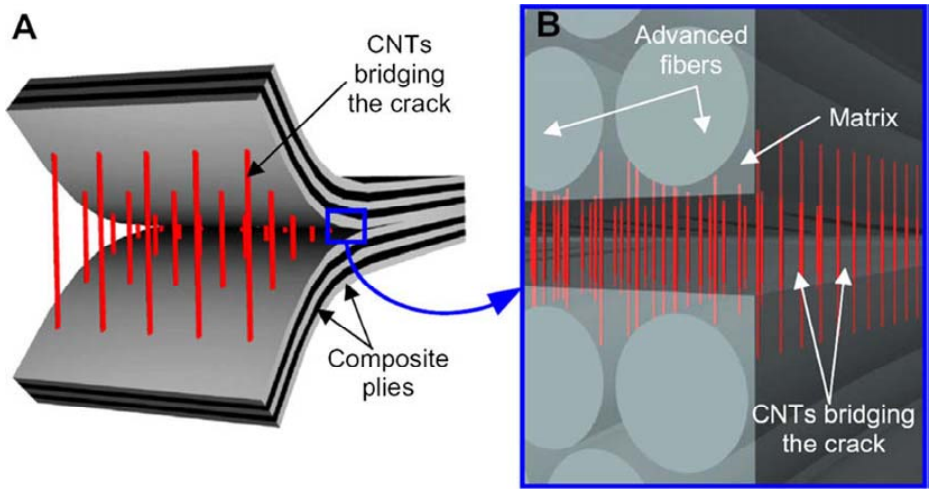

Figure 2.21 Schematic representation of CNTs bridging the crack in a fibre reinforced composite [42].

Many other attempts have been made by researchers in recent years, to modify the interlaminar surface by incorporating perfectly aligned CNT forests specifically for crack bridging (see Figure 2.21). Recent approaches integrated the idea of aligned CNT forests into carbon fabric prepregs [42, 122]. The CNT forests initially grown on a silicon substrate were then 'transfer-printed' to the tacky surface of carbon fibre prepregs, so that they are oriented in the laminate thickness direction. An increase in Mode I fracture toughness of 1.5 - 2.5 times was observed for the CNT modified interface composites, justified by CNT bridging and pull-out. This idea was taken further in [39] where a interlaminar and intralaminar CNT reinforcement was created by growing CNT on fibres in an alumina fibre woven fabric using the CVD process, as shown in Figure 2.22. Improvements of 76% for steady state Mode I interlaminar fracture toughness were associated to CNT pull-out and bridging. Although this improvement is stated to be comparable to that provided by stitching and z-pinning

[39], this contradicts results on these techniques demonstrated in [123]. Improvements of about 440% are obtained for 0.5% tufted DCB specimens when compared to the untufted material. Figure 2.23 show evidence of this extraordinary improvement. However, the presence of these tufts can compromise the in-plane properties of the composite [98]. In contrast, improvements in the in-plane properties, such as bearing stiffness and strength reported in [39], can prove advantageous when using CNTs as reinforcements instead of stitches and z-pins.

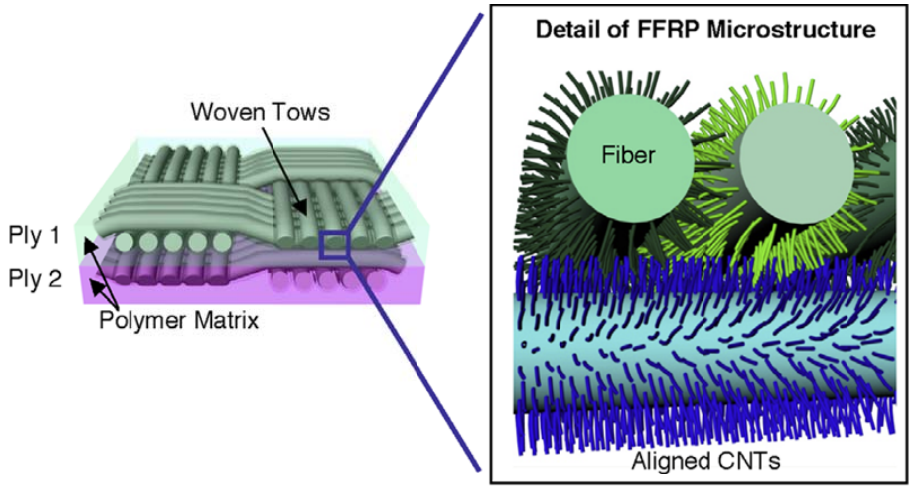

Figure 2.22 Illustration of fuzzy-fibre-reinforced multiscale composite showing radially aligned CNTs grown on advanced fabric [39].

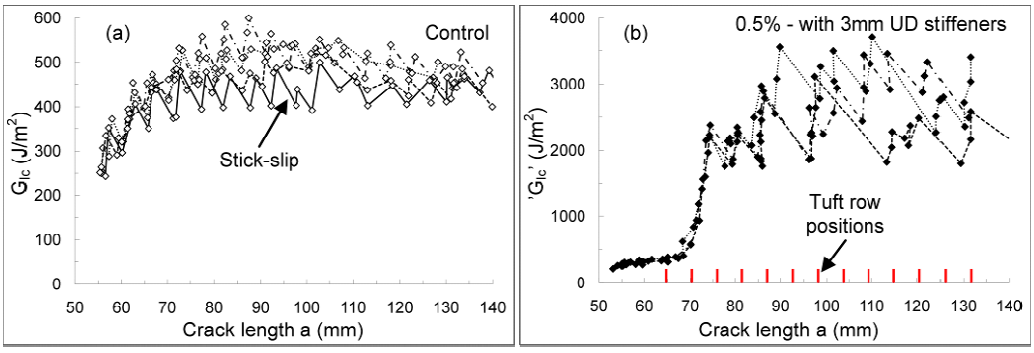

Figure 2.23 R-curves for mode I testing of a) control and b) 0.5% tufted DCB specimens [123].

3 Materials

This chapter describes the materials utilised for the preparation of conductive nanocomposites and multiscale composites. The first section includes the chemical characterisation and properties of the epoxy system, while the second and third sections provide a description of carbon nanoparticles properties and the fibrous reinforcements utilised, respectively.

3.1 Epoxy resin LY 564 and amine hardener HY2954

The resin system used in this work was a two-component thermoset epoxy resin (Huntsman Araldite LY564) with an amine hardener (Huntsman Aradur 2954). The epoxy chemical constituents are butanedioldiglycidyl ether (14.00 – 22.00 %) and bisphenol A- (epichlorhydrin) (78 – 90%); while the hardener is 2,2'-dimethyl-4,4'methylenebis (cyclohexylamine) [124].

This is a low viscosity resin (900 mPas) suitable for RTM applications. The epoxy to hardener ratio is 100/35, and the recommended cure cycle is 1h at 80° C, followed by post cure at 140° C for 8 hours. This system offers advantages over monocomponent resins, since the dispersion of carbon nanoparticles only takes place in one of the components, the epoxy, avoiding problems with premature initiation of cure during processing. This is particularly important as it gives more flexibility when higher temperatures are required during dispersion processing.

3.2 Carbon nanoparticles

3.2.1 Carbon nanotubes

Multiwalled carbon nanotubes (MWCNT) were used to modify the epoxy resin described in section 3.1. Three unmodified MWCNTs, namely P940, C100 and Hyperion, and one system of surface modified MWCNTs were utilised as modifiers. P940 and C100 were supplied in a powder form, whilst Hyperion and surface modified MWCNTs were supplied by BAE Systems in a pre-batch form. Figures 3.1 and 3.2

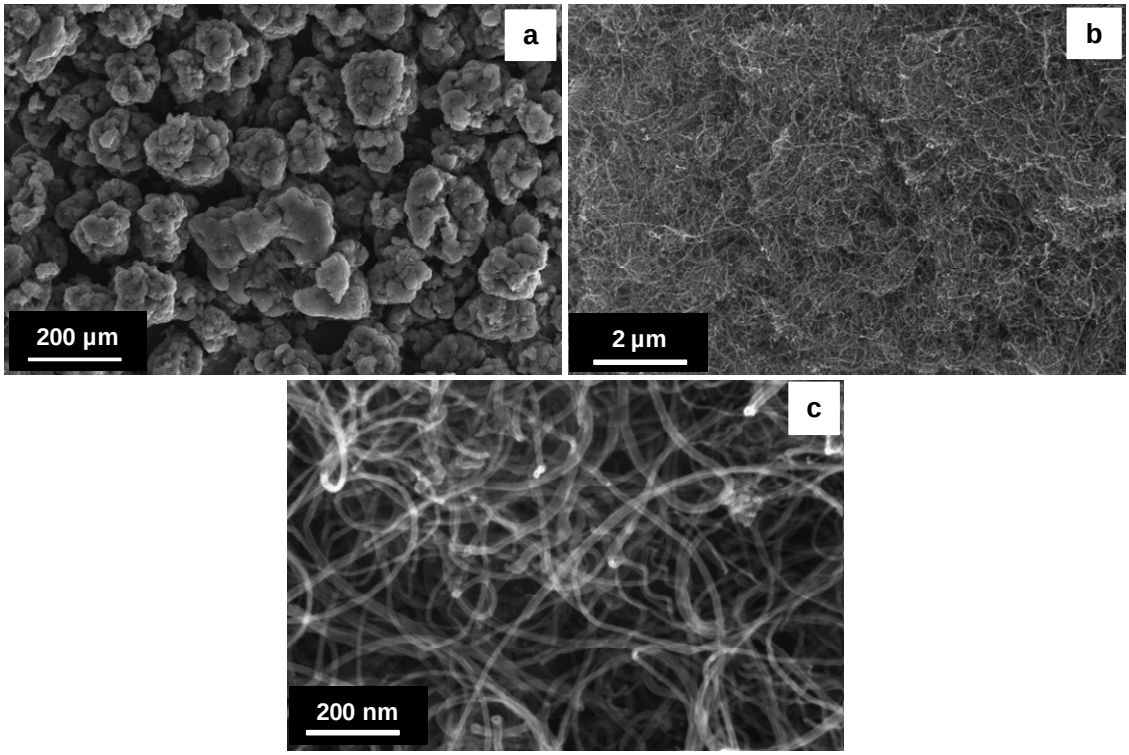

Figure 3.1 SEM micrographs of as received P940 MWCNTs.

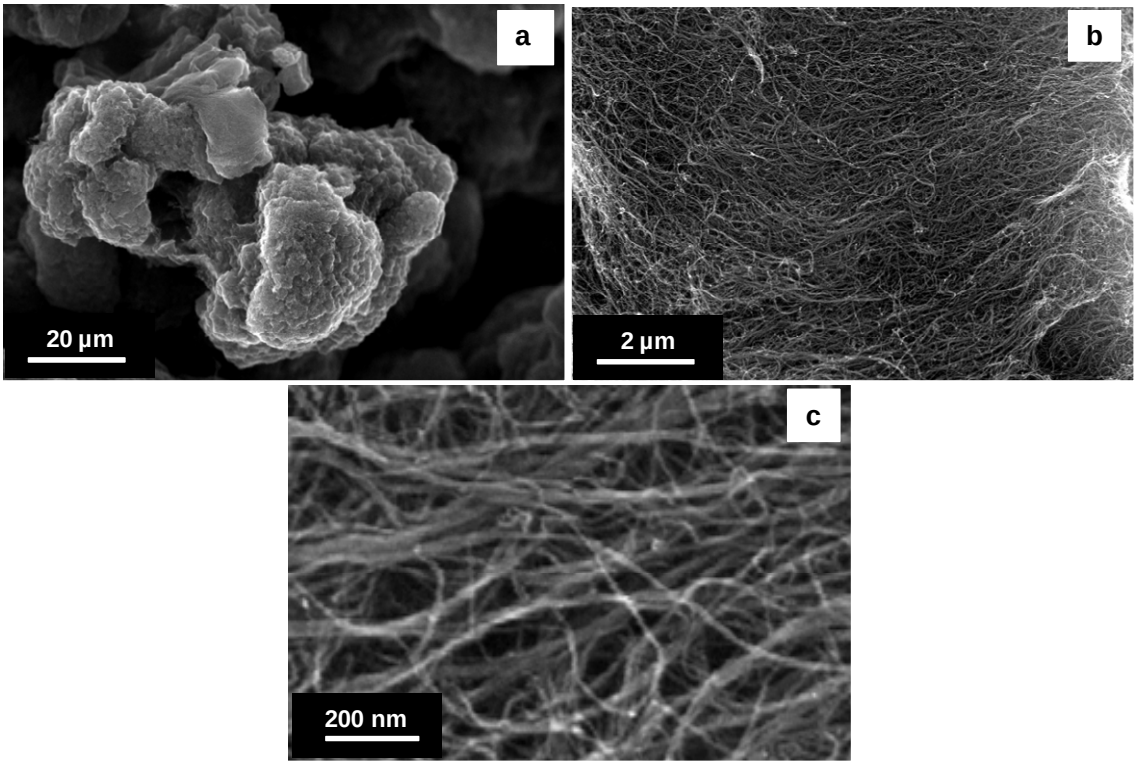

Figure 3.2 SEM micrographs of as received C100 MWCNTs.

show SEM micrographs of the highly entangled structure of as-received MWCNTs at different magnifications. The characteristics of the unmodified MWCNTs as provided by the manufacturers are summarised in Table 3.1.

Table 3.1 Characteristics of MWCNTs (adapted from the respective manufacturers datasheets)

	P940	**C100**
Manufacturing process	CVD	CVD
Manufacturer	Thomas Swan	CNT Co.
Diameter	10 – 12 nm	10 – 40 nm
Length	tens of microns	1 – 25 μm
Purity	70 – 90 %	> 93 wt.%
Average BET* surface area (m^2/g)	250 – 300	150 – 250
Metal oxide content	< 5wt.%	< 7 wt.%

**BET stands for the initials of the scientists who invented the technique, namely Brunner, Emmet and Teller.*

3.2.2 Carbon nanofibres

The carbon nanofibres (CNF) used to modify the two-component epoxy resin are PR-24-XT-LHT [125] manufactured by Pyrograf Products, Inc. and supplied by BAE Systems in the form of a black powder. High magnification SEM micrographs of the structure of this powder material are illustrated in Figure 3.3. The diameters of these nanoparticles vary between 60 nm and 115 nm. This grade material is produced by CVD and heat treated at 1500°C. This thermal treatment converts any chemically vapour deposited carbon on the surface to a short range ordered structure. Hence, the inherent electrical conductivity of the fibre is enhanced. The properties of the CNF as provided by the manufacturer are detailed in Table 3.2.

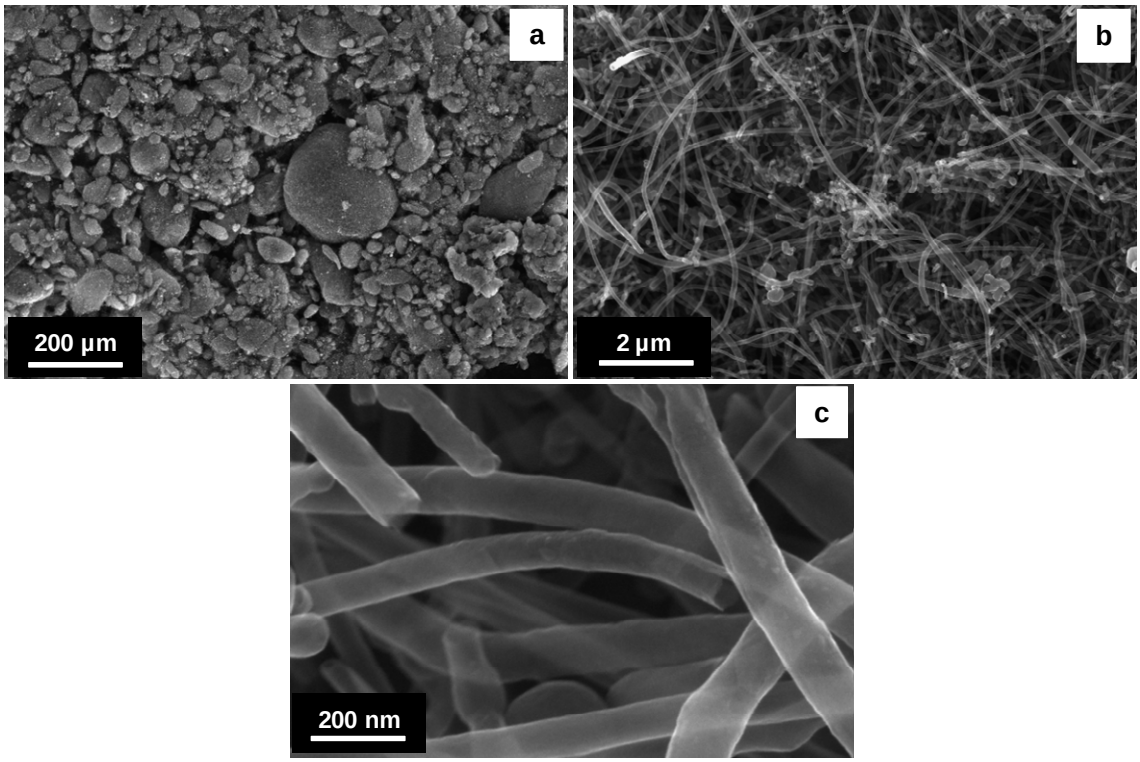

Figure 3.3 SEM micrographs of CNFs powder.

Table 3.2 CNF properties as provided by the supplier [125, 126]

	CNF
Fibre diameter (average)	100 nm
Fibre length	30 – 100 µm
Overall surface area	43 m^2/g
Bulk density	16 – 48 kg/m^3
Iron content	< 14000 ppm

3.3 Fibrous reinforcement

Two pseudo-unidirectional (uniweave) carbon and glass fabrics were selected to reinforce the composite panels manufactured by RTM.

3.3.1 Uniweave carbon fabric

A uniweave carbon fabric was supplied by Toho Tenax in the form of a 1.3 m wide roll. The warp filament is a high tensile strength carbon fibre and the dry fabric areal weight as evaluated *in-situ* is 280 g/m^2. The fabric architecture and description are specified in Figure 3.4 and Table 3.3.

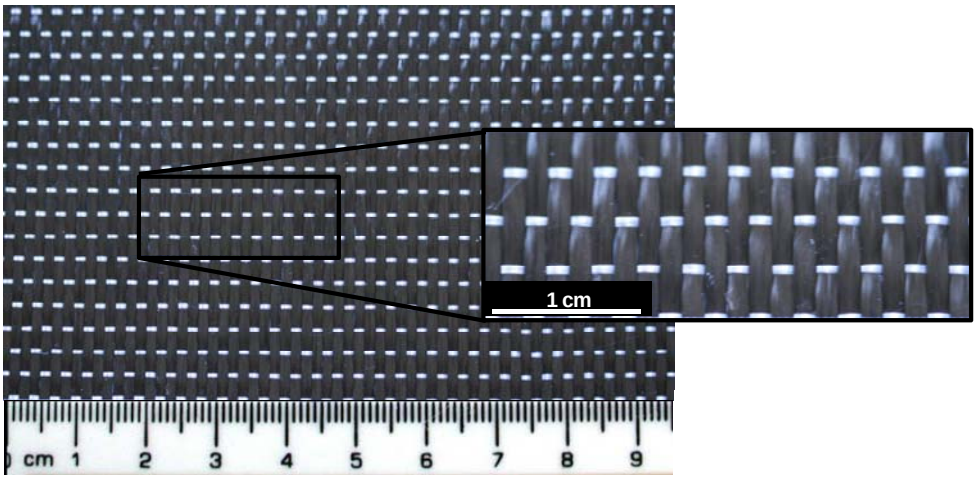

Figure 3.4 Uniweave carbon fabric

Table 3.3 Uniweave carbon fabric description

Warp					Weft (stitch)	
Primary fibre type	**Fibre tex**	**Count ends/cm**	**Filaments/tow**	**areal weight (g/m^2)**	**Filament type**	**Coups-picks/cm**
Carbon	400	6.6	6k	280	glass	3

3.3.2 Uniweave glass fabric

A uniweave E-glass fabric UT-E500 (Figure 3.5) manufactured by SP Gurit in the form of a 0.5 m wide roll, was supplied by Marineware. The areal weight of the dry fabric as measured *in-situ* is 480 g/m^2. Fabric characterisation as provided by the manufacturer is described in Table 3.4.

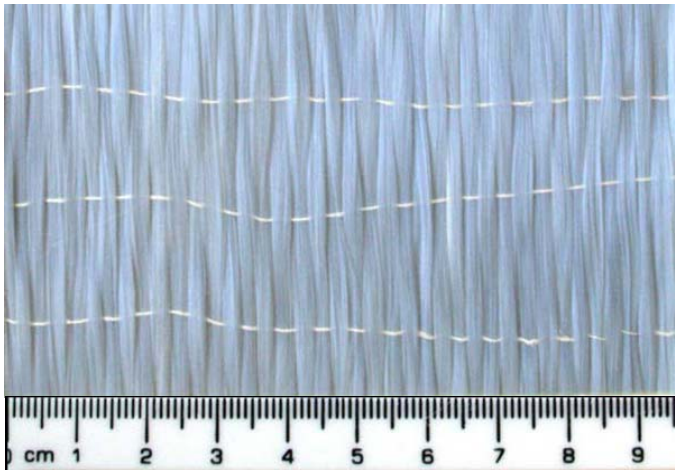

Figure 3.5 Uniweave glass fabric

Table 3.4 Glass fabric description (adapted from SP Gurit datasheet)

Warp				Weft (stitch)			
Primary fibre type	**Fibre tex**	**Count ends/cm**	**theoretical areal weight (g/m^2)**	**Filament type**	**Fibre tex**	**Count ends/cm**	**theoretical areal weight (g/m^2)**
E-glass	1200	4.16	500	polyester	10	0.56	2

4 Experimental methods and manufacturing

This chapter presents the procedures utilised for the preparation and characterisation of carbon nanoparticles filled epoxies and the corresponding multiscale composites. The first section includes the processing techniques utilised for dispersing carbon nanoparticles in the two component epoxy resin. The second section describes the microscopic methods utilised to characterise the morphology of as-received carbon nanoparticles, liquid and cured nanocomposites and delamination fracture surfaces of the multiscale composites. In addition, this section details the procedure utilised for estimating the intermediate resin-rich layer thickness of the multiscale composites manufactured by RTM. In section 4.3, the electrical conductivity techniques used to characterise liquid and solid state nanomodified suspensions, and multiscale composites are detailed. Section 4.4 reports the rheological technique utilised to evaluate the viscosity of the suspensions. Section 4.5 details the RTM manufacturing process utilised to produce multiscale composites. Section 4.6 describes the C-scan technique utilised to evaluate fibre composites quality. Sections 4.7 and 4.8 explain the procedures employed for the determination of multiscale composites toughness, and the compressive yield strength of the corresponding nanocomposites, respectively.

4.1 Dispersion of carbon nanoparticles

4.1.1 Dispersion monitoring

Several suspensions containing P940 carbon nanotubes at various loadings were prepared utilising two distinct dispersion techniques in order to evaluate the relationship between the state of dispersion and electrical conductivity. Each suspension was ultrasonicated up to a total energy input of 1300 J/g, utilising a Branson S-450D horn sonicator shown in Figure 4.1; whilst the others were shear mixed at 2400rpm up to 72000 cycles, at 50˚ C, in a DISPERMAT CN F2 high shear mixer, shown in Figure 4.2.

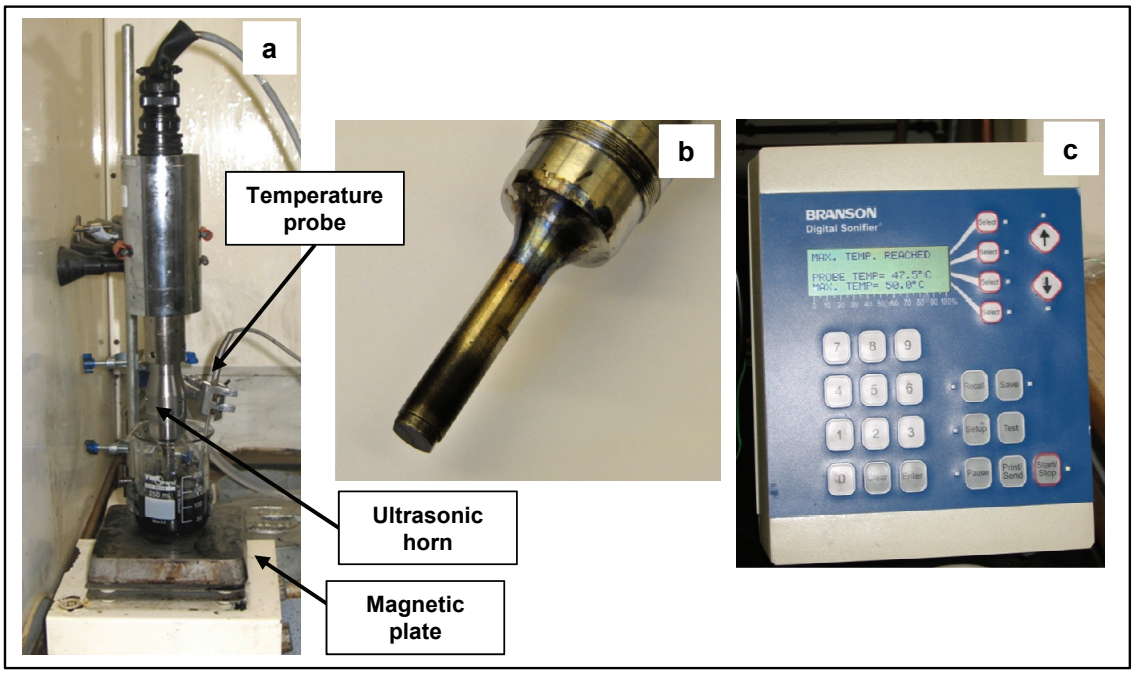

Figure 4.1 Ultrasonication set up (a), ultrasonic horn (b) and ultrasonic cell disruptor (c).

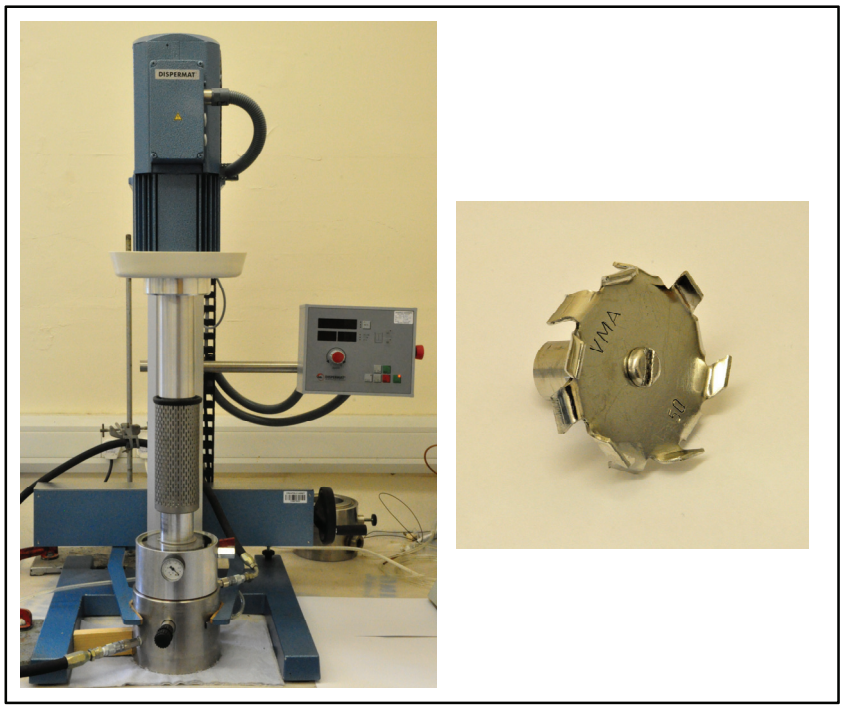

Figure 4.2 Dispermat high shear mixer and dissolver disc (stirrer).

Ultrasonication was carried out using the setup shown in Figure 4.1 (a). The 1/2" titanium ultrasonic horn (Figure 4.1 (b)), with a mean operating frequency of 19.95 ± 0.1 kHz, was immersed in the suspension mixture together with a temperature probe.

Both ultrasonic horn and temperature probe are connected to a Branson S-450D Digital Sonifier® (Figure 4.1 (c)) which controls the ultrasonic input. In order to guarantee efficient dispersion throughout the resin, the suspension containing a magnetic stirrer was placed on a magnetic plate during ultrasonication. The ultrasonic horn was operated under the maximum temperature mode at 40% amplitude, which corresponds to 160W of applied power. The temperature range during the process was set so that ultrasonication was applied to the suspension until a temperature of 50^{o}C was reached, after which the ultrasonication was temporarily suspended until the temperature dropped 3^{o}C below the setpoint. The ultrasonication was stopped after the chosen level of energy was reached. Similar ultrasonication and high shear mixing procedures were followed for suspensions containing CNFs at various loadings. The suspensions were stored in a freezer at -18^{o}C after the dispersion process.

4.1.2 RTM batches

A process step achieving the dispersion of 0.25 wt% carbon nanoparticles in the resin was performed prior to the injection of nano filled resin in the RTM mould. Before processing, each suspension was split into three batches of approximately 130g, in order to guarantee a better efficiency of the dispersion process. The two suspensions containing unmodified nanotubes (C100 and P940) were processed in situ using a distinct dispersion step, whereas modified CNTs were supplied as a ready to use suspension. The suspension containing Hyperion CNTs was supplied pre-processed by BAE SYSTEMS using triple roll milling. In addition, this suspension was ultrasonicated in-situ up to a total energy input of 100J/g.

C100 nanotubes were dispersed in the epoxy resin at a loading of 1.5 wt% by four passes at 50 rpm in a triple roll milling (TRM Torrey Hills Technologies), illustrated in Figure 4.3. This high concentration suspension was then diluted in resin to a concentration of 0.3375 wt%, which upon addition of the hardener results in a 0.25 wt% loading. The suspension was shear mixed for 15000 cycles, at 1500 rpm, in a high shear mixer and then ultrasonicated with a total energy input of 650 J/g. P940 carbon nanotubes were dispersed by ultrasonication up to a total energy input of 800 J/g, whilst CNFs were dispersed by high shear mixing at 2400 rpm up to 72000 cycles at 50˚ C.

These conditions were selected based on monitoring of the evolution of resistivity during the process. The procedure for these tests is described in section 4.3.1 and the corresponding results in sections 5.1, 5.2, 6.1 and 6.2.

Figure 4.3 Triple roll mill

In the following, the same CNT content is reported for both the liquid and cured resins, however, this value corresponds to the cured state concentration of CNTs, which takes into account the amount of hardener added after the dispersion process. The reference materials, either the liquid or the cured resin, as well as fibrous composites are referred to as 'control'.

4.2 Morphological characterisation

4.2.1 Optical microscopy

The state of dispersion of the CNTs in the epoxy resin at any given stage of dispersion was ascertained by examining the samples by transmission optical microscopy using an Olympus BH-2 microscope. A droplet of sufficient size of the liquid suspension was placed between a microscope glass slide and a cover slip. The average sample thickness was 20 ± 10 μm.

Cured samples of the resin containing P940 and C100 MWCNTs were also examined by transmission optical microscopy. A droplet of the two component resin system with CNTs was placed between a glass slide and a cover slip and allowed to cure in an oven

at 80 ºC for 1h 30 min and post cured at 140 ºC for 8h. The cured film thickness was 40 μm and 60 μm for the C100 and P940 nanocomposites respectively.

4.2.2 Scanning electron microscopy

Dry carbon nanoparticles, cured nanocomposites, delamination fracture surfaces and transverse and longitudinal surfaces of multiscale composites were examined by SEM. The electron microscope used for the analysis of these specimens was a FEI FEG-SEM.

The preparation of dry carbon nanoparticle powders for SEM analysis was carried out by placing a carbon conductive tape strip on an aluminium stub and immersing it into the as-received carbon nanoparticles container. Carbon nanoparticle aggregates become easily attached to the adhesive tape and any excess is removed by tapping the edge of the stub on a firm surface covered with a damp cloth, in order to collect any nanoparticles released from the stub.

Cured suspensions were prepared by cryofracture. The specimens were initially cut in the shape of a small prism and a small notch was made with a diamond saw installed in a low speed cutting machine. The notched specimens were fractured immediately after immersion in liquid nitrogen for 2-5 min.

Delamination fracture surfaces of the fibre composite panels tested under DCB mode I were also investigated by SEM in order to evaluate the extent of filtration along the mould. Areas of approximately 10x20mm were cut at approximately 100mm and 200mm away from the inlet.

Two 20x3.3 mm representative sections of the transverse and longitudinal surfaces of a carbon fibre reinforced composite manufactured by RTM were cut with a low speed saw and polished before SEM analysis in order to evaluate the thickness of the resin-rich mid-layer of these composites. High magnification pictures (500x) were randomly taken along the specimen mid-layer, for both the transverse and longitudinal surfaces. For every picture several measurements of the resin thickness at the mid-layer were taken using the image analysis software AxioVision Rel. 4.6.

The fractured nanocomposites, the delamination specimens and the two cross-section specimens cut from the multiscale composites were glued to an aluminium stub, with the surface of interest facing up, using conductive silver paste (Acheson Electrodag 1415M). The specimens on the stub were subsequently sputtered with a silver-palladium coating in order to make the surface of these composites conductive for imaging by SEM.

4.3 Electrical conductivity

The set up utilised for all the electrical conductivity measurements consists of two copper cylinders with adjustable gap, as shown in Figure 4.4. The sample was placed between the two cylinders and full contact between the sample surfaces was ensured during the experiment. The electrodes are then connected to the respective AC or DC measurement equipment.

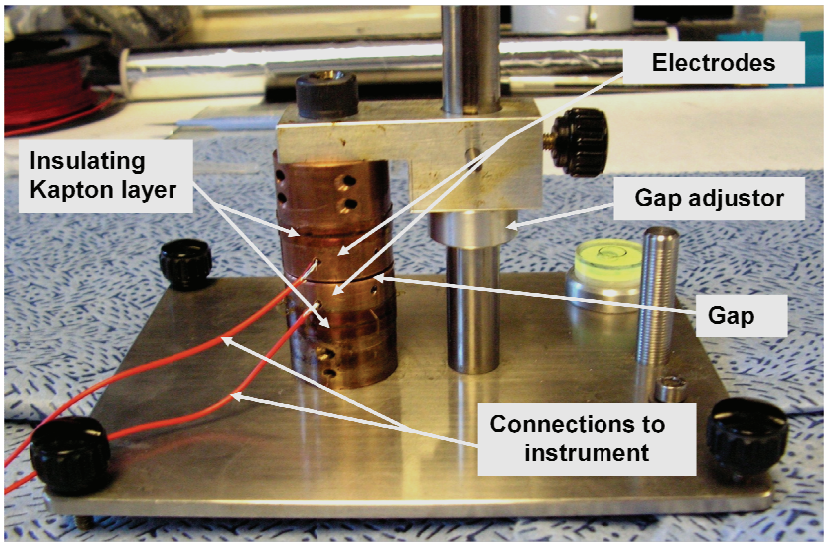

Figure 4.4 Electrical measurement cell

4.3.1 Liquid suspensions

A droplet of liquid suspension was placed between the two copper concentric electrodes, with a gap set to 1mm, in order to fill the complete cavity. Any excess of material was removed with the help of a scraper. The AC and DC electrical conductivity of these suspensions was subsequently measured.

The AC electrical response of liquid suspensions was measured via AC impedance spectroscopy using a Solartron SI 1260 frequency response analyser at different stages of processing. Twenty five frequencies from 1 Hz to 1MHz were swept on a logarithmic scale. The electrical resistance of the samples was determined from the peak value of the imaginary impedance spectrum as described in [127] as follows,

$$R = 2 \times Z''_{peak} \tag{4.1}$$

The DC electrical resistivity of carbon composite samples was measured using a DC precision current source (Keithley model 6220) and a nanovoltmeter (Keithley model 2182A) via the three-point delta current reversal technique. The volume resistivity of the samples was calculated according to

$$\rho = \frac{R \cdot A}{t}, where\ A = \pi r^2 \tag{4.2}$$

where R is the resistance measured, A is the specimen cross-sectional area, r is the copper cylinder radius and t is the thickness of the specimen.

4.3.2 Cured nanocomposites

CNF filled suspensions dispersed by shear mixing and ultrasonication processes were cast into moulds and cured to evaluate the conductivity of the corresponding solid nanocomposites. The mould used for the manufacture of these specimens was assembled using a 3mm thick U-shaped silicone shim placed between two released glass plates (10x10cm) held together with the help of metal clamps. Each suspension was poured into the standing mould and cured in an oven at 80ºC for 1 hour. After cure, each specimen was demoulded, and post-cure was carried out in an oven at 140ºC for 8 hours. The 3.5x3.5 cm nanocomposites surfaces were coated with conductive silver paste for the measurement. The resistance of these nanocomposites was measured with a Keithley 6517 electrometer, which measures resistances up to $10^{12}\Omega$. The resistivity of the CNF nanocomposites was calculated according to equation (4.2).

4.3.3 Multiscale composites

The electrical measurements of cured samples of fibrous composites were carried out on rectangular specimens with dimensions of 30 × 30 × 3.2 mm for carbon fibre composites and 30 × 30 × 3.7 mm for glass fibre composites. The surfaces of interest were painted with a silver paste, as shown in Figure 4.5.

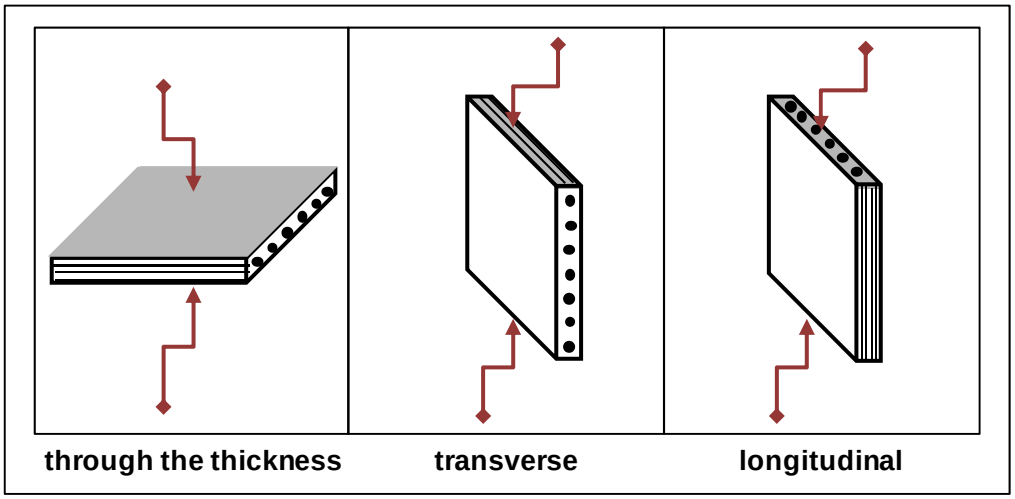

Figure 4.5 Schematic of the electrical conductivity measurement directions of multiscale composites.

The DC electrical resistivity of carbon composite samples was measured using the same equipment utilised for the liquid suspensions. The measurements were performed in three directions (through thickness, transverse and longitudinal), as depicted in Figure 4.5, using a current of 100 μA.

Through thickness AC measurements of the glass composite samples were carried out during this investigation. Twenty nine frequencies from 1 Hz to 1 MHz were swept on a logarithmic scale. The electrical resistance of the samples was determined from the peak value of the imaginary impedance spectrum using equation (4.1).

4.4 Rheological analysis of the carbon nanoparticle filled LY564

Samples of the suspensions utilised for RTM were collected for rheological measurements. A Bohlin CVO rheometer with a 4º/40 mm cone and plate geometry (Figure 4.6) was used in steady shear mode, at the corresponding mould temperature. The viscosity of the suspensions was measured in the 0.1 to 1000 s^{-1} shear rate range.

Figure 4.6 Bohlin CVO rheometer

4.5 Resin transfer moulding

Moulding was carried out with a newly commissioned Isojet piston driven RTM setup, shown in Figure 4.7 (a). This computer controlled equipment allows both flow rate and pressure controlled resin injections, along with online monitoring of the process parameters like resin temperature and volume, mould temperature, injection and vacuum pressures and flow rate.

Twelve layers of one of the uniweave fabrics were laid up on the mould cavity in the 0º direction (Figure 4.7 (b)), in order to attain a final composite theoretical fibre volume fraction of approximately 57% and 59%, for carbon and glass fibre reinforced composites, respectively. The theoretical fibre volume fraction of each fibre reinforced panel was calculated according to equation (4.3), which is based on the number of dry

fabric layers n, the areal density of the fabric $\rho_{A,f}$, the density of the fibre ρ_f, and the final panel thickness t.

$$V_f(\%) = \frac{n \cdot \rho_{A,f}}{\rho_f \cdot t} \tag{4.3}$$

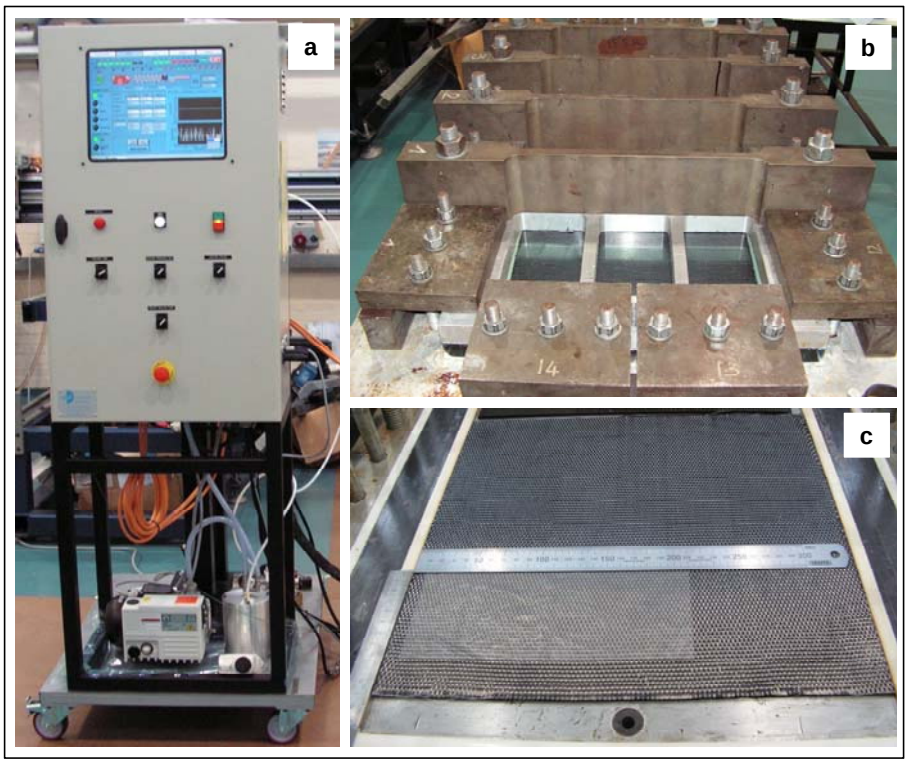

Figure 4.7 Isojet RTM unit (a), mould (b) and PTFE film placement (c)

The areal weight of each fabric includes the combined weight of either the carbon or the glass fibres and the non-structural stitching yarn per unit area. The areal weight was determined by measuring the weight of three samples with a minimum area of 200 x 200 mm.

A 10-15 μm PTFE insert film, supplied by GoodFellow was placed at laminate mid thickness, as indicated in Figure 4.7 (c), which introduces a pre-crack necessary for DCB tests. The cavity thickness was controlled by metal shims and silicone seals of variable thickness placed around the mould. Before each resin injection, the mould

cavity and the top cover were released with at least two layers of release system (Chemlease® PMR-90, Chem Trend), to guarantee an easy detachment of the composite panels from the mould surfaces after cure.

The resin suspension was heated up to 40º - 50º C in order to reduce the viscosity and facilitate the diffusion of gases and moisture retained in the resin during the degassing stage. This process was carried out in a vacuum chamber for a period of 20 - 30 min. When degassing was finished the hardener was added to the resin and the mixture was stirred for two minutes. A final degassing step of the mixture was preformed for a period no longer than 10 min. Subsequently, the resin mixture was placed inside the piston chamber of the Isojet equipment at a temperature of 30 ºC. No temperature drop is expected from the piston chamber to the inlet of the mould since the inlet pipe passes within a heated tube set to 30 ºC. Lineal infusion, which uses one edge of the mould along which the resin is injected and allows injection along a linear flow front, was selected for all the cases. This type of infusion was found suitable to minimise particle filtration, since the main direction of the flow occurs primarily along the fibre direction of the unidirectional layup and not across fibre bundles. Filling was performed under 2 bar pressure. The mould used for the infusion is an aluminium tool, provided with internal heat-cartridge elements, and with a glass top cover, allowing visual monitoring of the flow front position during injection. The mould temperature at injection was set between 65 ºC – 75ºC. The cure cycle for all systems was 1h 30min at 80 ºC (1 bar). Post cure was carried out in an oven at 140 ºC for 8h. The panels were left to cool in the oven in order to avoid high thermal stresses due to rapid cooling. The panel in-plane dimensions were 340 × 340 mm.

4.6 C-scan

Composite panels manufactured by RTM and subsequently post-cured were examined for defects, such as dry spots, incomplete impregnation and to confirm location of the PTFE film inserted at mid-thickness, using the immersion-reflector plate C-scan method. Each panel was immersed in a water tank and placed over a glass reflector plate. The panels were supported at the edges with small PMMA blocks keeping them flat at about 10 mm above the glass plate. The transducer is a 5 MHz ultrasonic probe,

positioned normal to the panel, was immersed in the water tank in order to allow transmission of the ultrasonic waves to the composite. To measure the time of flight or attenuation of the ultrasonic signal, the ultrasonic scan was utilised in pulse-echo mode, i.e. using a single pulser/receiver transducer. This transducer is used to generate ultrasonic sound waves and receive the reflected beams from the glass plate located underneath the composite panel. The transducer obtains the travelling sound-waves amplitude signal with time, which is displayed on the oscilloscope. A computer gathers the amplitudes over the panel and forms a scan image. C-scan images of the panels were acquired with a resolution of 0.5 mm.

4.7 Mode I Interlaminar fracture toughness

DCB mode I tests were performed on carbon nanoparticle modified epoxy carbon reinforced composites to evaluate the effect of various carbon nanoparticles on the toughness resistance of these composites. These tests were carried out to measure the interlaminar fracture toughness G_{IC} according to BS ISO 15024:2001.

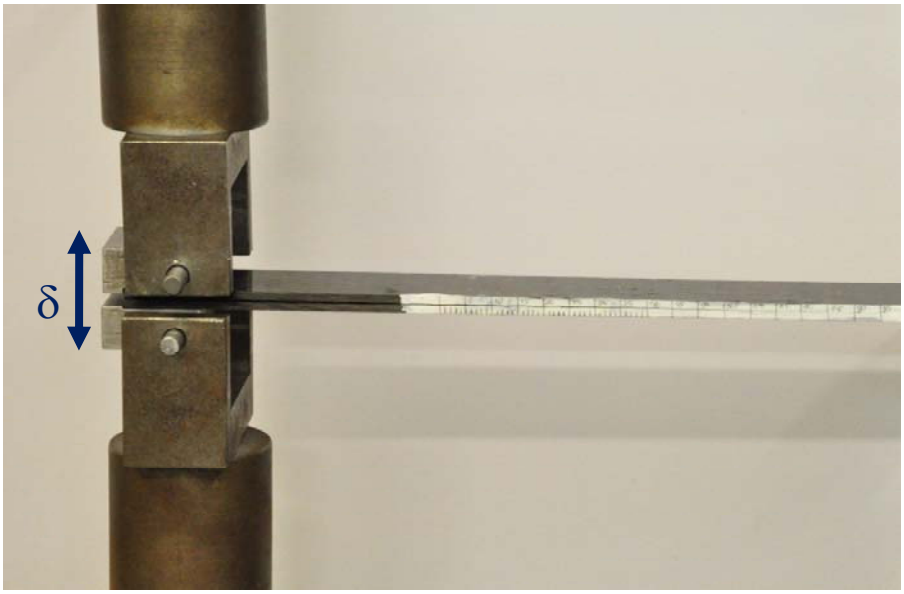

Figure 4.8 DCB specimen mounted on test jig

Samples were cut to the specified width and length (20 mm and minimum of 125 mm respectively) with their longitudinal axes parallel to the fibre direction. Specimens approximately 3.3 mm thick were used for this study. Specimen dimensions were measured three times along the width and thickness to make sure that tolerances (width

±0.5 mm; thickness ±0.1 mm) were according to BS ISO 15024:2001. The specimens were then painted on one side with white correction fluid. Two mm increments were marked for the first 40 mm and then every 5 mm over the total specimen length (Figure 4.8). This technique allows the monitoring of the crack tip propagation during the test. The PTFE insert film creates an existing sharp crack opening in the material, and causes minimal disturbance of the individual plies and the resin flow front behaviour during infusion.

Load blocks were bonded onto the edge of the specimen using super glue (cyanoacrylate based adhesive). This adhesive guarantees a fast and good attachment of the specimen to the load-blocks. The specimen was then loaded in the testing machine by means of two loading pins made to pass through the load block holes and the test machine fixture. A Zwick Z010 screw driven controlled displacement test machine, equipped with a 2 kN cell was utilised for this study with a cross-head displacement of 2 mm/min.

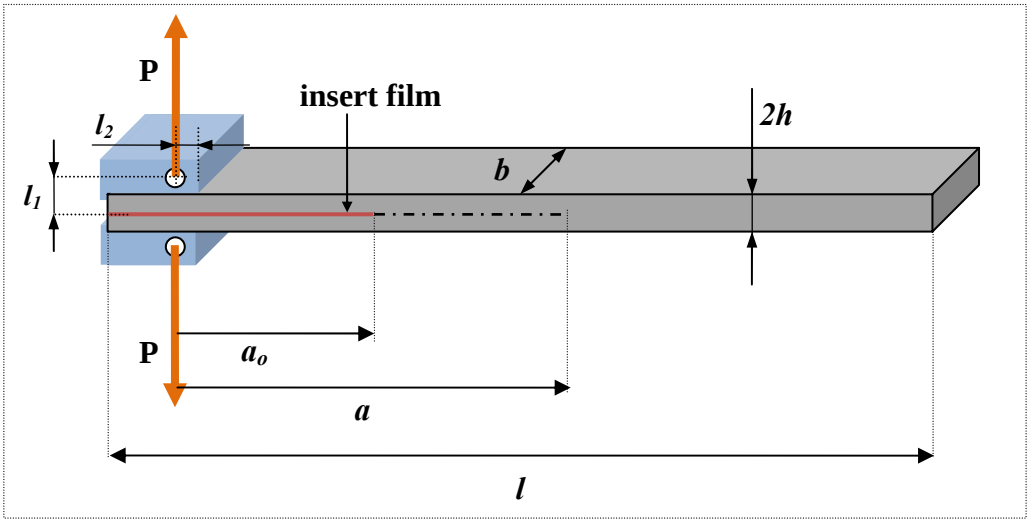

Figure 4.9 Geometry for the DCB carbon fibre reinforced composite specimen with a starter delamination and bonded loading blocks.

Every specimen was wedge pre-cracked by hand to identify the tip of the insert film position and to extend it 2-3 mm further. This is done to guarantee that initiation data (VIS point) gathered during the delamination test starts within the material do not correspond to the insert film.

The position of the crack tip was monitored by means of a hand held magnifying glass and a desk lamp with a mechanism to allow the light bulb to be tilted. As the specimen deformed the load and head displacement (loading point deflection) were recorded by the data acquisition system. The crack tip position was noted down as the crack tip progressed through the marks drawn on the specimen. Simultaneously the data acquisition system was triggered to plot markers on the load vs. displacement curve. When the test was completed these markers were correlated with the crack tip position values. Subsequent analysis allows the calculation of initiation and propagation values for G_{IC} as a function of the delamination length. There are three ways to determine the initiation fracture according to BS ISO 15024:2001, such as the NL, the VIS and the 5% MAX point. The difference between them lies on how initiation is identified in the force vs. displacement curve. The 5% MAX point was selected as the initiation value for the calculation of the initiation fracture toughness G_{IC} in the comparative analysis of results. G_{IC} was determined utilising the corrected beam theory (CBT) as follows

$$G_{IC} = \frac{3P\delta}{2b\,(a+|\Delta|)} \times \frac{F}{N} \tag{4.4}$$

where P is the load, δ the load line displacement, b the specimen width, a the delamination length, as represented in Figure 4.9. This method takes into account three correction factors F and N described by equations (4.5) and (4.6), and $|\Delta|$ which corresponds to the x-intercept of the linear fit data extrapolation in the $(C/N)^{1/3}$ vs. delamination length graph. $|\Delta|$ extends the beam theory approach, which underestimates the compliance, to account for a specimen that is not perfectly built-in, by considering a longer delamination length. l_1 and l_2 are represented in Figure 4.9.

$$F = 1 - \frac{3}{10}\left(\frac{\delta}{a}\right)^2 - \frac{2}{3}\left(\frac{\delta\, l_1}{a^2}\right) \tag{4.5}$$

$$N = 1 - \left(\frac{l_2}{a}\right)^3 - \frac{9}{8}\left[1 - \left(\frac{l_2}{a}\right)^2\right]\frac{\delta\, l_1}{a^2} - \frac{9}{35}\left(\frac{\delta}{a}\right)^2 \tag{4.6}$$

The large displacement correction F, accounts for large displacements and is especially significant if $\frac{\delta}{a} > 0.4$. The stiffening caused by the load blocks is corrected by factor N.

4.8 Compressive Yield Strength

Uniaxial compressive tests were performed on nanocomposite specimens for determining compressive yield stress σ_{yc}, according to the ISO 604:2003 standard. Nanocomposite specimens were cut either from off cuts of the 0.25 wt% CNP multiscale composites manufactured by RTM or from comparable cast nanocomposites. The latter comprise a 0.5 wt% CNF nanocomposite shear mixed up to 72000 cycles and a 0.25 wt% P940 nanocomposite dispersed by ultrasonication up to 1300 J/g. The specimens were cut using a diamond blade installed in a low speed saw. Specimen thickness was left unchanged, while length and width followed the dimensions specified in the standard ISO 604:2003, as shown in Figure 4.10 (b). Special care was taken during machining to guarantee flat and parallel surfaces and sharp edges. At least five specimens were prepared for each system, except the control for which 3 specimens were used. Before testing, all the test specimens were placed in a desiccator for 24h.

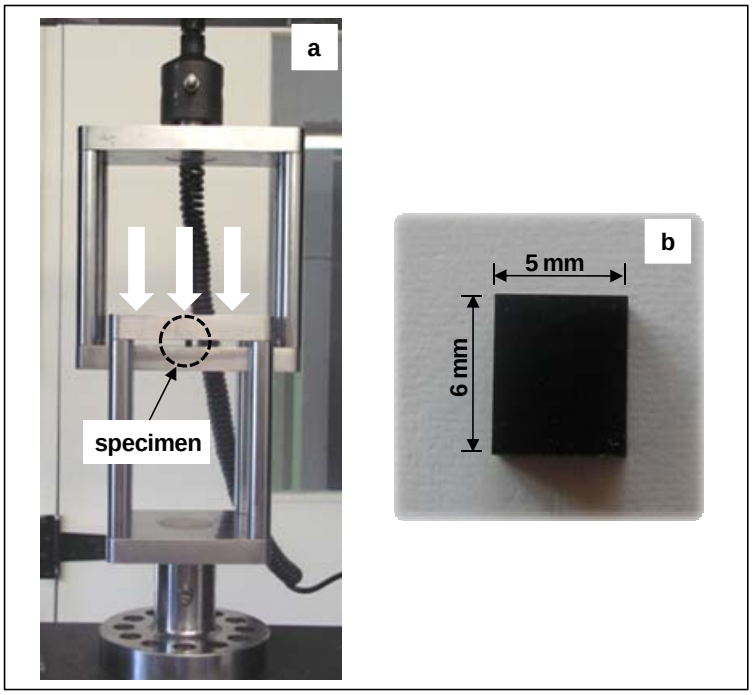

Figure 4.10 Compression test set up (a) and specimen dimensions (b).

The compression tests were carried out at 22ºC on an Instron 5500R displacement controlled test machine with a 5kN load cell. An Instron compression cage, loaded in tension, allowed the compression of the nanocomposite specimens placed between two

parallel plates as shown in Figure 4.10 (a). The specimens were compressed along their major axis at a constant speed of 0.6 mm/min [128] until yielding was observed, and force and displacement were recorded.

The σ_{yc} values of the nanocomposites were taken from the maximum value of the corrected stress vs. strain curves, when present, or otherwise from the intersection point between the test curve and a straight line with the same slope as the linear part of the stress vs. strain curve, offset by 5%. The compressive stress is described by the ratio between F and the corrected cross-sectional area of the specimen, as follows

$$\sigma_c = \frac{F}{A_o + \Delta A}, \quad \Delta A = A_o \nu \varepsilon \tag{4.8}$$

where A_o is the initial cross-section area, ν the Poisson's ratio and ε the strain value.

5 RTM processing and electrical performance of carbon nanotube modified epoxy/fibre composites

This chapter was adapted from a paper accepted by *Composites Part A - Applied Science and Manufacturing* journal. It is focused on the transfer of the enhanced electrical properties of CNT modified resin to the final multiscale composite structure. Microscopy was utilised to evaluate the state of dispersion in the liquid and cured nanocomposite states, whilst electrical conductivity allowed the selection of the most appropriate dispersion methods. A range of different CNT modified suspensions were used to infuse both carbon and glass fibre fabrics using the RTM process, where adjustments in processing conditions were highlighted. The extent and nature of particle filtration were identified and the electrical conductivity of the produced multiscale composites was evaluated.

5.1 Effect of dispersion on the electrical properties of MWCNT suspensions

5.1.1 Liquid nanocomposite suspensions

The effects of varied CNT content and different mixing processes on the dispersion state and the electrical conductivity of the liquid samples were investigated, as basis for the selection of adequate suspensions to be utilised in the infusion of carbon and glass reinforcements.

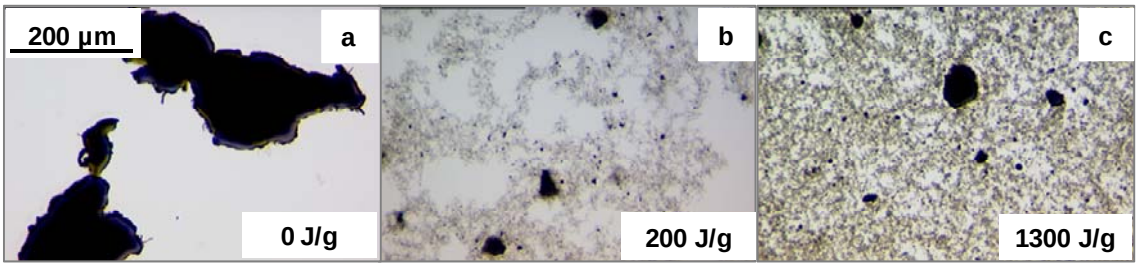

Figure 5.1 Liquid state optical transmission micrographs of 0.5 wt% P940 filled epoxy at different dispersion/processing levels: before ultrasonication (a); initial stages (b) and after completion of the process (c).

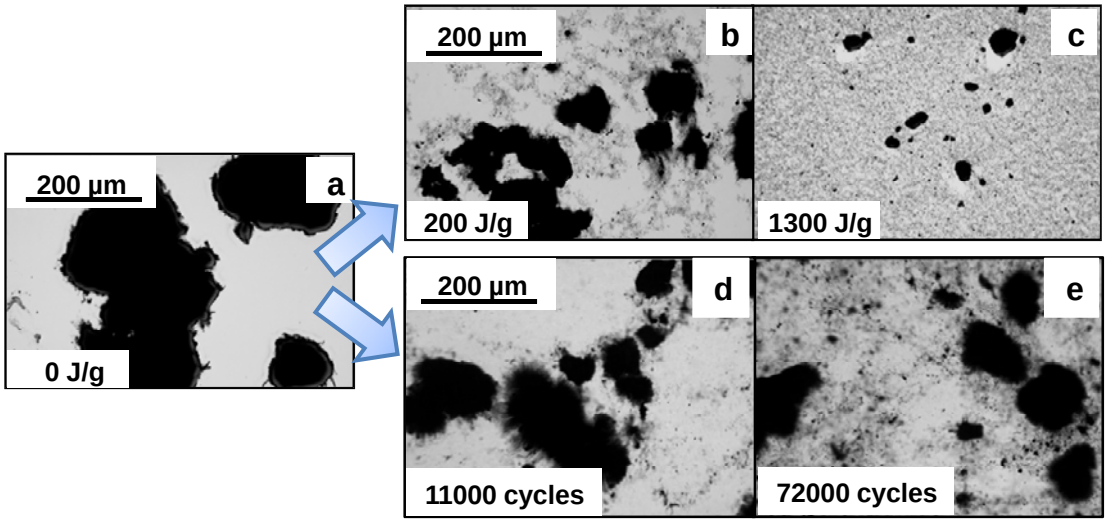

Figure 5.2 Liquid state optical transmission micrographs of 0.25 wt% P940 filled suspensions at different dispersion/processing levels: before dispersion (a); initial stages of ultrasonication (b) and high shear mixing (d); after completion of the process of ultrasonication (c) and high shear mixing (e).

Figures 5.1 and 5.2 illustrate the evolution of microstructure associated with the dispersion of 0.5 wt% and 0.25 wt% P940 MWCNTs in the epoxy resin. Figures 5.4 and 5.5 summarise the evolution of AC and DC electrical conductivity of the suspensions during dispersion processing. Highly entangled large and isolated MWCNTs primary aggregates with well defined boundaries characterise the initial resin suspension (Figures 5.1(a) and 5.2 (a)). As the total ultrasonic energy input to the suspension increases, the aggregate boundaries become blurred as CNTs gradually unravel forming areas of separate and individual CNTs around the aggregate dense core (Figures 5.1 (b) and 5.2 (b)). Although dimensionally large aggregates are still present at intermediate levels of dispersion, such as those shown in Figures 5.1 (b) and 5.2 (b), a significant increase of the electrical conductivity of all the suspensions is observed (Figure 5.4), which implies that at this stage, the number of conductive links formed increases considerably. Further ultrasonication of the 0.25 wt% and 0.5 wt% P940 suspension, up to 1300 J/g, results in suspensions characterised predominantly by a homogenous distribution of carbon nanotubes where few dense aggregates with a maximum dimension of up to 50 µm and 70 µm respectively can be observed.

The electrical conductivity of all ultrasonicated suspensions rises sharply after the initial stages of ultrasonication. After 350 J/g and 200 J/g of processing, the conductivity of suspensions filled with 0.5 wt%, 0.25 wt% and 0.125 wt% P940 becomes approximately constant until the end of the process (Figure 5.4). Higher electrical conductivity is associated with efficient dispersions containing increasing content of dispersed CNTs. However, the electrical conductivity results for 0.25 wt% and 0.5 wt% P940 suspensions dispersed by ultrasonication are similar. Considerably lower electrical conductivity, of about one order of magnitude, is obtained for the suspension containing 0.125 wt% P940 CNTs when processed by ultrasonication.

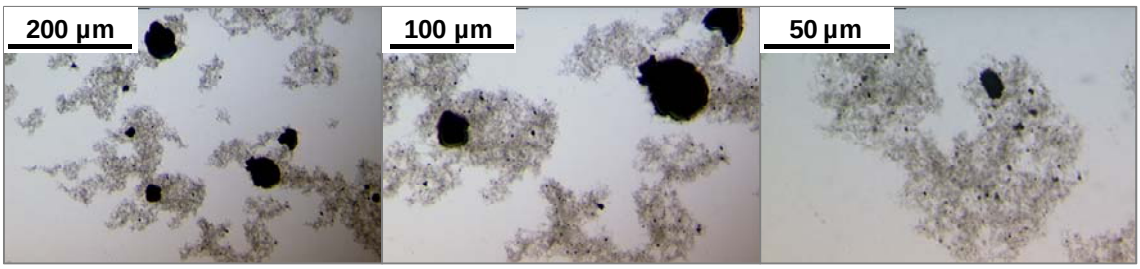

Figure 5.3 Liquid state optical transmission micrographs of 0.125 wt% P940 filled epoxy resin after 1300 J/g ultrasonication input, at increasing magnification.

The transmission optical microscopy pictures shown in Figure 5.3 are representative of the state of dispersion of this suspension after the final ultrasonication stage. This suspension is characterised by irregularly shaped loose CNT aggregates (secondary aggregates) surrounding a number of very dense and nearly round primary aggregates ranging from few microns to 150 µm diameter, in a medium of large areas of neat resin. A better dispersion state would lead to reduced size of the areas microscopically deprived of CNTs and would instead be characterised by a homogenous distribution of CNTs over the entire suspension. In general, these features are associated to suspensions with enhanced electrical conductivity properties.

High shear mixing is not as effective as ultrasonication in reducing the size of large primary aggregates in suspension. At the initial stages (11000 cycles), CNTs start to unravel from considerably large primary aggregates into loose aggregates or individual particles (Figure 5.2 (c)). At the final stage of dispersion (72000 cycles), very large primary aggregates with approximately 100 µm diameter and large resin rich areas are still present, despite the increase in loose aggregate areas seen in suspension (Figure 5.2

(d)). This indicates a very different morphology and dispersion level from the ultrasonicated material at the end of processing.

The conductivity of the 0.5 and 0.25 wt% high shear mixed suspensions is very similar both at the initial and at the final stage of dispersion (72000 cycles). At an intermediate stage (33000 cycles and 36000 cycles) the conductivity of the 0.5 wt% suspension appears higher than the one with half the CNT loading. The overall effect of ultrasonication process is a step change of electrical conductivity of the suspension by nearly three orders of magnitude. In contrast, the electrical conductivity of the high shear mixed liquid suspensions shows an increase by two orders of magnitude (Figure 5.4). These results indicate that ultrasonication is a more effective route of dispersing unmodified nanotubes in the epoxy system of this study.

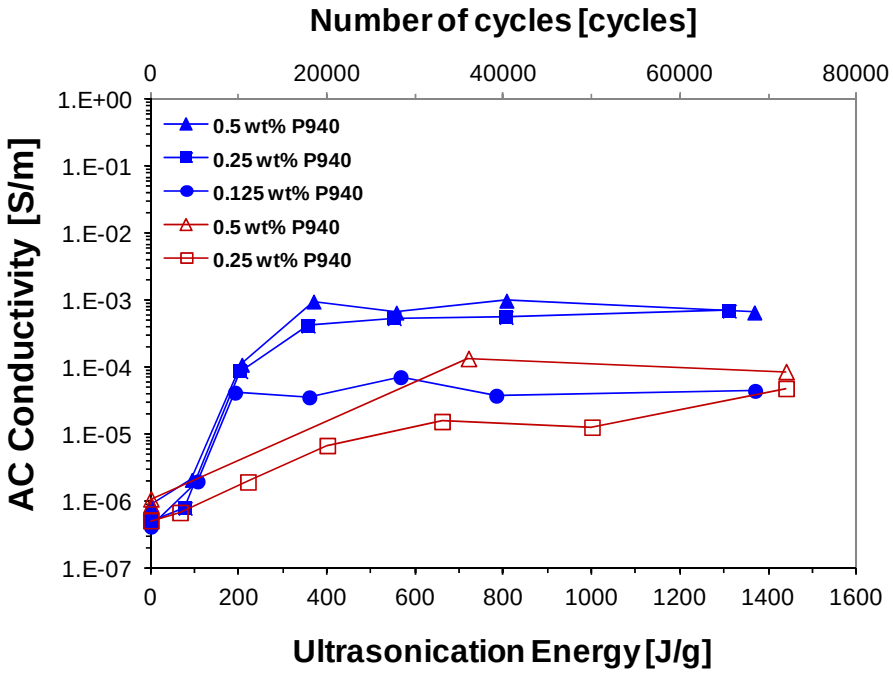

Figure 5.4 Evolution of the AC electrical conductivity during ultrasonication and shear mixing of P940 filled epoxy at different loading (filled symbols represent ultrasonicated material; open symbols represent high shear mixed suspensions).

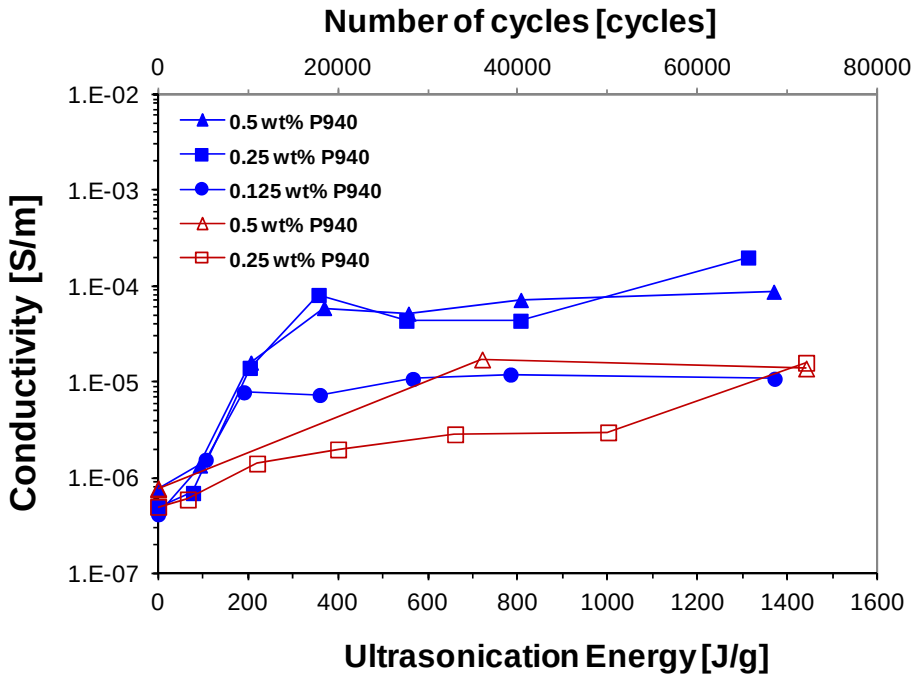

Figure 5.5 Evolution of the DC electrical conductivity during ultrasonication and shear mixing of P940 filled epoxy at different loading (filled symbols represent ultrasonicated material; open symbols represent high shear mixed suspensions).

An electrical conductivity plateau region is observed for ultrasonication energy inputs between 550 J/g and 1.3 kJ/g for both 0.25 and 0.5 wt% loaded suspensions. Consequently, for RTM manufacturing purposes a total energy input of 800 J/g was chosen to disperse P940 CNTs in the epoxy resin at 0.25 wt% CNT loading, since 0.5 wt% CNT contents lead to extremely viscous suspensions.

A similarity between the trends for AC and DC electrical conductivity of suspensions with the same CNT content and dispersed utilising the same technique can be observed in Figures 5.4 and 5.5. Despite this apparent resemblance between curve trends, DC results are approximately one order of magnitude lower than AC. Polarisation effects are believed to influence the DC response, causing this divergence between results [129]. These effects are particularly relevant at lower frequencies, especially in the case of DC measurement, where time is required for response stabilisation. These effects are also present in the complex impedance response at lower frequencies [130]. However, the AC conductivity is evaluated from the complex impedance spectra at a frequency region were charge migration is the main conduction mechanism and polarisation can be

neglected. Therefore, for these reasons the AC conductivity method is preferred when comparing different materials.

Higher electrical conductivity results were associated with efficient dispersed suspensions containing increasing content of CNTs. However, for 0.25 wt% and 0.5 wt% P940 suspensions dispersed by ultrasonication the electrical conductivity evolution was found to be very similar along the entire dispersion range. The same is not verified at intermediate stages of dispersion when these suspensions are dispersed by means of high shear mixing technique. Only at the final stage of dispersion (72000 cycles) by high shear mixing, the suspension containing 0.25 wt% P940 reaches conductivity values identical to the one filled with 0.5 wt% P940 CNTs.

5.1.2 Dispersion monitoring of liquid CNT nanocomposites using dielectric spectroscopy

The response to an AC field is related to the reorientation of permanent and induced dipoles and electrical conduction [131]. The complex resistivity spectra obtained from AC spectroscopy can provide information about the effect the evolution of CNT dispersion has on electrode polarisation, charge migration and dipolar relaxation phenomena occurring in thermosetting resins [132]. The CNT suspension can be described by two parallel RC sub-circuits connected in series, where the bulk represents the conductive areas, corresponding to primary or secondary aggregates and the interface corresponds to the insulating resin rich areas separating these conductive regions (Figure 5.6). This equivalent circuit is based on the bricklayer model used to simulate the behaviour of polycrystalline ceramics [133], and allows the determination of the resistor and capacitive elements of each phase.

The results of impedance spectroscopy for the 0.25 wt% P940 CNT/epoxy resin are presented in Figure 5.7. The evolution of dispersion observed in the ultrasonicated and the shear mixed material, illustrated in Figure 5.2 (a) and (b), was accompanied by an improvement of the suspension electrical conductivity, which is demonstrated by the drop in the complex impedance peak magnitude. At the initial state (0 J/g ultrasonication energy and 0 cycles) the imaginary resistivity of the unprocessed material decreases slightly up to 10 Hz, rising sharply after that up to 1 kHz, frequency

at which a peak followed by a linear drop towards higher frequencies occur. This behaviour is typical of thermosetting materials, when the spectrum is dominated by charge migration. At the initial stage, the resistivity is independent of the CNT content and very similar to that of the liquid epoxy [134], since a percolated network has not been formed yet. This behaviour is also observed for the 0.5wt% (Figure 5.8) and 0.125 wt% (Figure 5.9) CNT suspensions.

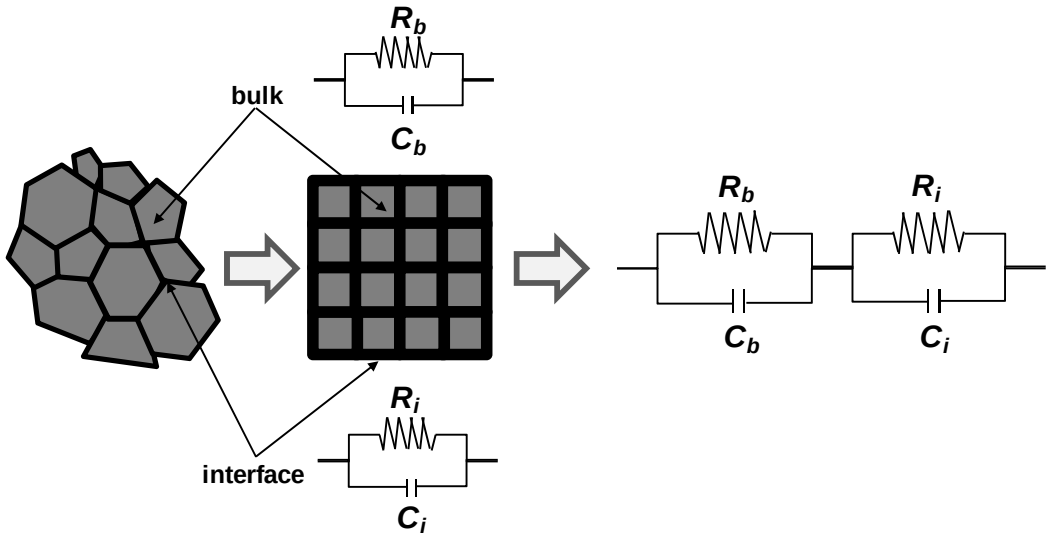

Figure 5.6 Schematic of the bricklayer model for polycrystalline materials and equivalent circuit (adapted from [132]).

Both dispersion processes change the appearance of these impedance spectra considerably and differently, with a movement towards lower resistivities, which corresponds to the increase in conductivity shown in Figure 5.4. In addition, the impedance spectra of the 0.25 wt% and 0.5 wt% P940 suspensions dispersed by ultrasonication at lower frequencies changes considerably after an energy input of 350 J/g, with the appearance of a knee towards lower impedance resistivities before the peak.

The impedance spectrum of the 0.125 wt% P940 suspension (Figure 5.9) shows the narrowing of the peak present at intermediate frequencies, together with the appearance of a secondary peak at higher frequencies, representative of an interfacial relaxation mechanism. This is due to the production of a conductive phase covering a larger volume of the suspension, as the CNT particles break up from primary aggregates forming loose aggregates.

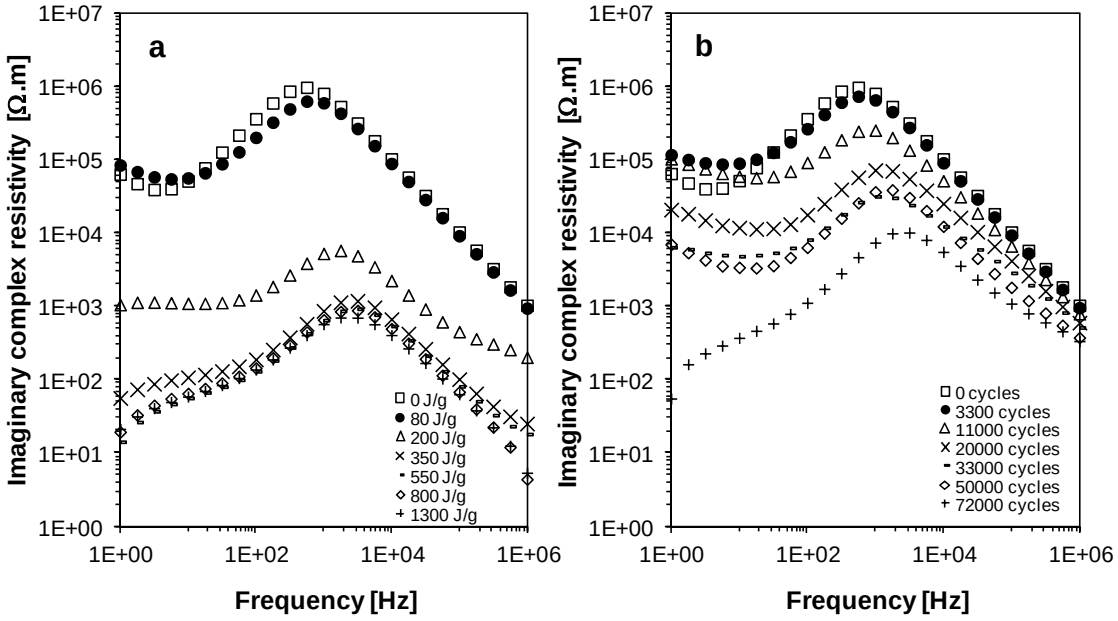

Figure 5.7 Evolution of imaginary impedance spectrum during the dispersion of 0.25 wt% P940 CNT/epoxy nanocomposite by ultrasonication (a) and shear mixing (b).

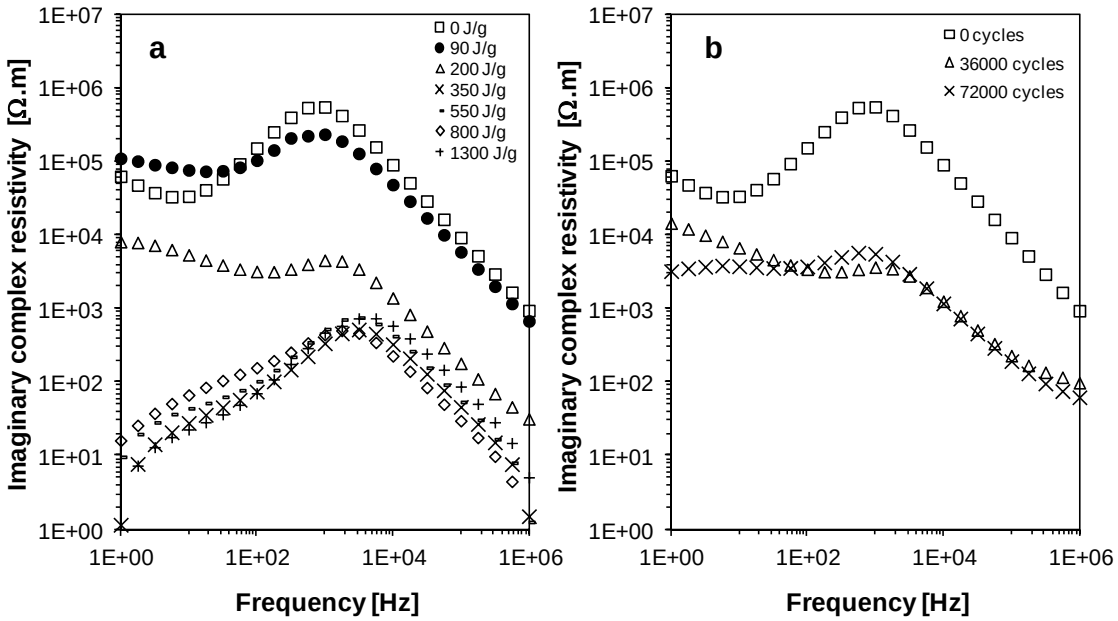

Figure 5.8 Evolution of imaginary impedance spectrum during the dispersion of 0.5 wt% P940 CNT/epoxy nanocomposite by ultrasonication (a) and shear mixing (b).

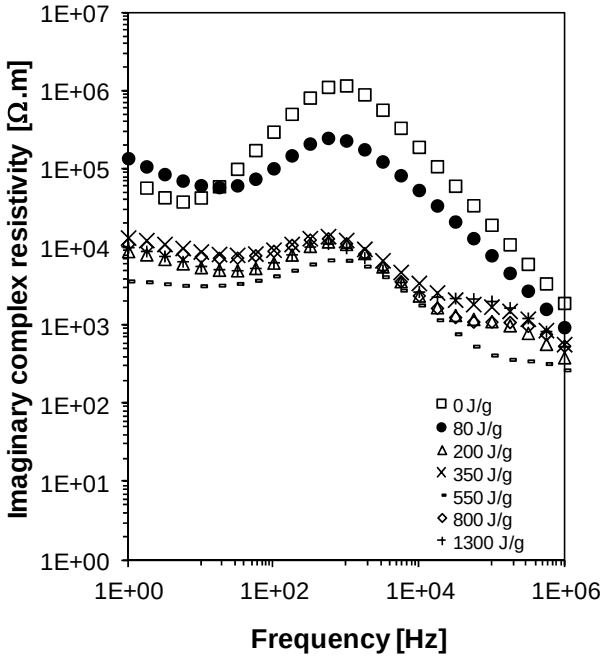

Figure 5.9 Evolution of imaginary impedance spectrum during the dispersion of 0.125 wt% P940 CNT/epoxy nanocomposite by ultrasonication.

Both dispersion processes result in impedance resistivity peaks moving towards slightly higher frequencies. Ultrasonication seems to be a better way of dispersing these CNTs in epoxy than high shear mixing, as only an ultrasonic input of 200 J/g results in a distinctive reduction of the impedance resistivity by more than two orders of magnitude. In addition, at the end of processing the impedance resistivity is consistently lower for ultrasonicated materials than high shear mixed ones.

5.1.3 Cured nanocomposites

Figure 5.10 shows SEM micrographs of the fracture surfaces of P940 cured nanocomposites, used to evaluate the combined effect of ultrasonication and cure on the final morphology of the carbon nanotube network.

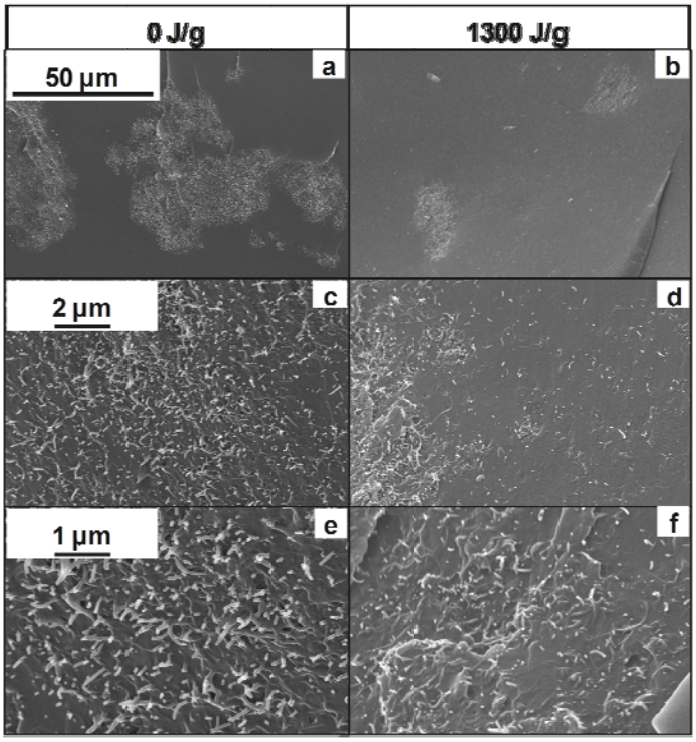

Figure 5.10 SEM micrographs of fracture surfaces of P940/epoxy nanocomposites at the beginning ((a), (c) and (e)) and end ((b), (d) and (f)) of the ultrasonication process.

Similarly to the optical microscopy results, large and dense agglomerates are present in the unprocessed resin (Figure 5.10 (a)). At the end of ultrasonication (1.3 kJ/g) a considerable reduction of the average size of CNT aggregates and of the number of aggregates larger than 50 µm is observed (Figure 5.10 (b)). Transitional areas between dense aggregates and dispersed CNTs are characteristic of the nanocomposite and can be seen in Figure 5.10 (d). These areas represent the unravelling of the CNTs at the boundaries of the dense aggregates with the resin. These unravelled CNTs eventually become loose and spread into the resin. Figures 5.10 (e) and (f) are high magnification images of CNT aggregates and represent the different morphology of dense and loose aggregates within the resin before and after the ultrasonication, respectively. Dense aggregates are characterised by a higher level of CNT entanglement and areal density, which is evidenced by the close proximity between individual CNTs. In contrast, in loose aggregates, as the one shown in Figure 5.10 (f), the mean distance between CNTs appears larger.

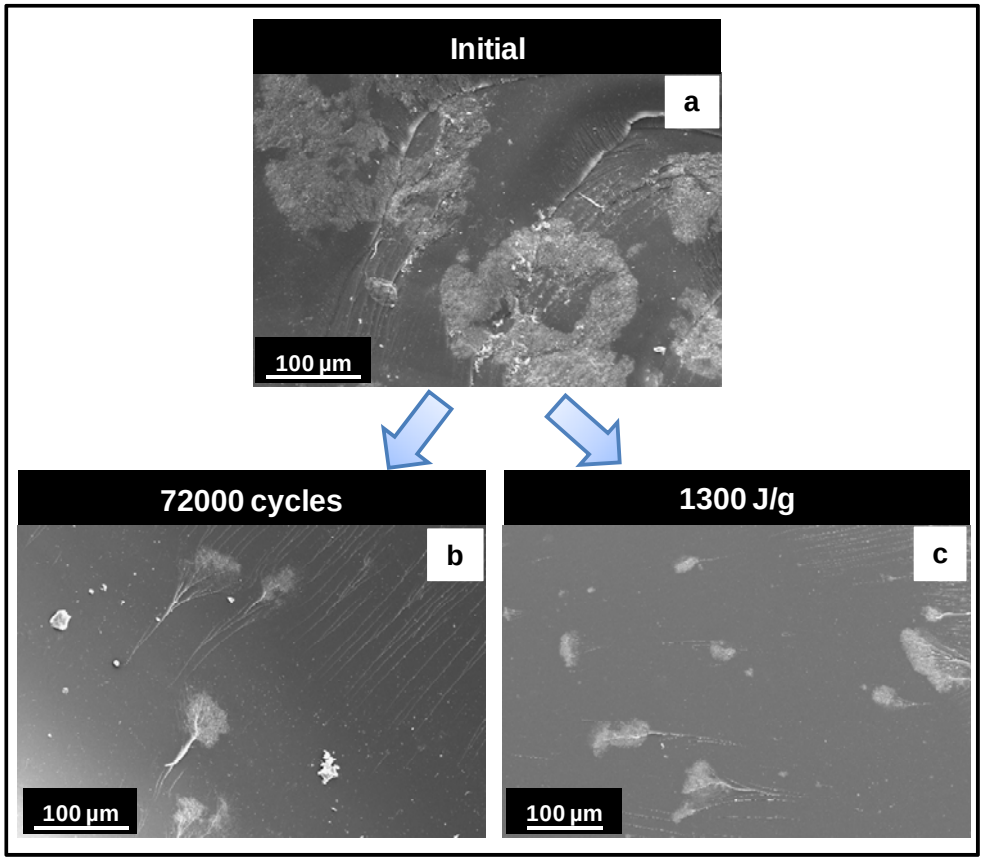

Figure 5.11 SEM micrographs of fracture surfaces of 0.5 wt% P940/epoxy nanocomposites prior processing (a) and after completion of shear mixing (b) and ultrasonication (c) processing.

Figures 5.11 and 5.12 show SEM micrographs of the fracture surfaces of 0.5 wt% P940 cured nanocomposites at different levels of dispersion. The initial state of dispersion prior to processing is depicted in Figure 5.11 (a), where large aggregates of about 200 µm can be observed. After completion of ultrasonication and high shear mixing processing, a significant reduction of the aggregates dimensions was observed, as shown in Figures 5.11 (b) and (c) respectively. Aggregates ranging from about 10 µm up to 100 µm can still be seen after complete ultrasonication (Figure 5.11 (b)), whereas after high shear mixing a range of aggregates from about 30 to 55 µm dimension are present (Figure 5.11 (c)). Despite the similarity between suspensions processed by ultrasonication or high shear mixing, possible damage caused to CNTs during high shear mixing could have compromised the electrical conductivity of the nanocomposite.

Figure 5.12 presents the intricate morphology and level of CNT entanglement at the core of CNT aggregates, which are present in suspension even after completing the

dispersion processing. Transitional areas between aggregates and resin, observed by optical microscopy in Figure 5.1, were also seen by SEM in Figure 5.13.

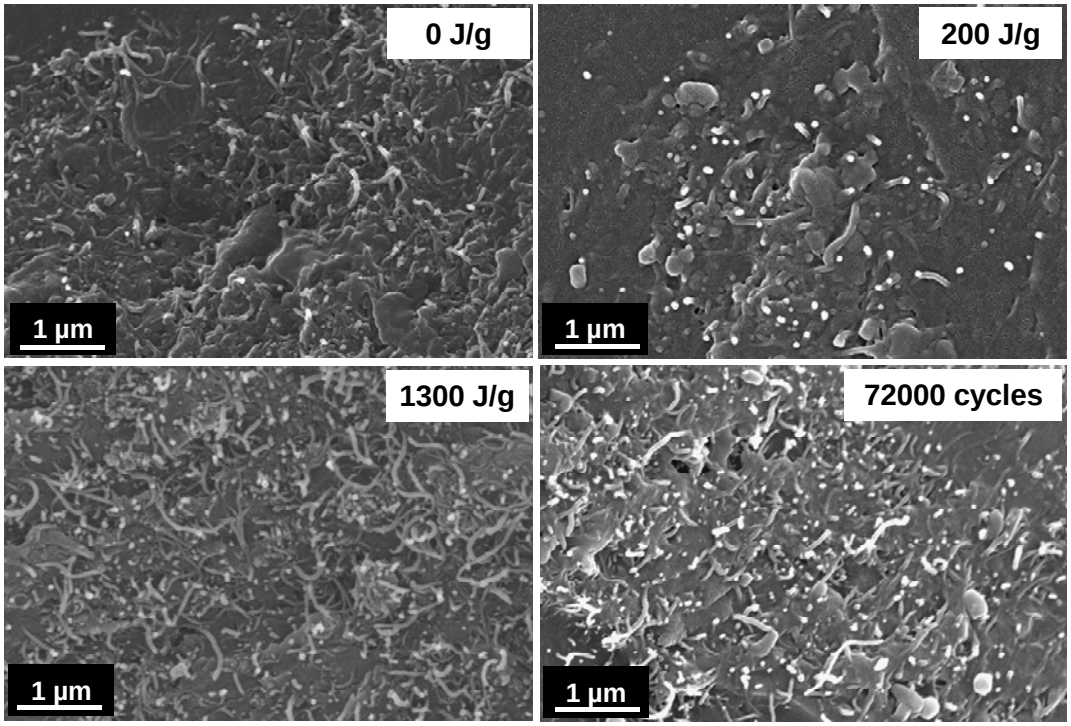

Figure 5.12 SEM micrographs of fracture surfaces of 0.5 wt% P940/epoxy nanocomposites

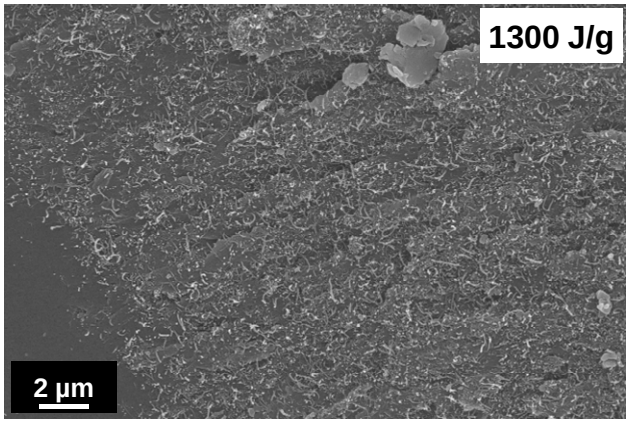

Figure 5.13 SEM micrograph of the fracture surface of 0.5 wt% P940/epoxy nanocomposites after completion of the ultrasonication process.

5.1.4 RTM suspensions

Figure 5.14 summarises the liquid electrical conductivity values for the various suspension formulations of this study. Dispersion processing of the C100 nanotube system by triple roll milling and high shear mixing leads to an increase in conductivity by two orders of magnitude, as shown in Figure 5.14. Further processing by ultrasonication causes a slight reduction in the electrical conductivity of the suspension, which may be explained by damage (reduction of the aspect ratio) of the CNTs during ultrasonication; indeed Figure 5.15 indicates a finer structure of loose aggregates in the ultrasonicated material. The sharp reduction in conductivity observed when the suspension of C100 nanotubes was heated up for 30 min at 40ºC (Figure 5.14) is due to reaggregation of the carbon nanotubes, accelerated by the elevated temperature. Such reaggregation could disrupt the conductive network formed by the nanotubes during dispersion processing. However, the conductivity remains higher than that of the original suspension, which indicates that the reaggregated agglomerates of nanotubes exhibit a looser structure compared to the aggregates of the material prior to dispersion. The electrical conductivity of the initial C100 suspension is lower than that of the corresponding P940 suspension, which is consistent with the lower average aspect ratio for the C100 system.

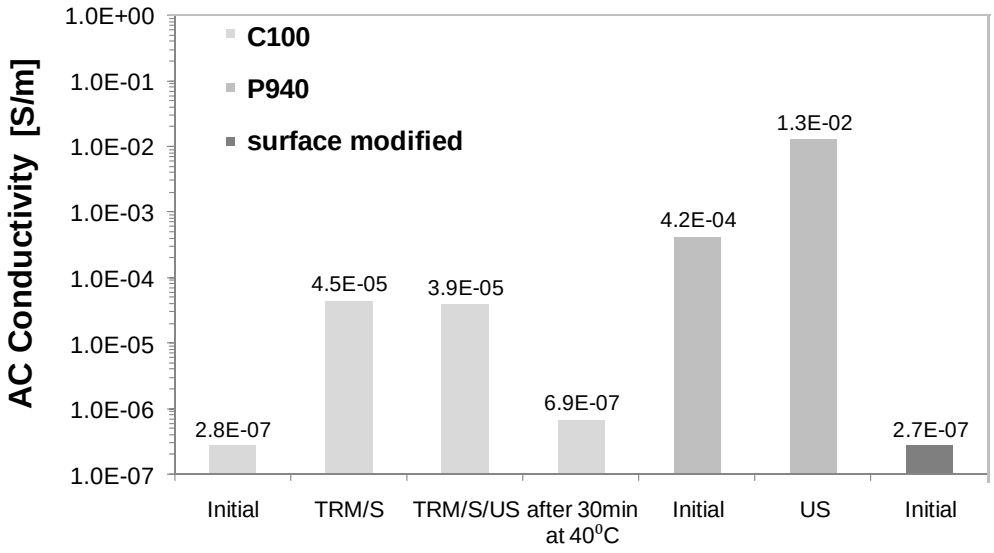

Figure 5.14 Electrical conductivity of CNT filled liquid resins.

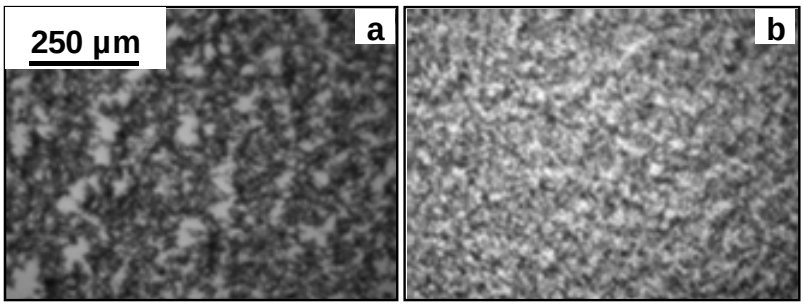

Figure 5.15. Liquid state transmission optical micrographs of the C100 filled suspensions at different dispersion steps: after triple roll milling and shear mixing (a) and after ultrasonication (650 J/g) (b).

Micrographs of the surface modified MWCNT filled suspension are shown in Figure 5.16, characterised by a stable and uniform dispersion of CNTs throughout the resin. Relatively small and loose aggregates and individual carbon nanotubes coexist in suspension, surrounded by areas of clear epoxy resin. The suspension conductivity of the surface modified system is low and comparable with the conductivity of the C100 system. This can be attributed to the limited tendency of the surface modified system to aggregate and form a conductive network and the effect of surface modification to the conductivity of the network of CNTs.

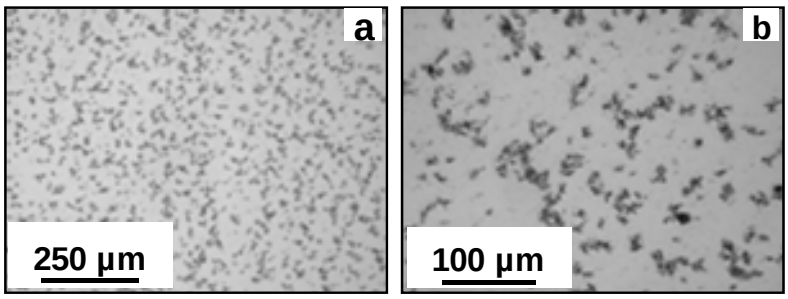

Figure 5.16 Liquid state optical transmission micrographs of the surface modified CNT filled epoxy at low (a) and high (b) magnification.

The phenomenon of cure-induced reaggregation was investigated for the cases of C100 and P940 nanotubes, as shown in Figure 5.17. Reaggregation observed in both materials was manifested as an increase in the amount and size of clear resin areas and by the formation of relatively denser (darker) aggregates.

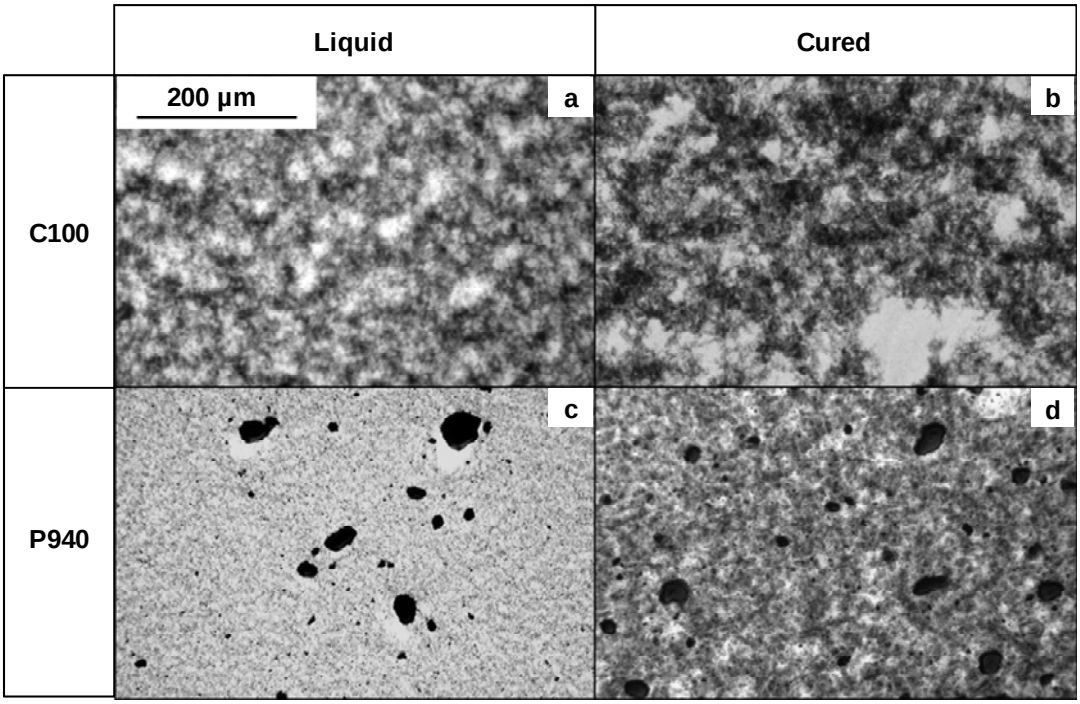

Figure 5.17 Liquid and cured state transmission micrographs of C100 and P940 filled epoxy: liquid C100 system (a); cured C100 system (b); liquid P940 system (c); cured P940 system (d).

5.2 RTM adaptation and processing issues in manufacture of multiscale composites

Pseudo-unidirectional uniweave fabrics were selected as reinforcement to avoid complications in processing that could result from multiple fibre orientation as the permeability of the fabrics and the rate of filtration of nanoparticles is expected to be uniform across the thickness. Also, the electrical properties measured after infusion and curing correspond to a single fibre orientation, allowing an evaluation of the effects of carbon nanotube addition to material properties to be made.

Compared to normal composite processing, RTM infusion with carbon nanoparticle filled resins requires process modification regarding the degassing steps as well as the selection of an appropriate mould filling temperature to compensate for the increased viscosity of the resin. CNT reaggregation during degassing was observed in the case of the P940/epoxy system. High suspension viscosity at the standard degassing temperature of 40ºC for this system resulted in an unacceptably long degassing process.

Ultimately the suspension was heated up to 50 ºC to reduce the suspension viscosity sufficiently to allow efficient removal of volatiles. The duration of this process was approximately one hour and the dispersion state was compromised as a consequence, with slightly larger aggregates present in the sample after degassing. In the case of the C100 system as well as of the surface modified material changes to the procedure of resin degassing were not required, as the lower viscosity of these systems allowed the process to be completed at 40 ºC within an acceptable time.

These results and the results on the electrical response of nanocomposites presented in the previous section point to the difficulties arising due to the interplay between the state of dispersion, processability and electrical performance. Dispersion states corresponding to high conductivities such as these observed in the P940 nanocomposite are inherently more difficult to degas and require modification of the degassing cycle usually involving higher temperatures and/or longer process times. A balance between the benefits of degassing and the loss of electrical performance due to extensive reaggregation is necessary when designing the modified process.

5.2.1 Rheology

Figure 5.18 shows the viscosity dependence on the shear rate for all the suspensions utilised for liquid moulding at the corresponding filling temperature. Shear rate dependent suspensions such as the ones filled with unmodified CNTs show higher viscosities. In contrast, the unfilled and the surface modified CNT filled epoxy show negligible shear rate dependence and have lower viscosity. The viscosities of the P940 system are the highest observed at low and intermediate strain rates. This result is consistent with the observations during degassing where modification of the schedule is required to complete the process for this system. As the shear rate increases the viscosity of all systems tends to plateau at a level that is similar to that of the unfilled epoxy.

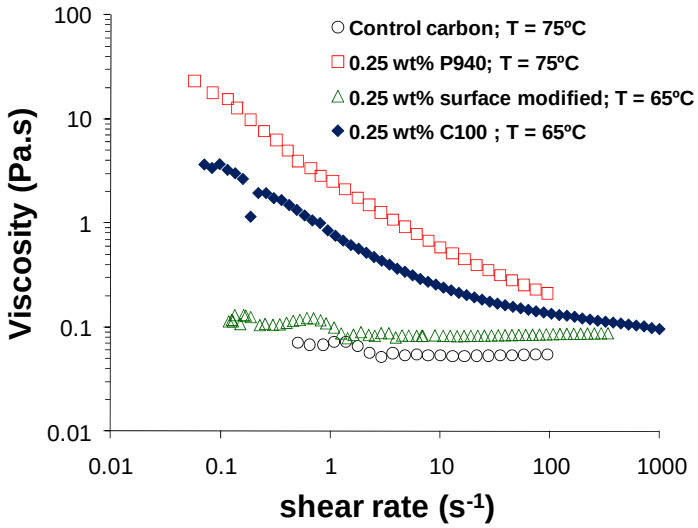

Figure 5.18 Suspension viscosity as a function of shear rate.

5.2.2 Filtration

Figure 5.19 shows the resin flow front during RTM injection together with a close view of the flow front where inter-tow and intra-tow flow can be distinguished, for the case of C100 CNTs and glass fabric. CNT filtration was observed macroscopically for the systems containing unmodified CNT. Resin was seen running clear at the outlet gate for the injection of carbon reinforcement composite with P940 filled suspension. In glass reinforced composites infused with C100 filled epoxy some colour variation in the final composite was a clear indication of CNT filtration by the porous media. In contrast, surface modified CNTs did not show macroscopic and qualitative evidence of filtration, since resin was not seen running clearer at the outlet gate.

The solution of Darcy's problem for a fluid of constant viscosity η, in a porous medium of constant effective permeability K and porosity ε in an one dimensional situation with prescribed pressures at the inlet and outlet can be described by the following expression:

$$h(t) = \sqrt{\frac{2K}{\varepsilon\eta}(p_o - p_\infty)t} \tag{5.1}$$

Here *h(t)* denotes the flow front position at time *t*, and p_o and p_∞ are the prescribed pressures at the inlet and outlet of the mould respectively. This solution implies a linear dependence of flow front position on the square root of time.

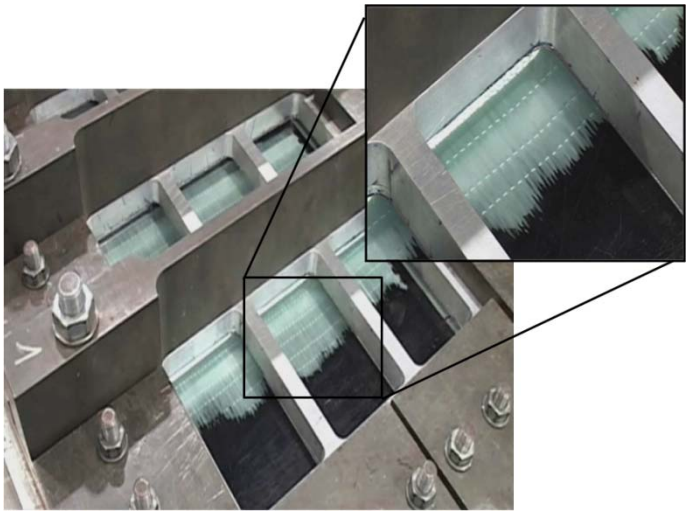

Figure 5.19 Resin flow front during RTM injection of glass composite with C100 filled suspension.

Figure 5.20 illustrates the measured resin flow front position versus the square root of time alongside a linear fit using Eq. (5.1). Significant deviation from the linear behaviour is observed in both cases of unmodified CNTs. In contrast, the control and surface modified carbon nanotubes filled material follow the linear fit closely. Deviation from the square root dependence can be attributed both to the highly non Newtonian behaviour of the modified resin and the retention of nanoparticles by the reinforcement which modifies the resin viscosity and influences slightly the local permeability of the fabric. Longer filling times were also characteristic of the two unmodified CNT filled materials. This can be attributed to their intrinsically higher viscosity profiles and the reduction of the reinforcement porosity caused by the clogging of the available pores through which resin circulates, which is expected to be a secondary effect.

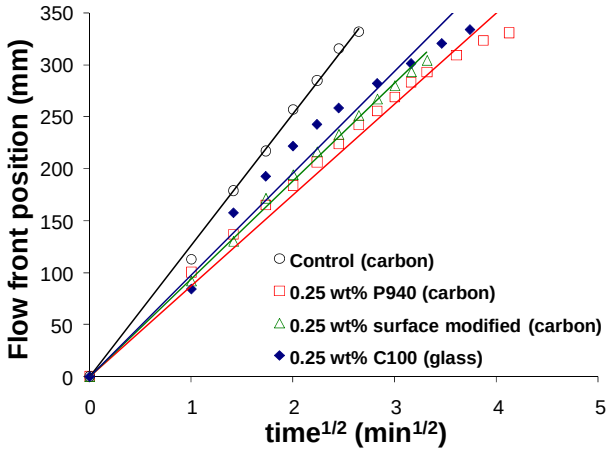

Figure 5.20 Resin flow front profiles during RTM injection.

The distribution of CNTs at the inlet and outlet regions, and on delamination surfaces of the composite panel was investigated for all the systems by means of SEM. Very large aggregates (~ 50 μm) were found at the inlet for the case of P940 CNTs. A partial view of one of these aggregates is shown in Figure 5.21(a). The composite structure incorporates two pore scales through where resin flow occurs (100 μm and 10 μm). These are characteristic of the inter and intra-tow spacing dimensions. Large and highly entangled CNT aggregates concentrated in resin rich pockets, located between the carbon tows and the non structural stitches, are observed on the composite delamination surface of the P940 material in Figures 5.21 (c) and (d). These aggregates become less frequent away from the resin inlet due to filtration. Furthermore, the resin located at the outlet region contains virtually no CNT agglomerates as shown in Figure 5.21 (b). These observations indicate the occurrence of cake filtration at a microscopic level. Size exclusion is considered as the main filtration mechanism for this CNT system. In addition, the non-Newtonian behaviour of the suspension associated to hydrodynamic effects, caused by a non-uniform shear field during fluid flow and nonsphericity of the particles [54], can also contribute to preferential particles deposition especially in stagnation zones where low shear strains are present. Though not observed in SEM, other potential mechanisms of filtration in fibrous media for CNT filled suspensions such as inertial effects and direct interception with the fibre surface could be active.

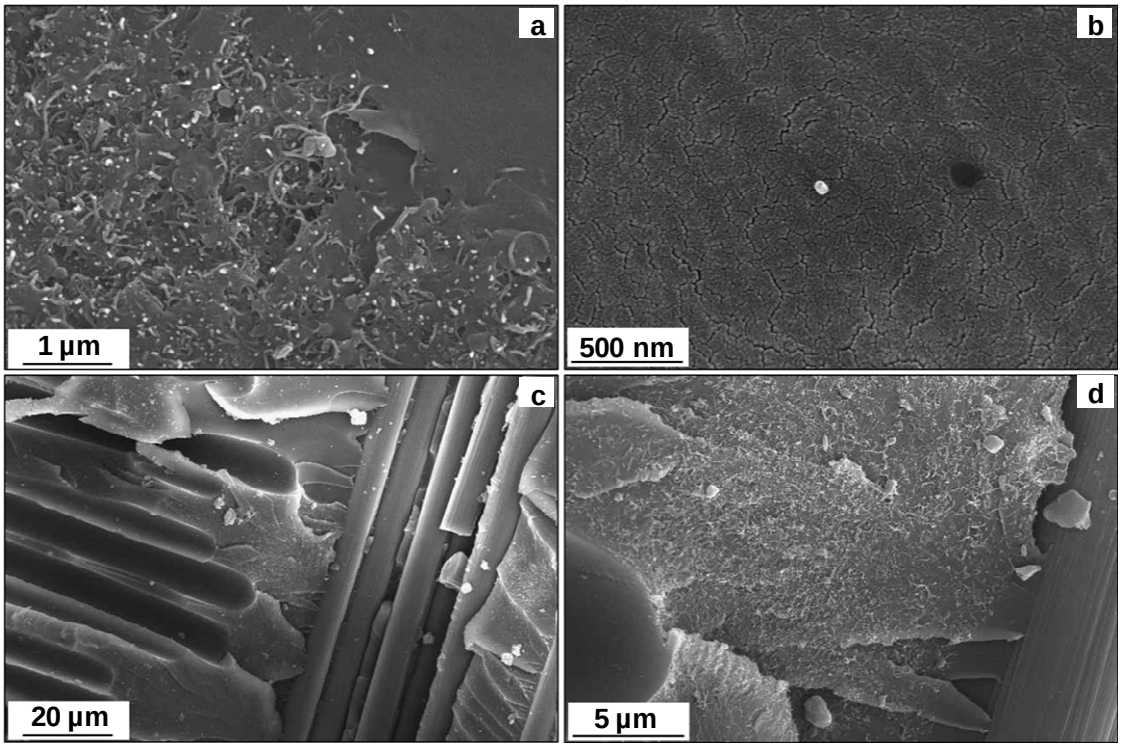

Figure 5.21 SEM micrograph of the fracture surface of the P940 filled resin at the inlet (a) and outlet region (b); and delamination surface of the corresponding fibre composite 100 mm away from the inlet (c) showing CNT filtration at resin rich pockets (d).

C100 nanotubes were also filtered when passing through the glass porous media. However, smaller and looser aggregates (10 µm maximum dimension) than the ones seen in P940 filled resin were present at the inlet region as illustrated in Figure 5.22. Also small and loose CNT aggregates were found in resin rich pockets and inter-fibre areas of the composite as shown on Figure 5.22 (c). In contrast to the P940 system where cake filtration is observed, the gradient in nanotube concentration in the C100 system is significantly lower which indicates that deep bed filtration is the dominant mechanism in this system in the initial stage of filling. Later in the process the accumulation of retained nanoparticles might lead to retention via size exclusion and cake filtration.

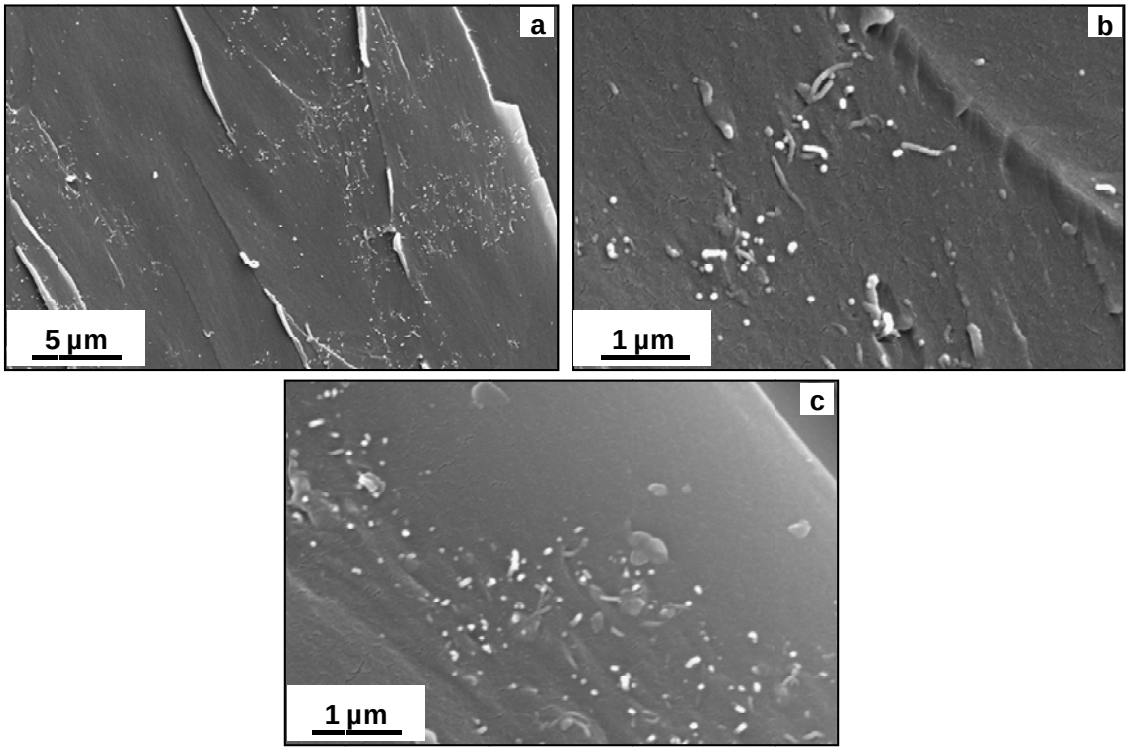

Figure 5.22 SEM images of the inlet region (a and b) of the C100 filled resin; and delamination surface of the corresponding fibre composite at approximately 130 mm away from the inlet (c)

The potential reaggregation of CNTs is a significant factor in the interaction between flow and filtration in unmodified systems such as the P940 and C100 nanotubes. The reaggregation would lead to gradually increased size of filtered nanoparticles and eventually promote cake filtration.

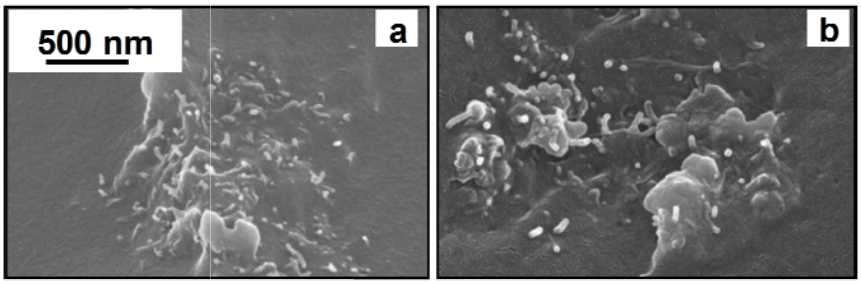

Figure 5.23 SEM micrograph of the fracture surface of the composite with surface modified CNTs: inlet (a) and outlet (b) resin.

This effect is not present in modified systems like the surface modified nanotubes used in this study. This fact in combination with the small initial aggregate size leads to

negligible filtration as evidenced by the uniform presence of 2-3 μm size loose aggregates both at the inlet and outlet regions of surface modified CNT panels as illustrated in Figure 5.23.

5.3 Evaluation of composites quality

Visual inspection and c-scanning were utilised to evaluate the existence of dry spots and the impregnation. Figure 5.24 shows the output c-scans of the composites produced.

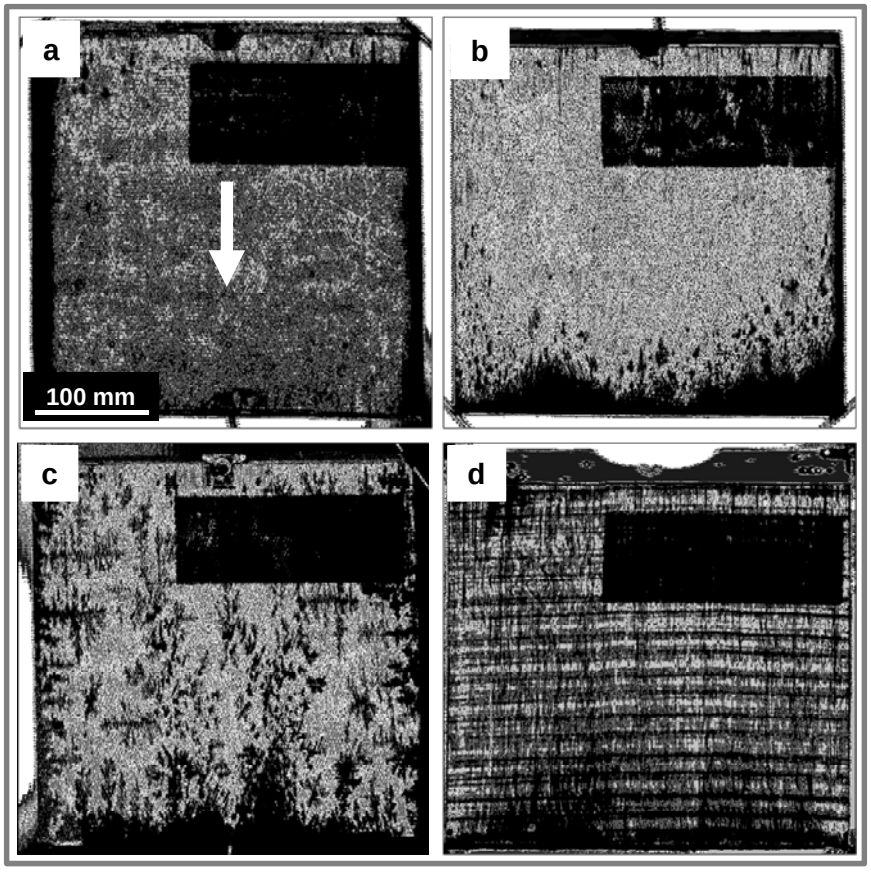

Figure 5.24 C-scan images of the control carbon composite (a), P940 (b), surface modified (c) and C100 (d) CNT multiscale composites

Darker regions define the presence of defects, i.e. porosity. The black rectangle present on the right hand side of each panel corresponds to the location of a PTFE film necessary to generate a pre-crack for the composite DCB specimens (section 4.7). The dark regions at the outlet side of each composite and all over the surface modified CNT composite are representative of incomplete saturation of the top surface of these composites, as confirmed by inspection of cross sections across these regions. The only

exception is the dark region at the right hand side corner of the P940 CNT composite (Figure 5.24 (b)), where dry fibres can be seen by visual inspection. The surface dry areas are associated with insufficient degassing of these suspensions, relatively high viscosity of the suspension at the infusion temperature to allow adequate removal of volatiles, and insufficient amount of resin in the case of the surface modified CNT composite (Figure 5.24 (c)). Special care was taken to avoid testing specimens within these regions.

5.4 Electrical properties of the CNT modified fibre composites

The results of electrical measurements of carbon laminates indicate highly anisotropic electrical behaviour of the composite as shown in Figure 5.25. The electrical conductivity in the fibre direction is two to three orders of magnitude higher that the conductivity in the in-plane transverse and through thickness directions respectively. This is expected as the carbon fibres form continuous conductive paths in the unidirectional material, governing the conductivity in this direction. The drop in the longitudinal electrical conductivity when adding CNTs to the composite is within the scatter of results. The conductivity in the in-plane transverse direction is one order of magnitude higher than that in the through thickness direction. In this case the level of contact between adjacent carbon fibres is the governing parameter and the packing of fibres in the in-plane direction is denser than that between successive layers in the out-of-plane direction. Consequently, the addition of carbon nanotubes has an effect only in the conductivity of the through thickness direction of carbon composites where the electrical behaviour of resin rich areas plays a more significant role. The improvement in through thickness conductivity of carbon laminates is more significant for the unmodified CNTs (P940) than the surface modified system due to the tendency of unmodified nanotubes to form a conductive network via reaggregation. However, the scattering in conductivity values is higher in the unmodified system which is indicative of non-uniformity caused by filtration in this material.

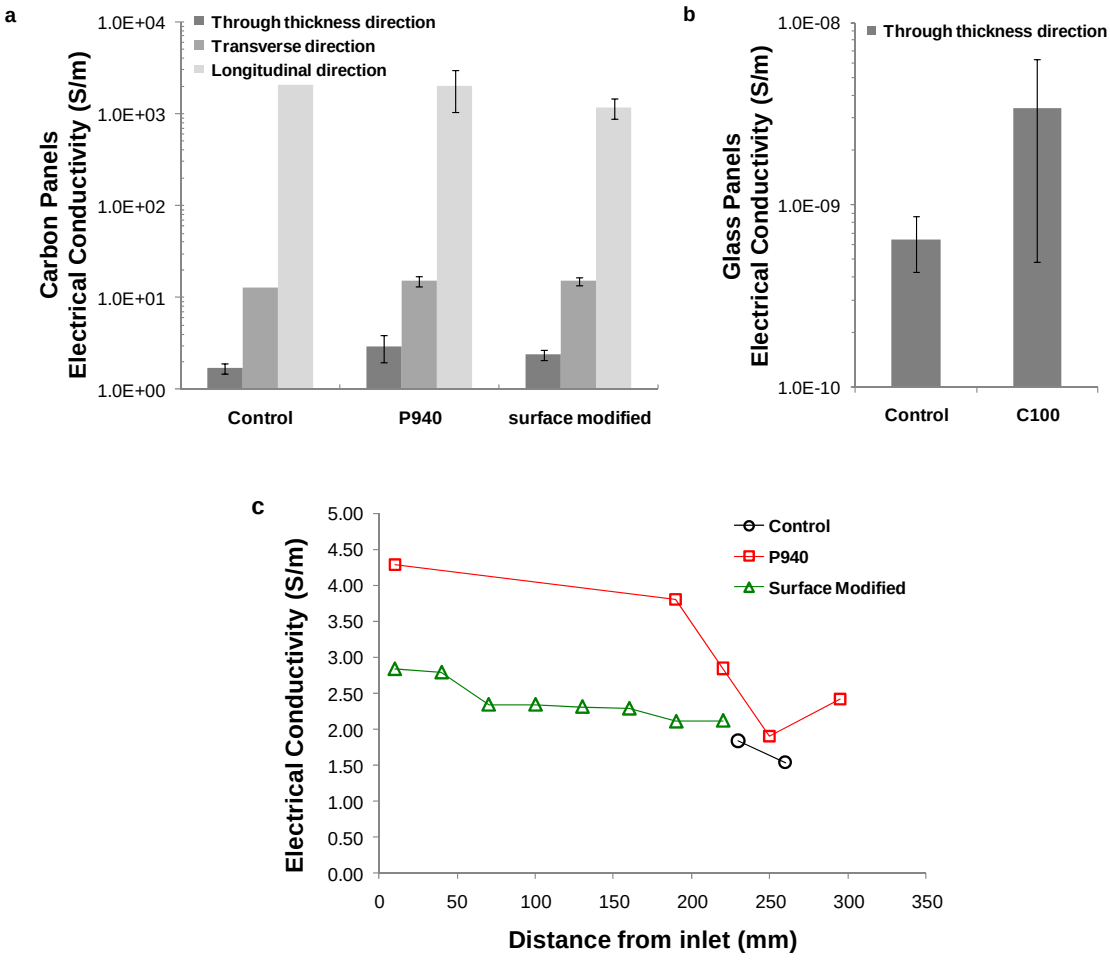

Figure 5.25 Electrical conductivity of the CNT filled carbon (a) and glass fibre composites (b), and evolution of through thickness electrical conductivity of the nanoparticle filled carbon composites as a function of the distance from the inlet gate (c).

The addition of C100 carbon nanotubes in the glass composite also increases the through thickness conductivity of the glass composite. The increase is relatively modest (approximately one order of magnitude), a result which is in line with the relatively low conductivity of the C100 suspension reported in Figure 5.14. Similarly to the unmodified CNT system used with carbon fibres, the conductivity of the CNT loaded material exhibits high scatter in its values, as a result of filtration effects.

Filtration is also investigated in Figure 5.25 (c), by identifying spatial variations of through thickness conductivity of carbon reinforced composites. A slight reduction of the electrical conductivity of the composite can be observed. This phenomenon occurs even in the case of surface modified CNTs indicating filtration at the microscopic level.

5.5 Conclusions

The outcome of this investigation demonstrates the feasibility of processing realistic aerospace grade composites, comprising aerospace materials, such as high temperature epoxies and carbon fibres at high fibre volume fraction, with CNT loaded epoxy matrices, resulting in enhanced electrical performance. A range of possibilities exists for the design of the process and the selection of materials.

The modification of epoxy resins by carbon nanotubes lead to the need to modify the process route for the manufacture of multiscale composite laminates via liquid resin moulding processes. A dispersion step needs to be added before the filling process during which the nanotubes are suspended in the liquid resin with the aim of maximising their eventual performance enhancement effects. The state of dispersion can be evaluated successfully by carrying out measurements of electrical conductivity during the dispersion process. In the formulations tested here it was found that additional dispersion processing was only necessary for unmodified carbon nanotubes which enter the process in an aggregated form and also have the tendency to reaggregate during processing. Electrical conductivity measurements have shown that ultrasonication is a better way of dispersing P940 CNTs when compared to high shear mixing. P940 contents of 0.5 wt% were found to cause just a slight improvement in the electrical conductivity of the suspension when compared to 0.25 wt%. In addition, the higher viscosity of the 0.5 wt% suspension was found to be inappropriate for RTM. Therefore, the CNT loading for all the systems was kept at 0.25 wt%.

Degassing schedules for well dispersed unmodified CNT-containing systems need to be carried out at elevated temperatures, to compensate for the increase in viscosity. This process modification is not straightforward as the increase in temperature also accelerates reaggregation effects that could potentially degrade the efficiency of nanotube addition with respect to electrical performance and can also initiate the curing reaction and increase the viscosity of the system further. The increase in viscosity also plays a role during the filling stage of liquid moulding processes by slowing down the progression of the flow front.

Surface modified nanotubes offer an easy processing solution, requiring minimum process modifications but at the cost of higher material cost and lower achievable electrical conductivity compared to the composites made with unmodified multiwalled nanotubes. Unmodified nanotubes require adaptations both in the degassing and filling stages of the RTM process. The cost of these needs to be set against the higher raw material cost of unmodified tubes and higher potential for enhancement of the electrical behaviour.

The interaction of suspended and aggregated nanotubes with the reinforcement fibres results in filtration effects that can be significant in unmodified CNT- containing systems. The state of dispersion of the nanoparticles and their tendency to reaggregate governs the type of filtration behaviour. Cake filtration dominates in situations where aggregates with sizes comparable to the pores of the reinforcement are present in the suspension. In these systems relatively large CNT aggregates are found in resin rich-pockets closer to the inlet side of the mould, whereas very few nanoparticles are present in the outlet side of the composite. In contrast deep bed filtration occurs in situations where the size of aggregates remains relatively small compared with the pores. Filtration effects affect the macroscopic resin flow in the mould due to the dependence of viscosity and permeability on the local concentration of nanoparticles as well as the modification of porosity with the accumulation of retained particles on the fabric.

Both carbon and glass fibre reinforced composites containing the CNT-filled matrix were prepared, resulting in fibre volume fractions of 57% and 59% respectively. The enhancement of electrical behaviour by the addition of CNTs in carbon composites followed the anisotropic character of these materials. The through-thickness conductivity almost doubled with the addition of nanotubes and the enhancement was stronger for unmodified nanotubes. The conductivity in the in-plane directions, which is dominated by that of the carbon fibre, remained unaffected. The electrical conductivity of glass composites increased by one order of magnitude with the addition of nanotubes, to a level which can still be considered modest. Electrical conductivity measurements of specimens at different locations in the mould were found useful to evaluate the extent of CNT filtration during injection, especially for the case of surface modified CNTs. Despite the larger extent of filtration verified for the unmodified CNT system, these

CNTs provide a better improvement of the composite electrical conductivity properties when compared to surface modified CNTs.

6 RTM processing and electrical properties of CNF modified epoxy/fibre composites

This chapter focuses on the transfer of the enhanced electrical properties of a CNF modified resin to the final multiscale composite structure. Optical microscopy and SEM was utilised to evaluate the state of dispersion in the liquid and cured nanocomposite, of varied content of CNF modified suspensions when using ultrasonication and high shear mixing processes. Electrical conductivity measurements of these suspensions allowed the selection of the most appropriate dispersion method for this modified system. A 0.25 wt% CNF modified suspension was used to infuse a pseudo UD carbon fabric using the RTM manufacturing process. Adjustments to the processing conditions were carried out and the quality of the produced composite was evaluated. The extent and nature of particle filtration were identified microscopically and macroscopically and the electrical conductivity of the fibre composite was evaluated.

6.1 Effect of dispersion on the electrical conductivity of liquid nanocomposites

The effects of different mixing processes and CNF content on the dispersion state and the electrical conductivity of CNF liquid samples were investigated, as basis for the selection of adequate suspensions to be utilised in the infusion of carbon reinforcements. Figures 6.1 and 6.2 illustrate the evolution of microstructure associated with the dispersion of 0.5 wt% and 1 wt% CNFs in the epoxy resin, respectively, by means of ultrasonication and high shear mixing. Figure 6.3 summarises the evolution of AC electrical conductivity of these suspensions during dispersion processing. Entangled aggregates found in a variety of dimensions ranging from a few microns to 250 μm, are seen surrounded by individual CNF nanoparticles in both initial suspensions (Figure 6.1 (a) and Figure 6.2 (a)). The AC conductivity of the unprocessed suspension containing 1 wt% CNF is approximately 3 orders of magnitude higher than the corresponding one loaded with 0.5 wt% CNF.

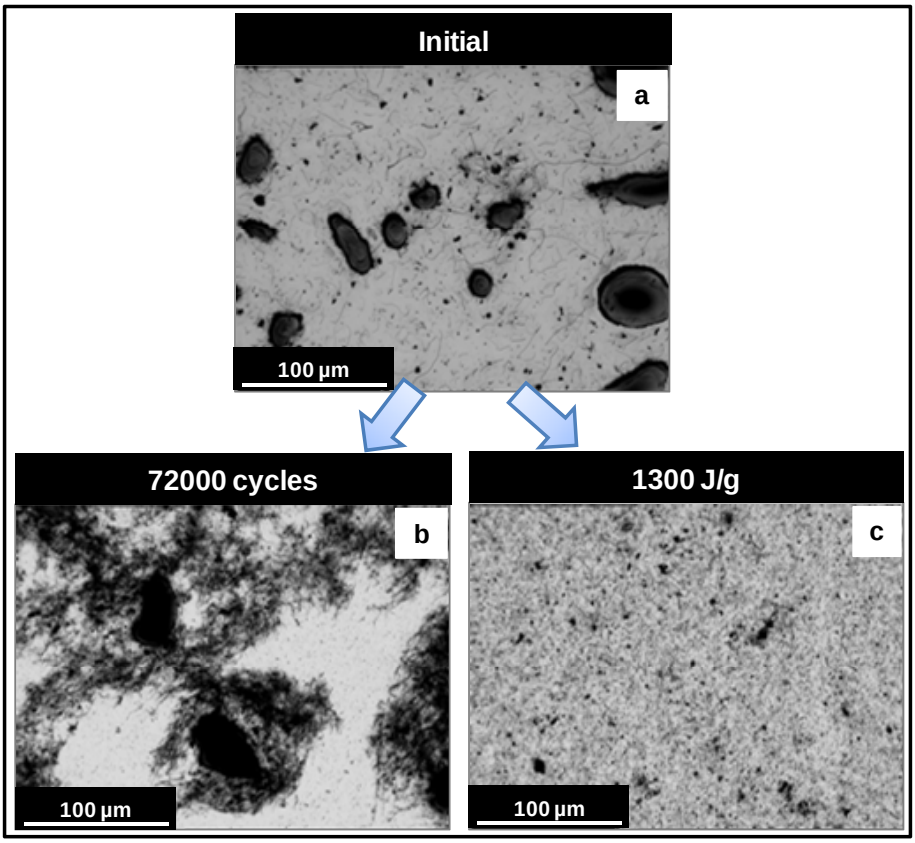

Figure 6.1 Liquid state optical transmission micrographs of the 0.5 wt% CNF filled suspensions at different dispersion/processing levels: before processing (a); after completion of high shear mixing (b) and ultrasonication (c) processes.

Ultrasonication and high shear mixing processing lead to very distinct states of dispersion, as shown in Figures 6.1 (b) and (c), and Figures 6.2 (c) and (d). At the initial stages of dispersion processing by high shear mixing (11000 cycles) the AC conductivity of the suspension loaded with 1 wt% CNF reaches a maximum value. At this point, the majority of large and dense aggregates have been unravelled, and form regions of looser aggregates at the periphery of the smaller dense aggregates (Figure 6.2 (b)). As processing continues the AC conductivity drops slightly and by the end of processing reaches values similar to the unprocessed suspension. Despite the detrimental effect on the conductive network caused by continuous processing, the final state of dispersion shown in Figure 6.2 (c) reveals a loosely aggregated structure, characterised by very small dense aggregates and individual CNFs. In contrast, continuous shear mixing of 0.5 wt% CNF suspension led to an improvement of the AC conductivity by as much as two orders of magnitude, which implies that at this stage the

number of conductive links formed increases considerably. Nonetheless, the considerably more aggregated morphology of this suspension seems to suggest that a certain level of aggregation benefits the overall electrical conductivity. This is confirmed by the extremely poor electrical performance of CNF suspensions processed by ultrasonication, where a finer morphology and a more homogenous dispersion are observed (Figures 6.1 (b) and 6.2 (d)). Although ultrasonication improves the state of dispersion, the overall effect on the electrical conductivity of the suspensions filled with 0.5 wt% CNFs is considered negligible, whereas for the case of suspensions with 1 wt% CNFs ultrasonication was detrimental. Ultrasonication might be impeding the formation of a percolated conductive network and/or causing damage to the CNFs. These results indicate that high shear mixing is a more effective method of dispersing CNFs in the epoxy system of this study.

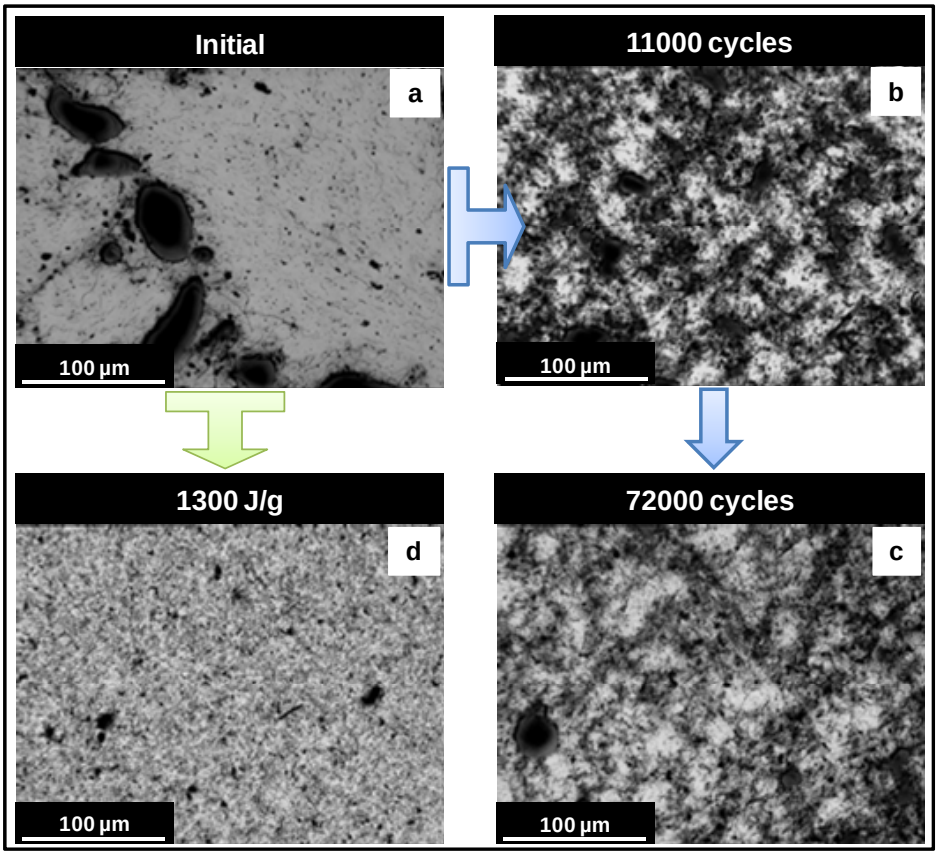

Figure 6.2 Liquid state optical transmission micrographs of the 0.5 wt% and 1 wt% CNF filled suspensions at different dispersion/processing levels.

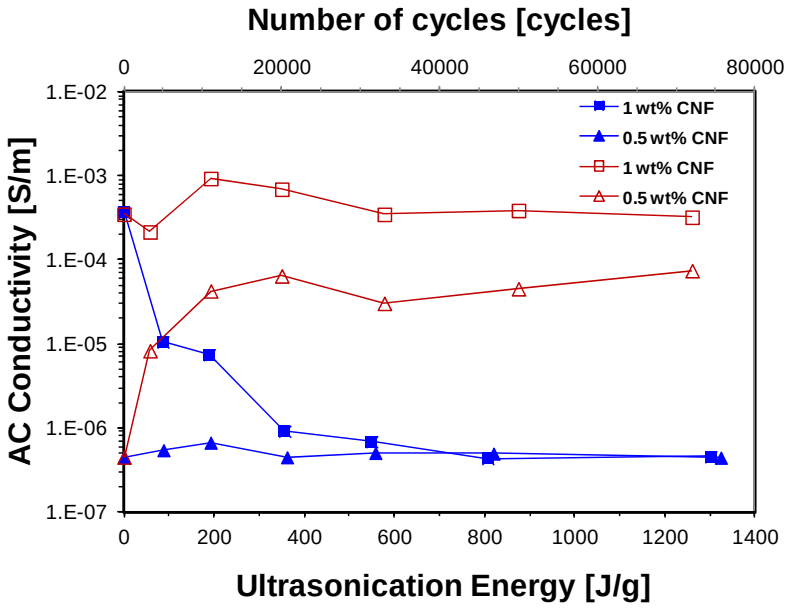

Figure 6.3 Evolution of the AC electrical conductivity during ultrasonication and shear mixing of CNF filled epoxy (filled symbols represent ultrasonicated material; open symbols represent high shear mixed suspensions).

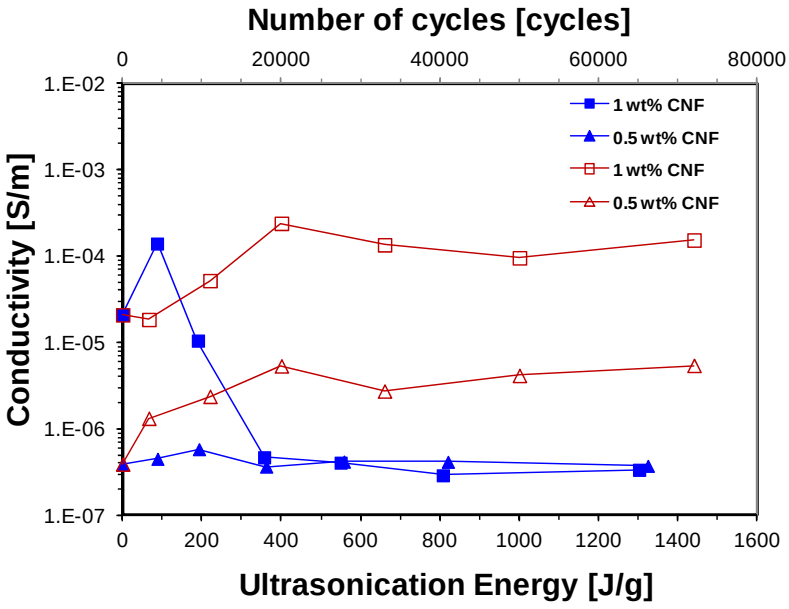

Figure 6.4 Evolution of the DC electrical conductivity during ultrasonication and shear mixing of CNF filled epoxy (filled symbols represent ultrasonicated material; open symbols represent high shear mixed suspensions).

The evolution of DC electrical conductivity of the suspensions during dispersion processing is shown in Figure 6.4. For most of the cases the conductivity values for each suspension are nearly one order of magnitude lower than for the corresponding AC conductivity results, with the exception of the ultrasonicated suspension containing 0.5 wt% CNF. Deviations between DC and AC results are dominated by polarization effects present when utilising the DC method [129]. Therefore, for the reasons described in section 5.1, the AC conductivity method was preferred when comparing different materials.

6.2 Dispersion monitoring of liquid CNF nanocomposites using dielectric spectroscopy

The results of impedance spectroscopy for the 0.5 wt% CNF modified epoxy resin are presented in Figure 6.5. The evolution of dispersion observed in the ultrasonicated material, illustrated in Figure 6.1 (a) to (c), was not accompanied by an improvement of the suspension electrical conductivity. This is manifested by little variation in the complex impedance peak position and magnitude (Figure 6.5 (a)). In contrast, when the same content of CNF is dispersed by high shear mixing, the impedance spectrum changes considerably with the enhancement of the level of dispersion, as shown in Figure 6.5 (b).

At the initial state (unprocessed material) the imaginary resistivity remains practically constant up to 10 Hz, after which a rise in resistivity results in a peak at 600 Hz followed by a linear drop towards higher frequencies.

After the initial stage of dispersion (3300 cycles) the impedance behaviour is considerably different from that of the unprocessed suspension. The peak value decreases by more than one order of magnitude, and becomes broader than that of the unprocessed suspension. Continuous dispersion enhances these effects and results in the appearance of a knee at high frequencies indicating an interfacial relaxation mechanism.

When 1 wt% CNF loadings are used the impedance spectra becomes distinctively different than the one observed for 0.5 wt% CNF modified epoxy. The unprocessed material is characterised by a considerably small imaginary resistivity. The dispersion by ultrasonication seems to cause a detrimental effect on the electrical properties of the

suspension. Higher and slightly narrower imaginary resistivity peaks are observed for increasing dispersion steps, as shown in Figure 6.6. (a). Similarly, high shear mixing process also results in impedance spectra where higher imaginary resistivity peaks tend to move towards lower frequencies as the processing level increases.

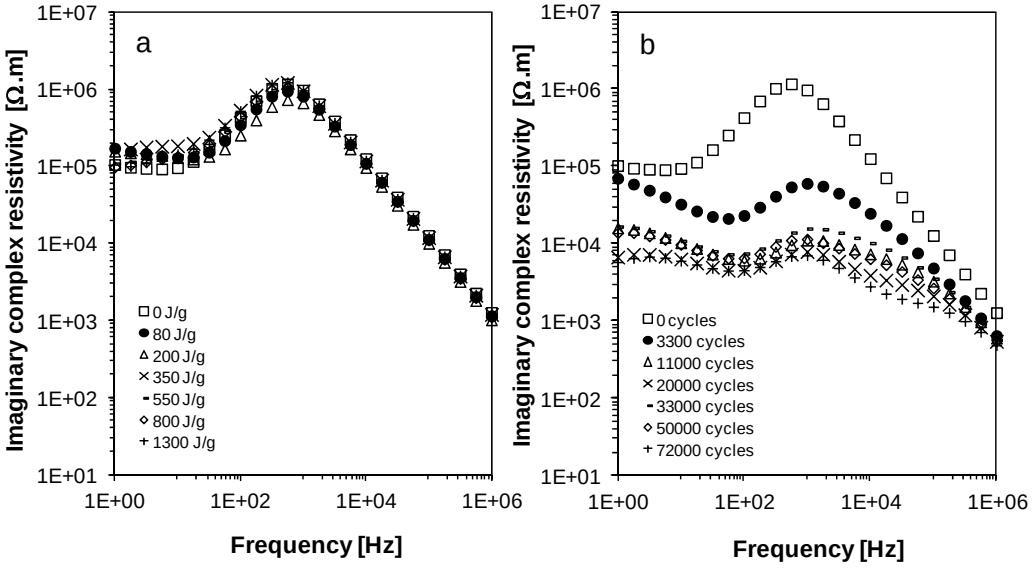

Figure 6.5 Evolution of imaginary impedance spectrum during the dispersion of 0.5 wt% CNF/epoxy nanocomposite by ultrasonication (a) and shear mixing (b).

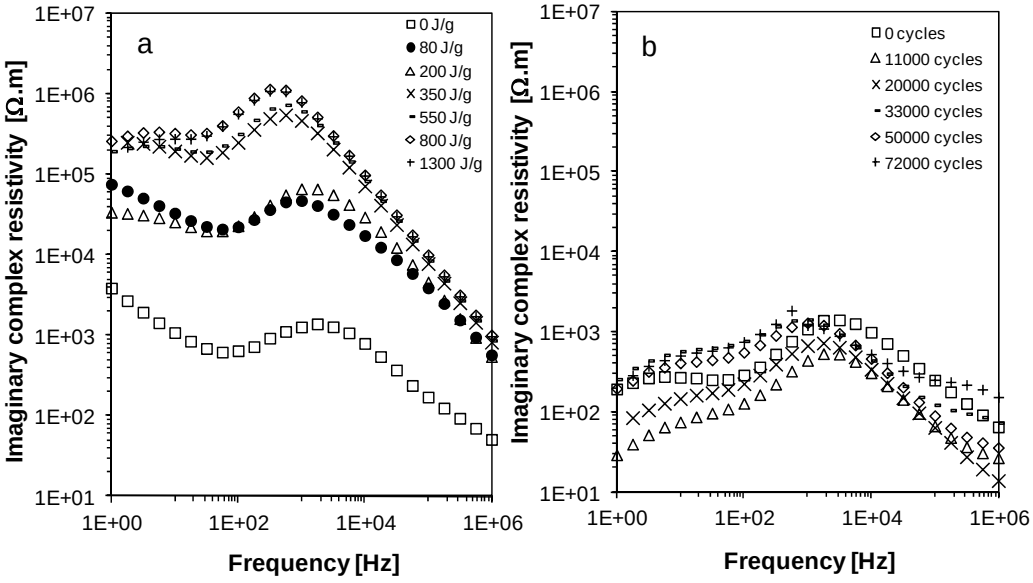

Figure 6.6 Evolution of imaginary impedance spectrum during the dispersion of 1 wt% CNF/epoxy nanocomposite by ultrasonication (a) and shear mixing (b).

6.3 Effect of dispersion on the electrical conductivity of cured nanocomposites

The electrical conductivity of the cured nanocomposites was investigated, as shown in Figure 6.7. Cured nanocomposites processed by high shear mixing and containing higher content of CNFs lead to nanocomposites with enhanced electrical conductivity. This is in agreement with the conductivity results obtained in the liquid state. Despite the similar conductivity results between the two ultrasonicated suspensions in the liquid state at the end of processing, the same behaviour is not verified after cure of these suspensions. The conductivity of 1 wt% CNF ultrasonicated nanocomposite is more than 4 orders of magnitude higher than the corresponding nanocomposite at a lower concentration of 0.5 wt% CNF. Cure induced reaggregation is likely to have occurred to a certain extent together with re-establishment of CNF conductive links, causing the rise in conductivity of the 1 wt% CNF ultrasonicated nanocomposite to a value similar to the corresponding shear mixed nanocomposite.

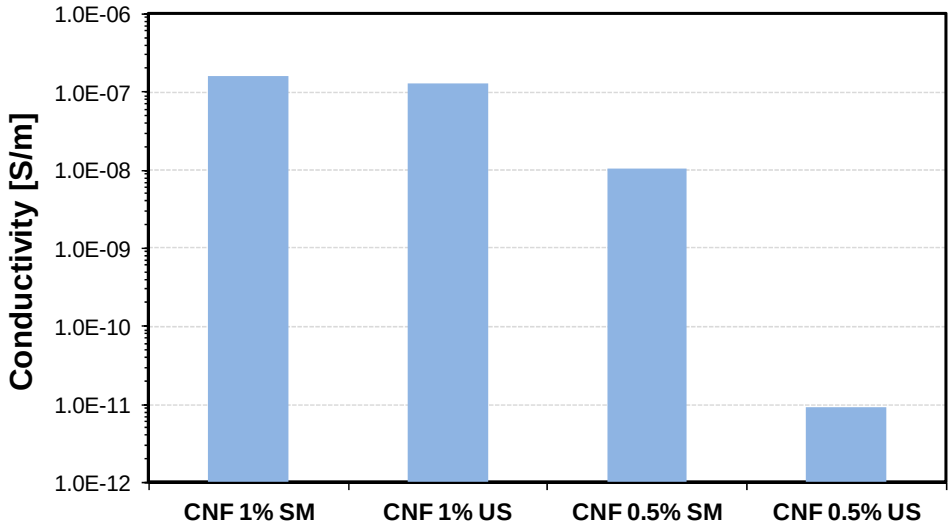

Figure 6.7 Electrical conductivity of the cured CNF filled epoxy at the end of ultrasonication and shear mixing processing.

Figure 6.8 illustrates the initial state of dispersion of 0.5 wt% and 1 wt% CNF/epoxy nanocomposites using SEM. Similarly to what was observed by optical microscopy of the untreated suspensions in the liquid state, the fracture surface of the nanocomposite

containing higher CNF loading (Figure 6.8 (b)) exhibits a larger number of aggregates, ranging from a few microns to more than 100 µm dimension, than the nanocomposite loaded with 0.5 wt% CNFs (Figure 6.8 (a)).

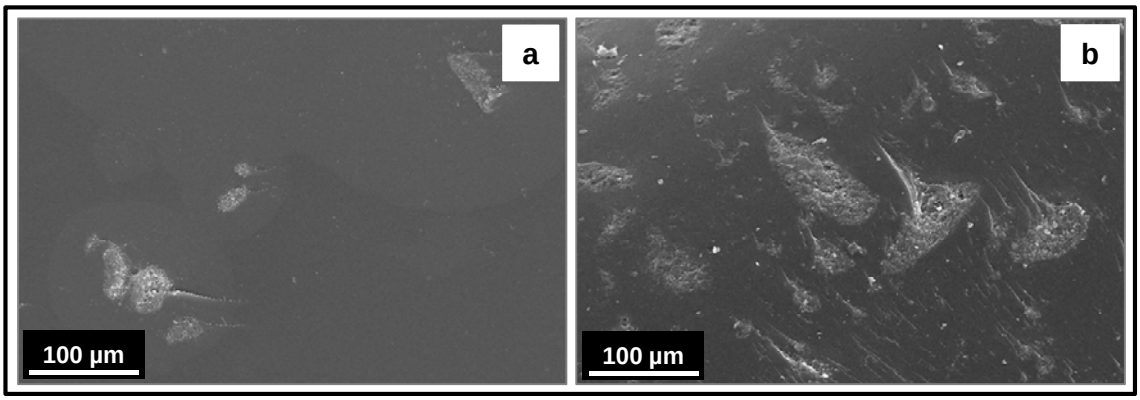

Figure 6.8 SEM micrographs of fracture surfaces of 0.5 wt% (a) and 1 wt% CNF (b) epoxy nanocomposites at the beginning of processing.

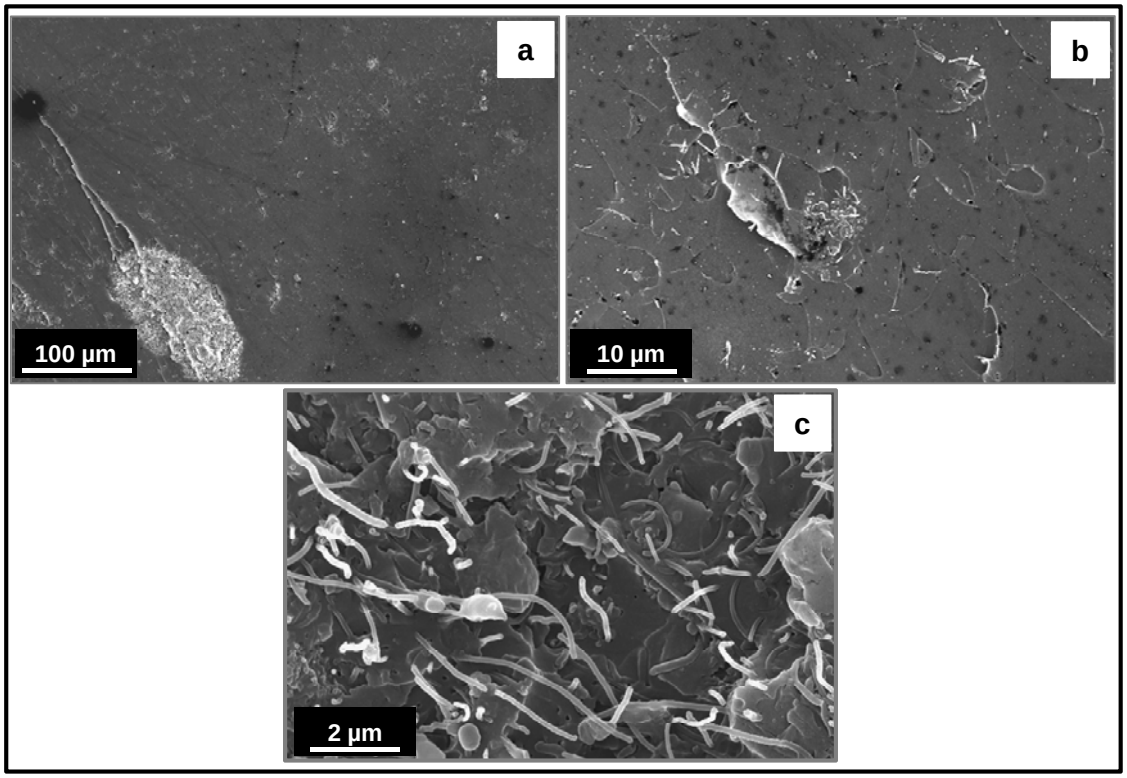

Figure 6.9 SEM micrographs of the fracture surface of 0.5 wt% CNF/epoxy nanocomposite at the end of high shear mixing process.

At the end of processing by high shear mixing, very large aggregates of approximately 150 µm dimension can still be seen on both nanocomposite fracture surfaces (Figures

6.9 (a) and 6.10 (a)). These highly entangled aggregates are surrounded by individual CNFs as observed in Figures 6.9 (b) and 6.10 (b).

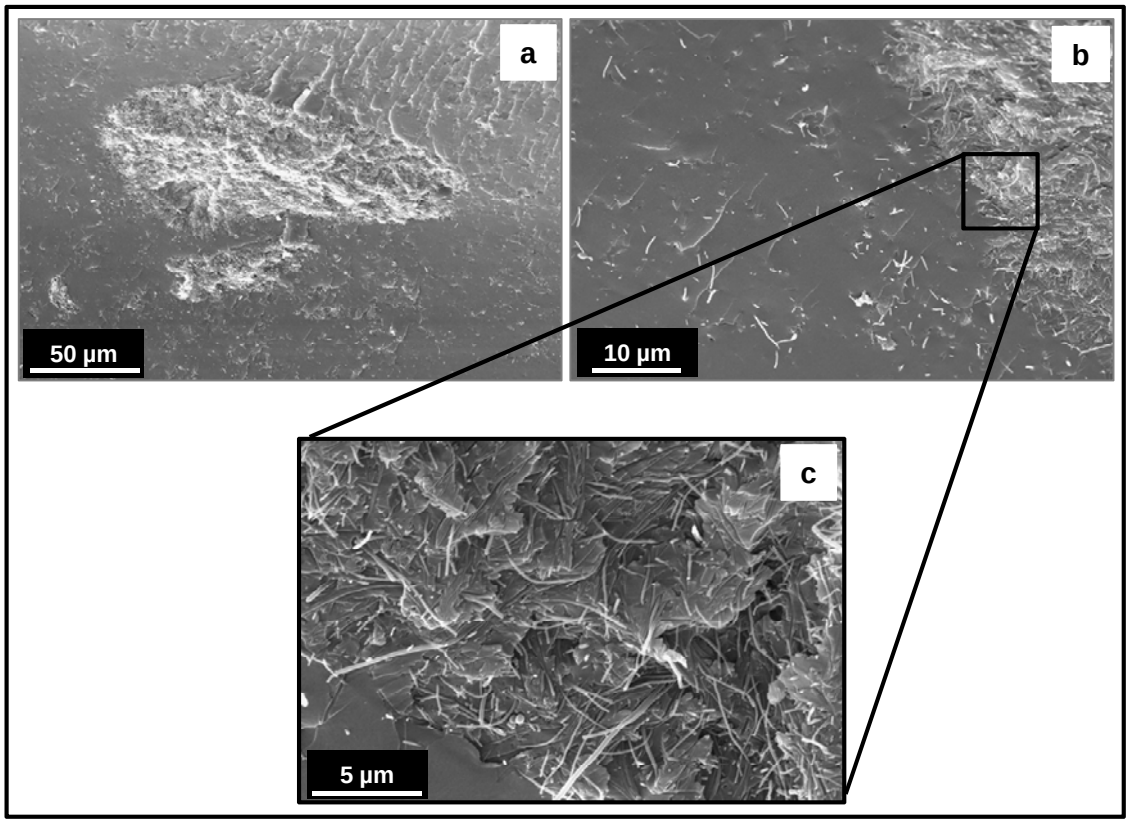

Figure 6.10 SEM micrographs of the fracture surface of 1 wt% CNF/epoxy nanocomposite at the end of high shear mixing process.

The smoother fracture surface shown in Figure 6.8 becomes rougher as the dispersion level is improved, such as in the fully ultrasonicated systems (Figure 6.11). This feature indicates a relatively more homogeneous distribution of CNFs within the epoxy. However, medium size aggregates of approximately 15 µm dimension (Figure 6.12 (b) and (c)) can still be found among individual CNFs in the fracture surface of 0.5 wt% CNF nanocomposite after completion of the ultrasonication process. The high level of entanglement of one of these dense aggregates can be seen in Figure 6.12 (d). High shear mixing although not as effective as ultrasonication in reducing dense aggregate size and achieving a more homogenous dispersion, leads to better electrical conductivity of CNF filled nanocomposites.

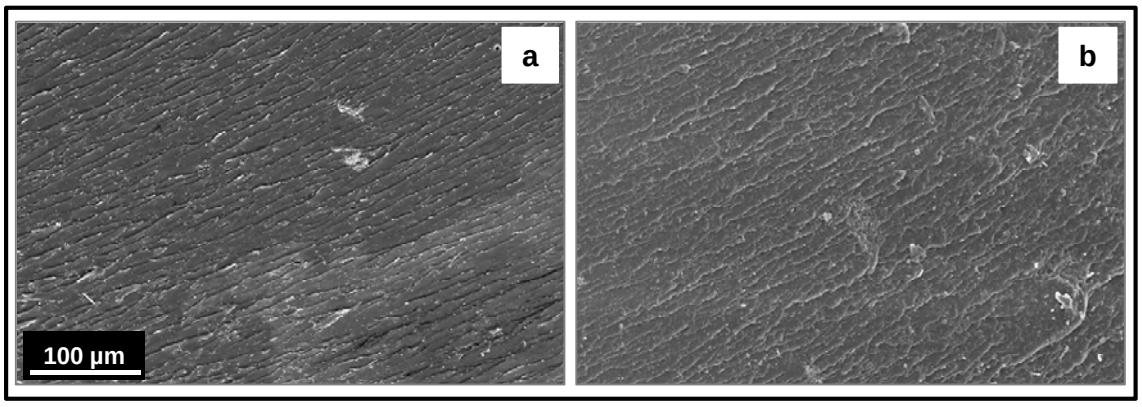

Figure 6.11 SEM micrographs of the 0.5 wt% and 1 wt% CNF filled suspensions at the end of the ultrasonication process.

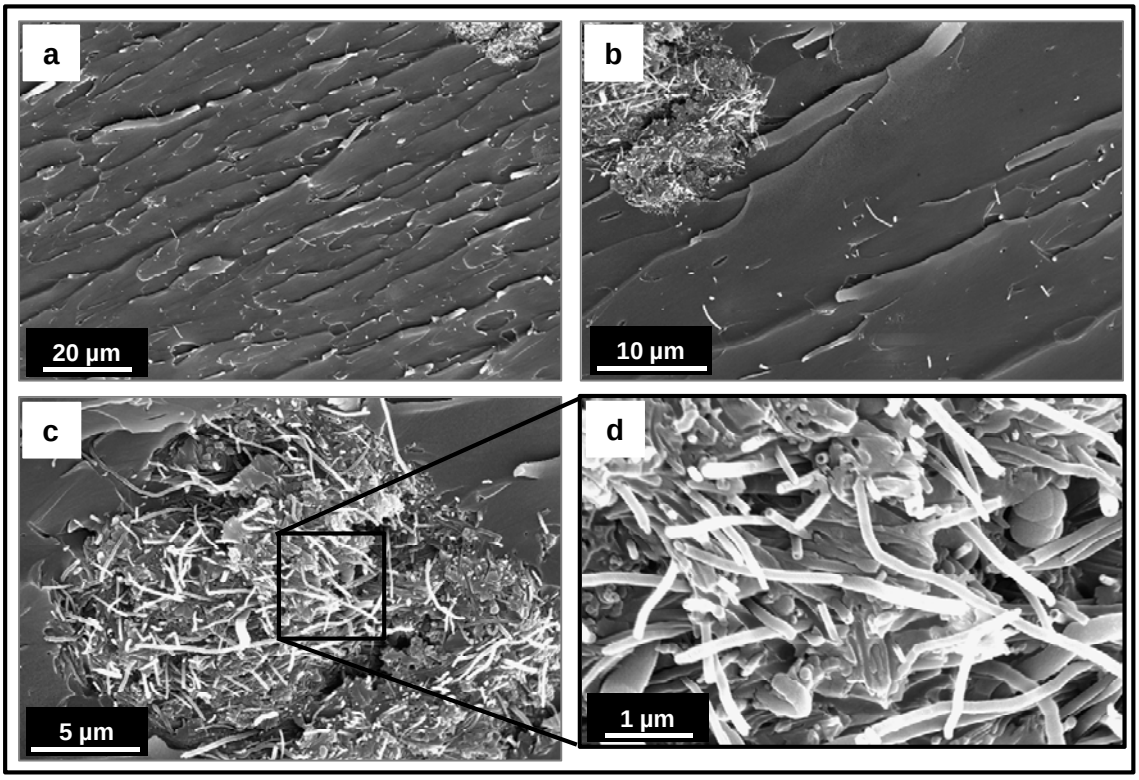

Figure 6.12 SEM micrographs of the fracture surface of 0.5 wt% CNF/epoxy nanocomposite at the end of the ultrasonication process.

6.3.1 Dispersion state of 0.25 wt% CNF/epoxy suspension during processing

The dispersion state of the 0.25 wt% CNF filled epoxy was assessed by transmitted optical microscopy at different stages of processing, as illustrated in Figures 6.13 and 6.14. The initial suspension (0 cycles) is characterised by a variety of extremely entangled aggregates, whose dimensions range from few micrometers to more than 300 μm (Figure 6.13). These aggregates appear as black regions of low transmission of light, whose fuzzy boundaries reveal the outer ends of individual CNFs entangled within the aggregate core. The high light transmission zones around the CNF aggregates are areas of clear epoxy resin where randomly dispersed individual CNFs can be found. As the number of cycles increases, the aggregate boundaries become blurred as CNFs gradually disentangle forming areas of looser CNF aggregates around the dense core, or even separate from it. After 11000 cycles, the number of loose aggregates dispersed in the resin increases considerably. In addition, a global interconnected network of CNFs is formed between loose and dense CNF aggregates. Extremely large and dense aggregates (~500 μm) can still be observed in suspension. However, their extremely fuzzy edges reveal loosening of the CNFs from within the highly entangled aggregate core, as shown in the inset of Figure 6.13.

Reaggregation of loose aggregates in suspension can be observed in Figure 6.14 with continuous processing by high shear mixing. As the processing time increases, the loose and structurally fine aggregates within the epoxy resin tend to assemble into larger and darker aggregated structures. Further high shear mixing up to 72000 cycles results in a suspension characterised by a range of dimensionally distinct loose aggregates, where a small number of very dense aggregates with a maximum dimension of 170 μm can be observed.

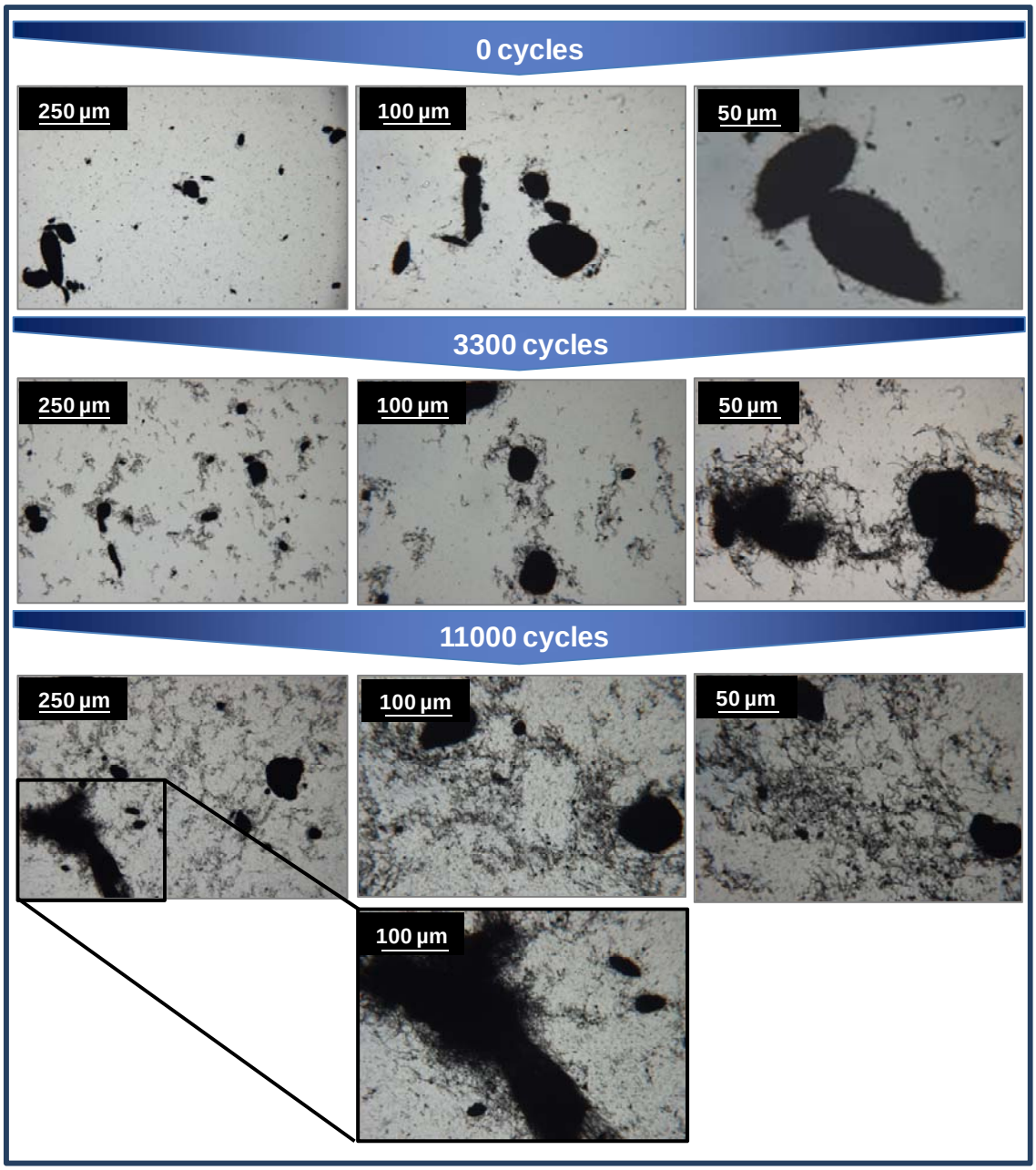

Figure 6.13 Liquid state optical transmission micrographs of the 0.25 wt% CNF filled suspensions at different dispersion/processing levels (from 0 to 11000 cycles).

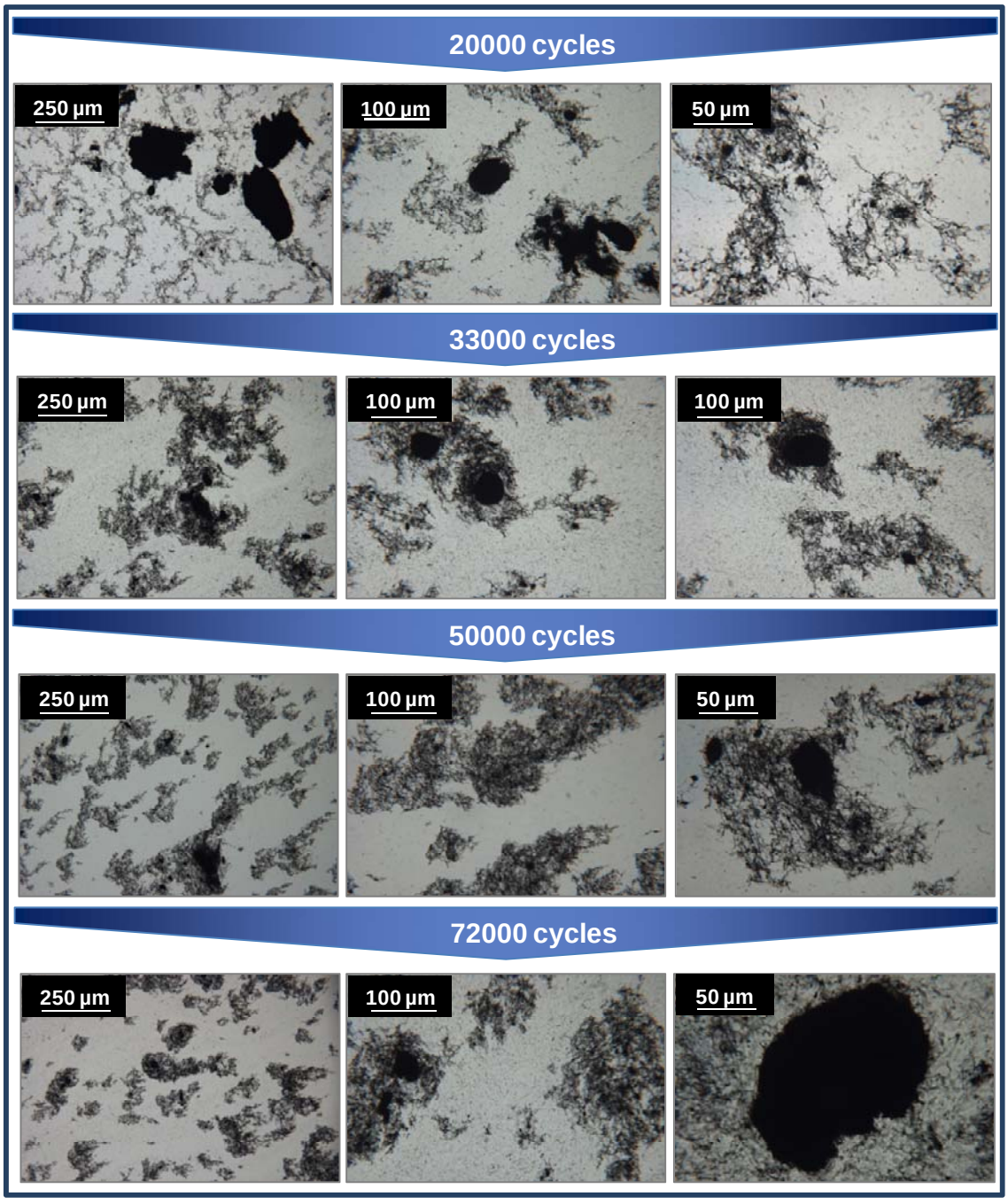

Figure 6.14 Liquid state optical transmission micrographs of the 0.25 wt% CNF filled suspensions at different dispersion/processing levels (from 20000 to 72000 cycles).

6.4 RTM processing

An epoxy suspension containing 0.25 wt% CNF dispersed by high shear mixing was chosen for RTM purposes, since higher contents, such as 0.5 wt% and 1 wt% CNF result in extremely viscous suspensions for infusion. High viscosity suspensions can lead to very slow infusions, and can ultimately result in incomplete filling of the fibrous reinforcement. High shear mixing was selected for processing this suspension since the results obtained for higher CNF contents (section 6.1) indicate that this is a better process than ultrasonication for enhancing the electrical properties of these nanocomposites.

6.4.1 RTM adaptation

A preliminary preparation and assessment of the CNF dispersed suspension is mandatory when infusing nanomodified resins by RTM. A pseudo-unidirectional uniweave carbon fabric was utilised as reinforcement for this 0.25 wt% CNF/epoxy system. The selection of this reinforcement is explained in detail in section 5.2. RTM infusion involving CNFs filled resins, similarly to other nanoparticle filled resins such as CNTs filled epoxies, require process modifications with respect to degassing temperature and time as well as selection of appropriate mold filling temperature, in order to overcome potential issues arising from the increased resin viscosity. In order to facilitate the degassing process of this CNF filled suspension, degassing took place during shear mixing processing at about 50º C, which guaranteed lower suspension viscosity and efficient removal of volatiles due to the continuous shearing action.

6.4.2 Rheology

Figure 6.15 shows the viscosity dependence on shear rate for the reference epoxy (control) and the CNF filled suspension utilised for liquid moulding at the corresponding filling temperature. The viscosity behaviour of the CNF filled epoxy is similar to the CNT modified systems reported in section 5.2.1. This system is a shear rate dependent suspension showing higher viscosity values than the unfilled epoxy resin at the temperatures studied. In contrast, the viscosity of the reference epoxy does not vary significantly with shear rate. As the shear rate increases the viscosity of the CNF

filled epoxy tends to plateau to a level similar to that of the reference epoxy. During infusion, due to the dual pore scale nature of the fabric, the resin is expected to be subjected to a range of shear rates.

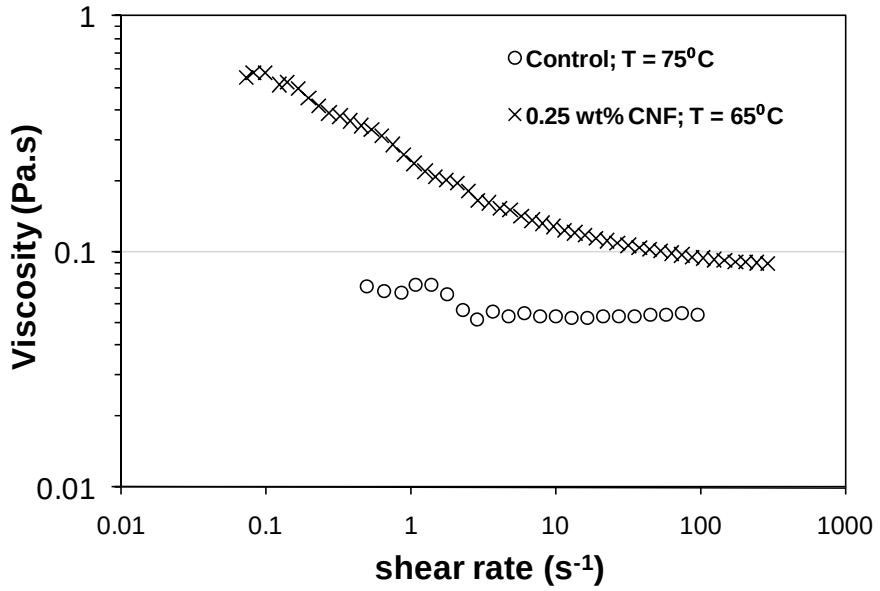

Figure 6.15 Suspension viscosity as a function of shear rate

6.4.3 Filtration

Figure 6.16 illustrates the resin flow front position versus the square root of time together with a linear fit using 1D Darcy's solution (Eq.5.1).

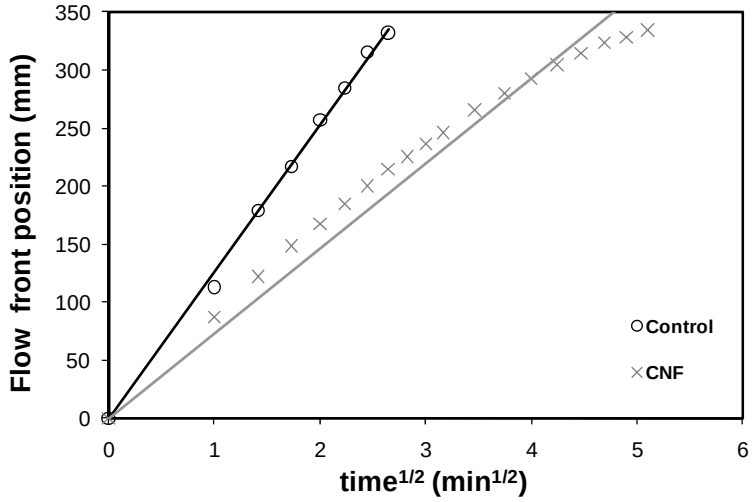

Figure 6.16 Resin flow front profiles during RTM injection of carbon fibre reinforcements.

In contrast to the control system, which follows the linear fit closely, the CNF filled epoxy deviates significantly from the linear behaviour predicted by Eq.5.1. This deviation from the square root of time linear dependence, also observed in some of the CNT modified systems, is attributed both to the non Newtonian behaviour of the nanomodified resin and the retention of nanoparticles by the reinforcement. Particle filtration leads to variations primarily in viscosity but also in the local permeability of the fabric. In addition, longer filling times were typical of the nanomodified systems, such as the CNF suspension. Despite the low CNF content in the epoxy resin, intrinsically high viscosities and particle filtration led to a very long infusion time of about 30 min.

Filtration was observed macroscopically for this CNF system, as resin was seen running clear at the outlet gate. This phenomenon was also investigated microscopically by SEM of the fracture surfaces of the CNF multiscale composite at the inlet and outlet regions (Figure 6.17).

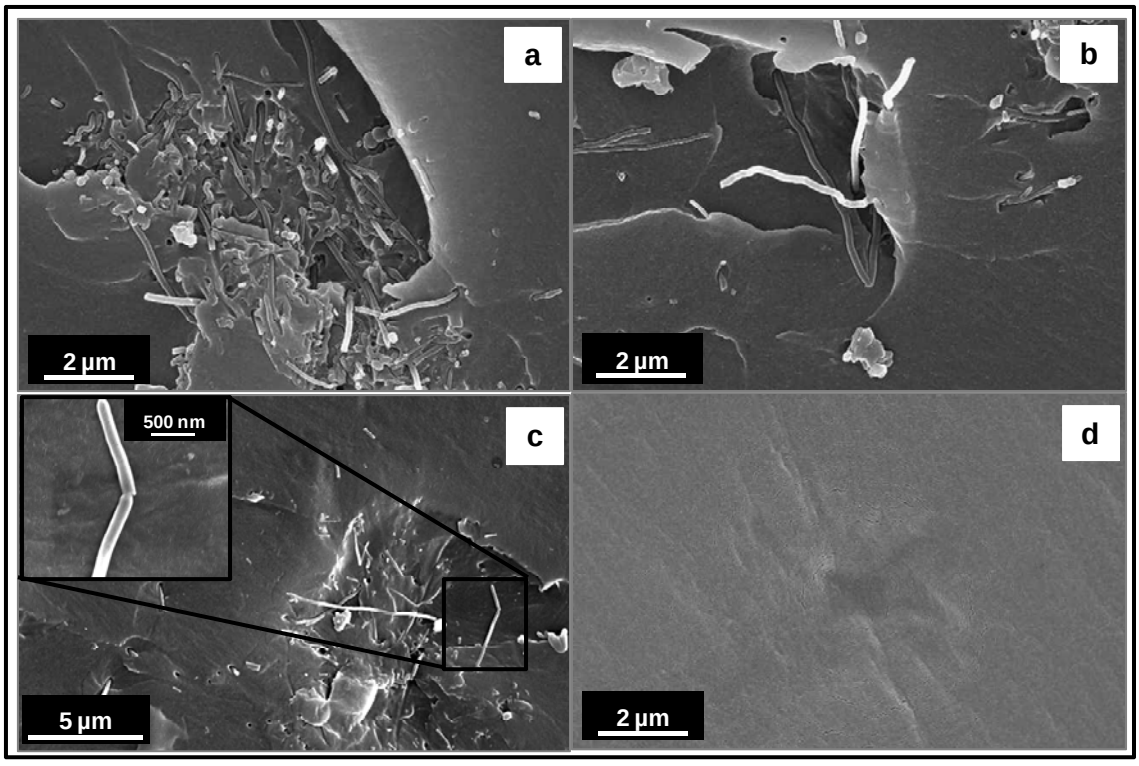

Figure 6.17 SEM micrographs of fracture surfaces at the inlet (a-c) and outlet (d) regions of CNF modified carbon fibre composite.

Aggregates of about 10 µm size and individual CNFs were found at the inlet region, as shown in Figure 6.17 (a) to (c), while no evidence of these CNF structures were seen at the outlet region (Figure 6.17 (d)). The existence of bent (Figure 6.17 (b)) and fractured CNFs at the inlet region (Figure 6.17 (c)) indicates CNF damage possibly caused during shear mixing processing, as no damaged CNFs were observed in the as-received material by SEM.

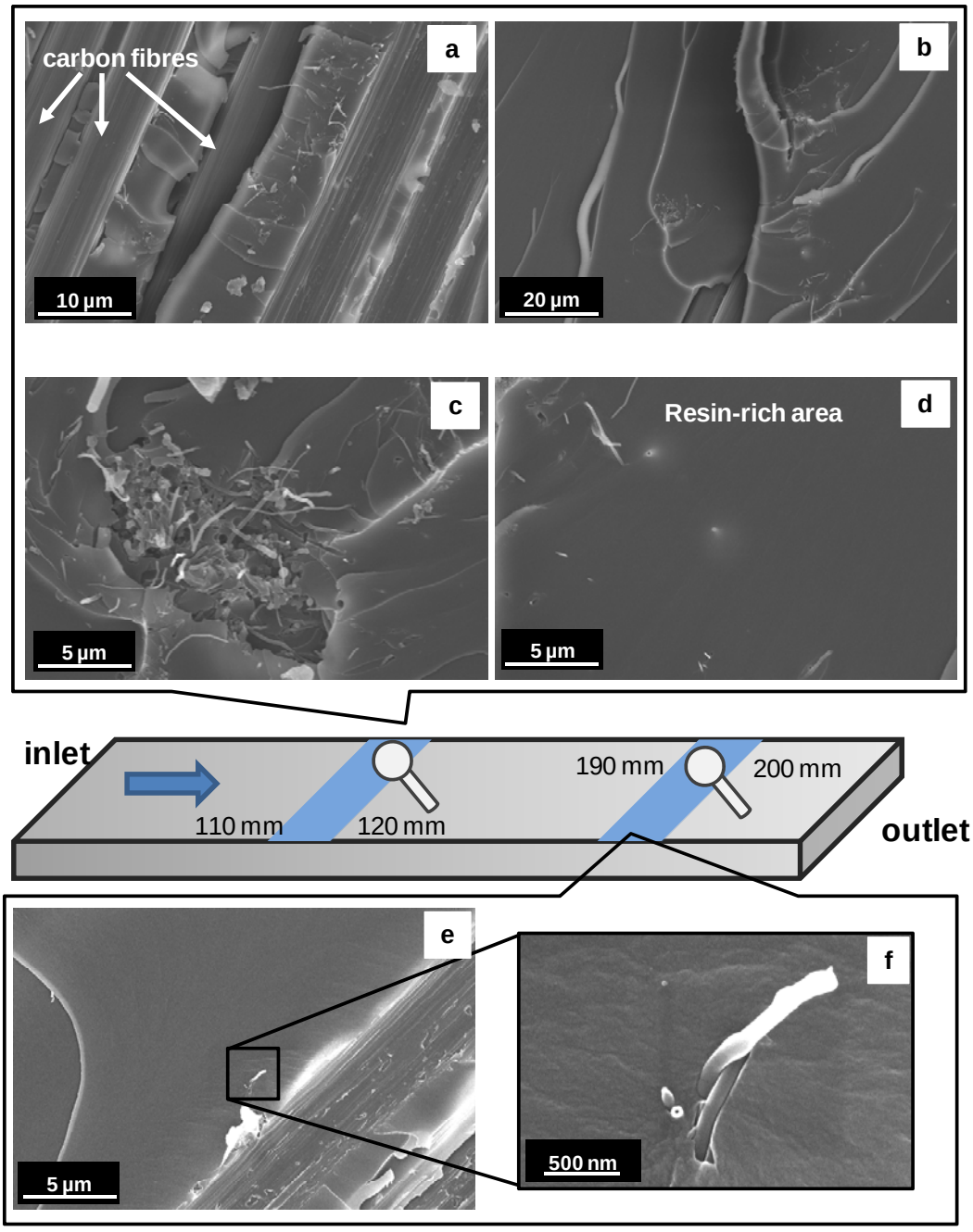

Figure 6.18 SEM micrographs of the delamination fracture surfaces of CNF/epoxy filled carbon composites at increasing distance from the inlet.

Despite the absence of CNFs in the outlet gate resin, both individual and aggregated CNF structures were observed in the composite delamination fracture surface as far as 110-120 mm away from the inlet. CNF aggregates were found within the carbon fibre bundles at the intra tow level (Figure 6.18 (a)). In addition, CNF aggregates as large as 15 μm and individual CNFs were also found in resin-rich pockets, as shown in Figure 6.18 (b) to (d). At distances from the inlet of 190-200 mm, the amount of CNFs per area drops considerably. Only very few CNFs, such as the ones shown in Figure 6.18 (e) and (f) were found in a resin rich pocket in that region.

This nanomodified system is characterised by intrinsically long CNFs and the presence of a number of very large aggregates, which are more likely to be captured by the fibrous reinforcement. In fact, any of the large CNF aggregates present in the injected resin, as observed by optical microscopy in Figure 6.14, were found at this location. Therefore, size exclusion is considered the governing filtration mechanism for this nanomodified resin system. Aggregates dimensionally larger than the pore channels would be filtered microscopically by cake filtration, while the absence of smaller aggregates and even some individual CNFs in the outlet resin indicates deep filtration along the porous bed.

6.5 Evaluation of composite quality

Visual inspection and c-scanning were utilised to evaluate the existence of dry spots and complete impregnation of the fibrous reinforcement during infusion of the post-cured multiscale composite. Figure 6.19 (a) shows the output of a c-scan. Darker areas represent the presence of defects, i.e. porosity. The black rectangle corresponds to the PTFE film necessary to generate a pre-crack for the composite DCB specimens (section 4.7). Despite the dark patch at the bottom right corner of the panel, where dry fibres can be seen by visual inspection, the remaining dark regions are mainly representative of incomplete saturation of the top surface of the composite panel (Figure 6.19 (b)), as verified by examination of cross sections across these regions. However, special care was taken to avoid testing specimens within these regions. This localised surface roughness is associated with insufficient degassing of the CNF filled suspension,

possibly after adding in the hardener, and relatively high viscosity of the suspension at the infusion temperature to allow efficient extraction of volatiles in the liquid resin.

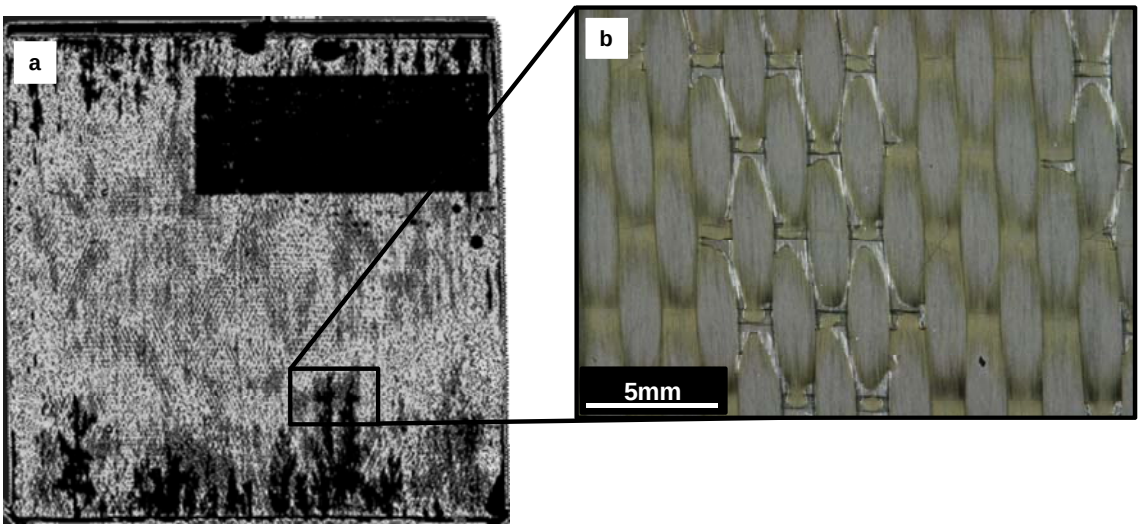

Figure 6.19 C-scan image of CNF carbon composite (a) and corresponding panel top surface showing partial fibre impregnation (b).

6.6 Electrical properties of the CNF multiscale composites

The electrical properties of the control and CNF filled carbon fibre composites are shown in Figure 6.20. As discussed in section 5.4, these composites exhibit an anisotropic electrical conductivity response, which is fibre dominated especially in the in plane directions. Therefore, the effect of CNFs in these directions can be considered negligible. The major contribution of the presence of nanoparticles, such as CNFs, to the composite electrical conductivity is in the through thickness direction. CNFs cause a considerable increase of about 84% in the through thickness average electrical conductivity of the carbon fibre composite when compared with the control composite. Through thickness electrical conductivity results were obtained for specimens cut along the panel and are presented in Figure 6.21. However, these results are inconclusive concerning to the spatial evaluation of particle filtration, since SEM micrographs shown in Figure 6.18 indicate significant particle filtration before a drop in conductivity is observed in Figure 6.21.

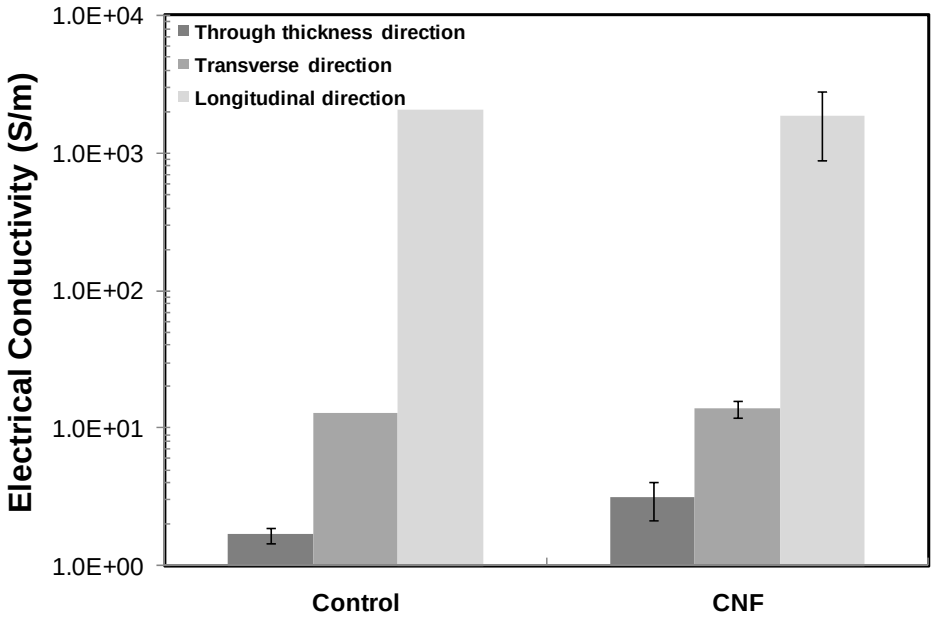

Figure 6.20 Electrical conductivity of the CNF filled carbon fibre composite.

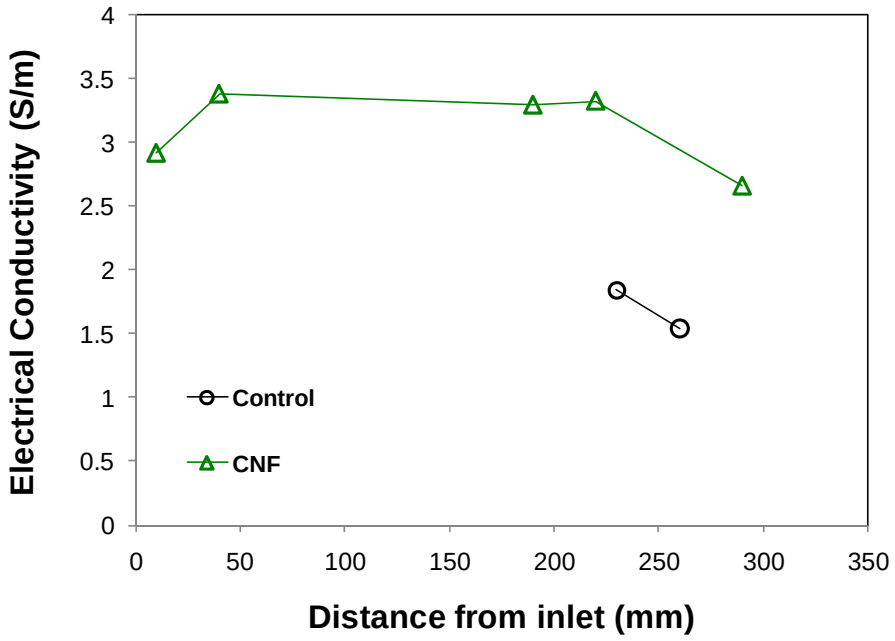

Figure 6.21 Evolution of through thickness electrical conductivity of CNF filled carbon composites as a function from the distance from the inlet gate.

6.7 Conclusions

An aerospace grade composite with a 57% fibre volume fraction and enhanced electrical properties was successfully manufactured by RTM process, when an appropriate process was selected to disperse CNFs in epoxy prior infusion of a uniweave carbon preform. CNFs offer a less costly alternative to CNTs, in providing improved electrical properties to polymer composites. Processing of CNF multiscale composites requires the incorporation of a dispersion step preceding filling, in order to guarantee efficient transfer of CNFs properties to the final composite. The level of dispersion was evaluated by electrical measurements of the liquid suspensions. High shear mixing, though not as effective as ultrasonication in dispersing highly entangled CNF aggregates in epoxy, was found to be a better way of achieving a percolated CNF network. For RTM purposes, the CNF content was limited to 0.25 wt%, since higher CNF loadings, despite providing better electrical properties, led to extremely viscous suspensions for infusion. However, even at this lower CNF content, the high viscosity of the suspension together with particle filtration resulted in a long infusion. The flow of resin can be significantly affected by filtration, due to viscosity and permeability dependence on the local CNF concentration and porosity variation with particle build up on the fabric channels. Cake filtration and deep bed filtration are considered the main filtration mechanisms taking place during infusion of this CNF carbon composite. Particle filtration leads to structures with gradient in properties; this phenomenon if controlled can provide the possibility of introducing high CNF content into critical areas of a component. These multiscale composites have a highly anisotropic electrical behaviour, where improvements in the through thickness electrical conductivity of ~84% were obtained. In contrast, the conductivity in the in-plane directions is mainly dominated by the carbon fibres.

7 Delamination properties of fibrous composites filled with carbon nanoparticles

This chapter presents the effect of carbon nanoparticles on the delamination properties of fibrous composites, under mode I interlaminar fracture. A range of four different carbon nanoparticles comprising three types of CNTs and one of CNFs were utilised to modify a carbon fibre uniweave fabric composite. The results for initiation and propagation toughness under mode I are presented and discussed. The fracture surfaces of these specimens were analysed by SEM in order to identify the type of failure (cohesive or interfacial) and the presence of toughening mechanisms characteristic of toughening by rod-shaped nanoparticles. The potential of carbon nanoparticles in toughening this fibrous composite was evaluated by means of an elasto-plastic model. This model was utilised to estimate the size of the plastic zone which was compared with the thickness of the interlaminar resin-rich layer in these composites to asses the potential of toughening of the fibrous material.

7.1 Effect of carbon nanoparticles on Mode I interlaminar fracture toughness of multiscale composites

DCB test specimens of carbon nanoparticle multiscale composites, reinforced with carbon fibres arranged in a uniweave fabric, were manufactured according to the specification described in section 4.1.2 and 4.5, and prepared for testing as detailed in section 4.7. Two sets of experiments were performed for the measurement of crack delamination resistance of DCB specimens. The initiation toughness results presented herein consist of results acquired from both experimental sets. Crack propagation results are acquired from just one trial set, which involved careful monitoring of the crack re-initiation and arrest positions during crack propagation. The number of specimens tested for the crack initiation and crack propagation analysis is indicated in Table 7.1and Table 7.2, respectively.

Figure 7.1 and Table 7.1 report the results for initiation. In general the presence of carbon nanoparticles as modifiers does not result in statistically significant modification of initiation toughness. However, there is a tendency for a very slight increase in the

critical energy. The higher increase in $G_{IC\ init}$ was observed for the CNF filled panel. This could be related with CNFs considerably larger size, when compared to MWCNTs. In addition, despite filtration of these particles by the carbon reinforcement during RTM infusion, SEM images taken at the onset of the crack delamination region, located at ~110 mm away from the inlet, revealed extended CNF presence between fibres and in the resin-rich areas, as demonstrated in 6.4.3. CNFs presence at this region might have played a role in inhibiting the initiation of the crack and contributing therefore to an increase in initiation toughness.

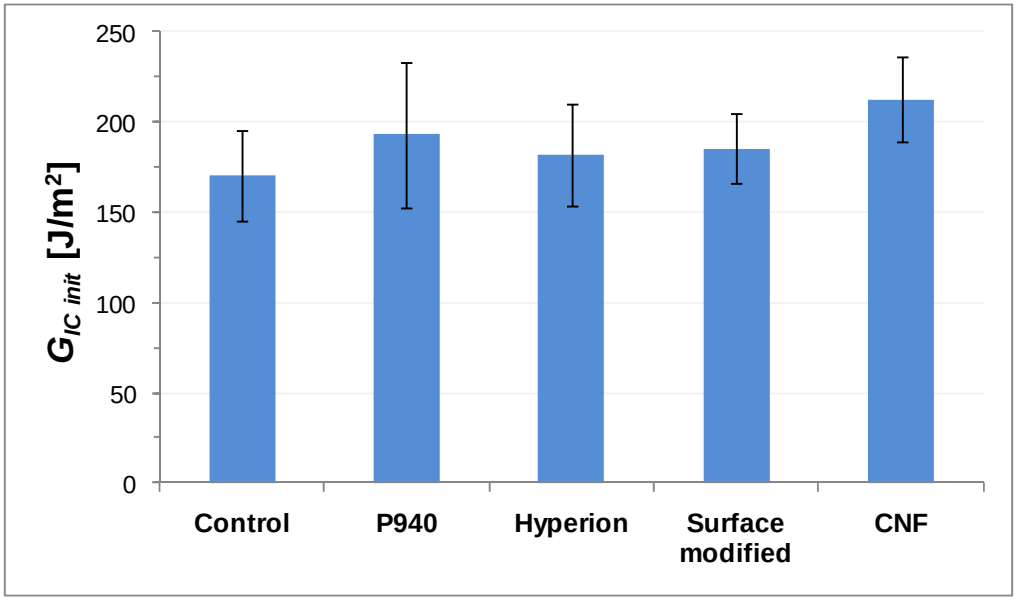

Figure 7.1 Crack initiation toughness (5% Max) in Mode I (error bars represent the standard deviation value).

Table 7.1 Increase in crack initiation resistance for carbon nanoparticle filled composite specimens

Plate ID	No. of specimens	$G_{IC\ init}$ increase [%]
Control	8	-
P940	8	~ 13
Hyperion	6	~ 7
Surface modified	6	~ 9
CNF	6	~ 24

A ‘saw-tooth’ response R-curve was observed for all the specimens tested in the second set of experiments. The standard procedure BS ISO 15024:2001, was developed for normal unidirectional laminates, which have generally a smooth propagation R-curve. This type of curve, presented in Figure 7.2, is characteristic of a ‘stick-slip’ behaviour, similar to what was reported and explained by the fibre arrangement of orthogonal woven fabrics utilised by Alif et al. [135].

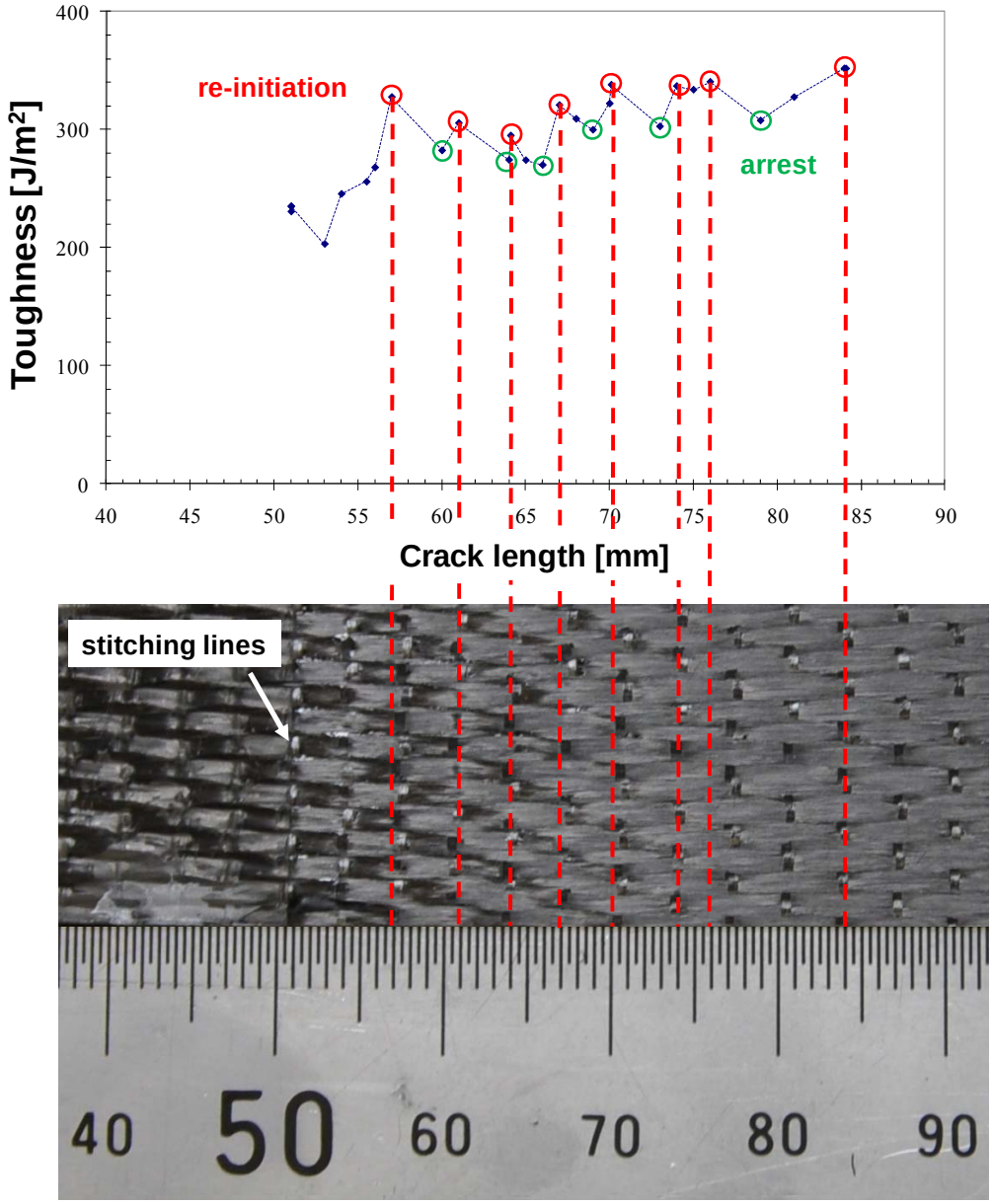

Figure 7.2 R-curve of a P940 filled specimen representative of stick-slip behaviour and correspondence between the specimen stitching lines and the crack re-initiation peaks.

The presence of non-structural stitches holding the carbon fabric together in the orthogonal direction relative to the crack propagation, located at approximately 3-4 mm intervals in the fabric is the cause of the stick-slip nature of crack propagation in these samples. The location of these stitching lines corresponds exactly to points of crack re-initiation in the R-curve, as demonstrated in Figure 7.2. The arrest points represented in the R-curve in Figure 7.2 correspond generally to inter-stitch regions. Similar evidence was found by Brunner et al. [136] when investigating the delamination fracture of 0º/90º cross-ply laminates and comparing it with unidirectional ones. Steeper R-curves observed in cross-ply laminates, reflect the higher delamination resistance of these composites when compared to unidirectional lay-ups.

Figure 7.3 illustrates some characteristic R-curves corresponding to the delamination of control and carbon nanoparticle modified composite specimens. The overlapping of these curves shows the absence of statistically significant toughening due to the presence of nanoparticles.

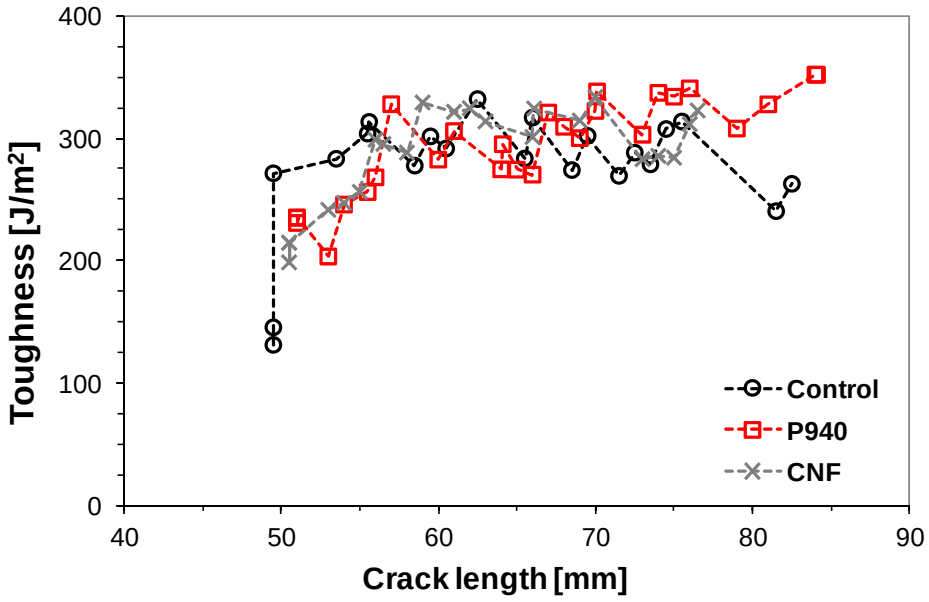

Figure 7.3 Representative delamination R-curves.

For comparison reasons, all the crack propagation results were analysed separately in terms of crack re-initiation and arrest toughness, as presented in Figure 7.4 and Table 7.2. This analysis was done for crack lengths between 65 and 85 mm, a region characterised by stable crack propagation. Only specimens characterised by stable R-

curves were compared. This resulted in only one specimen considered for the analysis of both CNF and Hyperion CNT filled composites.

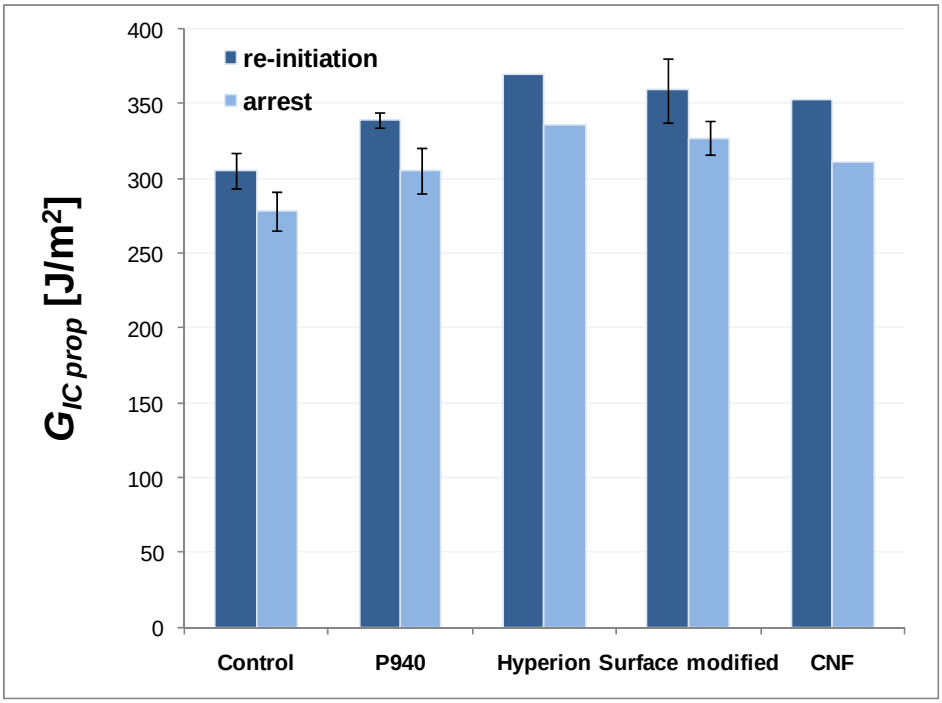

Figure 7.4 Crack re-initiation and arrest toughness values during crack propagation in carbon multiscale composites (error bars represent the standard deviation value, where appropriate).

Table 7.2 Increase in crack re-initiation and arrest toughness values during crack propagation in carbon multiscale composites

Plate ID	No. of specimens	$G_{IC\,re\text{-}init}$ increase [%]	$G_{IC\,arrest}$ increase [%]
Control	2	-	-
P940	4	~ 11	~ 10
Hyperion	1	~ 18	~ 18
Surface modified	2	~ 21	~ 21
CNF	1	~ 16	~ 12

Table 7.2 shows a similar increase for both re-initiation and arrest toughness for most of the carbon nanoparticle modified systems, when compared to the unmodified composite, with the exception of the CNF filled material. The highest increase in

propagation delamination resistance in both crack re-initiation and crack arrest values was observed for the surface modified CNTs system (~ 21%). Improved toughness has been reported by several authors [36, 116, 119] for composites containing surface functionalised carbon nanoparticles, when compared to composites filled with non-functionalised ones. Functionalisation is thought as fundamental for toughening through improved interfacial bonding between particles and matrix. As perceived by the analysis of these data sets, carbon nanoparticles do not cause a detrimental effect in the composite delamination resistance but are able to cause a slight improvement on this property. This modest toughening effect shown by the carbon nanoparticles is counter to the considerably high improvements claimed by many other authors [36, 119, 137, 138] when utilising carbon nanoparticles randomly dispersed in the resin.

The filtration of particles observed for the P940 and CNF systems, described in chapter 5 could also explain the lower crack propagation toughness increase in relation to initiation values. For the systems where particle filtration can be considered negligible, as for surface modified and Hyperion systems, the increase in propagation toughness is considerably higher than the increase for initiation toughness, which suggests some form of CNT toughening.

7.2 Fractography

The delamination fracture surface of DCB specimens representative of each composite panel have been examined by SEM according to the procedure described in section 4.2.2. Some evidence of poor interfacial bonding between matrix and fibres was observed for all the composite specimens. Figure 7.5 to Figure 7.7 depict carbon fibre imprints of a fibrous reinforcement detached from the resin matrix, indicative of predominant interfacial failure.

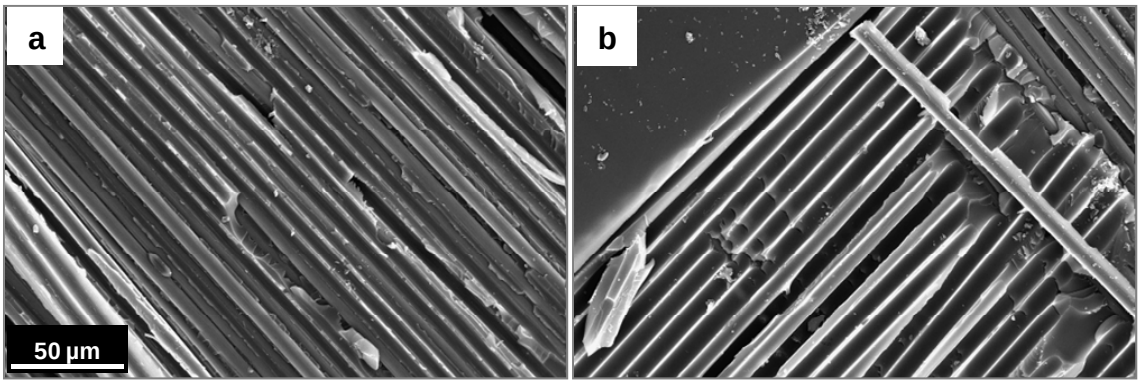

Figure 7.5 Delamination surface of control specimen showing interfacial debonding both on the carbon fibres (a) and stitches (b)

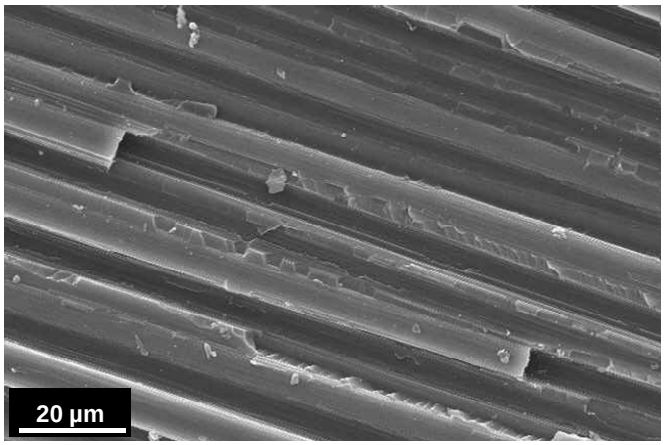

Figure 7.6 Delamination fracture surface of CNF multiscale composite specimen (carbon fibre imprint)

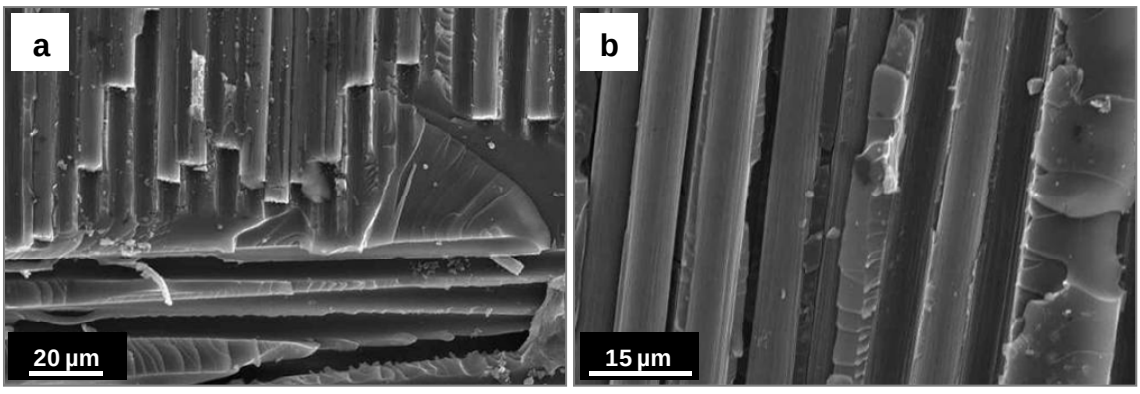

Figure 7.7 0.25 wt% surface modified delamination fracture surface composite: glass stitches and carbon imprint (a) carbon fibres and respective imprint (b)

Despite the existence of areas of interfacial failure, the P940 and Hyperion systems present some regions of better interfacial adhesion between the epoxy matrix and the fibres, as shown in Figures 7.8 and 7.9. These areas which are representative of good adhesion between the constituents of the composite were not identified in the other systems.

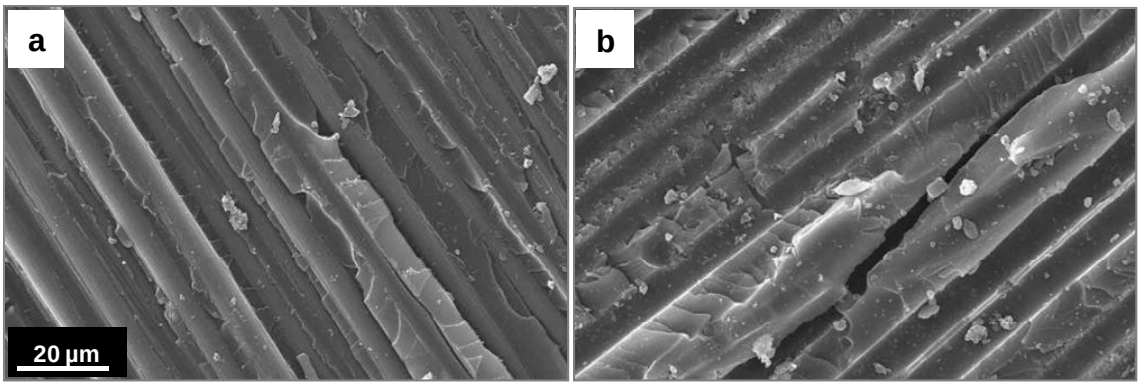

Figure 7.8 0.25 wt% P940 delamination fracture surface composite: carbon imprint (a) and stitch imprint (b)

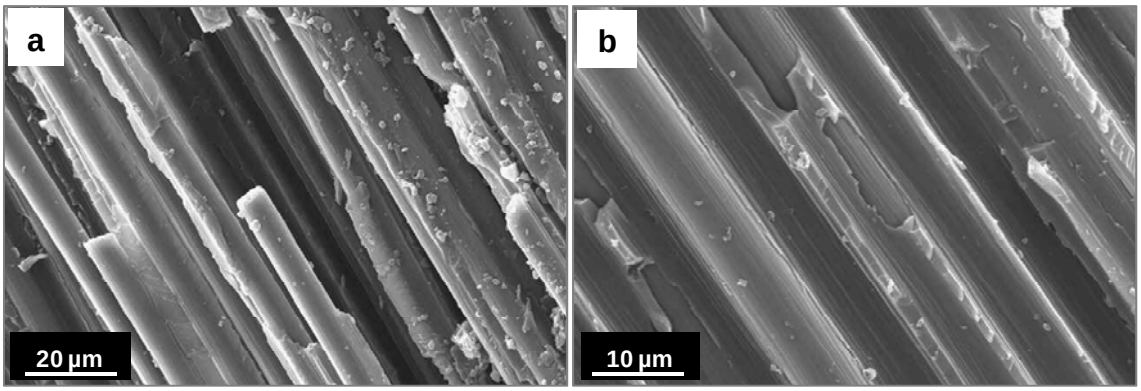

Figure 7.9 Delamination fracture surface of P940 (a) and Hyperion (b) modified composite specimens showing regions of good interfacial adhesion.

The participation of P940 CNTs in the failure process was observed, as they are seen on the fracture surfaces in Figure 7.10. P940 CNTs are shown in Figure 7.11 bridging secondary cracks in resin rich areas. Other regions show holes left by individual CNTs which had been pulled-out, as indicated by the white circles in Figure 7.12. These are common toughening mechanisms when utilising rod-shaped carbon nanoparticles as modifiers. However, the extent at which they occur does not contribute to a significant enhancement of the composite interlaminar properties. The increase in propagation

toughness of approximately 11% for the P940 modified composite which is within the statistical uncertainty of the measurements agrees with this observation.

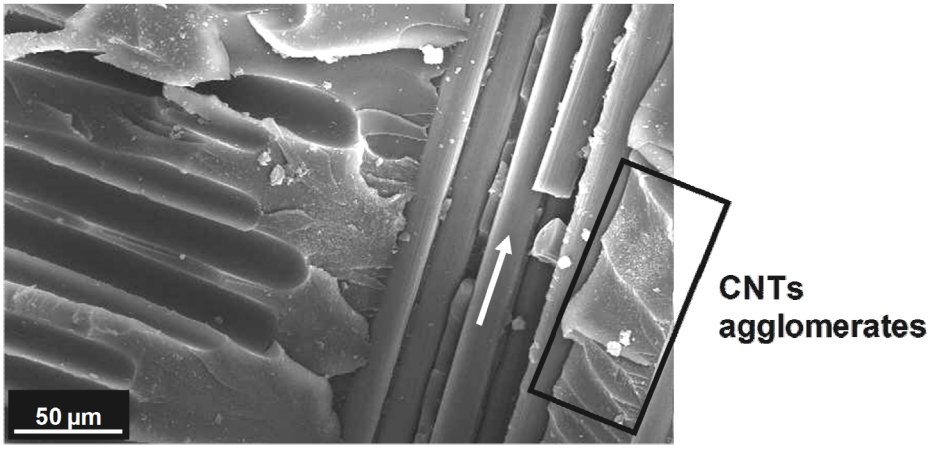

Figure 7.10 Delamination fracture surface of P940 multiscale composite showing interfacial debonding and CNTs on the fracture surface (a: 60-65 mm and arrow indicates primary fibre direction)

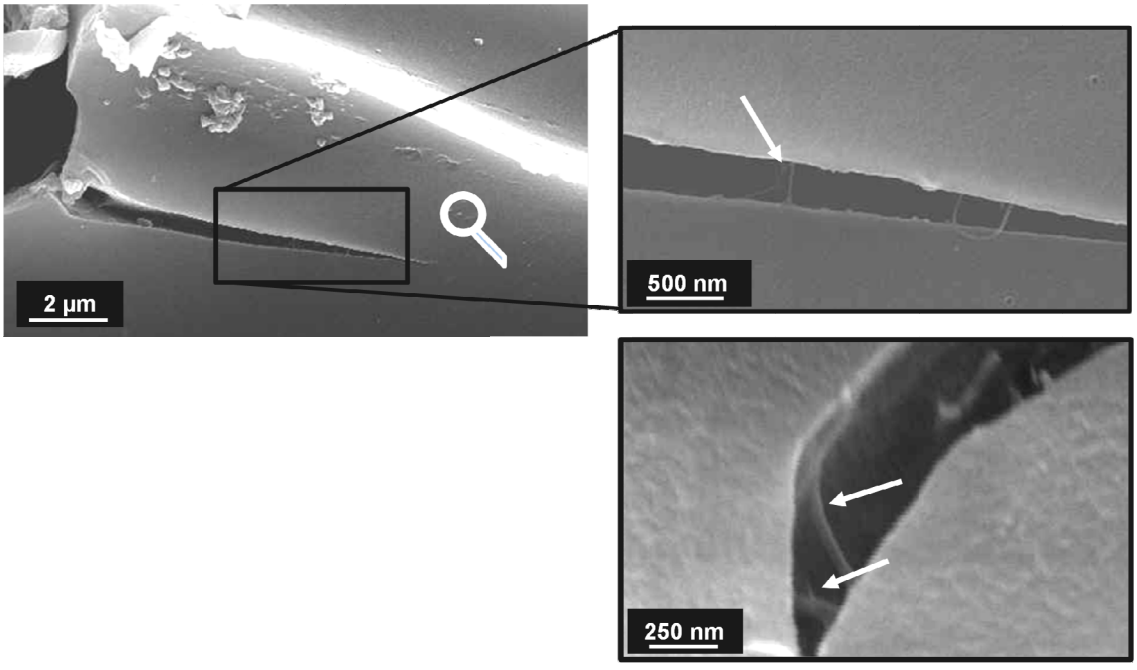

Figure 7.11 Cracks in resin rich areas being bridged by P940 CNTs (a: 60-65 mm).

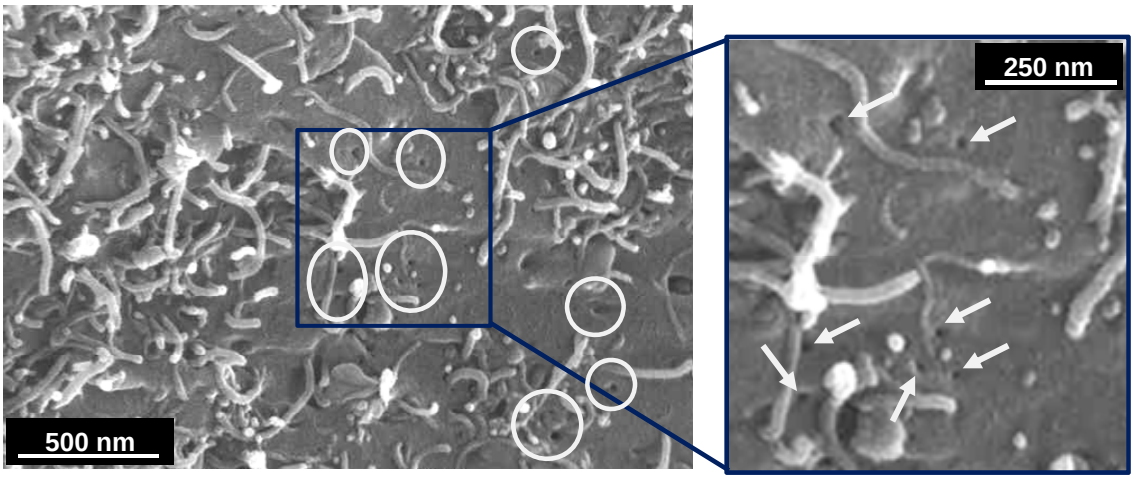

Figure 7.12 Delamination fracture surface of P940 multiscale composite specimen, where CNT pull-out holes seen in a resin rich area have been highlighted with white circles (a: 60-65 mm)

7.3 Evaluation of the effect of carbon nanoparticles on the plastic deformation region

The development of a plastic zone at the crack tip of the interlaminar resin rich layer in a fibre reinforced composite, under Mode I crack growth, determines the crack resistance of this bond. In addition, an adequate thickness of the bonding zone is paramount for attaining the maximum G_{IC} value possible for the system. Kinloch and Shaw [139] developed an elastic-plastic model, using bulk adhesive properties, for the determination of the deformation zone $2r_{Iy}$ around the crack tip, when using a plane-stress (Eq. (7.1)) or a plane-strain (Eq. (7.2)) condition,

$$r_{Iy} = \frac{1}{6\pi}\frac{E_f G_{ICbulk}}{\sigma_{yt}^2} \tag{7.1}$$

$$r_{Iy} = \frac{1}{6\pi}\frac{E_f G_{ICbulk}}{\sigma_{yt}^2}\frac{1}{(1-\nu^2)} \tag{7.2}$$

where r_{Iy} is the plastic zone radius, E_f is the flexural modulus of the resin, G_{ICbulk} is the initiation fracture toughness of the bulk material, σ_{yt} is the uniaxial tensile yield stress of the nanocomposite and ν is the Poisson's ratio.

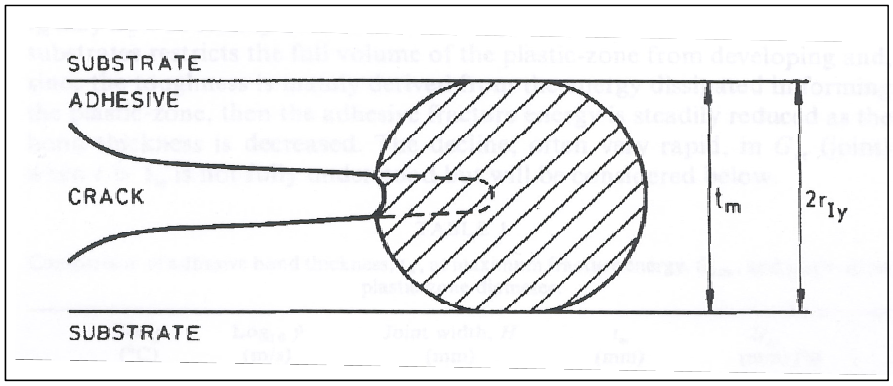

Figure 7.13 Simple elastic-plastic model for deformation zone at adhesive crack tip [139].

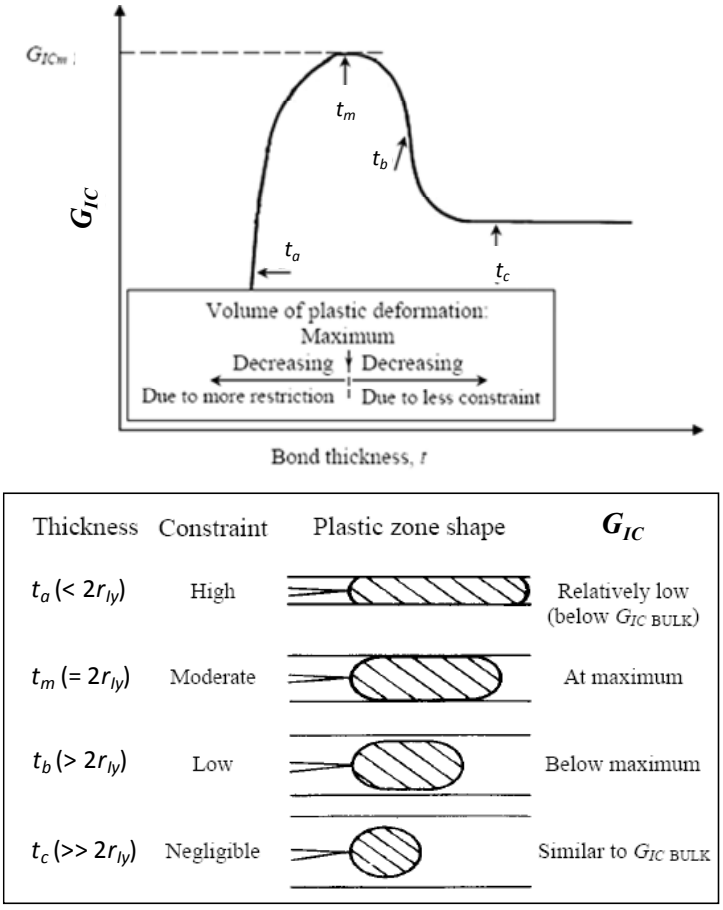

Figure 7.14 Relationship between bond thickness *t* and plastic zone diameter, and consequent degree of constraint affecting $G_{IC\ joint}$ (adapted from [139]).

According to Kinloch and Shaw [139], a maximum value of $G_{IC\ joint}$ is achieved when the bond thickness (t_m) equals the diameter of the crack tip plastic zone ($2r_{Iy}$). These relationships are described in Figure 7.14.

The fracture toughness G_{IC} of the surface modified nanocomposite and respective reference material were obtained from equation (7.3), considering E_f and K_{IC} values reported in [115]. Improvements in fracture toughness of ~174% were obtained for this surface modified nanocomposite with respect to the unmodified polymer. The value of σ_{yt} for the surface modified nanocomposite is reported in [115]. The Poisson's ratio for both materials was assumed to be 0.3.

$$E_f \sim \frac{K_{IC}^2}{G_{IC}} \tag{7.3}$$

The yield behaviour of the nanocomposites, corresponding to the multiscale composites tested under mode I, was evaluated under uniaxial compression, since epoxy resins tend to have a brittle fracture before yielding under uniaxial tension. Therefore, the value of σ_{yt} was obtained from the compression test results [139] according to Eq. (7.4), where σ_{yc} is the uniaxial compression yield stress.

$$\sigma_{yt} \approx 0.75 \cdot \sigma_{yc} \tag{7.4}$$

Representative compression curves of each nanocomposite system tested are shown in Figure 7.15. The values obtained for the compressive yield stress are listed in Table 7.3. The incorporation of CNPs within the epoxy resin did not cause a significant effect on the material yielding properties. The compressive yield stress values are very similar to these obtained for the control material. The highest increase was obtained for the surface modified CNT filled epoxy. Functionalisation promotes the bonding between resin molecules and CNTs, which may lead to an increase of the stiffness of the nanocomposite system due to a reduction of the mobility of the matrix by interfacial interactions. The epoxy filled with 0.5 wt% CNF showed the second highest increase in σ_{yc}. This increase was considered very modest when compared with the yield stress values of the nanocomposites containing half the amount of CNPs. Slightly lower values were obtained for the systems containing unfunctionalised MWCNTs.

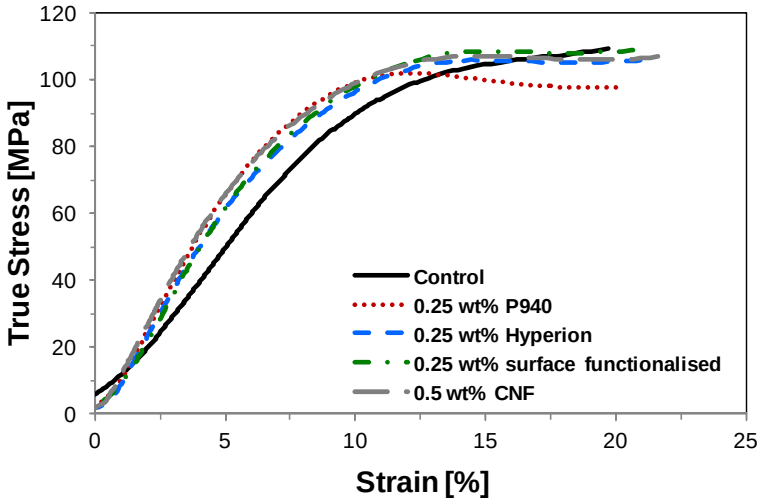

Figure 7.15 Compression curves of representative carbon nanoparticle filled nanocomposites.

Table 7.3 Compression yield stress for different nanocomposites

System	σ_{yc} (MPa)
Control	105 (± 1)
P940	100 (± 2)
CNF	107 (± 2)
Hyperion	103 (± 2)
Surface Functionalised	108 (± 1)

The size of the plastic zone for plane strain was selected for comparison with the actual thickness of the resin-rich mid-layer. The diameter of the plastic zone and the main parameters utilised for its calculation are listed in Table 7.4.

Table 7.4 Properties of the reference and nanocomposite material described in [115]

	Control	0.34 wt% surface modified CNTs [115]
K_{IC} (MPa.m$^{1/2}$)	0.72 [1]	1.23 [2]
G_{IC} (J/m^2)	165 [1]	917
E_f (GPa)	3	1.65 [2]
σ_{yt} (MPa)	78	66 [2]
$2r_{ly}$ (μm)	~10	~41

[1] [140]; [2] [115]

The thickness of the resin-rich mid-layer was evaluated for only one material since the type of fabric, fibre volume fraction and mould thickness were kept the same during the manufacture of the different composite panels. It was assumed that viscosity changes among different CNP filled systems would not cause significant variation on the range of thickness values.

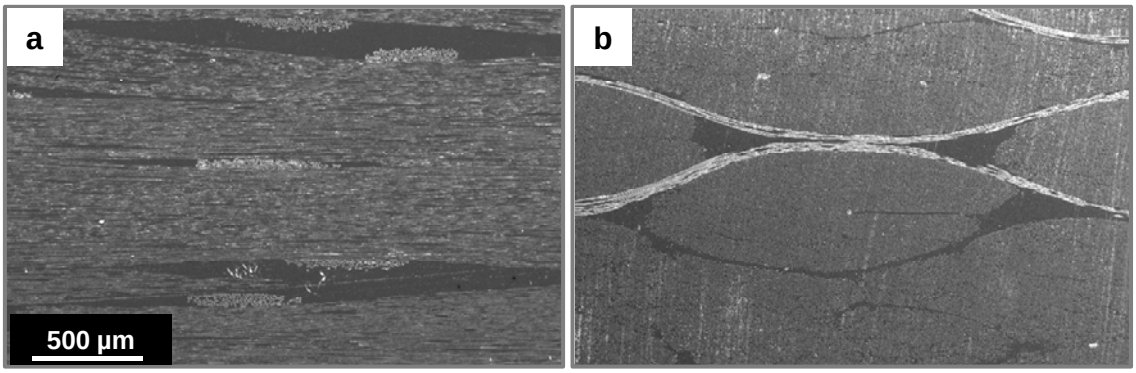

Figure 7.16 SEM micrographs of the longitudinal (a) and transverse (b) cross-sections of a carbon fibre composite specimen.

The resin-rich mid layer dimension varies between about 2 μm to 200 μm, depending mainly on the level of nesting between fabric layers. However, the average thickness of the interlaminar resin-rich layer is considered to be ~30 μm. Figure 7.16 shows this variation in the resin-rich area diameter. Since the resin-rich layer thickness is not constant, toughness is expected to vary from region to region. Therefore, the fabric architecture and the degree of nesting influence the level of constraint of the plastic zone. For the majority of the locations measured, along the longitudinal and transverse

surfaces, the thickness of the resin at the mid-layer is considerably larger than the plastic zone diameter measured for the control resin (~10 μm) This means that the interface is considered to be unconstrained for the majority of the cross-sectional area, and for that reason the $G_{IC\ interface}$ is similar to the $G_{IC\ bulk}$. In contrast, if a nanomodified resin system like the one reported in [115], which provides enhanced toughness at the nanocomposite level and generates a larger plastic zone of ~41μm, would be utilised to impregnate this fabric, the plastic zone would be higher than the thickness of the resin-rich layer for the majority of the cross-sectional area. Hence, in this case the plastic zone would be over-constrained and the $G_{IC\ interface}$ would be below the possible maximum. Therefore, the toughening effect caused by the presence of carbon nanoparticles at the nanocomposite level would become weaker in the fibre composite. The existence of similar relationships could have also inhibited potential enhancement of these composites toughness. Although the objective of this work was not the optimisation of the resin rich layer thickness to match the plastic zone diameter, this effect can be relevant when exploiting the potential of CNPs in increasing composites toughness.

7.4 Conclusions

The presence of different carbon nanoparticles as modifiers of fibre reinforced composites at 0.25 wt% loading in the resin did not result in statistically significant improvements in toughness. Despite the cases of CNP pull out and bridging observed by SEM, filtration, interfacial failure and constraints in the plastic zone are considered as the main reasons for this behaviour.

8 Modelling flow and filtration in liquid composite moulding of nanoparticle loaded thermosets

This chapter was adapted from a paper submitted to *Composites Science and Technology*. It presents the derivation of an analytical solution for the linear flow of carbon nanoparticle filled resins during liquid moulding of composites. In addition a finite difference filling simulation methodology accounting for porosity, permeability and viscosity variations with time and position is implemented for the non-linear case. The two models are compared and the convergence of the numerical model is investigated. The limits of validity of the linear approximation associated with the analytical solution are explored over a wide range of processing conditions. The process design capability of these models is evaluated for two scenaria where either a uniform or a localised concentration of carbon nanoparticles in the final composite is required.

8.1 Model development

8.1.1 Boundary value problem

The physics of flow and filtration are represented by conventional Darcy's law (Eq.(8.2)) associated with a continuity condition (Eq. (8.1)) and a particle mass conservation (Eq.(8.3)) combined with filtration kinetics (Eq.(8.4)) [76, 77]. The suspension Darcy velocity U is driven by the pressure gradient in the cavity, and is proportional to the permeability over viscosity ratio K/η. The mass balance represented by Eq.(8.3) accounts for the amount of particles entering and exiting the domain, which corresponds to the total flux of retained and suspended particles. The concentration time derivative of retained $\partial\sigma/\partial t$ and suspended particles $\partial\varepsilon C/\partial t$, together with the flux of suspended particles along the reinforcement length $U\,\partial C/\partial x$ contribute to the total balance of particles in the composite at each time step and position. A constitutive law (Eq.(8.4)) describes the kinetics of retention and possible re-suspension of particles. The first term of Eq.(8.4) corresponds to the retention of particles which is proportional to the flux of suspended particles UC. The proportionality constant k_o is called the filtration constant. The second term in the RHS of Eq.(8.4) represents the rate of particle re-suspension. The latter is considered to be proportional to the product of the

concentration of retained particles by the flux of suspended particles and k_r represents the re-suspension constant.

$$\frac{\partial U}{\partial x} = 0 \tag{8.1}$$

$$U = -\frac{K}{\eta}\frac{\partial P}{\partial x} \tag{8.2}$$

$$\frac{\partial(\sigma + \varepsilon C)}{\partial t} + U\frac{\partial C}{\partial x} = 0 \tag{8.3}$$

$$\frac{\partial \sigma}{\partial t} = k_0 UC - k_r \sigma UC \tag{8.4}$$

The resin flow front position (h) is considered equal to zero at the beginning of the filling process. Throughout the injection period, the concentration of suspended particles at the inlet equals the initial concentration of particles in the resin C_0, whilst the retention of particles at the resin flow front position is considered to be equal to zero. The pressure at the flow front position is equal to the vacuum pressure P_∞.

The boundary condition of the flow problem at the inlet of the flow can be of the first type (Dirichlet), the second type (Neumann) or a combination of the two depending on the control strategy implemented in production. When considering a pressure controlled injection, the pressure at the inlet position corresponds to the injection pressure P_o. In the case of flow control the resin flow at the inlet V_o is kept constant throughout the process. In the case of flow control with a maximum pressure constraint, which is the most realistic condition for an industrial setup, the resin flow is constant at V_o up to the time t_o at which the pressure required to sustain the constant flow exceeds a certain pressure limit P_o. This type of boundary condition is implemented as a complementarity problem. Eqs. (8.5) - (8.6c) summarise this set of boundary conditions.

$$h(0) = 0,\ C(0,t) = C_0,\ \sigma\left(h(t),t\right) = 0,\ P\left(h(t),t\right) = P_\infty \tag{8.5}$$

$$P(0,t) = P_o \tag{8.6a}$$

$$U(0,t) = \varepsilon V_o \tag{8.6b}$$

$$\left(P(0,t) - P_o\right)\cdot\left(U(0,t) - \varepsilon V_o\right) = 0,\ \ P(0,t) - P_o < 0,\ \ U(0,t) - \varepsilon V_o < 0 \tag{8.6c}$$

where Eq.(8.6a) corresponds to a prescribed pressure condition at the inlet, Eq.(8.6b) to prescribed flow and Eq.(8.6c) to prescribed flow subject to a pressure constraint.

8.1.2 Analytical solution of the linear problem

The solution for the concentration of suspended C and retained particles σ presented in Eqs.(8.7) and (8.8) is independent of the inlet flow boundary condition type (Eq.(8.6)) and is determined via combination of Eq.(8.3) and (8.4) and considering the linear assumptions of constant permeability, viscosity and porosity; zero re-suspension of particles ($k_r = 0$), assuming that the direction and magnitude of the flow are held constant during filling; and retention rate proportional to the flux of particles.

$$C = C_o \exp\left(-k_o x\right) \tag{8.7}$$

$$\sigma(x,t) = \varepsilon k_o C_o \exp\left(-k_o x\right)\ [h(t) - x] \tag{8.8}$$

Term $h\ (t)$ refers to the flow front evolution which depends on the inlet boundary condition. Under linearity the concentration of suspended particles is dependent only on position as a consequence of the assumptions of zero re-suspension and proportionality of retention rate to the flux of particles. In contrast, the concentration of retained particles is time dependent due to the cumulative character of filtration.

The total concentration of nanoparticles T is obtained by combining Eqs.(8.7) - (8.8) with the solutions of the linear free boundary 1-D Darcy's. The solution for the case of prescribed pressure at the inlet (Eq.(8.6a)) is:

$$T(x,t) = C_o e^{-k_o x}\left[1 + \varepsilon k_o\left(\sqrt{\frac{2K}{\varepsilon\eta}\left(P_o - P_\infty\right)\ t} - x\right)\right] \tag{8.9}$$

In the case of prescribed flow at the inlet (Eq. (8.6b)) the boundary value problem yields

$$T(x,t) = C_o e^{-k_o x}\left[1 + k_o\left(V_o t - \varepsilon x\right)\right] \tag{8.10}$$

In the case of the combined boundary condition expressed by Eq. (8.6c) the solution is:

$$T(x,t)=\begin{cases} C_o e^{-k_o x}\left[1+k_o\left(V_o t-\varepsilon x\right)\right], & t\le \dfrac{\varepsilon K}{V_o^{\,2}\eta}\left(P_o-P_\infty\right) \\ C_o e^{-k_o x}\left[1+\varepsilon k_o\left(\sqrt{\dfrac{2K\ t}{\varepsilon\eta}\left(P_o-P_\infty\right)-\left(\dfrac{K}{\eta V_o}\right)^2\left(P_o-P_\infty\right)^2}-x\right)\right], & t>\dfrac{\varepsilon K}{V_o^{\,2}\eta}\left(P_o-P_\infty\right) \end{cases} \tag{8.11}$$

8.1.3 Non-linear material models

Filtration of carbon nanoparticles by the reinforcement results in variations in material properties. These variations need to be addressed for an accurate prediction of the flow solution, when some of the linearity assumptions break down.

The narrowing of the reinforcement flow channels caused by the accumulation of nanoparticles results in a reduction of porosity as the resin flow front progresses. The following relation is adopted to account for this effect:

$$\varepsilon(x,t)=\varepsilon_o-\frac{\sigma\left(x,t\right)}{\rho_{NP}} \tag{8.12}$$

where ε_o denotes initial porosity and ρ_{NP} the density of the nanoparticles. The volume of entrapped liquid resin between retained CNPs and/or between retained CNPs and the fibre reinforcement, which does not participate in the flow, can be neglected for dilute suspensions and/or small retention of CNPs.

The Kozeny-Carman relation can be used to describe the dependence of permeability on porosity [141, 142] as follows:

$$K(x,t)=A\frac{\varepsilon\left(x,t\right)^3}{\left(1-\varepsilon\left(x,t\right)\right)^2} \tag{8.13}$$

where A represents a constant.

Variations in suspended particle concentration lead to variations in viscosity. The model presented in [143] was adopted here to represent this effect as follows:

$$\eta(x,t)=\eta_o\left(1-\frac{C\ (x,t)}{\varphi_m\rho_{NP}}\right)^{-\eta_I\varphi_m} \tag{8.14}$$

Here η_o denotes the viscosity of the liquid medium, φ_m is the packing fraction of the filler and η_I is the intrinsic viscosity of the filler which expresses the sensitivity of the suspension viscosity to the filler volume fraction at the limit of negligible filler content. The implementation of this macroscopic model where flow is described by Darcy's law requires the assumption of a constant shear rate for the description of the viscosity dependence on concentration. Therefore, the shear rate dependence with pore size was assumed to be zero.

8.1.4 Finite difference formulation and implementation

A 1-D finite difference model accounting for the material nonlinear behaviour was developed. The formulation is suitable for the simulation of both 1-D in-plane flow in an RTM scenario and through the thickness flow in infusion. It should be noted that the implementation also allows for the incorporation of a generic filtration kinetics equation instead of Eq.(8.4). However, the type of kinetics presented in Eq. (8.4) is used here, whilst all the results presented concern the case of zero re-suspension coefficient.

The finite difference implementation uses a uniform grid representation of the domain of total length L comprising N grid points with coordinates

$$x_i = i\Delta x, \quad i = 0,...,N, \quad \Delta x = L/N-1 \tag{8.15}$$

The time discretisation is non uniform and allows a convenient treatment of the one dimensional free boundary problem by selecting a time step that matches the movement of the flow front from its current position to the next grid point as follows:

$$t^o,...,t^j,...,t^M, \qquad t^j - t^{j-1} = \varepsilon_{i-1}^{j-1}\Delta x / U^{j-1} \tag{8.16}$$

Here M is the total number of time increments in the solution, which is not known a priori and is governed by the length of the modelling domain and the evolution of velocity during the solution. The pressure, concentration of suspended, concentration of retained and total concentration of particles are denoted at the spatial-temporal nodal points (x_i, t^j) as P_i^j, C_i^j, σ_i^j, and T_i^j respectively. Due to the 1-D character of the problem Darcy velocity does not vary in space but only in time with nodal values U^j corresponding to time t^j. The flow front position at time t^j is denoted as h^j. Porosity,

permeability and viscosity are also considered as spatial-temporal variables with discretised values ε_i^j, K_i^j, and η_i^j respectively.

The implementation performs the solution of the filtration and flow problems as well as property updating as shown in Figure 8.1.

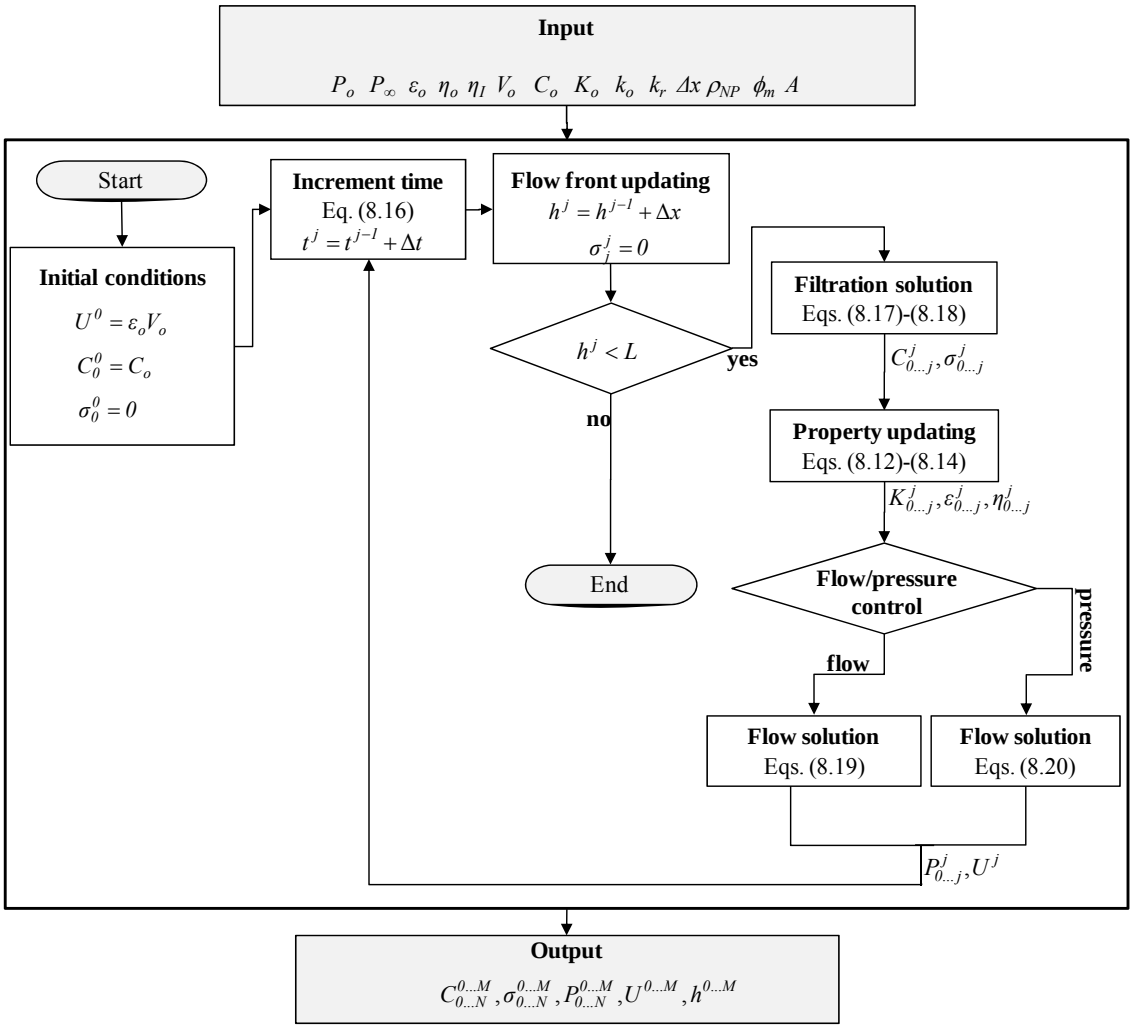

Figure 8.1 Flow chart of the flow and filtration FD model implementation.

The solution of the filtration problem is performed first at each increment via the discretised forms of Eqs. (8.3) and (8.4). Using a forward scheme Eq. (8.4) yields

$$\sigma_i^j = \sigma_i^{j-1} + \left(t^j - t^{j-1}\right)\left(k_0 U^{j-1} C_i^{j-1} - k_r U^{j-1} \sigma_i^{j-1}\right), \quad i = 0...j-1 \tag{8.17}$$

which accompanied by the boundary condition at the flow front ($\sigma_i^j = 0$) allows the explicit calculation of the retained concentration profile at time t^{j+1} based on the solution for the previous increment.

The finite difference form of Eq. (8.3) follows a backward time-forward space scheme

$$C_{i+1}^j = C_i^j + \frac{\Delta x}{U^{j-1}}\left[-\varepsilon_i^{j-1}\frac{C_i^j - C_i^{j-1}}{t^j - t^{j-1}} - \frac{\sigma_i^j - \sigma_i^{j-1}}{t^j - t^{j-1}}\right], \quad i = 0...j-1 \tag{8.18}$$

which accompanied by the condition of prescribed concentration at the inlet ($C_0^j = 0$) allows the explicit calculation of the suspended concentration at nodal points, using the suspended concentration solution for the previous increment and the retained concentration solution for the current increment. The calculation of the retained and suspended concentration allows the updating of material properties via Eqs. (8.12) - (8.14), which enables the solution of the flow problem to be made taking into account the non-linearities due to filtration. The finite difference formulation of the flow problem differs depending on the type of boundary condition at the inlet (Eq.(8.6)). In the case of flow control (Eq.(8.6b)) the fluid velocity is known a priori and Eq.(8.2) can be solved explicitly using a trapezoidal scheme

$$P_{i-1}^j = P_i^j + V_0\left(\varepsilon_{i-1}^j\frac{\eta_{i-1}^j}{K_{i-1}^j} + \varepsilon_i^j\frac{\eta_i^j}{K_i^j}\right)\frac{\Delta x}{2}, \quad i = 0...j-1 \tag{8.19}$$

subject to the boundary condition of prescribed pressure at the flow front ($P_i^j = P_\infty$).

In the case of pressure control (Eq.(8.6a)) a centered approximation of Eqs.(8.1) and (8.2) yields

$$P_{i+1}\left(\frac{K_{i+1}}{\eta_{i+1}} + \frac{K_i}{\eta_i}\right) - P_i\left(\frac{K_{i+1}}{\eta_{i+1}} + 2\frac{K_i}{\eta_i} + \frac{K_{i-1}}{\eta_{i-1}}\right) + P_{i-1}\left(\frac{K_i}{\eta_i} + \frac{K_{i-1}}{\eta_{i-1}}\right) = 0, \quad i = 0...j-1 \tag{8.20}$$

which accompanied by the outlet condition and the inlet pressure boundary condition ($P_0^j = P_o$) form a system of equations that is solved to compute the pressure profile approximation.

The implementation of the flow solution follows the generic boundary condition expressed by Eq.(8.6c). When the code starts flow control is enabled and at the end of each increment the pressure at the inlet is compared with the pressure constraint P_o. If the inlet pressure is greater than P_o pressure control is enabled. The monotonous increase of pressure at the inlet ensures that once pressure control is enabled the status of the type of solution required does not change.

8.2 Results and discussion

8.2.1 Convergence and stability of the finite difference model

Successful simulation of the non linear flow/filtration fields using finite differences is conditional on the appropriate numerical behaviour of the scheme proposed. The convergence of the scheme is supported by theoretical evidence available for the linear version of the problem as well as empirical evidence that concerns the full non-linear version of the flow and filtration set of differential equations (Eqs.(8.1)-(8.6) and (8.12) -(8.14)).

The linear version of the filtration problem, where properties are constant and re-suspension is considered negligible ($k_r=0$), can be addressed by applying the Von Neumann stability analysis on the combination of Eqs.(8.17)-(8.18). Taking into account the relation between time step and velocity (Eq.(8.16)) yields

$$C_{i+1}^{j} = C_i^{j-1} - k_o \Delta x C_i^{j-1} \tag{8.21}$$

which corresponds to the following error growth factor

$$g(l) = \frac{1 - k_o \Delta x}{\exp(I\, l \Delta x)} \tag{8.22}$$

with $\sqrt{I} = -1$. Stability is ensured if $|g(l)|^2 \le 1$ which holds unconditionally. The stability of the retained concentration solution for the linear case follows, as the integration implied by Eq.(8.17) converges when the term k_oUC is bounded and continuous. The linear versions of Eqs.(8.19)-(8.20) result in linear systems of equations with a bounded inverse matrix and thus are unconditionally stable.

The consistency of the finite difference scheme in the linear case is tested via a comparison with the analytical solution of the flow/filtration problem (Eqs.(8.7)-(8.11)). The input parameters utilised, which correspond to in-plane filling of an epoxy/0.25 wt.% CNT carbon fibre composite, are listed in Table 8.1 (column Linear case). The inlet boundary condition of the flow problem is flow control under a pressure constraint (Eq.(8.6c)). Finite difference simulations were carried out using a grid size ranging from 3.125 mm to 100 mm. A comparison between the finite difference solution and the analytical model is illustrated in Figure 8.2.

Table 8.1. Input parameters used in simulations. Column Linear case corresponds to the comparison between linear finite differences and analytical solution in section 8.2.1; column Non-linear case 1 corresponds to the stability analysis for the non-linear finite differences model in section 8.2.1;column non-linear case 2 corresponds to the study of limits of validity of the analytical solution in section 8.2.2.

Parameters	Linear case	Non-linear case 1	Non-linear case 2
K [m^2]	$1.57\ 10^{-11}$	$1.57\ 10^{-11}$	$1.57\ 10^{-11}$
η_o[Pas]	-	0.054	0.054
η[Pas]	0.211	-	-
ε_o	0.43	0.43	0.43
P_o [Pa]	$2.0\ 10^5$	$2\ 10^5$	$2\ 10^5$
P_∞ [Pa]	$2.0\ 10^3$	$2\ 10^3$	$2\ 10^3$
V_o[m/s]	$7.43\ 10^{-3}$	$7.43\ 10^{-3}$	$7.43\ 10^{-3}$
C_o [kg/m^3]	2.78	5.56	2.78, 6.95
ρ_{NP} [kg/m^3]	1660	1660	1660
A	-	$6.4\ 10^{-11}$	$6.4\ 10^{-11}$
ϕ_m	-	0.55	0.55
η_I	-	812.6	812.6
k_o[1/m]	0.1	0.1	0.01-10
k_r	0	0	0
L[m]	0.3	0.2	0.001-10

The simulation converges to the analytical solution as the relative error in the computation of pressure, flow front position, and retained and suspended concentrations

is about 5% for a grid size below 6 mm and 2% for a grid size below 3 mm (Figure 8.2(a)). The evolution of the flow front position predicted by the finite difference solution converges to the analytical solution as the grid is refined (Figure 8.2(b)), with the solutions being practically indistinguishable for a mesh size below 10 mm. The distributions of field variables (pressure, particle concentration) become virtually identical to the analytical solution as the grid is refined; the results in Figure 8.2(c) and (d) showing the distribution of pressure and retained particles at a flow front position of 0.2 m are typical of all filling times.

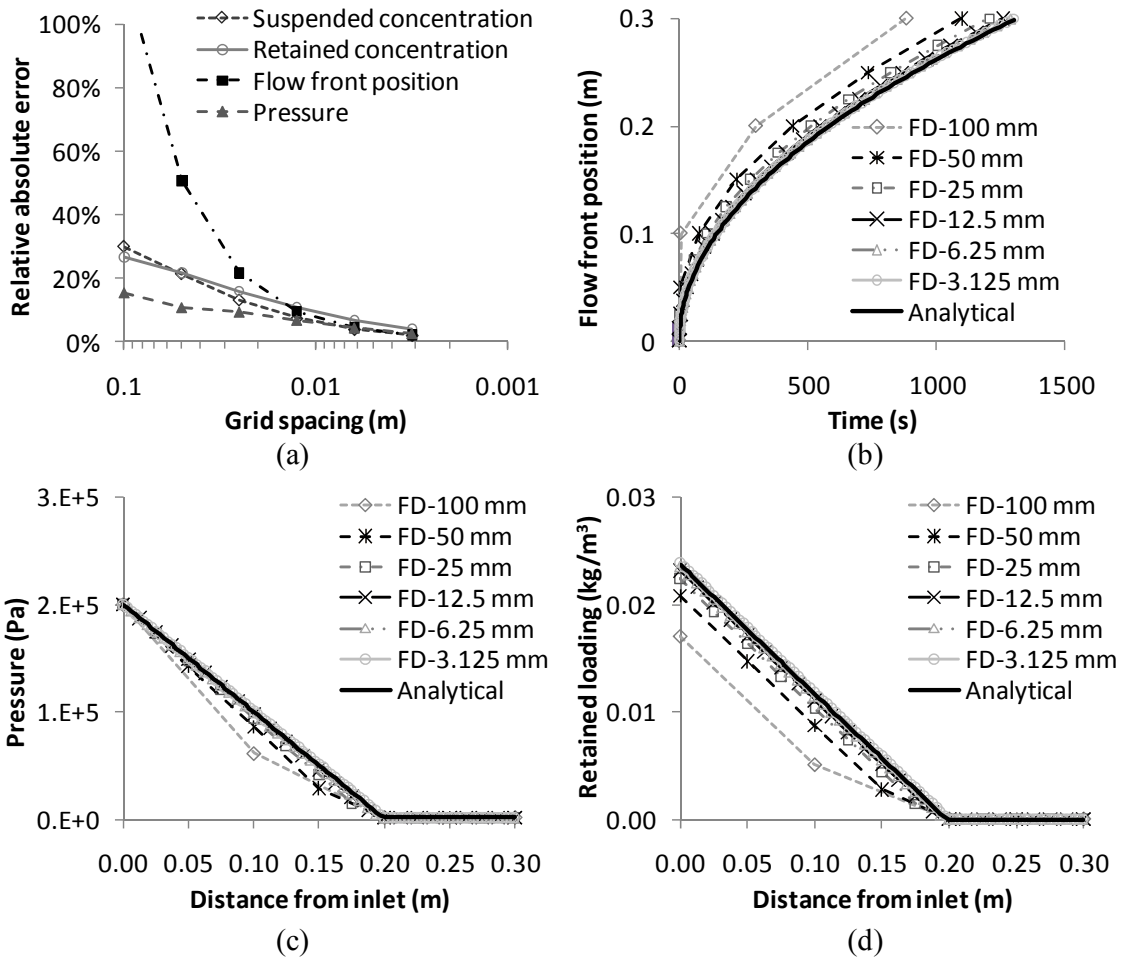

Figure 8.2 Consistency and convergence of the finite difference solution based on a comparison with the analytical solution in the linear case: (a) average relative error against the analytical solution; (b) flow front position evolution; (c) pressure distribution for flow front at 0.2 m; (d) distribution of retained loading for flow front at 0.2 m. The parameters of the model are listed in Table 8.1 (Linear case).

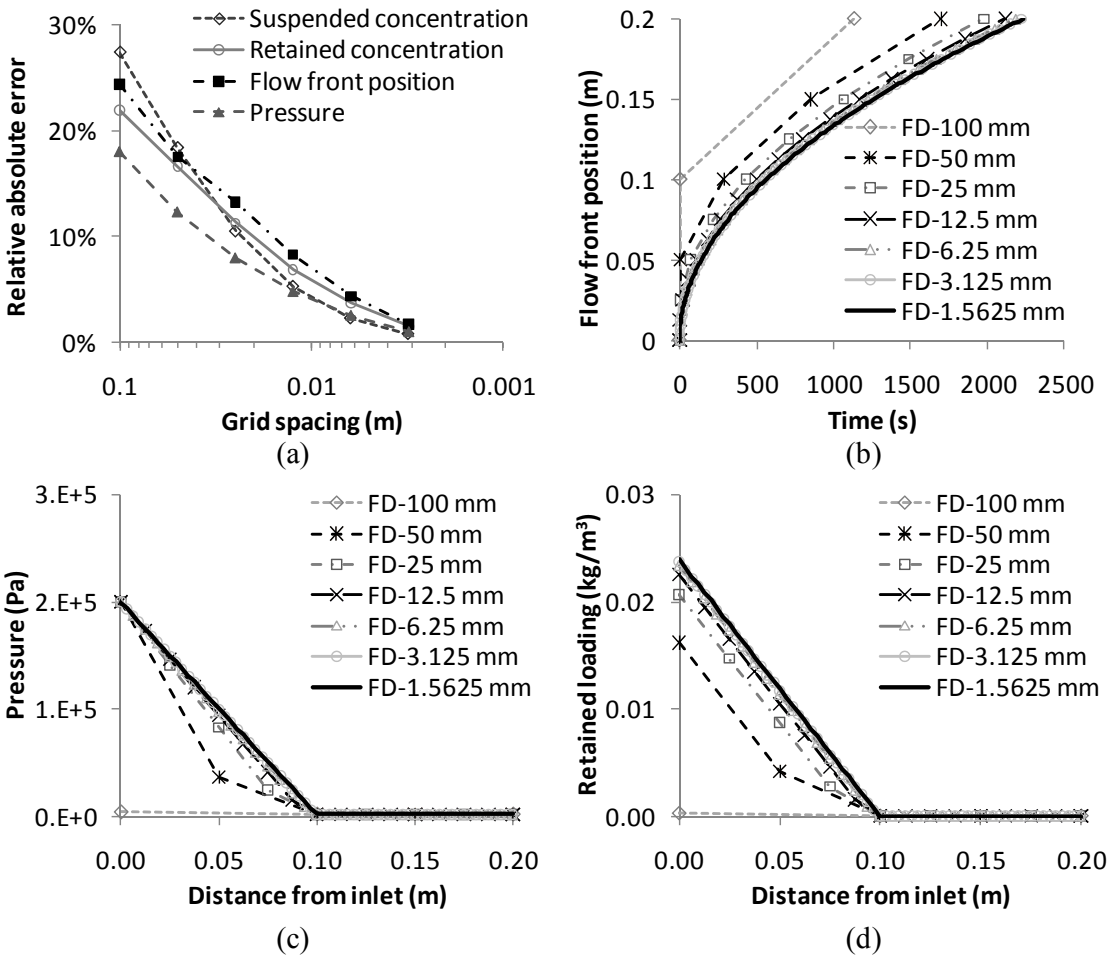

Figure 8.3 Stability of the finite difference solution with respect to mesh refinement: (a) average relative error against the finest mesh (1.5625 mm); (b) flow front position evolution; (c) pressure distribution for flow front at 0.1 m; (d) distribution of retained loading for flow front at 0.1 m. The parameters of the model are listed in Table 8.1 (Non-linear case 1).

Further evidence of the convergence properties of the finite difference scheme can be obtained by a mesh stability analysis for the case of non-linear properties. The model inputs for this investigation are listed in Table 8.1 (column Non-linear case 1) and the results are illustrated in Figure 8.3. The finite difference solution of a very fine mesh (grid size of 0.15625 mm) is used as a reference for the calculation of the error. The average relative error is below 5% for grid size below 5 mm and decreases to values below 2% at a grid size of about 3 mm. The flow front position converges to the finer mesh values for a grid size below 10 mm (Figure 8.3(b)). Equivalent stability is observed for the pressure distribution and concentrations; the results for pressure and

retained concentration at a flow front position of 10 cm (Figure 8.3(c) and (d)) are characteristic of the whole solution.

The analysis presented here demonstrates the validity of the finite difference model solution as the linear case can be shown to be stable and consistent with the analytical solution. Furthermore, the non-linear version of the finite difference model is stable with mesh refinement. Thus, the numerical implementation can be considered appropriate. Future experimental validation will allow testing of the validity of the material laws used.

8.2.2 Range of applicability of the analytical model

The analytical model is preferable in the context of process design mainly due to the computational efficiency, when iterative use is necessary, as well as the relative simplicity of its input. An evaluation of the range and extent of its validity in approximating a non-linear situation is valuable in deciding whether its usage is adequate in a certain design situation. Two process parameters were identified as the most appropriate set for evaluating the effect of non-linearity; namely the filtration constant (k_o), which was varied between 0.01 and 10 1/m, and the length of the filling domain (L), which was varied between 1 mm and 10 m. The study was carried for two different nanoparticle loadings (0.25 and 0.625 wt%). Other factors influencing non-linearity such as intrinsic viscosity as well as porosity and permeability variations could be included in such a study. However, these are limited in a relatively narrow range for realistic systems and their variations can be considered of secondary importance.

Simulations were carried out using the inputs listed in Table 8.1 (column Non-linear case 2) and the average relative difference between the results of the analytical simulation and the non-linear finite difference solution was calculated. Figure 8.4 summarises the error distributions over the filtration constant-length space for the two loading levels investigated. The error of the analytical solution increases as both the filtration constant and length increase, showing a stronger effect of non-linearity for higher values of these parameters as expected.

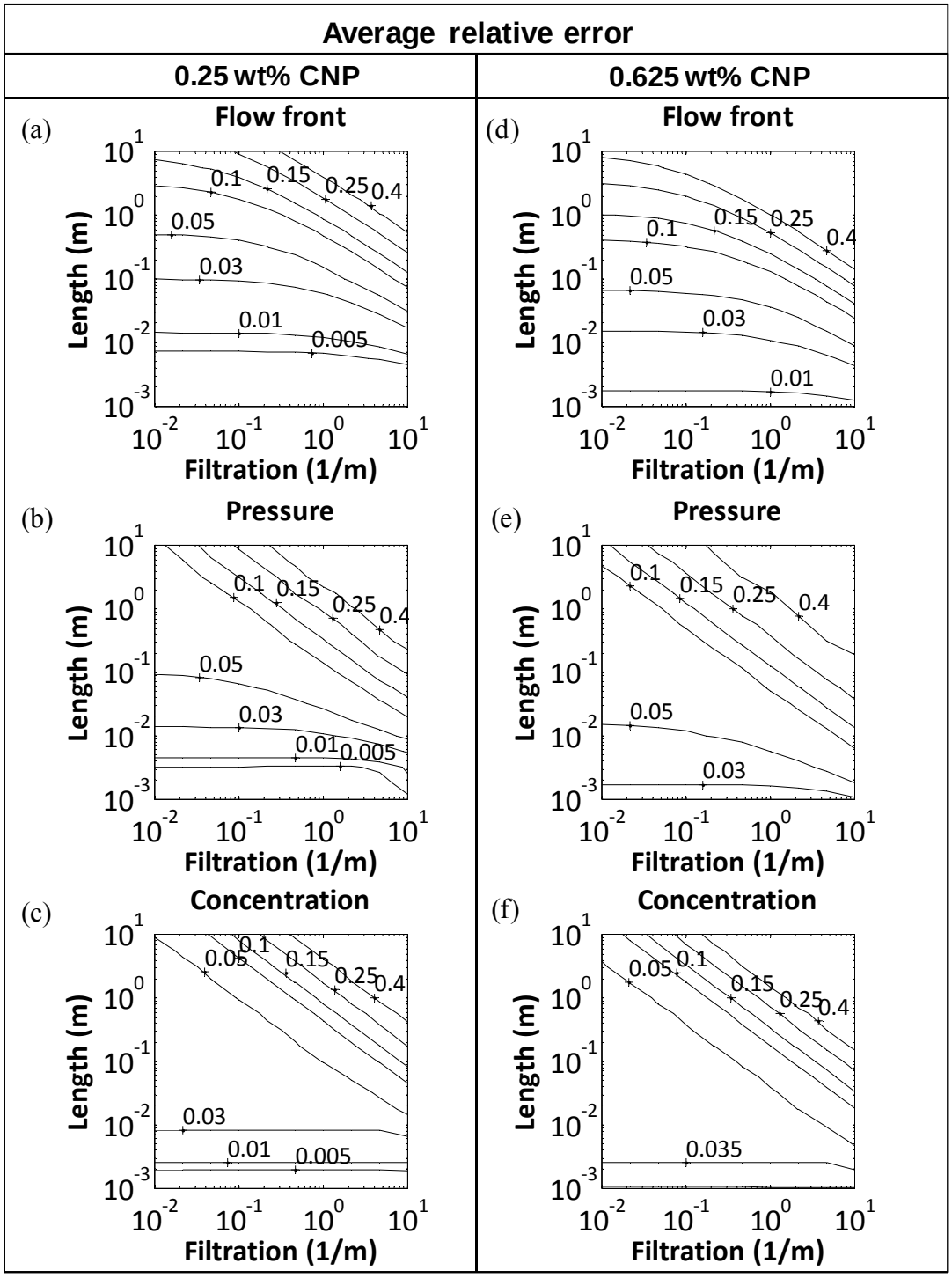

Figure 8.4 Limits of applicability of the linear analytical solution using the non linear finite difference solution as a benchmark: (a)-(c) average relative error in flow front position, pressure and total concentration for low nanoparticle content (0.25 wt%); (d)-(f) average relative error in flow front position, pressure and total concentration for high nanoparticle content (0.625 wt%); The parameters of the model are listed in Table 8.1 (Non-linear case 2).

The effect of loading is also positive on the error as it can be seen by comparing Figure 8.4 (a)-(c) with Figure 8.4 (d)-(f). For the low loading (Figs.(a)-(c)) the error of the analytical solution is limited below approximately 3 % for lengths up to 1 cm. This result is relevant for through thickness infusion and shows that the analytical approximation can be used in this scenario. The sensitivity to the filtration constant is also limited in this range of lengths with the error remaining practically constant up to filtration constant levels over 100 %/m. As the length increases the sensitivity to the filtration constant increases, with error approaching 10% in the 10-50 %/m filtration constant range (Figure 8.4 (a)-(c)) for lengths corresponding to in-plane filling (~1 m). Thus, the applicability of the analytical solution in in-plane processes is limited to the cases of low filtration constants. The errors in total concentration (Figure 8.4 (c)) tend to be lower than for pressure and flow front position as a result of the significant steady state component in the solution for suspended concentration. The results for high loading (0.625 wt.%) follow the same trends with an overall stronger effect of non-linearity. Thus, the low error area is limited to lengths below a few millimetres – a value which is still relevant to through thickness infusion. Similarly, the transition to levels of error over 10 % for lengths relevant to in-plane processes (~1 m) occurs in the 1-10 %/m filtration constant range. Overall, these results indicate that the analytical solution is useful in through thickness infusion and limited to only very low filtration constants in in-plane infiltration of hybrid composites. Use of the finite difference model is appropriate in conditions outside this envelope.

8.2.3 Demonstration of process design capabilities

The application of the numerical model proposed is mainly on process design. Two realistic situations are presented here for the production of carbon nanoparticle multiscale composites in a RTM scenario with controlled concentration profiles, where either a uniform or a localised carbon nanoparticle profile are required. The parameters utilised for the process design simulations are listed in Table 8.2.

The first case presented aims at manufacturing of a multiscale composite with a uniform nanofiller distribution throughout the whole structure. For that purpose the boundary

condition describing the concentration of incoming resin at the inlet gate (Eq.(8.5)) was replaced by Eq.(8.23).

Table 8.2 Parameters utilised for the two process design simulation cases

Parameters	Uniform concentration profile	Localised concentration profile
K [m^2]	1.57 10^{-11}	1.57 10^{-11}
η_o[Pas]	0.054	0.054
ε_o	0.43	0.43
P_o [Pa]	2.0 10^5	2 10^5
P_∞ [Pa]	2.0 10^3	2 10^3
V_o[m/s]	7.43 10^{-3}	7.43 10^{-3}
C_o [kg/m^3]	5.56	5.56
ρ_{NP} [kg/m^3]	1660	1660
A	6.4 10^{-11}	6.4 10^{-11}
ϕ_m	0.55	0.55
η_I	812.6	812.6
k_o[1/m]	3	3 and 5
k_r	0	0
a, b, c	-	2, 0.1, 0.05
L[m]	0.3	0.3

This linear equation controls the adjustment of the nano filled suspension concentration at the inlet gate, by decreasing its value to compensate for the continuous capture of particles during impregnation. Coefficient w controls the adjustment of the initial concentration during filling in order to achieve an uniform particle distribution in the final composite.

$$C(0,\, t) = w \cdot C_o + (1 - w) \cdot C_o \frac{(L - h)}{L} \tag{8.23}$$

The RTM filling of a 0.3 m long carbon nanoparticle multiscale composite, where a uniform particle concentration is required, was simulated using the non-linear model described in Figure 8.1 with the input parameters detailed in Table 8.2, alongside with Eq. (8.23) as a boundary condition for the inlet. The results for this simulation are

presented in Figure 8.5, for a range of *w* values. When *w* is equal to 1 the boundary condition at the inlet is equivalent to Eq.(8.5). A coefficient equal to 0.2 results in an approximately uniform distribution of nanoparticles in the final composite.

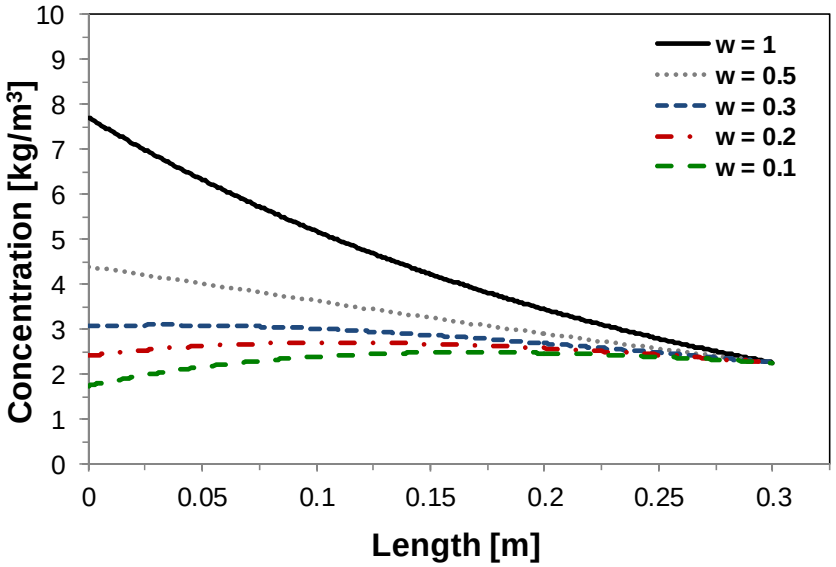

Figure 8.5 Carbon nanoparticle concentration profile design of a composite which requires an uniform particle distribution.

When localised carbon nanoparticle reinforcement is required, e.g. in the case of a location that is expected to carry a high current density during lightning strike, the boundary condition for the inlet concentration as a function of time needs to be modified in order to describe the target shape of the concentration profile. The boundary condition can be described by the following equation

$$C(0,\, t) = a\, C_o \cdot \exp\left(-\frac{(h-b)}{2c^2} \right) \tag{8.24}$$

where a, b and c correspond to the coefficients governing the peak height, its position and its breadth respectively.

This situation was simulated for an RTM filling scenario, utilising the non-linear model described in Figure 8.1 with the input parameters detailed in Table 8.2 for the localised concentration profile, and Eq.(8.24) as boundary condition. The results for the final concentration profile of suspended and retained particles are presented in Figure 8.6,

when considering two different filtration coefficients. A better control of the process can be achieved when lower filtration coefficients are present.

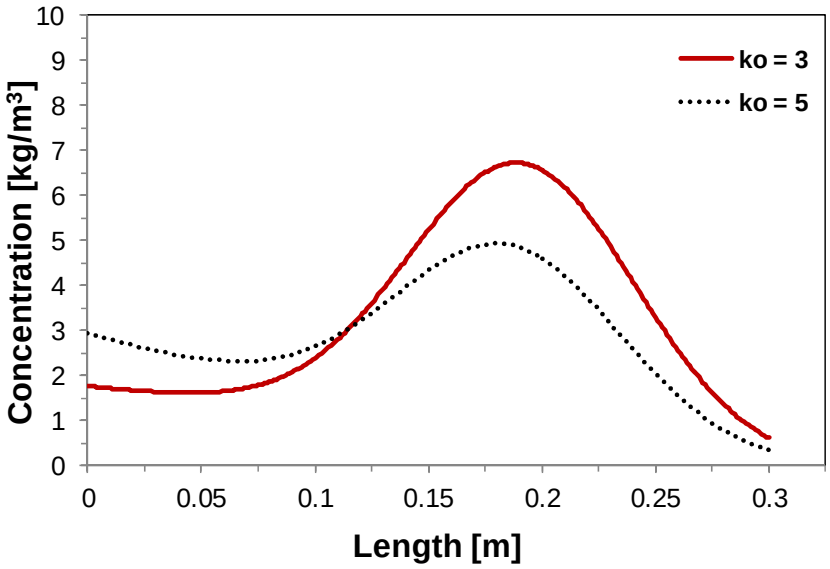

Figure 8.6 Carbon nanoparticle concentration profile design for a composite which requires localised reinforcement.

8.3 Conclusions

The analytical approximation and the non-linear finite difference model developed here offer a complementary range of solutions for the simulation of flow and filtration in liquid moulding of nanoparticle loaded resins. The analytical approximation can be applied to processes involving short filling lengths, i.e. through thickness infusion. The non-linear numerical approximation is appropriate for processes involving infiltration lengths in the meter range, e.g. resin transfer moulding.

The models have been verified in terms of consistency and, for the numerical case, convergence. Future experimental validation will allow evaluation of the material models selected here as well as of the basic physical laws used for the representation of the flow and filtration phenomena. Extensions to different material models, which can incorporate different retention or suspension kinetics, different viscosity and permeability dependence on loading as well shear rate dependent rheological behaviour of the suspensions, can be implemented as part of the current numerical formulation.

The models can find direct application to the expanding field of processing of hybrid composites. Process feasibility investigations are possible using both the analytical and the numerical solutions. The analytical model lends itself to process design due to its computational efficiency and simplicity in input parameters. Furthermore, these models enable process design of graded nanocomposites to be made. The capability to predict the distribution of concentration of nanoparticles will lead to the development of processes producing hybrid composites with strategically selected nanoparticles distribution, maximising both performance and efficiency of the reinforcement. Examples of two design process scenaria presented here are proof of that, and confirm the relevance of such models in an industrial scale.

9 Overall discussion and suggestions for further research

9.1 Overall discussion

This study focused on the incorporation of carbon nanoparticles, in particular CNTs and CNFs, within continuous fibre reinforcements for the manufacture of multifunctional composite materials. The enhancement in electrical conductivity and the potential for improved delamination properties makes this class of materials highly attractive for aerospace applications, in particular for lightning strike protective structures. In this study, different carbon nanoparticles at 0.25 wt% content were utilised to modify aerospace grade composites, comprising carbon fibre reinforcement at high volume fraction impregnated with a thermosetting epoxy resin suitable for RTM applications.

In the last decade, the transfer of the exceptional properties of these nanofillers to polymer nanocomposites and ultimately to fibre reinforced composites has been attracting an intense interest. Achieving a homogeneous and stable dispersion of these nanoparticles in the polymer is still seen as a challenging task, especially when utilising unmodified and highly entangled carbon nanoparticles as modifiers. The state of dispersion can be qualitatively and easily accessed by optical transmission microscopy of the suspensions produced. In this study the state of dispersion was accessed successfully with microscopy techniques and complemented with measurements of CNT and CNF filled epoxy electrical conductivity at different stages of dispersion processing. A strong correlation between the suspension electrical conductivity, the state of dispersion and the type and concentration of carbon nanoparticle in suspension was found for the systems studied. It should be noted that the existence of this correlation hinges on the presence of primary aggregates in the unprocessed system, with released nanoparticles forming a percolated network upon dispersion. The electrical conductivity of a suspension can be improved when utilising higher contents of nanofiller, as long as an appropriate dispersion technique is selected for that particular nanofiller. For instance, ultrasonication was found to be a better way of dispersing unmodified CNTs in the epoxy of this study, whilst high shear mixing is a more effective method of dispersing CNFs in the same material. Despite the better

dispersion state achieved by ultrasonicated CNF suspensions, when compared to high shear mixed ones, which present a large number and size of primary aggregates, ultrasonication was detrimental in achieving enhancement of electrical properties using these fillers. This behaviour proves that not always the best dispersion leads to enhanced target properties, as generally assumed in many research studies. In addition, the effect of temperature activated reaggregation in the electrical conductivity of the material should be studied, as excessive reaggregation might disrupt the conductive network. Unmodified CNTs can provide enhanced electrical conductivity at lower loadings than CNFs and the surface modified CNTs of this study. The type of CNP and its aspect ratio, the level and type of dispersion processing as well as the suspension stability under high temperature, are closely interconnected and govern the properties of the final composite material. These relationships should be taken into account when designing composites for a specific application.

The viscosity of carbon nanoparticle suspensions increases significantly with filler content and improved dispersion state. In addition, generally higher nanofiller contents lead to enhanced electrical properties. However when this increase is not significant enough to compensate for the rise in viscosity associated with higher filler content, as seen for the case of 0.5 wt% and 0.25 wt% unmodified CNT suspensions dispersed by ultrasonication, the lower loading should be selected. The significant increase in viscosity makes highly loaded suspensions unsuitable for the production of multiscale composites by liquid moulding routes, as it leads to extremely slow progression of the resin flow front and could ultimately result in incomplete filling of the fibrous preform. Prepregs and hand-layup processes offer alternative solutions in this situation.

The studies of dispersion allowed the selection of the appropriate suspensions for infusion by RTM, where the nanofiller loading was kept at 0.25 wt% in order to avoid high viscosity during infusion. Modifications to the liquid moulding process need to be made in order to guarantee successful infusions of carbon nanoparticle modified suspensions. These include the incorporation of a dispersion step of the carbon nanofilled suspension prior to infusion and optimised degassing strategies. The dispersion process is tailored to maximise the eventual performance of the final composite structure. Control over the aggregate size governs the type of filtration

occurring during filling, i.e. cake filtration or deep bed filtration. Optimisation of degassing guarantees the efficient removal of volatiles without compromising the level of dispersion of the suspension. Moreover, a good control of the rheological behaviour of the suspension can offer the possibility of adjusting process variables such as mould temperature and pressure in order to avoid deceleration of filling and premature cure.

Very small amounts of unmodified carbon nanoparticles in the epoxy resin, i.e. 0.25 wt%, lead to enhanced performance, especially in what concerns the electrical behaviour of these multiscale composites. The electrical conductivity almost doubles for unmodified CNP carbon composite systems. Despite the minimal dispersion processing required when utilising surface modified CNTs, the capability of providing significant enhancement of electrical properties to composites is hindered by the functionalisation process which inhibits reaggregation phenomena. However, virtually uniform concentration distribution can be achieved with these functionalised particles. Electrical conductivity measurements of specimens along the composite length offer a simple method to access particle filtration.

Despite the better capability of unmodified CNPs to provide enhanced electrical properties, when compared with surface functionalised systems, their incorporation in the production of large composite structures using in-plane flow routes at an industrial scale is not viable at this concentration. High suspension viscosity associated with extensive particle filtration would result in difficulties in achieving complete filling of the preform. In this case, surface modified CNP should be considered as an alternative, despite their higher cost and reduced capacity in providing enhanced electrical properties.

Ideally a multifunctional composite would combine electrical performance with improved resistance to delamination. However, the limited presence of toughening mechanisms, like CNP pull-out and bridging, alongside potential localised inelastic deformation, prevents significant improvements in the delamination properties of the composites in this study. Despite the general belief by significant part of the community on the extreme toughenability provided by CNP to fibrous composites, the results presented here show that this is not possible in composites based on neat epoxies. The fillers used in this study represent a large part of the range of carbon nanoparticles,

whist their processing has been optimised to address incorporation via liquid moulding. Improvements in the delamination behaviour are expected to occur with CNTs and CNFs as long as manufacturing routes such as grafting of aligned carbon particles, due to their capability of incorporating high fractions of nanoparticles at critical locations.

The resin flow front progression for all the systems was monitored during the infusion. The flow through a porous medium can be described by Darcy's law. However, the viscosity dependence on particle concentration for unmodified carbon nanoparticle systems, alongside the filtration of particles by the reinforcement occurring during infusion, lead to deviations from the square root dependence on time described by the 1-D Darcy's law result. For these situations a non-linear solution for the flow and filtration problem is required, in order to account for changes in suspension viscosity due to reduction of suspended particles in the moving resin to the porous media and local variations in the fibrous reinforcement porosity and permeability. An analytical solution for the 1-D linear flow and filtration was derived for liquid composite moulding of carbon nanoparticle filled thermosets. This solution is based on 1-D Darcy's law, associated with a continuity condition and a conservation of mass for the particles combined with a filtration kinetics equation. Based on the latter a finite difference scheme, accounting for permeability, porosity and viscosity variations with time and position, which allows for the solution of the non-linear problem was developed. The finite difference solution for the pressure, flow front position and concentration of suspended and retained particles is consistent and converges to the analytical solution. The analytical model is suitable for the flow and filtration problem when lower filtration coefficients and shorter filling lengths are simulated, i.e. in a through thickness infusion by VARTM, whilst the non-linear approach offers a solution outside this range, i.e. for processes involving infusion of longer components like RTM, where higher particle filtration is expected. The models proposed in this study require validation of the property sub-models and the kinetics of filtration, in order to allow for its incorporation in process design of composite components produced by liquid moulding at an industrial scale.

The incorporation of the viscosity dependence on particle concentration along with shear rate effects is important to access since the dual scale pore nature of conventional

fibre reinforcements, results in two distinct flow profiles, i.e. a faster velocity in inter-fibre pores, followed by a slower movement of the suspension at the intra-tow level. Addressing this aspect within the model developed in this study, where a continuum medium is assumed, could require the incorporation of a second flow model descriptive of the microscopic flow.

A measurement method for the determination of the concentration of suspended and retained carbon nanoparticles at different locations of the composite needs to be established in order to allow model validation. Thermogravimetric analysis (TGA) can be utilised to access particle concentration in the resin. This method can be utilised as long as the relative content of filler in the specimen tested is higher than the residual weight of the pan and resin. CNP contents lower than 0.3 wt.% are extremely difficult to access, without the use of preliminary processes where controlled degradation of the resin at temperatures below the carbon degradation, would allow to concentrate a specific amount of material. These measurements would allow a better description of the kinetics of filtration, by incorporation of a coefficient of filtration which is a function of retained particles and changes as filling progresses.

The phenomenon of filtration plays an important role in the morphology of the final multiscale composite, with high filtration effects observed in injection of material with unmodified nanotubes, leading to significant gradients in nanofiller concentration. This naturally leads to gradients of properties, especially electrical conductivity, in the cured component. Although this can be considered a problem, it could also be seen as an opportunity offered by the possibility of introducing high carbon nanoparticle loading into critical areas of the component where high electrical conductivity is required. The models developed in this study allow process design of these multiscale composites around this concept. Modification of boundary conditions is an example of this, allowing control over the distribution of carbon nanoparticle concentration in the composite structures produced, for the cases where localised or uniform properties are required.

9.2 Suggestions for further research

Validation of the 1-D flow and filtration model

The flow and filtration non-linear model proposed in this study requires validation, especially of the viscosity dependence on suspended concentration and the filtration kinetics equation. The viscosity dependence on concentration of suspended particles can be checked by evaluating the viscosity response of different filler contents dispersed similarly in epoxy for a selected CNT/resin system. The development of methodologies which allow accurate evaluation of the concentration of particles at different locations and/or at specified times can be useful in describing the kinetics of filtration for a particular system.

Development of new modelling approaches for LCM of CNP loaded thermosets

Improvements to the 1-D flow and filtration macroscopic model developed in this study could be implemented in future research, by the incorporation of microscopic models which account for pore and aggregate size distributions, as well as interactions between particles, suspended fluid and fibre walls, as well as viscosity dependence on shear rate at the intra-tow pores. In addition, the development of a 2-D model, can offer advantages in predicting flow and filler concentration gradients for peripheral or central infusion scenaria, for filling of complex shaped components and through thickness infusions with a significant planar flow component.

Fabrication of electrically optimised CNP hybrid composites for lightning strike protection applications

Electrically conductive CNP filled composites have been obtained for carbon composites, as shown in Figure 5.25. The capability of optimising liquid moulding processes of CNT modified thermosets is extremely important in order to achieve adequate concentration distribution, hence properties profile capable of providing dissipation of high currents carried by lightning strikes, without compromising the integrity of the composite structure. The relationship between particle distribution profiles, particle concentration and the corresponding electrical properties needs to be

known in order to meet the electrical behaviour requirements required for lightning strike protection.

Investigation of the potential of CNP/epoxy films of varied thickness for providing maximal toughness to multiscale composite

Delamination properties might have been hindered by the level of constraining caused by the fibre reinforcement to the plastic zone. The ability to maximise fibre composites toughness when utilising suspensions of randomly dispersed CNP to impregnate the preform, could rely on the capability of controlling the thickness of the interlaminar resin-rich layer to values identical to the dimension of the plastic zone of the corresponding nanocomposite system. The incorporation of nanomodified epoxy films with controlled thicknesses at the interlaminar region can be investigated for a range of different carbon nanoparticles and loadings.

10 Conclusions

The main conclusions of this study are:

- Electrical conductivity can be utilised to assess the state of dispersion of CNPs in epoxy resins.
- CNTs can provide enhanced electrical conductivity at lower loadings than CNFs and surface modified CNTs.
- For the purpose of enhancing nanocomposites electrical conductivity: high shear mixing is a better way of dispersing CNFs in the epoxy of this study, while ultrasonication is a better technique of dispersing unmodified CNTs.
- Manufacturing of CNP multiscale composites requires adaptation of conventional composites processing by incorporation of a dispersion step and the modification of the degassing stage.
- Unmodified CNPs are more prone to filtering by the fibrous reinforcement than surface modified CNTs.
- Unmodified carbon nanoparticle filled suspensions do not follow a linear Darcy flow behaviour.
- Electrical conductivity almost doubles for 0.25 wt% unmodified CNP carbon fibre composites, whilst a modest increase of one order of magnitude occurs in fibrous glass composites.
- Electrical conductivity measurements can be utilised to assess particle filtration by the fibrous reinforcement.
- 0.25 wt% and 0.5 wt% CNP loadings led to a modest increase of the nanocomposites uniaxial compressive yield stress.
- CNPs at 0.25 wt% did not provide statistically significant improvements of carbon composites toughness.
- CNFs provide the highest increase in initiation toughness.
- Toughening mechanisms for rod-shaped particles, like CNT bridging and pull-out as well as potential localised inelastic deformation are present, however the extent at which they occur is not sufficient to cause significant improvement on composites toughness.

- An analytical solution of the 1-D linear flow and filtration problem is possible.
- The non-linear finite difference scheme developed is stable and consistent.
- The range of applicability of the analytical model is limited to lower filtration coefficients and shorter filling lengths, while the numerical model offers a solution outside this range.
- The models developed here can be used for designing a process resulting in prescribed nanoparticle concentration distributions

References

1. Chung, D. (2002), Composites get smart, *Materials Today*, **5**(1), p. 30-35.

2. LM Wind Power, Full-scale testing (2011), available from: http://www.lmwindpower.com/Blades/Products/Reliability/Fullscale%20test.aspx/ (accessed 12th September 2011).

3. Composites World, Lightning strike protection for composite structures (2009), available from: http://www.compositesworld.com/articles/lightning-strike-protection-for-composite-structures/ (accessed 9th October 2011).

4. Bekyarova, E., Thostenson, E., Yu, A., Kim, H. *et al.* (2007), Multiscale carbon nanotube-carbon fiber reinforcement for advanced epoxy composites, *Langmuir*, **23**(7), p. 3970-3974.

5. Kupke, M., Wentzel, H.-P. and Schulte, K. (1998), Electrically conductive glass fibre reinforced epoxy resin, *Materials Research Innovations*, **2**(3), p. 164-169.

6. Böger, L., Wichmann, M., Meyer, L. and Schulte, K. (2008), Load and health monitoring in glass fibre reinforced composites with an electrically conductive nanocomposite epoxy matrix, *Composites Science and Technology*, **68**(7-8), p. 1886-1894.

7. Fiedler, B., Gojny, F. H., Wichmann, M., Bauhofer, W. *et al.* (2004), Can carbon nanotubes be used to sense damage in composites?, *Annales de Chimie*, **29**(6), p. 81-94.

8. Thostenson, E. T. and Chou, T. W. (2006), Carbon nanotube networks: sensing of distributed strain and damage for life prediction and self healing, *Advanced Materials*, **18**(21), p. 2837-2841.

9. Barkoula, N., Paipetis, A., Matikas, T., Vavouliotis, A. *et al.* (2009), Environmental degradation of carbon nanotube-modified composite laminates: a study of electrical resistivity, *Mechanics of Composite Materials*, **45**(1), p. 21-32.

10. Kupke, M., Schulte, K. and Schüler, R. (2001), Non-destructive testing of FRP by d.c. and a.c. electrical methods, *Composites Science and Technology*, **61**(6), p. 837-847.

11. Netcomposites (2011), available from: http://www.netcomposites.com/ (accessed 23rd July 2011).

12. Fan, Z., Hsiao, K.-T. and Advani, S. G. (2004), Experimental investigation of dispersion during flow of multi-walled carbon nanotube/polymer suspension in fibrous porous media, *Carbon*, **42**(4), p. 871-876.

13. Gojny, F. H., Wichmann, M. H. G., Fiedler, B., Bauhofer, W. *et al.* (2005), Influence of nano-modification on the mechanical and electrical properties of conventional fibre-reinforced composites, *Composites Part A*, **36**(11), p. 1525-1535.

14. Iwahori, Y., Ishiwata, S., Sumizawa, T. and Ishikawa, T. (2005), Mechanical properties improvements in two-phase and three-phase composites using carbon nano-fiber dispersed resin, *Composites Part A*, **36**(10), p. 1430-1439.

15. Wichmann, M. H. G., Sumfleth, J., Gojny, F. H., Quaresimin, M. *et al.* (2006), Glass-fibre-reinforced composites with enhanced mechanical and electrical properties - Benefits and limitations of a nanoparticle modified matrix*, Engineering Fracture Mechanics*, **73**(16), p. 2346-2359.

16. Kim, M., Park, Y. B., Okoli, O. I. and Zhang, C. (2009), Processing, characterization, and modeling of carbon nanotube-reinforced multiscale composites*, Composites Science and Technology*, **69**(3-4), p. 335-342.

17. Thostenson, E. T., Gangloff, J. J., Li, C. Y. and Byun, J. H. (2009), Electrical anisotropy in multiscale nanotube/fiber hybrid composites*, Applied Physics Letters*, **95**(7), p. 073111.

18. Qiu, J. J., Zhang, C., Wang, B. and Liang, R. (2007), Carbon nanotube integrated multifunctional multiscale composites*, Nanotechnology*, **18**(27), p. 1-11.

19. Zhou, Y., Pervin, F., Lewis, L. and Jeelani, S. (2008), Fabrication and characterization of carbon/epoxy composites mixed with multi-walled carbon nanotubes*, Materials Science and Engineering: A*, **475**(1-2), p. 157-165.

20. Qian, H., Greenhalgh, E. S., Shaffer, M. S. P. and Bismarck, A. (2010), Carbon nanotube-based hierarchical composites: a review*, Journal of Materials Chemistry*, **20**(23), p. 4751-4762.

21. Fiedler, B., Gojny, F. H., Wichmann, M. H. G., Nolte, M. C. M. *et al.* (2006), Fundamental aspects of nano-reinforced composites*, Composites Science and Technology*, **66**(16), p. 3115-3125.

22. Thostenson, E. T., Ren, Z. and Chou, T.-W. (2001), Advances in the science and technology of carbon nanotubes and their composites: a review*, Composites Science and Technology*, **61**(13), p. 1899-1912.

23. Freiman, S. W., Hooker, S., Migler, K. and Arepalli, S. (2008), Measurement issues in single-wall carbon nanotubes, Special Publication (SP) 960-19, National Institute of Standards and Technology (NIST) - U.S. Department of Commerce,

24. Kovacs, J. Z., Velagala, B. S., Schulte, K. and Bauhofer, W. (2007), Two percolation thresholds in carbon nanotube epoxy composites*, Composites Science and Technology*, **67**(5), p. 922-928.

25. Grossiord, N., Loos, J., Regev, O. and Koning, C. E. (2006), Toolbox for dispersing carbon nanotubes into polymers to get conductive nanocomposites*, Chemistry of Materials*, **18**(5), p. 1089-1099.

26. Xie, X.-L., Mai, Y.-W. and Zhou, X.-P. (2005), Dispersion and alignment of carbon nanotubes in polymer matrix: A review*, Materials Science and Engineering Reports*, **49**(4), p. 89-112.

27. Ma, P.-C., Siddiqui, N. A., Marom, G. and Kim, J.-K. (2010), Dispersion and functionalization of carbon nanotubes for polymer-based nanocomposites: A review*, Composites Part A: Applied Science and Manufacturing*, **41**(10), p. 1345-1367.

28. Advani, S. G. (2007), *Processing and properties of nanocomposites*, World Scientific Publishing Co Pte Ltd, Singapore.

29. Kashiwagi, T., Fagan, J., Douglas, J. F., Yamamoto, K. *et al.* (2007), Relationship between dispersion metric and properties of PMMA/SWNT nanocomposites*, Polymer*, **48**(16), p. 4855-4866.

30. Battisti, A., Skordos, A. A. and Partridge, I. K. (2009), Monitoring dispersion of carbon nanotubes in a thermosetting polyester resin*, Composites Science and Technology*, **69**(10), p. 1516-1520.

31. Sandler, J., Shaffer, M. S. P., Prasse, T., Bauhofer, W. *et al.* (1999), Development of a dispersion process for carbon nanotubes in an epoxy matrix and the resulting electrical properties*, Polymer*, **40**(21), p. 5967-5971.

32. Gojny, F. H., Wichmann, M. H. G., Köpke, U., Fiedler, B. *et al.* (2004), Carbon nanotube-reinforced epoxy-composites: enhanced stiffness and fracture toughness at low nanotube content*, Composites Science and Technology*, **64**(15), p. 2363-2371.

33. Thostenson, E. T. and Chou, T.-W. (2006), Processing-structure-multi-functional property relationship in carbon nanotube/epoxy composites*, Carbon*, **44**(14), p. 3022-3029.

34. Kim, J. A., Seong, D. G., Kang, T. J. and Youn, J. R. (2006), Effects of surface modification on rheological and mechanical properties of CNT/epoxy composites*, Carbon*, **44**(10), p. 1898-1905.

35. Shaffer, M. S. P., Fan, X. and Windle, A. H. (1998), Dispersion and packing of carbon nanotubes*, Carbon*, **36**(11), p. 1603-1612.

36. Sadeghian, R., Gangireddy, S., Minaie, B. and Hsiao, K.-T. (2006), Manufacturing carbon nanofibers toughened polyester/glass fiber composites using vacuum assisted resin transfer molding for enhancing the mode-I delamination resistance*, Composites Part A: Applied Science and Manufacturing*, **37**(10), p. 1787-1795.

37. Zhang, Q., Liu, J., Sager, R., Dai, L. *et al.* (2009), Hierarchical composites of carbon nanotubes on carbon fiber: Influence of growth condition on fiber tensile properties*, Composites Science and Technology*, **69**(5), p. 594-601.

38. Garcia, E. J., Wardle, B. L., John Hart, A. and Yamamoto, N. (2008), Fabrication and multifunctional properties of a hybrid laminate with aligned carbon nanotubes grown *in situ, Composites Science and Technology*, **68**(9), p. 2034-2041.

39. Wicks, S. S., de Villoria, R. G. and Wardle, B. L. (2010), Interlaminar and intralaminar reinforcement of composite laminates with aligned carbon nanotubes*, Composites Science and Technology*, **70**(1), p. 20-28.

40. Liao, Y. H., Liang, Z., Park, Y. B., Wang, B. *et al.* (2006), Fabrication and characterization of carbon nanotube/glass fiber-reinforced multiscale composites, in: *47th AIAA/ASME/ASCE/AHS/ASC Structures, Structural Dynamics, and Materials Conference*, Vol.Newport, Rhode Island, 1-4 May 2006, Newport, Rhode Island.

41. Prolongo, S. G., Gude, M. R. and Urena, A. (2010), Rheological behaviour of nanoreinforced epoxy adhesives of low electrical resistivity for joining carbon fiber/epoxy laminates, *Journal of Adhesion Science and Technology*, **24**(6), p. 1097-1112.

42. Garcia, E. J., Wardle, B. L. and John Hart, A. (2008), Joining prepreg composite interfaces with aligned carbon nanotubes, *Composites Part A*, **39**(6), p. 1065-1070.

43. Alvarez, A. C., Bedrikovetsky, P. G., Hime, G., Marchesin, A. O. *et al.* (2006), A fast inverse solver for the filtration function for flow of water with particles in porous media, *Inverse Problems*, **22**(1), p. 69-88.

44. Shapiro, A. A., Bedrikovetsky, P. G., Santos, A. and Medvedev, O. O. (2007), A stochastic model for filtration of particulate suspensions with incomplete pore plugging, *Transport in Porous Media*, **67**(1), p. 135-164.

45. Santos, A., Bedrikovetsky, P. and Fontoura, S. (2008), Analytical micro model for size exclusion: Pore blocking and permeability reduction, *Journal of Membrane Science*, **308**(1-2), p. 115-127.

46. Iliuta, I. and Larachi, F. (2005), Modeling simultaneous biological clogging and physical plugging in trickle-bed bioreactors for wastewater treatment, *Chemical Engineering Science*, **60**(5), p. 1477-1489.

47. Geissler, S., Wintgens, T., Melin, T., Vossenkaul, K. *et al.* (2005), Modelling approaches for filtration processes with novel submerged capillary modules in membrane bioreactors for wastewater treatment, *Desalination*, **178**(1-3), p. 125-134.

48. Kanti Sen, T. and Khilar, K. C. (2006), Review on subsurface colloids and colloid-associated contaminant transport in saturated porous media, *Advances in Colloid and Interface Science*, **119**(2-3), p. 71-96.

49. Ryan, J. N. and Elimelech, M. (1996), Colloid mobilization and transport in groundwater, *Colloids and Surfaces A: Physicochemical and Engineering Aspects*, **107**, p. 1-56.

50. Vengimalla, R., Chase, G. G. and Ramarao, B. V. (1999), Modeling of filler retention in compressible fibrous media, *Separation and Purification Technology*, **15**(2), p. 153-161.

51. Grant, D. C., Liu, B. Y. H., Fisher, W. G. and Bowling, R. A. (1989), Particle capture mechanisms in gases and liquids: An analysis of operative mechanisms in membrane/fibrous filters, *The Journal of Environmental Sciences*, **32**(4), p. 43-51

52. Tien, C. and Payatakes, A. C. (1979), Advances in deep bed filtration, *American Institute of Chemical Engineers*, **25**(5), p. 737-759.

53. Induceramic, Filtration & Separation Application (2011), available from: http://www.induceramic.com/porous-ceramics-application/filtration-separation-application (accessed 15th June 2011).

54. Herzig, J. P., Leclerc, D. M. and Goff, P. L. (1970), Flow of suspensions through porous media - Application to deep filtration, *Industrial & Engineering Chemistry*, **62**(5), p. 8-35.

55. Sharma, M. M. and Yortsos, Y. C. (1987), Transport of particulate suspensions in porous media: Model formulation*, American Institute of Chemical Engineers*, **33**(10), p. 1636-1643.

56. Sharma, M. M. and Yortsos, Y. C. (1987), A network model for deep bed filtration processes*, American Institute of Chemical Engineers*, **33**(10), p. 1644-1653.

57. Sharma, M. M. and Yortsos, Y. C. (1987), Fines migration in porous media*, American Institute of Chemical Engineers*, **33**(10), p. 1654-1662.

58. Maroudas, A. and Eisenklam, P. (1965), Clarification of suspensions: a study of particle deposition in granular media: Part I - Some observations on particle deposition*, Chemical Engineering Science*, **20**(10), p. 867-873.

59. Sakthivadivel, R. (1969), Clogging of a granular porous medium by sediment, Report HEL, University of California, Berkely.

60. National Institute for Occupational Safety and Health (NIOSH), N95 Respirators and Surgical Masks (2011), available from: http://www.cdc.gov/niosh/blog/nsb101409_respirator.html (accessed 11th June 2011).

61. Ives, K. J. (1975), *The Scientific Basis of Filtration*. NATO Advanced Study Institute Series, NATO Scientific Affairs Division.

62. Jegatheesan, V. and Vigneswaran, S. (2005), Deep bed filtration: Mathematical models and observations*, Critical Reviews in Environmental Science and Technology*, **35**(6), p. 515-569.

63. Darcy, H. (1856), *Les fontaines publiques de la ville de Dijon*. Exposition et application des principes a suivre et des formules a employer dans les questions de distribution d'eau, Dalmont, Victor, Paris.

64. Iwasaki, T. (1937), Some notes on sand filtration*, Journal of the American Water Works Association*, **29**, p. 1591-1602.

65. Mohanka, S. S. (1969), Theory of multilayer filtration*, Journal of the Sanitary Enginnering Division, ASCE*, **95**, p. 1079-1095.

66. Wennberg, K. E. and Sharma, M. M. (1997), Determination of the filtration coefficient and the transition time for water injection wells, in: *European Formation Damage Conference*, Society of Petroleum Engineers, Inc., 2-3 June 1997, The Hague, Netherlands.

67. Destephen, J. A. and Choi, K. J. (1996), Modelling of filtration processes of fibrous filter media*, Separations Technology*, **6**(1), p. 55-67.

68. Altoé F, J. E., Bedrikovetsky, P., Siqueira, A. G., de Souza, A. L. S. *et al.* (2006), Correction of basic equations for deep bed filtration with dispersion*, Journal of Petroleum Science and Engineering*, **51**(1-2), p. 68-84.

69. Elgafy, A. and Khalid, L. (2006), Carbon nanoparticle-filled polymer flow in the fabrication of novel fiber composites*, Carbon*, **44**(9), p. 1682-1689.

70. Elgafy, A. and Khalid, L. (2007), Engineering solution in monitoring nanoparticle-fluid flow during nanocomposites processing*, Journal of Nanoparticle Research*, **9**(3), p. 441-454.

71. Lam, Y. C., Chen, X., Tan, K. W., Chai, J. C. *et al.* (2004), Numerical investigation of particle migration in poiseuille flow of composite system*, Composites Science and Technology*, **64**(7-8), p. 1001-1010.

72. Fernberg, S. P., Sandlund, E. J. and Lundstrom, T. S. (2006), Mechanisms controlling particle distribution in infusion molded composites*, Journal of Reinforced Plastics and Composites*, **25**(1), p. 59-70.

73. Nordlund, M., Fernberg, S. P. and Lundström, T. S. (2007), Particle deposition mechanisms during processing of advanced composite materials*, Composites Part A: Applied Science and Manufacturing*, **38**(10), p. 2182-2193.

74. Erdal, M., Güçeri, S. and Danforth, S. C. (1999), Impregnation molding of particle-filled preceramic polymers: Process modeling*, Journal of the American Ceramic Society*, **82**(8), p. 2017-2028.

75. Chohra, M., Advani, S. G., Gokce, A. and Yarlagadda, S. (2006), Modeling of filtration through multiple layers of dual scale fibrous porous media*, Polymer Composites*, **27**(5), p. 570-581.

76. Lefevre, D., Comas-Cardona, S., Binetruy, C. and Krawczak, P. (2007), Modelling the flow of particle-filled resin through a fibrous preform in liquid composite molding technologies*, Composites Part A: Applied Science and Manufacturing*, **38**(10), p. 2154-2163.

77. Lefevre, D., Comas-Cardona, S., Binetruy, C. and Krawczak, P. (2009), Coupling filtration and flow during liquid composite molding: Experimental investigation and simulation*, Composites Science and Technology*, **69**(13), p. 2127-2134.

78. Akinyede, O., Sankar, J., Mohan, R. and Kelkar, A. (2007), Investigation of particulate filtration of alumina nano-particles in VARTM processing of hybrid composites*, ASME Conference Proceedings*, **2007**(43076), p. 157-162.

79. Gojny, F. H., Wichmann, M. H. G., Fiedler, B., Kinloch, I. A. *et al.* (2006), Evaluation and identification of electrical and thermal conduction mechanisms in carbon nanotube/epoxy composites*, Polymer*, **47**(6), p. 2036-2045.

80. Bauhofer, W. and J.Z., K. (2009), A review and analysis of electrical percolation in carbon nanotube polymer composites*, Composites Science and Technology*, **69**(10), p. 1486-1498.

81. Clingerman, M. L., Weber, E. H., King, J. A. and Schulz, K. H. (2003), Development of an additive equation for predicting the electrical conductivity of carbon-filled composites*, Journal of Applied Polymer Science*, **88**(9), p. 2280-2299.

82. Kirkpatrick, S. (1973), Percolation and conduction*, Reviews of Modern Physics*, **45**(4), p. 574-588.

83. Balberg, I., Anderson, C. H., Alexander, S. and Wagner, N. (1984), Excluded volume and its relation to the onset of percolation*, Physical Review B*, **30**(7), p. 3933-3943

84. Celzard, A., McRae, E., Deleuze, C., Dufort, M. *et al.* (1996), Critical concentration in percolating systems containing a high-aspect-ratio filler*, Physical Review B: Condensed Matter*, **53**(10), p. 6209-6214.

85. Martin, C. A., Sandler, J. K. W., Shaffer, M. S. P., Schwarz, M. K. *et al.* (2004), Formation of percolating networks in multi-wall carbon-nanotube-epoxy composites*, Composites Science and Technology*, **64**(15), p. 2309-2316.

86. Schueler, R., Petermann, J., Schulte, K. and Wentzel, H.-P. (1997), Agglomeration and electrical percolation behavior of carbon black dispersed in epoxy resin*, Journal of Applied Polymer Science*, **63**(13), p. 1741-1746.

87. Bauhofer, W. and Kovacs, J. Z. (2009), A review and analysis of electrical percolation in carbon nanotube polymer composites*, Composites Science and Technology*, **69**(10), p. 1486-1498.

88. Lee, S.-B., Choi, O., Lee, W., Yi, J.-W. *et al.* (2011), Processing and characterization of multi-scale hybrid composites reinforced with nanoscale carbon reinforcements and carbon fibers*, Composites Part A: Applied Science and Manufacturing*, **42**(4), p. 337-344.

89. Owston, C. N. (1970), Electrical properties of single carbon fibres*, Journal of Physics D: Applied Physics*, **3**(11), p. 1615.

90. Schulte, K. and Baron, C. (1989), Load and failure analyses of CFRP laminates by means of electrical resistivity measurements*, Composites Science and Technology*, **36**(1), p. 63-76.

91. Vavouliotis, A., Tsotra, P., Kostopoulos, V., Karapappas, P. *et al.* (2006), MWCNT-modified fiber reinforced composites with nano-sensing capabilities: A way towards the development of the new functional materials for space applications, in: *AIAA 57th International Astronautical Congress, IAC 2006*, Vol.8, 2-6 October 2006, Valencia, Spain, p. 5523-5530.

92. Veedu, V. P., Cao, A. Y., Li, X. S., Ma, K. G. *et al.* (2006), Multifunctional composites using reinforced laminae with carbon-nanotube forests*, Nature Materials*, **5**(6), p. 457-462.

93. Brandt, J., Drechsler, K. and Arendts, F. J. (1996), Mechanical performance of composites based on various three-dimensional woven-fibre preforms*, Composites Science and Technology*, **56**(3), p. 381-386.

94. Dell'Anno, G., Cartié, D. D., Partridge, I. K. and Rezai, A. (2007), Exploring mechanical property balance in tufted carbon fabric/epoxy composites*, Composites Part A: Applied Science and Manufacturing*, **38**(11), p. 2366-2373.

95. Jain, L. K. and Mai, Y.-W. (1995), Determination of mode II delamination toughness of stitched laminated composites*, Composites Science and Technology*, **55**(3), p. 241-253.

96. Yan, W., Liu, H.-Y. and Mai, Y.-W. (2004), Mode II delamination toughness of z-pinned laminates*, Composites Science and Technology*, **64**(13-14), p. 1937-1945.

97. Lee, L., Rudov-Clark, S., Mouritz, A. P., Bannister, M. K. *et al.* (2002), Effect of weaving damage on the tensile properties of three-dimensional woven composites, *Composite Structures*, **57**(1-4), p. 405-413.

98. Mouritz, A. P. and Cox, B. N. (2010), A mechanistic interpretation of the comparative in-plane mechanical properties of 3D woven, stitched and pinned composites, *Composites Part A: Applied Science and Manufacturing*, **41**(6), p. 709-728.

99. Treiber, J. W. G. (2011), Performance of tufted carbon fibre/epoxy composites, (unpublished PhD thesis), School of Applied Sciences (SAS), Composites Centre, Cranfield University, Cranfield.

100. Bucknall, C. B. and Partridge, I. K. (1983), Phase separation in epoxy resins containing polyethersulphone, *Polymer*, **24**(5), p. 639-644.

101. Wilkinson, S. P., Ward, T. C. and McGrath, J. E. (1993), Effect of thermoplastic modifier variables on toughening a bismaleimide matrix resin for high-performance composite materials, *Polymer*, **34**(4), p. 870-884.

102. Kinloch, A. J., Shaw, S. J. and Hunston, D. L. (1983), Deformation and fracture behaviour of a rubber-toughened epoxy: 2. Failure criteria, *Polymer*, **24**(10), p. 1355-1363.

103. Bandyopadhyay, S. (1990), Review of the microscopic and macroscopic aspects of fracture of unmodified and modified epoxy resins, *Materials Science and Engineering: A*, **125**(2), p. 157-184.

104. Moloney, A., Kausch, H., Kaiser, T. and Beer, H. (1987), Parameters determining the strength and toughness of particulate filled epoxide resins, *Journal of Materials Science*, **22**(2), p. 381-393.

105. Norman, D. A. and Robertson, R. E. (2003), Rigid-particle toughening of glassy polymers, *Polymer*, **44**(8), p. 2351-2362.

106. Johnsen, B. B., Kinloch, A. J., Mohammed, R. D., Taylor, A. C. *et al.* (2007), Toughening mechanisms of nanoparticle-modified epoxy polymers, *Polymer*, **48**(2), p. 530-541.

107. Kinloch, A. J. and Taylor, A. C. (2002), The toughening of cyanate-ester polymers: Part I. Physical modification using particles, fibres and woven-mats, *Journal of Materials Science*, **37**(3), p. 433-460.

108. Gojny, F. H., Wichmann, M. H. G., Fiedler, B. and Schulte, K. (2005), Influence of different carbon nanotubes on the mechanical properties of epoxy matrix composites - A comparative study, *Composites Science and Technology*, **65**(15-16), p. 2300-2313.

109. Faber, K. T. and Evans, A. G. (1983), Crack deflection processes - 1. THEORY, *Acta Metallurgica*, **31**(4), p. 565-576.

110. Vasconcelos, H. C. and Barreto, M. C. (2011), Tailoring the microstructure of sol-gel derived hydroxyapatite/zirconia nanocrystalline composites, *Nanoscale Research Letters*, **6**(20), p. 1-5.

111. Fiedler, B., Gojny, F. H., Wichmann, M. H. G., Nolte, M. C. M. *et al.* (2006), Fundamental aspects of nano-reinforced composites*, Manufacturing, Processing and Characterisations of Polymer Composites*, **66**(16), p. 3115-3125.

112. Kinloch, A. J. and Young, R. J. (1983), *Fracture behaviour of polymers*. 1st ed, Applied Science Publishers.

113. Gojny, F. H., Wichmann, M. H. G., Kopke, U., Fiedler, B. *et al.* (2004), Carbon nanotube-reinforced epoxy-compo sites: enhanced stiffness and fracture toughness at low nanotube content*, Composites Science and Technology*, **64**(15), p. 2363-2371.

114. Cheng, Q. F., Wang, J. P., Wen, J. J., Liu, C. H. *et al.* (2010), Carbon nanotube/epoxy composites fabricated by resin transfer molding*, Carbon*, **48**(1), p. 260-266.

115. Lachman, N. and Daniel Wagner, H. (2010), Correlation between interfacial molecular structure and mechanics in CNT/epoxy nano-composites*, Composites Part A: Applied Science and Manufacturing*, **41**(9), p. 1093-1098.

116. Sager, R. J., Klein, P. J., Lagoudas, D. C., Warren, G. L. *et al.* (2008), Fracture toughness of woven carbon fiber/epoxy laminates with carbon nanotube/epoxy thin films in: *49th AIAA/ASME/ASCE/AHS/ASC Structures, Structural Dynamics, and Materials Conference*, 7-10 April 2008, Schaumburg p.

117. Partridge, I. K. and Cartie, D. D. R. (2004), Suppression of initiation of delamination cracking in unidirectional composites by self-same resin interleaving, in: Moore, D. R., (editor), *The Application of Fracture Mechanics to Polymers, Adhesives and Composites*, Vol. 33, European Structural Integrity Society, Elsevier, p. 265-272.

118. Arai, M., Noro, Y., Sugimoto, K.-i. and Endo, M. (2008), Mode I and mode II interlaminar fracture toughness of CFRP laminates toughened by carbon nanofiber interlayer*, Composites Science and Technology*, **68**(2), p. 516-525.

119. Godara, A., Mezzo, L., Luizi, F., Warrier, A. *et al.* (2009), Influence of carbon nanotube reinforcement on the processing and the mechanical behaviour of carbon fiber/epoxy composites*, Carbon*, **47**(12), p. 2914-2923.

120. Thostenson, E. T., Li, W. Z., Wang, D. Z., Ren, Z. F. *et al.* (2002), Carbon nanotube/carbon fiber hybrid multiscale composites*, Journal of Applied Physics*, **91**(9), p. 6034-6037.

121. Kepple, K. L., Sanborn, G. P., Lacasse, P. A., Gruenberg, K. M. *et al.* (2008), Improved fracture toughness of carbon fiber composite functionalized with multi walled carbon nanotubes*, Carbon*, **46**(15), p. 2026-2033.

122. Blanco, J., Garcia, E. J., De Villoria, R. G. and Wardle, B. L. (2009), Limiting Mechanisms of Mode I Interlaminar Toughening of Composites Reinforced with Aligned Carbon Nanotubes*, Journal of Composite Materials*, **43**(8), p. 825-841.

123. Treiber, J. W. G., Cartie, D. D. R. and Partridge, I. K. (2011), Delamination behaviour of tufted non-crimped carbon fibre fabric/epoxy composites*, Engineering of Fracture Mechanics*, (submited).

124. Huntsman (2006), LY564/HY2954 material data sheet

125. Pyrograf Products Inc., Pyrograf®-III Carbon Nanofiber (2011), available from: http://pyrografproducts.com/Merchant5/merchant.mvc?Screen=cp_nanofiber (accessed 24th August 2011).

126. Pyrograf-III, Pyrograf®-III (2001), available from: http://www.apsci.com/ppi-pyro3.html (accessed 24th August 2011).

127. Mijovic, J. and Yee, C. F. W. (1994), Use of complex impedance to monitor the progress of reactions in epoxy/amine model systems, *Macromolecules*, **27**(25), p. 7287-7293.

128. Salinas-Ruiz, M. (2009), Development of a rubber toughened epoxy adhesive loaded with carbon nanotubes, for aluminium – polymer bonds, (unpublished PhD thesis), School of Applied Sciences (SAS), Composites Centre, Cranfield University, Cranfield.

129. Fleischer, M., Wagner, V., Hacker, G. and Meixner, H. (1995), Comparision of a.c. and d.c. measurement techniques using semiconducting Ga_2O_3 sensors, *Sensors and Actuators B: Chemical*, **26**(1-3), p. 85-88.

130. Skordos, A. A. (2000), Modelling and monitoring of resin transfer moulding, (unpublished PhD thesis), School of Applied Sciences (SAS), Composites Centre, Cranfield University, Cranfield.

131. Kremer, F. and Schonhals, A. (2003), *Broadband dielectric spectroscopy*. 2nd ed, Springer.

132. Battisti, A. and et al. (2009), Dielectric monitoring of carbon nanotube network formation in curing thermosetting nanocomposites, *Journal of Physics D: Applied Physics*, **42**(15), p. 155402.

133. Irvine, J. T. S., Sinclair, D. C. and West, A. R. (1990), Electroceramics: Characterization by Impedance Spectroscopy, *Advanced Materials*, **2**(3), p. 132-138.

134. Skordos, A. A. and Partridge, I. K. (2004), Determination of the degree of cure under dynamic and isothermal curing conditions with electrical impedance spectroscopy, *Journal of Polymer Science Part B: Polymer Physics*, **42**(1), p. 146-154.

135. Alif, N., Carlsson, L. A. and Boogh, L. (1998), The effect of weave pattern and crack propagation direction on mode I delamination resistance of woven glass and carbon composites, *Composites Part B: Engineering*, **29**(5), p. 603-611.

136. Brunner, A. J. and Blackman, B. R. K. (2003), Delamination fracture in cross-ply laminates: What can be learned from experiment?, in: Williams, J., Pavan, A. and Blackman, B. R. K., (editors), *Fracture of Polymers, Composites and Adhesives II (3rd ESIS TC4 Conference)*, Vol. 32, European Structural Integrity Society, Elsevier, p. 433-444.

137. Karapappas, P., Vavouliotis, A., Tsotra, P., Kostopoulos, V. *et al.* (2009), Enhanced fracture properties of carbon reinforced composites by the addition of multi-wall carbon nanotubes, *Journal of Composite Materials*, **43**(9), p. 977-985.

138. Yokozeki, T., Iwahori, Y., Ishiwata, S. and Enomoto, K. (2007), Mechanical properties of CFRP laminates manufactured from unidirectional prepregs using CSCNT-dispersed epoxy, *Composites Part A: Applied Science and Manufacturing*, **38**(10), p. 2121-2130.

139. Kinloch, A. J. and Shaw, S. J. (1981), The fracture resistance of a toughened epoxy adhesive*, The Journal of Adhesion*, **12**(1), p. 59-77.

140. Huntsman, Composite Resins Selector Guide (2011), available from: http://www.huntsman.com/advanced_materials/Media/GENERAL_INDUSTRY_SG.pdf (accessed 11th July 2011).

141. Gebart, B. R. (1992), Permeability of unidirectional reinforcements for RTM*, Journal of Composite Materials*, **26**(8), p. 1100-1133.

142. Advani, S. G. and Sozer, E. M. (2010), *Process modeling in composites manufacturing*. 2nd ed. Manufacturing Engineering and Materials Processing, CRC Press, New York.

143. Krieger, I. M. and Dougherty, T. J. (1959), A mechanism for non-Newtonian flow in suspensions of rigid spheres*, Transaction of the Society of Rheology: Journal of Rheology* **3**(1), p. 137-152.

Appendices

Appendix A - 1D flow and filtration model code

```
Option Base 1

Option Explicit

Sub run()

Dim i As Integer, j As Integer, M As Integer, n As Integer, Coeffs_Size As Integer, Mesh_Size As Integer, dt As Double

Dim P() As Double, C() As Double, S() As Double, V() As Double, X() As Double

Dim eta() As Double, K() As Double, phi() As Double, Coeffs() As Double, Inf_time() As Double, position As Double, step As Double

'read inputs

Coeffs_Size = Application.Count(Worksheets("inputs").Range("B:B"))

ReDim Coeffs(Coeffs_Size) As Double

For i = 1 To Coeffs_Size

    Coeffs(i) = Cells(i, 2)

Next i

'coeffs(1) Po
'coeffs(2) ko
'coeffs(3) kr
'coeffs(4) Poo
'coeffs(5) Ko
'coeffs(6) Phi
'coeffs(7) eta
'coeffs(8) Vo
'coeffs(9) Co
```

'coeffs(10) Convergence_Limit
'coeffs(11)CNT density
'coeffs(12) Kozeny-Carman constant
'coeffs (13) viscosity of control resin
'coeffs (14) maximum packing fraction (viscosity function)
'coeffs (15) intrinsic viscosity (viscosity function)

'Read mesh

```
Mesh_Size = Application.Count(Worksheets("inputs").Range("C:C"))

ReDim P(Mesh_Size, Mesh_Size) As Double, C(Mesh_Size, Mesh_Size) As Double, S(Mesh_Size, Mesh_Size) As Double 'pos 1st index, time: 2nd index

ReDim V(Mesh_Size) As Double, X(Mesh_Size) As Double, Inf_time(Mesh_Size) As Double

ReDim eta(Mesh_Size, Mesh_Size) As Double, K(Mesh_Size, Mesh_Size) As Double, phi(Mesh_Size, Mesh_Size) As Double

For i = 1 To Mesh_Size

   X(i) = Cells(i + 1, 3)

Next i
```

Initial conditions

```
For i = 1 To Mesh_Size

   C(i, 1) = Coeffs(9)

   P(i, 1) = Coeffs(4)

   S(i, 1) = 0

   phi(i, 1) = porosity(S(i, 1), Coeffs)
```

```
    K(i, 1) = Permeability(C(i, 1), S(i, 1), phi(i, 1), Coeffs)
    eta(i, 1) = Viscosity(C(i, 1), Coeffs)
Next i
V(1) = Coeffs(8)
C(1, 1) = Coeffs(9)
Inf_time(1) = 0
'Incremental solution
For j = 2 To Mesh_Size
    Call Load_Previous_to_Current(j, K)
    Call Load_Previous_to_Current(j, phi)
    Call Load_Previous_to_Current(j, eta)
    Call Load_Previous_to_Current(j, P)
    Call Load_Previous_to_Current(j, C)
    Call Load_Previous_to_Current(j, S)
    Call Solve_Flow_Filtration(j, X, K, phi, eta, P, C, S, V, j, Coeffs, dt)
    Inf_time(j) = Inf_time(j - 1) + dt
Next j
-----------------------------------------------------------------------------------------------------
'output
    Sheet2.Cells(1, 1) = "t/P"
    Sheet3.Cells(1, 1) = "t/S"
```

```
    Sheet4.Cells(1, 1) = "t/C"

    Sheet5.Cells(1, 1) = "t"

    Sheet5.Cells(1, 2) = "F_F"

    Sheet6.Cells(1, 1) = "t"

    Sheet6.Cells(1, 2) = "V"

    Sheet10.Cells(1, 1) = "phi"

    Sheet12.Cells(1, 1) = "K"


For i = 1 To Mesh_Size

    Sheet2.Cells(1, i + 1) = X(i)

    Sheet4.Cells(1, i + 1) = X(i)

    Sheet3.Cells(1, i + 1) = X(i)

    Sheet10.Cells(1, i + 1) = X(i)

    Sheet11.Cells(1, i + 1) = X(i)

    Sheet12.Cells(1, i + 1) = X(i)


Next i

For j = 1 To Mesh_Size

    Sheet2.Cells(j + 1, 1) = Inf_time(j)

    Sheet3.Cells(j + 1, 1) = Inf_time(j)

    Sheet4.Cells(j + 1, 1) = Inf_time(j)
```

```
    Sheet5.Cells(j + 1, 1) = Inf_time(j)
    Sheet5.Cells(j + 1, 2) = X(j)
    Sheet6.Cells(j + 1, 1) = Inf_time(j)
    Sheet6.Cells(j + 1, 2) = V(j)

        For i = 1 To Mesh_Size
        Sheet2.Cells(j + 1, i + 1) = P(i, j)
        Sheet4.Cells(j + 1, i + 1) = C(i, j)
        Sheet3.Cells(j + 1, i + 1) = S(i, j)
        Sheet10.Cells(j + 1, i + 1) = phi(i, j)
        Sheet11.Cells(j + 1, i + 1) = eta(i, j)
        Sheet12.Cells(j + 1, i + 1) = K(i, j)
    Next i
Next j
End Sub
```

```
Sub Load_Previous_to_Current(step As Integer, Arr() As Double)
Dim i As Integer
For i = 1 To UBound(Arr, 1)
    Arr(i, step) = Arr(i, step - 1)
Next i
```

End Sub

Sub Solve_Flow_Filtration(step As Integer, X() As Double, K() As Double, phi() As Double, eta() As Double, P() As Double, C() As Double, S() As Double, V() As Double, Front_Position As Integer, Coeffs() As Double, dt As Double)

dt = (X(Front_Position) - X(Front_Position - 1)) * phi(Front_Position - 1, step - 1) / V(step - 1)

Call Solve_Filtration(step, X, phi, eta, V, C, S, Front_Position, dt, Coeffs())

Call Update_Properties(step, K, phi, eta, C, S, Coeffs(), Front_Position)

Call Solve_Flow(step, X, K, phi, eta, P, V, Front_Position, Coeffs())

End Sub

Sub Solve_Filtration(step As Integer, X() As Double, phi() As Double, eta() As Double, V() As Double, C() As Double, S() As Double, Front_Position As Integer, dt As Double, Coeffs() As Double)

Dim i As Integer, dx As Double

' x=0 C=Co

C(1, step) = Coeffs(9)

'x=flow_front S=0

S(Front_Position, step) = 0

'Filtration kinetics

```
For i = 1 To Front_Position - 1

   S(i, step) = S(i, step - 1) + dt * C(i, step - 1) * Filtr(C(i, step - 1), S(i, step - 1), Coeffs) * V(step - 1) + dt * S(i, step - 1) * Resusp(C(i, step - 1), S(i, step - 1), Coeffs)

Next i

'Mass conservation

For i = 2 To Front_Position

   dx = X(i) - X(i - 1)

 C(i, step) = C(i - 1, step) + dx / V(step - 1) * (-phi(Front_Position - 1, step - 1) *
*(C(i- 1, step) - C(i - 1, step - 1)) / dt - (S(i - 1, step) - S(i - 1, step - 1)) / dt)

Next i

End Sub
```

```
‘Properties Update

Sub Update_Properties(step As Integer, K() As Double, phi() As Double, eta() As Double, C() As Double, S() As Double, Coeffs() As Double, Front_Position As Integer)

Dim i As Integer

For i = 1 To Front_Position

    phi(i, step) = porosity(S(i, step), Coeffs)

   eta(i, step) = Viscosity(C(i, step), Coeffs)

   K(i, step) = Permeability(C(i, step), S(i, step), phi(i, step), Coeffs)

Next i

End Sub
```

‘Material sub-models:

‘Permeability

```
Function Permeability(C As Double, S As Double, phi As Double, Coeffs() As Double)

Permeability = Coeffs(12) * phi ^ 3 / ((1 - phi) ^ 2)

'Permeability = Coeffs(5) 'linear

End Function
```

‘Porosity

```
Function porosity(S As Double, Coeffs() As Double)

porosity = Coeffs(6) - (S / Coeffs(11))

'porosity = Coeffs(6) 'linear

End Function
```

‘Viscosity

```
Function Viscosity(C As Double, Coeffs() As Double)

Viscosity = Coeffs(13) * (1 - (C / (Coeffs(11) * Coeffs(14)))) ^ (Coeffs(14) * Coeffs(15))

'Viscosity = Coeffs(7) 'linear

End Function
```

```
Sub Solve_Flow(step As Integer, X() As Double, K() As Double, phi() As Double, eta() As Double, P() As Double, V() As Double, Front_Position As Integer, Coeffs() As Double)
```

```
Dim i As Integer, n As Integer

n = Front_Position

'Assuming flow control

For i = Front_Position To 2 Step -1

   P(i - 1, step) = Coeffs(8) * (phi(i - 1, step) * eta(i - 1, step) / K(i - 1, step) + (phi(i, step) * eta(i, step) / (K(i, step))) * (X(i) - X(i - 1)) / 2) + P(i, step)

Next i

V(step) = Coeffs(8)

If P(1, step) > Coeffs(1) Then  'Pressure control

   ReDim B(1 To n) As Double

   ReDim a(1 To n, 1 To n) As Double

   Dim AuxP() As Double

   For i = 2 To n - 1

      a(i, i - 1) = (K(i, step) / (eta(i, step)) + (K(i - 1, step)) / eta(i - 1, step))

      a(i, i + 1) = (K(i + 1, step) / eta(i + 1, step)) + (K(i, step) / eta(i, step))

      a(i, i) = -a(i, i - 1) - a(i, i + 1)

   Next i

   'p=po at x=0

   a(1, 2) = 0

   a(1, 1) = 1

   B(1) = Coeffs(1)
```

```
    'p=p∞ at flow front
    a(n, n - 1) = 0
    a(n, n) = 1
    B(n) = Coeffs(4)
    'solve system
    AuxP = SolveSystem(a, B)
    For i = 1 To n
        P(i, step) = AuxP(i)
    Next i
    V(step) = -(K(n, step) + K(n - 1, step)) / (eta(n, step) + eta(n - 1, step)) * ((P(n, step) - P(n - 1, step)) / (X(n) - X(n - 1)))
End If
End Sub
-----------------------------------------------------------------------------------------------------
Function Resusp(C As Double, S As Double, Coeffs() As Double)
Resusp = Coeffs(3)
End Function
-----------------------------------------------------------------------------------------------------
Function Filtr(C As Double, S As Double, Coeffs() As Double)
Filtr = Coeffs(2)
End Function
-----------------------------------------------------------------------------------------------------
```

```
Function SolveSystem(Amat() As Double, Bvec() As Double)

Dim AuxX As Variant

Dim AuxB As Variant

Dim AuxA As Variant

Dim i As Integer

Dim X() As Double

AuxA = Amat

AuxB = Bvec

AuxX = Application.MMult(Application.MInverse(AuxA),
Application.Transpose(AuxB))

ReDim X(LBound(AuxX, 1) To UBound(AuxX, 1))

For i = LBound(AuxX, 1) To UBound(AuxX, 1)

   X(i) = AuxX(i, 1)

Next i

SolveSystem = X

End Function
```

Appendix B - List of publications

- E. Reia da Costa, A.A. Skordos, I.K. Partridge, A. Rezai, *Flow of Carbon Nanoparticle Loaded Epoxy Resin in Liquid Molding*, 17th International Conference on Composite Materials; July 27-31, 2009, Edinburgh, UK

- E. Reia da Costa, A.A. Skordos and I.K. Partridge, *Flow and Filtration Modelling of Carbon Nanoparticle Loaded Thermosets in Liquid Moulding*, 10th International Conference on Flow Processes in Composite Materials; July 11-15, 2010, Ascona, Switzerland

- E. Reia da Costa, A.A. Skordos, I.K. Partridge, A. Rezai, *RTM processing and electrical performance of carbon nanotube modified epoxy/fibre composites*, submitted to Composites Part A : Applied Science and Manufacturing in January 2011

- E. Reia da Costa and A.A. Skordos, *Modelling flow and filtration in liquid composite moulding of nanoparticle loaded thermosets*, submitted to Composites Science and Technology in September 2011